Chiral properties of two-flavour QCD at zero and non-zero temperature

– Dissertation –
zur Erlangung des Doktorgrades
der Naturwissenschaften

vorgelegt beim Fachbereich Physik,
Mathematik und Informatik der
Johannes Gutenberg-Universität Mainz

Institut für Kernphysik

Bastian Benjamin Brandt
geboren in Münster

Mainz, 13. September 2012

Datum der Promotion: **22. November 2012**

Abstract

Lattice Quantum Chromodynamics (LQCD) is the preferred tool for obtaining non-perturbative results from QCD in the low-energy regime. It has by now entered the era in which high precision calculations for a number of phenomenologically relevant observables at the physical point, with dynamical quark degrees of freedom and controlled systematics, become feasible. Despite these successes there are still quantities where control of systematic effects is insufficient. The subject of this thesis is the exploration of the potential of todays state-of-the-art simulation algorithms for non-perturbatively $\mathcal{O}(a)$-improved Wilson fermions to produce reliable results in the chiral regime and at the physical point both for zero and non-zero temperature. Important in this context is the control over the chiral extrapolation. This thesis is concerned with two particular topics, namely the computation of hadronic form factors at zero temperature, and the properties of the phase transition in the chiral limit of two-flavour QCD.

The electromagnetic iso-vector form factor of the pion provides a platform to study systematic effects and the chiral extrapolation for observables connected to the structure of mesons (and baryons). Mesonic form factors are computationally simpler than their baryonic counterparts but share most of the systematic effects. This thesis contains a comprehensive study of the form factor in the regime of low momentum transfer q^2, where the form factor is connected to the charge radius of the pion. A particular emphasis is on the region very close to $q^2 = 0$ which has not been explored so far, neither in experiment nor in LQCD. The results for the form factor close the gap between the smallest spacelike q^2-value available so far and $q^2 = 0$, and reach an unprecedented accuracy at full control over the main systematic effects. This enables the model-independent extraction of the pion charge radius. The results for the form factor and the charge radius are used to test chiral perturbation theory (χPT) and are thereby extrapolated to the physical point and the continuum. The final result in units of the hadronic radius r_0 is

$$\left\langle r_\pi^2 \right\rangle^{\text{phys}} / r_0^2 = 1.87 \, \left({}^{+12}_{-10}\right) \left({}^{+\,4}_{-15}\right) \quad \text{or} \quad \left\langle r_\pi^2 \right\rangle^{\text{phys}} = 0.473 \, \left({}^{+30}_{-26}\right) \left({}^{+10}_{-38}\right) (10) \, \text{fm} \, ,$$

which agrees well with the results from other measurements in LQCD and experiment. Note, that this is the first continuum extrapolated result for the charge radius from LQCD which has been extracted from measurements of the form factor in the region of small q^2.

The order of the phase transition in the chiral limit of two-flavour QCD and the associated transition temperature are the last unkown features of the phase diagram at zero chemical potential. The two possible scenarios are a second order transition in the $O(4)$-universality class or a first order transition. Since direct simulations in the chiral limit are not possible the transition can only be investigated by simulating at non-zero quark mass with a subsequent chiral extrapolation, guided by the universal scaling in the vicinity of the critical point. The thesis presents the setup and first results from a study on this topic. The study provides the ideal platform to test the potential and limits of todays simulation algorithms at finite temperature. The results from a first scan at a constant zero-temperature pion mass of about 290 MeV are promising, and it appears that simulations down to physical quark masses are feasible. Of particular relevance for the order of the chiral transition is the strength of the anomalous breaking of the $U_A(1)$ symmetry at the transition point. It can be studied by looking at the degeneracies of the correlation functions in scalar and pseudoscalar channels. For the temperature scan reported in this thesis the breaking is still pronounced in the transition region and the symmetry becomes effectively restored only above $1.16\,T_C$. The thesis also provides an extensive outline of research perspectives and includes a generalisation of the standard multi-histogram method to explicitly β-dependent fermion actions.

Zusammenfassung

Die Gitter-Quantenchromodynamik (LQCD) ist das bevorzugte Mittel um nicht-perturbative Resultate im Rahmen der Quantenchromodynamik (QCD) im Bereich kleiner Energien zu erhalten. Derzeit befindet sich die LQCD in einer Phase, in der die präzise Berechnung einer Reihe von phänomenologisch relevanten Observablen am physikalischen Punkt mit dynamischen Quarks und voller Kontrolle über systematische Effekte möglich ist. Trotz dieser Erfolge gibt es immer noch Größen, bei denen die Kontrolle über die systematischen Fehler nicht gegeben ist. Der Gegenstand dieser Arbeit ist die Erforschung des Potentials der modernen Simulationsalgorithmen, für $\mathcal{O}(a)$-verbesserte Wilson Fermionen, im chiralen Regime und am physikalischen Punkt, sowohl bei verschwindenden als auch bei nicht-verschwindenden Temperaturen. Wichtig ist in diesem Zusammenhang insbesondere die Kontrolle über die systematischen Unsicherheiten verbunden mit der chiralen Extrapolation. Die Arbeit behandelt zwei spezielle Themengebiete: die Berechnung von hadronischen Formfaktoren bei verschwindender Temperatur mit zwei dynamischen Quarks und die Untersuchung der Eigenschaften des Phasenübergangs zum Quark-Gluon-Plasma im chiralen Limes.

Der elektromagnetische Iso-Vektor-Formfaktor des Pions ist ideal um die systematischen Effekte der chiralen Extrapolation bei die Struktur von Mesonen und Baryonen beschreibenden Größen zu untersuchen. Mesonische Formfaktoren sind einfacher zu berechnen als ihre baryonischen Gegenstücke, leiden aber unter vergleichbaren systematischen Fehlern. Diese Arbeit enthält eine detaillierte Studie des Formfaktors, insbesondere im Bereich sehr kleiner Impulsüberträge q^2 die bislang noch nicht untersucht werden konnten. Die im Rahmen der Arbeit erhaltenen Resultate für den Formfaktor haben eine bislang unerreichte Genauigkeit und schließen die Lücke zwischen dem bis dato kleinsten Impulsübertrag und $q^2 = 0$. Dies ermöglicht die modellunabhängige Bestimmung des Ladungsradius des Pions. Die Resultate für den Formfaktor und den Ladungsradius werden dann benutzt um die Anwendbarkeit der chiralen Störungstheorie (χPT) zu testen und den Ladungsradius zum physikalischen Punkt zu extrapolieren. Das finale Resultat in Einheiten des hadronischen Radius r_0 ist

$$\left\langle r_\pi^2 \right\rangle^{\text{phys}} / r_0^2 = 1.87 \, \binom{+12}{-10} \binom{+4}{-15} \quad \text{oder} \quad \left\langle r_\pi^2 \right\rangle^{\text{phys}} = 0.473 \, \binom{+30}{-26} \binom{+10}{-38} (10) \, \text{fm} \, ,$$

welches gut mit Resultaten aus der LQCD und aus dem Experiment übereinstimmt. Dies das erste zum Kontinuum extrapolierte Ergebnis für den Ladungsradius, welches aus Werten für den Formfaktor aus dem Bereich kleiner Impulsüberträge bestimmt wurde.

Die Ordnung des Phasenübergangs im chiralen Limes und die zugehörige kritische Temperatur sind die beiden verbleibenden unbekannten Eigenschaften des Phasendiagrams der QCD bei verschwindendem chemischen Potential. Einerseits besteht die

Möglichkeit, dass es sich um einen Phasenübergang zweiter Ordnung in der $O(4)$-Universalitätsklasse handelt, andererseits kann es ein Phasenübergang erster Ordnung sein. Da Simulationen bei verschwindender Quarkmasse nicht möglich sind, kann der Phasenübergang nur durch Simulationen bei endlichen Quarkmassen untersucht werden. Darauf folgt eine Analyse des Skalenverhaltens bei der Annäherung an den chiralen Limes. Die Arbeit enthält erste Resultate eines Projektes zur Untersuchung des chiralen Phasenüberganges, die eine ideale Plattform zur Untersuchung der Möglichkeiten und Grenzen der neuen Algorithmen bietet. Die Resultate eines ersten Scans bei einer konstanten Pionmasse von etwa 290 MeV sind vielversprechend und zeigen ein ausgeprägtes Signal für den Phasenübergang. Simulationen bei physikalischen Quarkmassen erscheinen möglich. Von besonderer Bedeutung für den Übergang im chiralen Limes ist die Stärke der anomalen Brechung der chiralen $U_A(1)$-Symmetrie am kritischen Punkt. Diese lässt sich durch die Entartung der Korrelationsfunktionen mit den Quantenzahlen pseudoskalarer und skalarer Mesonen untersuchen. Für den Phasenübergang bei 290 MeV ist die Symmetrie im kritischen Bereich immer noch relativ stark gebrochen und wird effektiv erst bei etwa $1.16\,T_C$ wieder hergestellt. Die Arbeit enthält außerdem eine Erweiterung der üblichen Multi-Histogram-Methode, die eine Anwendung auch bei Fermionen mit kopplungsabhängiger Fermiondeterminante erlaubt.

Contents

Introduction

Most of the visible matter in the universe is made of hadrons that, from the early days of the development of quantum chromodynamics (QCD) as the theory for the strong interactions, are known to be bound states of quarks and/or antiquarks. Quarks are ‘confined’ within these boundstates and do not appear as free particles, at least for temperatures present in the universe today. Asymptotic freedom [1,2] and the associated running of the strong coupling constant allow contact between perturbation theory and collider experiments in the high energy regime. It is also the reason why QCD in the low energy regime, the regime of quark boundstates, is difficult to explore theoretically. In this regime quarks and gluons are strongly coupled and perturbative methods do not work.

Soon after the discovery of asymptotic freedom another aspect of the running of the coupling became evident. At very high temperatures quarks and gluons only interact weakly and thus effectively behave like free particles, giving rise to a new state of matter [3,4], the quark-gluon plasma [5] (QGP). This property is consistent with earlier findings that hadronic (or confined) matter possesses a limiting temperature where thermodynamic properties diverge [6]. This state of matter had to be present at large temperatures in the evolution of the early universe shortly after the big bang. During the expansion the universe cooled down and passed through the phase boundary between QGP and hadronic matter. The related phase transition is subject to intense experimental studies using heavy ion collisions, carried out at RHIC [7] (Brookhaven) and the LHC [8] (CERN). Further experiments are planned at the future FAIR [9] facility (GSI) where matter is going to be probed at higher densities. Figure In.1 shows a picture of the conjectured phase diagram of QCD. Using the Hagedorn temperature, $T_C \approx 160$ MeV, as an estimate for the transition temperature it becomes evident from the running of the coupling that the transition takes place in the regime of strong coupling. Thus, as in the case of quark boundstates, the transition to the QGP happens in the regime where perturbation theory is not applicable and thus non-perturbative methods are needed to probe it.

If one is not willing to rely on model calculations, there are some possibilities how to obtain QCD results from first principles in the non-perturbative regime. The first set of possibilities are renormalisation group methods [10–12], Dyson-Schwinger equations [13–15], QCD sum rules [16, 17] or chiral perturbation theory [18] (χPT). For recent reviews see [19–21]. Even though there has been a lot of progress over the last few years it remains to be seen whether these methods will allow results with full control over systematic effects in the future. The main problem is the inherent need for truncations and approximations within these methods that cannot be improved systematically and do not allow for the estimation of the connected systematic uncertainty. Another option is to use a discretised form of QCD on a spacetime lattice, known as lattice QCD (LQCD). This theory, introduced by *Wilson* soon after the foundation of QCD [23], provides a natural regularisation of QCD and enables the numerical evaluation of observables by means of Monte-Carlo simulations [25, 26]. Starting directly from the path integral it avoids any contact with perturbation theory and thus provides an *ab initio* method to compute QCD

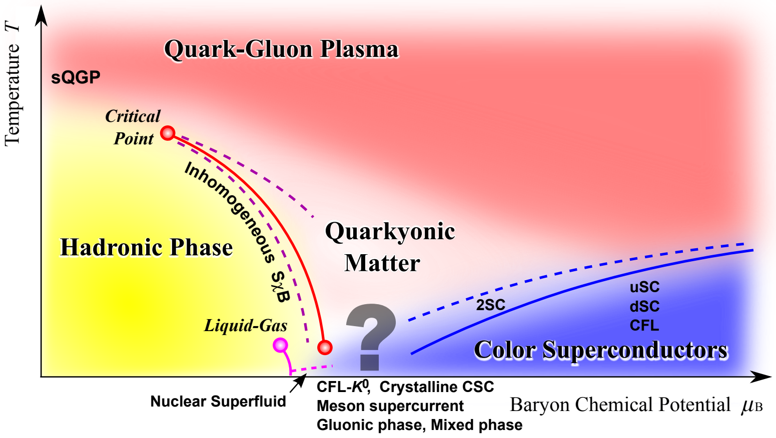

Figure In.1: The conjectured phase diagram of QCD in the plane of temperature and chemical potential, taken from [24].

observables. Furthermore, the concept of finite temperature is easily incorporated by using a small finite temporal extent.

After the first pioneering simulations of pure gauge theories around 1980 by *Creutz* [26] LQCD has by now entered the era in which high precision calculations of physical quantities at the physical point including dynamical fermionic degrees of freedom become feasible. This is true for a number of phenomenologically interesting quantities such as the masses of the lightest mesons that have been computed with remarkable precision by a number of collaborations (see [27] for a recent review). Figure In.2 shows the collection of results as presented in [28] and illustrates the excellent agreement with experiments. These results demonstrate the potential of LQCD simulations and support once more the notion that QCD is a correct theory for the strong interactions. Of course the potential of LQCD is not restricted to confirm experimentally known quantities. Its predictive potential can be seen by the collection of results for quark masses and other interesting quantities that are known with good precision from LQCD in the FLAG review [29]. For these quantities one would conclude that statistical and systematic uncertainties are under control. This progress has been made possible largely due to substantial algorithmic improvements, leading to a significant acceleration of the simulations and allowing to simulate with light dynamical quarks. It is also connected to the presence of a sound effective field theory framework, chiral perturbation theory [18], that allows to obtain reliable estimates at physical quark masses from simulations with unphysically heavy quarks.

Despite the successes mentioned above there are quantities where agreement between LQCD and experiment is less satisfactory. This includes quantities concerning properties of the nucleon (for a recent review see [30]). These provide a fundamental benchmark to show that QCD consistently describes the constituents of nuclear matter. Since one would hesitate to conclude that QCD as such is falsified by these observations one has to acknowledge the possibility that in those measurements systematic effects might not be under control. Since simulations are just enclosing on physical quark masses, one systematic

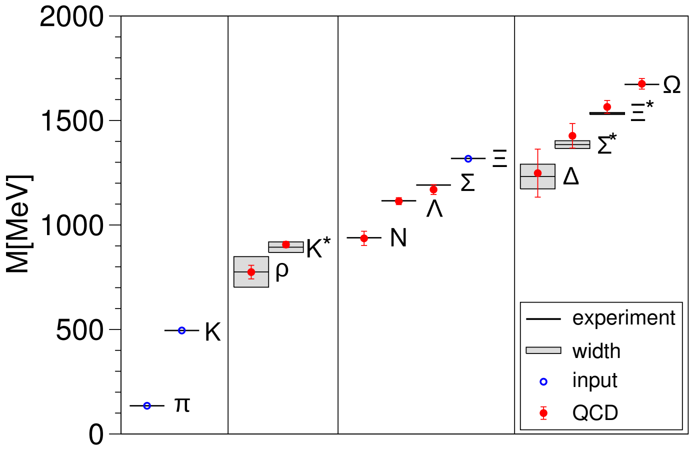

Figure In.2: Spectrum of light mesons from lattice QCD as presented in [28].

effect all of the problematic quantities share is the chiral extrapolation to the physical point. In fact, the failure to reproduce experimental results often goes hand in hand with the absence of a satisfactory effective field theory framework, at least for the range of quark masses available for these quantities. For a recent study on the accuracy and systematics of chiral extrapolations see also [31].

The situation for simulations probing the thermal phase diagram of QCD at zero chemical potential is similar, although contact with experiment is even more difficult in this case. Figure In.3 shows a sketch of the current understanding of the nature of the transition at vanishing density in the plane of averaged light (m_{ud}) and strange (m_s) quark masses. For most parts of the diagram the order of the transition and the associated critical temperature are known with controlled systematics (see [32, 33] for reviews and the discussion in section 7.2). However this is not the case for the transition in the chiral limit of the two lightest flavours. While symmetry demands a first order transition at $m_{ud} = m_s = 0$ [34] it is not clear whether this remains true for $m_s \neq 0$. However, it has to be a real phase transition since the light quark condensate constitutes a true order parameter [34]. A more detailed discussion of the possible scenarios will be given in section 7.2. Since simulations at zero quark mass are not possible the transition can only be probed by extrapolating results obtained at non-zero quark masses to the chiral limit. The behaviour of thermodynamic observables in the vicinity of the critical point will be guided by the scaling dictated by the universality class of the transition and a careful scaling analysis might reveal its order. However, the boundaries of the scaling region are not known *a priori*. This problem is similar to the one for the chiral extrapolation of hadronic quantities at zero temperature, where the upper bound of pion masses for which chiral perturbation theory is still valid is unknown.

The main purpose of this thesis is to shed light on the potential of state-of-the-art lattice simulations to produce results in the chiral regime with full control over systematic effects. Furthermore, the aim is to probe the quark mass range for which contact with χPT for zero temperature and scaling for finite temperature is possible. This of course is an ambitious

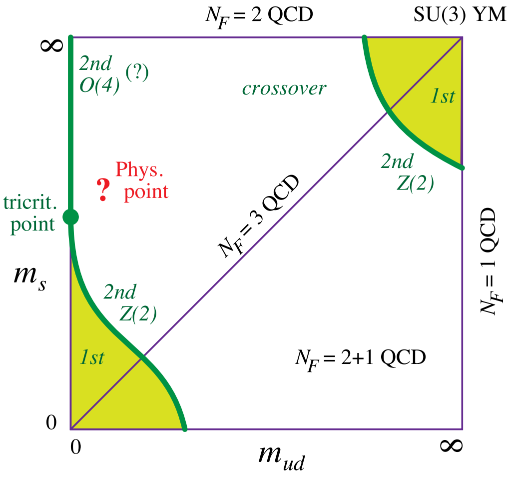

Figure In.3: Present understanding of the nature of the transition in parameter space of degenerate up and down quark masses and an additional strange quark [32].

project and on account of the limitations in terms of time, in particular simulation time, this aim can only be answered in parts within this thesis. The simulations are done using non-perturbatively $\mathcal{O}(a)$-improved Wilson fermions [23,35] for which developments in the last decade have led to a significant speed up. This particular fermion formulation has the advantage of a theoretically sound continuum limit and an undistorted particle spectrum at finite lattice spacings in contrast to staggered fermions [36] that are numerically cheaper. However, Wilson fermions explicitly break chiral symmetry at non-zero lattice spacing. While this is not so problematic for studies of hadronic quantities it is a problem for the examination of the phase transition in the chiral limit where chiral symmetry governs the dynamics of the system. Fermion actions that preserve chiral symmetry even at finite lattice spacing exist [37–41] but they are numerically much more expensive.

The electromagnetic iso-vector form factor of the pion provides a platform to study systematic effects and the chiral extrapolation for observables connected to the structure of mesons and baryons. Mesonic form factors are computationally simpler than their baryonic counterparts but share most of the systematic effects. Furthermore, the form factor is known in χPT to next-to-next-to leading order [42–44] (NNLO) and thus allows for an extensive comparison to lattice data. Besides offering the possibility of studying systematic effects in lattice simulations the form factor is an interesting observable to study in LQCD concerning the associated physics. In the regime of low momentum transfer q^2 the form factor is connected to the charge radius of the pion. In experiment the gap between $q^2 = 0$ and the first available non-zero momentum transfer prohibits the direct extraction of the charge radius [45]. It can only be calculated using models for the q^2-dependence of the form factor. A prominent example is the model of vector pole dominance [46,47]. Due to recent theoretical developments, known as 'partially twisted' boundary conditions [48–50], the form factor can be studied in LQCD at arbitrarily small q^2 [51,52] and thus allows to access the form factor in this previously inaccessible regime. This also enables the direct extraction of the charge radius without any model dependence. A more detailed introduction on the topic will be given in section 5.1. In this thesis results are presented that close the gap in the low q^2 region, at least at quark masses heavier than the physical one, with full control over the systematic effects. The remaining task is the chiral extrapolation which will also be discussed in detail. This presents a significant step towards a fully non-perturbative measurement for a quantity that is connected to the structure of hadrons with full control over most of the systematic effects.

Concerning the nature of the transition in the chiral limit of two-flavour QCD the physical object of interest is the transition itself, in particular the transition temperature and the order of the transition. As discussed earlier, it can only be addressed by extrapolating simulations at non-vanishing quark masses to the chiral limit. Recently it was realised by the tmfT-collaboration [53] that simulations at several quark masses corresponding to zero-temperature pions with masses smaller than 300 MeV, at least, are necessary to be able to extract information about the order of the transition by means of a scaling analysis. Furthermore, the explicit breaking of chiral symmetry for Wilson fermions at non-zero lattice spacings requires simulations that are close to the continuum. Thus one is forced to perform simulations at rather large lattices and small pion masses as discussed in more detail in section 9.1. This is a major challenge for simulation algorithms and presents the ideal testcase to study the limits of state-of-the-art simulations with Wilson fermions in the chiral regime. At the same time this renders the simulations computationally very demanding which prohibits the extraction of conclusive results for the order of the transition in the time available to finish the thesis. The setup, tests and results reported here constitute the starting point for the associated long term project which hopefully will lead to conclusive results in the future. The difficulty of the topic is also signified by noting that it presents the last remaining open question about the nature of the transition for vanishing chemical potential. A more detailed discussion about previous studies is given in section 7.2. Of particular relevance concerning the order of the transition in the chiral limit is the strength of the anomalously broken $U_A(1)$-symmetry at the transition point since it might provide valuable insight on the order of the transition [34]. It can be studied using mesonic correlation functions [54, 55] and the associated screening masses. A study of these observables is presented as well. In practice, the information about the transition is limited by the finite resolution in the vicinity of the transition point. This can in principle be overcome at the stage of the analysis by means of multi-histogram methods [56,57]. However, in their standard form they cannot be applied to non-perturbatively $\mathcal{O}(a)$-improved Wilson fermions. An extension of the method, allowing for applications to a broader range of problems, will be developed in chapter 8. In particular, it can also be used for non-perturbatively $\mathcal{O}(a)$-improved Wilson fermions.

The thesis is divided in four parts: Part I contains the foundations of QCD formulated on a spacetime lattice with *Wilson*'s fermion and gauge actions. In particular, the important topics of chiral symmetry and its breaking, $\mathcal{O}(a)$-improvement and renormalisation are discussed. It also contains brief reviews on chiral perturbation theory and alternative fermion formulations.

Part II introduces the numerical methods that are fundamental for simulations of LQCD. The focus is on the improved algorithms for the simulations and the construction of improved estimators for fermionic observables. It also contains a concise discussion of systematic effects and partially twisted boundary conditions.

Part III is devoted to the study of the electromagnetic iso-vector from factor of the pion. The first chapter of this part, chapter 5, focuses on the extraction of the form factor at small momentum transfers and full control over the main systematic effects at several points in the parameter space of quark masses and lattice spacings. In particular, it contains results for the form factor in the previously inaccessible region of very small momentum transfers and the connected model independent extraction of the pion charge radius. In chapter 6 the results are compared to chiral perturbation theory and extrapolated to the physical point. Chapter 6 also provides detailed conclusions and gives an account of the perspectives for future research.

The final part IV includes the study on the thermal transition in the chiral limit of two-flavour QCD. The fundamental concepts and the current status of research on the nature of the transition are reviewed in chapter 7. There the main observables, mesonic correlation functions and aspects of critical scaling are introduced that will eventually be used to extract the information about the order of the transition in the chiral regime. Chapter 8 contains the formalism for the extended multi-histogram analysis discussed earlier. First steps towards its implementation are reported as well. The last chapter, chapter 9, then contains the details of the simulation setup. Furthermore, it gives a detailed account on the benchmarks of algorithm and strategy and presents the results for the first scan along a line of constant physics in the chiral regime at a quark mass corresponding to a zero-temperature pion of 290 MeV. A discussion of algorithm tuning and performance is provided in appendix D.3. The last section in chapter 9 describes the basic setup and expectations for the future scaling analysis and singles out a good strategy to extract conclusive results. It also contains perspectives for related future research.

Thew thesis concludes with a summary and the perspectives for future research.

PART I: Fundamentals

1 QCD in the continuum at zero and finite temperature

This chapter serves to introduce QCD in the framework of euclidean path integrals. The first section starts with a historical perspective of the development of QCD in the framework of the standard model of particle physics. After this introduction the focus is on the quantisation of QCD in the path integral formalism with a special emphasis on chiral symmetry and its breaking.

1.1 The standard model of elementary particle physics

In the 1950's the physicists working in the field of elementary particle physics were puzzled by the discovery of a number of new particles appearing in experiments that used a new generation of more powerful particle accelerators. At the same time quantum electrodynamics (QED) had already been introduced as the quantum theory for the electromagnetic force and the theoretical focus was on the description of the other fundamental forces through analogous quantum field theories. This 'zoo' of new particles apparently spoiled the effort to describe the matter content and its interactions by a simple and elegant model with only a few free parameters.

The task at hand was the classification of these new particles and the first breakthrough was due to *Gell-Mann* and *Ne'eman*, who showed that hadrons can be classified according to the multiplets of the group $SU(3)$. The corresponding global symmetry was given the name flavour and was very successful in postulating new particles. Nevertheless, there were two main problems: The particles corresponding to the fundamental representation were still missing and three particles of the Baryon decuplet, namely Δ^{++}, Δ^{-} and Ω^{-}, possessed equivalent quantum numbers of spin and flavour and completely symmetric wave functions in contradiction to the well established Pauli principle.

The first problem was solved by *Gell-Mann* [58] and *Zweig* [59] in 1964 by postulating that hadrons are constructed from elementary constituents, so called 'quarks', that are the missing particles of the fundamental representation. Mysteriously quarks did not show up as free particles in any collider experiment even though one observed particle like scattering in deep inelastic Lepton scattering. This led to the postulation of quark confinement, stating that quarks do not appear unbound in nature. A theory of the interaction between quarks was needed in order to explain confinement theoretically.

The first step towards this theory was the invention of Yang-Mills theories [60] in 1954, which were shown to be asymptotically free by *Gross*, *Wilczek* [1] and *Politzer* [2] in 1973. At that time the Glashow-Weinberg-Salam theory [61, 62] had already combined the electromagnetic and weak interactions in a unified theory and the idea was to describe the strong interactions in the same framework. Soon it was postulated, that quarks should obtain new internal degrees of freedom connected to a local $SU(3)$ gauge theory, by *Han* and *Nambu* [63] and independently by *Greenberg* [64] and *Gell-Mann* [65]. This symmetry was later given the name 'colour' symmetry by *Fritzsch*, *Gell-Mann* and *Leutwyler* [66].

The corresponding quantum numbers of the quarks were named red, green and blue (rgb) and the associated theory named quantum chromodynamics (QCD).

The standard model of elementary particles (SM) combines the Glashow-Weinberg-Salam theory and QCD and is characterised by the associated $SU(3) \times SU(2) \times U(1)$ gauge group. The only fundamental force not included in the SM is the gravitational force and one of the main goals for theoretical physics at the moment is the combination of gravity and the SM in a unified framework. Nevertheless, at energy and length scales in reach with todays accelerators – at the LHC at CERN one expects energies of about 14 TeV [67] – the gravitational contributions to the scattering processes are expected to be negligible. Today the standard model is well established and proves to describe the fundamental interactions in a broad range of energy scales to high accuracy. Only a few months ago a candidate for the last missing particle of the SM, the Higgs boson, essential for the mechanism of spontaneous electro-weak symmetry breaking, was discovered in the ATLAS [68, 69] and CMS [70] experiment. Both experiments have a signal with a combined significance of about 6 standard deviations.

1.2 Quantum chromodynamics

Within the SM, QCD as the theory of the strong interactions is responsible for the stability of quark boundstates and atomic nuclei which constitute most of the visible matter in the universe. This part is devoted to the introduction of QCD at the level of classical field theory and its quantisation via path integrals. The presentation mainly follows the books by *Peskin* and *Schroeder* [71] and *Weinberg* [72], these can be consulted for further reading.

1.2.1 The QCD Lagrangian

QCD results from the demand that the Lagrangian of the quark content of the theory is invariant under local $SU_c(3)$ transformations. The quarks are represented by a Dirac field $\psi(x) = \psi_{f,c,\alpha}(x)$ in the fundamental representation of $SU_c(3)$. Here f, c and α are internal flavour, colour and spinor indices respectively. For more details of notation and conventions see appendix A.1. The only terms that may be constructed that are consistent with the demand for renormalisability and invariance under $SU_c(3)$ are

$$\mathcal{L}_{QCD}(\psi, \bar{\psi}, A_\mu) = \bar{\psi}(x)\ (i\,\gamma^\mu\, D_\mu - \mathcal{M}_b)\ \psi(x) - \frac{1}{4}\,\mathrm{Tr}\left(F^{\mu\nu}(x)\, F_{\mu\nu}(x)\right)\ . \tag{1.1}$$

Here $\mathcal{M}_b$ is the matrix of bare quark masses and the indices of the quark fields are conventionally suppressed. The coupling between quarks and gluons, the force mediating gauge bosons of the strong interactions, is included via the covariant derivative

$$D_\mu \equiv \partial_\mu - i\, g_s\, A^a_\mu(x)\, T^a\ . \tag{1.2}$$

Here T^a, $a = 1, \ldots, 8$ are the generators of the group $SU_c(3)$ and the gluons are represented by fields $A_\mu(x)$ which transform in the adjoint representation of $SU_c(3)$. The kinetic term for the gluonic fields is the second term in eq. (1.1) and includes the field strength tensor $F_{\mu\nu}$ defined by

$$F_{\mu\nu} \equiv F^a_{\mu\nu}\, T^a \equiv \frac{i}{g_s}\, [D_\mu\, ,\, D_\nu]\ . \tag{1.3}$$

$SU(3)$ is a non-abelian group and the generators T^a satisfy the commutation relation

$$\left[T^a\, ,\, T^b\right] = i\, f^{abc}\, T^c\ , \tag{1.4}$$

where f_{abc} are the structure constants. The Lagrangian eq. (1.1) thus includes cubic and quartic self-interaction terms for the gluons.

Here it is convenient to point out the relation between covariant derivative (1.2) and the concept of the parallel transporter of differential geometry. On a curved manifold the usual concept of a simple derivative is not well defined since the fields at two different points on the manifold cannot be compared directly. For comparison one has to introduce an object connecting fields at different points. Analogously, the interaction between quarks and gluons leads to a similar phenomenon and the fields obtain a $SU_c(3)$-phase factor from the gluonic field $A^a_\mu(x)$ when compared at different spacetime points. For two infinitesimally separated points x and $x+\epsilon_\mu$ one obtains

$$\begin{aligned}\lim_{\epsilon_\mu\to 0} \frac{1}{\epsilon_\mu}\Big(\psi(x+\epsilon_\mu) - U(x, x+\epsilon_\mu)\,\psi(x)\Big) \;&= \lim_{\epsilon_\mu\to 0} \frac{1}{\epsilon_\mu}\Big(\psi(x+\epsilon_\mu) - \psi(x)\Big) - \delta\psi(x)\\ &= \partial_\mu - \delta\psi(x)\ ,\end{aligned} \tag{1.5}$$

where $U(x, x+\epsilon_\mu) \in SU(3)$ is the parallel transporter on the $SU_c(3)$ manifold. Comparing eqs. (1.5) and (1.2) one can extract the infinitesimal version of the parallel transporter,

$$U(x, x+\epsilon_\mu) = 1 + i\, g_s\, \epsilon_\mu\, A^a_\mu(x)\, T^a \equiv U_\mu(x)\ . \tag{1.6}$$

The concept can be generalised to parallel transport along a path $\mathcal{C}$ of arbitrary length. By integration of eq. (1.6) one obtains

$$U(\mathcal{C}) = \exp\left(i\, g_s\, T^a \int_{\mathcal{C}} dz^\mu\, A^a_\mu(z)\right)\ . \tag{1.7}$$

One of the most important features of QCD is asymptotic freedom, or in other words its strong renormalised coupling $\alpha_s \equiv g^2_{s,R}/(4\pi)$ at small energy scales. When the relevant energy scale of the system is denoted as μ_R the running of the coupling is governed by the renormalisation group equation

$$\mu^2_R\, \frac{d\,\alpha_s}{d\mu^2_R} = \beta_{\text{cont}}(\alpha_s)\ . \tag{1.8}$$

Here $\beta_{\text{cont}}(\alpha_s)$ is the QCD β-function which is not known *ab initio*, but can be computed in perturbation theory. The fact that it is negative at leading order [1,2] shows that QCD is asymptotically free for large energies.

1.2.2 Euclidean path integral quantisation

The quantisation via path integrals follows *Feynman*'s pioneering idea to rewrite matrix elements in quantum mechanics as a continuous sum over paths [73]. Similarly the expectation value of an operator $\hat{O}$ in Minkowski space $\mathbb{R}^4$ can be written as a sum over all possible field configurations

$$\left\langle \hat{O} \right\rangle = \frac{1}{Z} \int \mathcal{D}\bar{\psi}\mathcal{D}\psi\mathcal{D}A \, O(\bar{\psi}, \psi, A^\mu) \, \exp\left(i \int_{\mathbb{R}^4} d^4x \, \mathcal{L}_{\text{QCD}}(\psi, \bar{\psi}, A^\mu) \right) . \tag{1.9}$$

Here $Z = \langle 1 \rangle$, $\mathcal{L}_{\text{QCD}}$ is defined in eq. (1.1) and $\bar{\psi}$ and ψ are Grassmann valued fields. The integration measure is given by

$$\mathcal{D}\bar{\psi}\mathcal{D}\psi\mathcal{D}A = \prod_{x \in \mathbb{R}^4} \left[d\bar{\psi}(x) \, d\psi(x) \prod_{a=1}^{8} \prod_{\mu=0}^{3} \left(dA^{a,\mu}(x) \right) \right] . \tag{1.10}$$

The integrand in eq. (1.9) oscillates due to the imaginary exponential factor and is not suited for numerical simulations where a real and non-negative weight factor is needed. A more convenient form is achieved by means of a Wick-rotation to imaginary times $t \to -ix^0$. This rotation transforms the Minkowski space into an Euclidean space $[-\infty, \infty] \times \mathbb{R}^3$ with metric $g_{\mu\nu} = \delta_{\mu\nu}$. The path integral is given by

$$\left\langle \hat{O} \right\rangle = \frac{1}{Z} \int \mathcal{D}\bar{\psi}\mathcal{D}\psi\mathcal{D}A \, O(\bar{\psi}, \psi, A^\mu) \, \exp\left(- \int_{[-\infty,\infty]\times\mathbb{R}^3} d^4x \, \mathcal{L}^E_{\text{QCD}}(\psi, \bar{\psi}, A^\mu) \right) , \tag{1.11}$$

where the measure (1.10) now includes the product over Euclidean space. The exponential factor includes the Euclidean action of QCD

$$S^E_{\text{QCD}} = \int_{[-\infty,\infty]\times\mathbb{R}^3} d^4x \, \mathcal{L}^E_{\text{QCD}}(\psi, \bar{\psi}, A^\mu) \tag{1.12}$$

with the Lagrangian

$$\mathcal{L}^E_{\text{QCD}}(\bar{\psi}, \psi, A^\mu) = \bar{\psi}(x) \, \left(\gamma^E_\mu \, D_\mu + \mathcal{M}_b \right) \, \psi(x) + \frac{1}{4} \, F^a_{\mu\nu} \, F^a_{\mu\nu} \, . \tag{1.13}$$

γ^E_μ are the Euclidean versions of the γ-matrices given in eq. (A.6). Since the rest of this thesis works within the Euclidean spacetime, the superscript E will be suppressed from now on.

The integral in eq. (1.11) is notoriously divergent due to the invariance under gauge transformations, leading to an integral over a continuous infinite number of gauge-equivalent field configurations. This is a serious problem if one is interested in a perturbative treatment of QCD. A way to overcome this problem is to fix the gauge using the method of *Faddeev* and *Popov* [74]. However, in this thesis the focus is on numerical simulations on a spacetime lattice, where the path integral is formulated with respect to the parallel transporters between the lattice points. The associated gauge group $SU(3)$ is compact, so that in a finite lattice volume, in which case the number of variables is finite, the functional integral is well defined even without gauge-fixing (see also section 3.2.3 in [75]).

1.3 Chiral symmetry

A fundamental symmetry concerning the phenomena observed in QCD is the approximate chiral symmetry of the lightest two or three quark flavours. The theory describing the dynamics associated with the explicit and spontaneous breaking of chiral symmetry, chiral perturbation theory (χPT), is important for lattice simulations since it provides an effective field theory framework for the extrapolation to physical quark masses. It is used in chapter 6 to perform the chiral extrapolation of the results for the pion form factor and the charge radius. The restoration of chiral symmetry at high temperatures is a main feature of the thermal transition of QCD. In particular, in the chiral limit and for light quarks it is expected to govern the dynamics in its immediate vicinity. This section introduces the main concepts of chiral symmetry for the case of two light flavours and its spontaneous and explicit breaking in the continuum and provides a brief overview over χPT.

1.3.1 Two-flavour symmetry

Even though fundamental, the masses of the quarks are among the least well known parameters of the SM. The reason is that they are only accessible via indirect measurements due to confinement. The best estimates for the masses of up (u), down (d) and strange (s) quarks from experiment [76] (exp) and theory [29] (th) are

$$\begin{aligned} m_u &= && 1.7-3.3 && \text{(exp)} && 2.19\,(15) && \text{(th)} && \text{MeV}\,, \\ m_d &= && 4.1-5.8 && \text{(exp)} && 4.67\,(20) && \text{(th)} && \text{MeV}\,, \\ m_s &= && 101\,(29) && \text{(exp)} && 95\,(\ 6) && \text{(th)} && \text{MeV}\,. \end{aligned} \tag{1.14}$$

The striking feature is the approximate degeneracy of the masses of u and d quarks that are small compared to the typical energy scale of QCD in the hadronic phase, $\Lambda_{\mathrm{QCD}} \approx 200$ MeV (see [77] and references therein). The latter is also true to some extent for the mass of the strange quark which is roughly a factor 2 smaller as Λ_{QCD}.

If up and down quarks are considered to be massless the Lagrangian is invariant under global $SU(2)_V \times U(1)_V \times SU(2)_A \times U(1)_A$ transformations. The generators of the associated symmetry group, known as chiral symmetry, are given by

$$G_V^a = \sigma^a \quad \text{and} \quad G_A^a = \gamma_5\,\sigma^a \tag{1.15}$$

for $SU_V(2) \times U(1)_V$ and $SU_A(2) \times U_A(1)$ respectively. Here σ^a, $a = 0,1,2,3$ includes the Pauli matrices ($a = 1,2,3$) defined in eq. (A.8) and the unit matrix ($a = 0$). Under a symmetry transformation the quark fields transform like

$$\begin{aligned} \psi(x) &\to e^{i\,\theta_V^a\,G_V^a}\,\psi(x)\,, & \bar\psi(x) &\to \bar\psi(x)\,e^{-i\,\theta_V^a\,G_V^a}\,, \\ \psi(x) &\to e^{i\,\theta_A^a\,G_A^a}\,\psi(x) \qquad \text{and} & \bar\psi(x) &\to \bar\psi(x)\,e^{i\,\theta_A^a\,G_A^a}\,. \end{aligned} \tag{1.16}$$

The associated conserved vector and axial vector currents are given by

$$J_V^{a;\mu}(x) = i\,\bar\psi(x)\,\gamma^\mu\,G_V^a\,\psi(x) \quad \text{and} \quad J_A^{a;\mu}(x) = i\,\bar\psi(x)\,\gamma^\mu\,G_A^a\,\psi(x)\,. \tag{1.17}$$

For massless quarks the amount of energy needed for the excitation of a quark-antiquark pair from the vacuum is small. As a consequence one expects to obtain a nonzero value for the chiral quark condensate [71]

$$\left\langle \bar{\psi}\, \psi \right\rangle = \left\langle \bar{\psi}_u\, \psi_u + \bar{\psi}_d\, \psi_d \right\rangle \neq 0\;. \tag{1.18}$$

The expectation value, eq. (1.18), is invariant under $SU_V(2) \times U_V(1)$ but not under $SU_A(2) \times U_A(1)$. Thus the axial symmetry is spontaneously broken in QCD (at least at low temperatures) and the vacuum mixes the two helicity states of the quarks leading to a non-vanishing effective mass. *Goldstone*'s theorem [78] then implies the existence of four massless Goldstone bosons. Nevertheless, this is true only if the currents $J_A^{a,\mu}$ from eq. (1.17) are conserved, which is required for the Goldstone theorem to hold. In fact, the zero component of the axial current, i.e. the current associated with the $U_A(1)$ symmetry, is not conserved at the quantum level. This effect, also known as the axial anomaly, can be studied in perturbation theory and is a special manifestation of the Adler-Bell-Jackiw anomaly (see e.g. section 19.3 in [71]). This anomaly and its possible restoration at high temperatures [34] is of special relevance for the properties of the phase transition to the quark-gluon plasma in the chiral limit of two-flavour QCD (cf. section 7.2). The other three currents $J_A^{i,\mu}$, $i = 1, 2, 3$ are conserved also at the quantum level and give rise to three massless Goldstone bosons.

It is natural to identify the Goldstone bosons with the lightest bound states made of two quarks, namely the three pions π^0, $\pi^\pm$. These have odd parity and can be created (or annihilated) by the axial current $J_A^{i,\mu}$. The corresponding matrix elements are conventionally parametrised as

$$\langle 0|\, J_A^{i,\mu}(x)\, \left|\pi^j(p)\right\rangle = -i\, p^\mu\, F_\pi\, \delta^{ij}\, e^{-i\,p\,x}\;. \tag{1.19}$$

Here the pion is on-shell and has momentum p^μ. F_π is the pion decay constant with dimension of mass. It can be extracted experimentally from the rate of the weak decay of the charged pions $\pi^\pm$ which yields [1] [76]

$$F_\pi = 92.21\,(3)(15)\;\mathrm{MeV} \tag{1.20}$$

where the first error is statistical and the second systematic.

So far up and down quarks were considered to be massless which is realised only approximately. Their mass term in the Lagrangian (1.1) breaks the $SU_A(2) \times U_A(1)$ symmetry explicitly and generates masses for the Goldstone bosons. Furthermore, when up and down quarks are non-degenerate also the $SU_V(2) \times U_V(1)$ symmetry is explicitly broken.

1.3.2 Chiral perturbation theory

The appropriate framework to describe the dynamics of these pseudo-Goldstone bosons is given by χPT which was first introduced by *Gasser* and *Leutwyler* in 1984 [18]. For an

---

[1] In the literature there are several conventions for F_π differing by factors of $\sqrt{2}$. The convention used in [76] quotes a value for $f_\pi = \sqrt{2}\,F_\pi$.

extensive review see [22], upon which this section is based on, and [79] for recent developments. As in the last section, the discussion is restricted to the case of an approximate two-flavour symmetry.

At energies up to a scale Λ_χ, associated with spontaneous symmetry breaking, the relevant degrees of freedom in χPT (with approximate chiral $SU_V(2) \times SU_A(2)$) are the three Goldstone bosons π^i. These are encoded in the fields

$$\Sigma(x) \equiv \exp\left(\frac{i}{F} \sum_{i=1}^{3} \sigma^i(x)\, \pi^i\right) . \tag{1.21}$$

Here F is a dimensionful quantity which is related to the pion decay constant in the chiral limit (cf. appendix A.5). The fields transform under $SU_V(2)$ and $SU_A(2)$ as

$$\begin{aligned} \Sigma(x) &\to V\, \Sigma(x)\, V^+ \qquad \text{with} \qquad V \in SU_V(2) \qquad \text{and} \\ \Sigma(x) &\to A^+\, \Sigma(x)\, A^+ \qquad \text{with} \qquad A \in SU_A(2) \, . \end{aligned} \tag{1.22}$$

This implies that $\Sigma(x)$ is in the adjoint representation of $SU_V(2)$ and that the vacuum, conventionally given by $\Sigma_0(x) = 1$, is not invariant under $SU_A(2)$. Recalling the discussion of the last section, this is exactly what is needed for the theory to ensure spontaneous breaking of chiral symmetry. To include also explicit breaking of chiral symmetry one has to include terms proportional to the mass matrix $\mathcal{M} = \mathrm{diag}(m_u, m_d)$ that should obey the virtual transformation law

$$\mathcal{M} \;\to\; R\, \mathcal{M}\, L^+ \, . \tag{1.23}$$

χPT to a given order in p/Λ_χ is defined by the most general Lagrangian constructed with the fields in eq. (1.21) and the mass matrix, symmetric under the transformation in eq. (1.22) and (1.23). Here p is a momentum or mass of the theory and derivatives contribute as $\partial^2 \sim p$ to the power counting. To leading order this yields the Lagrangian

$$\mathcal{L}_{\chi\mathrm{PT}} = \frac{F^2}{4}\left[\mathrm{Tr}\left(\partial_\mu \Sigma\, \partial^\mu \Sigma^+\right) - 2\, B\, \mathrm{Tr}\left(\mathcal{M}\, \Sigma^+ + \Sigma\, \mathcal{M}^+\right)\right] , \tag{1.24}$$

which contains two free parameters, the low energy constants (LECs) F and B. The mass terms in eq. (1.24) lead to degenerate pion masses given by

$$m_\pi^2 = m_0^2 \equiv 2\, B\, m_{ud} \quad \text{with} \quad m_{ud} \equiv \frac{1}{2}\,(m_u + m_d) \; . \tag{1.25}$$

This degeneracy, which is a feature of the $SU_V(2)$-symmetry, is realised to good accuracy in nature where the pion masses are found to be [76]

$$m_{\pi^0} = 134.9766(6)\ \mathrm{MeV} \quad \text{and} \quad m_{\pi^\pm} = 139.5702(4)\ \mathrm{MeV} \, . \tag{1.26}$$

When higher order terms are included additional LECs appear in the Lagrangian, represented by ℓ_n. These bare parameters are connected to renormalised LECs $\ell_n^r(\mu)$ appearing in the final formulae for physical quantities. The $\ell_n^r(\mu)$ still depend on the renormalisation scale μ and it is convenient to rewrite them in terms of scale invariant LECs $\bar{\ell}_n$ related to the $\ell_n^r(\mu)$ by

$$\ell_n^r(\mu) = \frac{\tilde{\gamma}_n}{2\,\tilde{N}} \left(\bar{\ell}_n + \tilde{N}\,\tilde{L}(m_{\text{ref}})\right) . \tag{1.27}$$

For compact notation the quantities

$$\tilde{N} \equiv 16\,\pi^2 \quad \text{and} \quad \tilde{L}(m) \equiv \frac{1}{N} \ln\left(\frac{m^2}{\mu^2}\right) \tag{1.28}$$

have been introduced and the anomalous dimensions $\tilde{\gamma}_n$ are given by

$$\tilde{\gamma}_1 = \frac{1}{3}\,, \quad \tilde{\gamma}_2 = \frac{2}{3}\,, \quad \tilde{\gamma}_3 = -\frac{1}{2}\,, \quad \tilde{\gamma}_4 = 2\,, \quad \tilde{\gamma}_5 = -\frac{1}{6} \quad \text{and} \quad \tilde{\gamma}_6 = -\frac{1}{3}\,. \tag{1.29}$$

Note that the mass m_{ref} in eq. (1.27) sets the reference scale for the scale independent LECs $\bar{\ell}_n$, since $\bar{\ell}_n \sim \ell_n^r(m_{\text{ref}})$. In practice, one is mostly interested in the renormalised LECs at the physical pion mass which corresponds to setting $m_{\text{ref}} = m_\pi^{\text{phys}}$ in eq. (1.27).

1.4 Thermal expectation values

To describe systems in different thermodynamic states it is essential to make contact to macroscopic properties such as temperature T, pressure P and volume V. While a finite volume is easy to realise in the QFT framework this is not the case for T and P. Indeed, it turns out that QFT as discussed above can be associated with a theory in the limit of zero temperature and pressure. The correct framework to describe equilibrated field theory at non-zero temperature is equilibrium statistics, in the application to field theories known as thermal field theory. This section contains the basics of QCD as a thermal field theory. In particular, it is shown how thermal expectation values can be evaluated in the uniform framework of Euclidean path integrals. For further reading see [80].

Within the scope of quantum field theories, where particles are persistently created and destroyed due to vacuum fluctuations, it is natural to work in the grand canonical ensemble. In this framework temperature, volume and chemical potential μ are fixed while energy and particle number are subject to fluctuations. The key quantity to compute collective properties of the system is the partition function

$$Z(T,V,\mu) = \text{Tr}\left(e^{-\beta_T\,(H-\mu\,N)}\right) , \tag{1.30}$$

where $\beta_T = T^{-1}$ is the inverse temperature and H is the Hamiltonian of the microscopic system. N is the conserved number operator for the constituents with associated chemical potential μ. The traces indicate summation over all possible microstates of the system. Similarly, the expectation value of an observable O is defined as

$$\langle O\rangle_{(T,V,\mu)} = \frac{1}{Z(T,V,\mu)}\,\text{Tr}\left(O\,e^{-\beta_T\,(H-\mu\,N)}\right) . \tag{1.31}$$

The factor Z^{-1} ensures the normalisation $\langle 1\rangle_{(T,V,\mu)} = 1$.

The thermodynamical potential, in this case the Helmholtz free energy

$$F = -T \, \ln \left[Z(T, V, \mu) \right] \; , \tag{1.32}$$

is related to macroscopic observables such as e.g. pressure and particle number,

$$P = -\left(\frac{\partial F}{\partial V} \right)_T \quad \text{and} \quad N = -\left(\frac{\partial F}{\partial \mu} \right)_T \; . \tag{1.33}$$

Contact with the path integral representation is made by evaluating the trace in eq. (1.31). To this end one has to introduce the Schrödinger operators $\hat{\phi}(\mathbf{x}, 0)$ and its eigenstates $|\phi\rangle$, associated with the classical field $\phi(x)$ of the theory, with the quantities for the canonical conjugate momentum $\hat{\pi}(\mathbf{x}, 0)$ and $|\pi\rangle$. It is convenient to use the composite field variable ϕ which contains all fields that appear in the theory, i.e. $\phi = (\bar{\psi}, \psi, A^\mu)$. The eigenstates $|\phi\rangle$ and $|\pi\rangle$ build a basis for the corresponding Hilbert space and obey the completeness relation

$$1 = \int d\phi \;\; |\phi\rangle \, \langle\phi| = \int d\pi \;\; |\pi\rangle \, \langle\pi| \; . \tag{1.34}$$

The trace over all possible microstates in eq. (1.31) can be expressed as

$$\langle O \rangle_{(T,V,\mu)} = \frac{1}{Z(T, V, \mu)} \int d\phi \; \langle\phi| \;\; \hat{O} \, e^{-\beta_T \, (H - \mu \, N)} \;\; |\phi\rangle \; . \tag{1.35}$$

Here $\hat{O}$ is the operator corresponding to the observable O expanded as a series in $\hat{\phi}$. The term $\exp(-\beta_T \, H)$ is similar to the time evolution operator in the Schrödinger picture after Wick rotation. Using the standard tools to obtain the path integral representation for a transition matrix element one obtains the final expression [80]

$$\langle O \rangle_{(T,V,\mu)} = \frac{1}{Z(T, V, \mu)} \int_{\mathrm{BC}} \mathcal{D}\phi \, O(\phi) \, \exp\left(- \int_{\Omega_T} d^4x \; \left(\mathcal{L}^E(\phi) + \mu \, N(\phi) \right) \right) \; . \tag{1.36}$$

BC is a placeholder for the boundary conditions for the fields at $x^0 = 0$ and $x^0 = \beta_T$. The path integral is defined in the Euclidean space

$$\Omega_T \equiv [0, \beta_T] \times \mathbb{R}^3 \; . \tag{1.37}$$

Note that x^0 is not a true time-coordinate since the system is considered to be in thermal equilibrium, which indicates that all macroscopic states are time independent. This is also reflected by the fact that the thermal theory has no direct equivalent in Minkowski space.

At this point one has to distinguish between bosonic and fermionic fields. For bosonic fields periodic boundary conditions are needed according to eq. (1.35). For fermionic degrees of freedom the picture is different due to the anti-commutation properties of the fields. Accordingly the boundary conditions for the fermionic part of eq. (1.36) have to be antiperiodic. Explicitly the boundary conditions are given by:

$$\begin{array}{llll} \textbf{bosons} & (A^a_\mu) & \text{periodic} & A^a_\mu(\mathbf{x}, 0) = A^a_\mu(\mathbf{x}, \beta_T) \\ \textbf{fermions} & (\psi) & \text{antiperiodic} & \psi(\mathbf{x}, 0) = -\psi(\mathbf{x}, \beta_T) \; . \end{array} \tag{1.38}$$

Due to the finite extent in the x^0-direction the corresponding frequencies ω_n, called Matsubara frequencies, are discrete,

$$\omega_n = \begin{cases} 2\pi\, n\, T & \text{for bosons } (A^a_\mu) \\ (2\,n+1)\,\pi\, T & \text{for fermions } (\psi) \end{cases} \quad \text{with } \; n \in \mathbb{Z}\,. \tag{1.39}$$

Replacing ϕ in eq. (1.36) one arrives at the path integral for thermal QCD

$$\begin{aligned} \langle O \rangle_{(T,V,\mu)} = \; & \frac{1}{Z(T,V,\mu)} \int_{\mathrm{BC}} \mathcal{D}\bar{\psi}\mathcal{D}\psi\mathcal{D}A\, O(\bar{\psi},\psi,A^\mu) \\ & \times \exp\left(- \int_{\Omega_T} d^4x \; \left(\mathcal{L}^E_Q CD(\bar{\psi},\psi,A^\mu) + \mu\, N(\bar{\psi},\psi,A^\mu) \right) \right) \,. \end{aligned} \tag{1.40}$$

The conserved number operator connected with quark number is given by

$$N(\bar{\psi},\psi,A^\mu) = \bar{\psi}(x)\,\gamma_0\,\psi(x). \tag{1.41}$$

Comparing eqs. (1.11) and (1.40) with $\mu = 0$ it is evident that both path integrals become equivalent in the limit $T \to 0$. In that case the Euclidean spacetime Ω_T from eq. (1.37) transforms into the space $[-\infty,\infty]\times\mathbb{R}^3$ from eq. (1.11). In addition, the discrete Matsubara frequencies become a continuum of energies. In fact, lattice simulations are necessarily done with a finite time interval, i.e. at finite temperature, and results in zero temperature QCD are obtained by taking the limit $T \to 0$. Note however that here the appearance of the Euclidean space is natural due to the evaluation of the trace in eq. (1.30). For the theory at zero temperature the Euclidean signature appears only as a consequence of the Wick rotation.

2 Lattice regularisation

This chapter deals with the formulation of QCD on a discrete spacetime lattice which provides the basis for numerical simulations. The focus is on the formulation of lattice actions due to *Wilson* [23] and its chiral aspects. The last section of this chapter provides an overview of alternative fermion actions and their properties. For further reading consult one of the textbooks of *Montvay* and *Münster* [75] or *Gattringer* and *Lang* [81] or one of the reviews [82, 83] that have been used as a guide for this chapter. For reviews on lattice gauge theories at finite temperature see [84, 85].

2.1 Quantisation in discrete spacetime

Following the pioneering idea of *Wilson* [23] it is possible to regularise a quantum field theory by putting the theory on a discretised version of Euclidean spacetime. The theory is then build up on the residual set of points

$$\begin{aligned}\Gamma_T \equiv \ \{x \in \Omega_T \mid x_\mu = a\, n_\mu;\ n_i \in 0,\ 1,\ \ldots,N_s - 1;\ n_0 = 0,\ 1,\ \ldots,N_t - 1\,;\\ \psi(x_0 = a\, N_t) = -\psi(x_0 = 0)\}\ .\end{aligned} \tag{2.1}$$

This set is denoted as a spacetime lattice and the parameter a is called lattice spacing [1]. The lattice in eq. (2.1) is defined at finite volume $V = a\, N_s^3$ which is suitable for the purpose of simulations where the working memory is naturally limited. Physical results are obtained in the continuum limit where $a \to 0$ and $V \to \infty$.

If a thermal system is considered the temperature is related to the finite temporal extent N_t of the lattice by

$$T = \frac{1}{a\, N_t}\ . \tag{2.2}$$

The antiperiodic boundary conditions in the temporal direction for the quark fields in eq. (2.1) per construction respect the boundary conditions for fermionic fields from eq. (1.38). The theory at zero temperature is obtained in the limit $a\, N_t \to \infty$.

The matter fields $\psi(x)$ are attached to the lattice points, whereas a naive transscription of gauge fields is not possible. In fact, the concept of local gauge invariance has no meaning for the discrete theory due to the introduction of a minimal length scale a. Gauge fields are thus introduced using the relation between gauge invariance and parallel transporters as discussed in section 1.2.1. Assuming a constant field $A_\mu(x)$ along the connecting lines of the lattice points, this concept is easily adopted to the lattice theory. The gauge degrees of freedom are then introduced by the parallel transporter connecting two neighbouring lattice points

$$U_\mu(x) \equiv e^{i\, g_0\, a\, A_\mu(x)}\ \hat{=}\ x \bullet\!\!\longrightarrow\!\!\bullet\ x + a\,\hat{\mu}\ . \tag{2.3}$$

Here g_0 is the bare lattice coupling.

---

[1] The lattices discussed in this thesis are chosen to be isotropic, i.e. $a_\mu = a$ and $N_{s,i} = N_s$ for simplicity. All lattices used in the simulations are of this type.

Upon discretisation the integration measure is transformed to a finite product of integrals, given by

$$\mathcal{D}A\,\mathcal{D}\bar{\psi}\,\mathcal{D}\psi \quad \to \quad d[U]\,d[\bar{\psi}]\,d[\psi] \equiv \prod_{x\in\Gamma_T}\left(\prod_{\mu=0}^{d-1} dU_\mu(x)\right) d\bar{\psi}(x)\,d\psi(x). \tag{2.4}$$

Observables are functionals of the fields $U, \bar{\psi}$ and ψ and its expectation value is given by the integral

$$\langle O\rangle = \frac{1}{Z}\int d[U]\,d[\bar{\psi}]\,d[\psi]\,O[U,\bar{\psi},\psi]\,e^{-S_G[U]-S_F[U,\bar{\psi},\psi]-S_\mu[\bar{\psi},\psi]}\;. \tag{2.5}$$

Here $S_G[U]$ and $S_F[U,\bar{\psi},\psi]$ are suitable discretisations of gauge and fermion actions and $S_\mu[\bar{\psi},\psi]$ is the term connected with chemical potential μ.

The momenta of the discretised theory belong to the dual lattice

$$\begin{aligned}\Gamma_T^* \equiv \quad & \Bigg\{ p\in\Omega_T^* \;\Bigg|\; p_\mu = \omega_{\mu,n_\mu};\; n_i = -\frac{N_i}{2},\,\dots\,,\frac{N_i}{2}-1\,, \\ & n_0 = -\frac{N_t}{2},\,\dots\,,\frac{N_t}{2}-1\;(T=0),\;\; n_0 = 0,\,\dots\,,N_t\;\,(T\neq 0)\Bigg\}\;,\end{aligned} \tag{2.6}$$

which is connected to Γ_T from eq. (2.1) via Fourier transformation. Here ω_{μ,n_μ} are the generalised Matsubara frequencies, given by

$$\begin{aligned}\omega_{i,n_i} = \quad & \frac{2\,\pi}{a\,N_s}\,n_i \\ \text{and} \quad \omega_{0,n_0} = \quad & \begin{cases} \dfrac{2\pi}{a\,N_t}\,n_0 & \text{for bosons} \\ \dfrac{\pi}{a\,N_t}\,(2\,n_0+1) & \text{for fermions}\,. \end{cases}\end{aligned} \tag{2.7}$$

The implications of eqs. (2.6) and (2.7) are twofold: (a) The momenta p_i are quantised and restricted to the first Brillouine zone; (b) The lattice introduces a momentum cut-off Λ^{lat},

$$|p_\mu| \le \Lambda^{\text{lat}} = \frac{\pi}{a} \quad \text{for} \quad T=0\;. \tag{2.8}$$

If the lattice is infinite in the spatial directions, i.e. $N_s \to \infty$, the momenta become continuous. The cut-off only depends on a and thus remains constant. Note that on the lattice there is an inherent difference between the temporal coordinates and the associated momenta at zero and finite temperature. This is connected to the antiperiodicity in the temporal direction which remains important in the continuum limit at finite temperature where $a\,N_t$ remains finite. The antiperiodicity does not affect the theory in the zero temperature limit, where $a\,N_t \to \infty$.

The cut-off Λ^{lat} serves as a regulator for the theory and the continuum limit implies its removal. Λ^{lat} thus represents a natural energy scale for the system. Following the discussion in section 1.2.1 this implies that the lattice coupling g_0 and the lattice spacing obey the renormalisation group equation,

$$a \, \frac{d \, g_0}{da} = -\beta_{\text{lat}}(g_0) \;, \tag{2.9}$$

in analogy to eq. (1.8). Here β_{lat} is the lattice β-function. Due to asymptotic freedom the coupling has to vanish for large energies, i.e. $g_0 \to 0$ for $a \to 0$. Inverting the solution $g_0(a)$ to eq. (2.9) yields the lattice spacing as a function of the bare coupling $a = a(g_0)$. In consequence, the continuum limit $a \to 0$ is reached for $g_0 \to 0$. To consider a thermal system the temperature $a N_t$ has to be fixed in the approach to the continuum. This implies that the temporal extent N_t has to be enlarged when a is decreased so that N_t is a measure for the lattice spacing at the transition point.

The lattice formulation offers some freedom for the choice of operators and actions at finite cut-off. To make sure that the expectation value in eq. (2.5) coincides with the one in the continuum it is necessary to fulfil

$$\lim_{a \to 0} O = O^{\text{cont}} \;, \quad \lim_{a \to 0} S_G = S_G^{\text{cont}} \quad \text{and} \quad \lim_{a \to 0} S_F = S_F^{\text{cont}} . \tag{2.10}$$

Each lattice operator can be written as a series in the lattice spacing a, as discussed in more detail in section 2.3. Equation (2.10) then fixes the constant term in this expression to the associated continuum operator.

2.2 Wilsons lattice actions

Fundamental to the properties of the lattice theory is the choice for the discretised version of the action. This section deals with the version of lattice actions introduced by *Wilson* [23] about 40 years ago. The advantage of these actions is their conceptual simplicity and the undistorted particle spectrum at non-zero lattice spacing. For further reading see [75] and [83].

2.2.1 Gauge action

The most important constraint for the gauge action is the invariance under $SU_c(3)$ gauge transformations. The link variables are in the adjoint representation of $SU_c(3)$ and thus transform as

$$U_\mu(x) \;\to\; \Lambda(x) \, U_\mu(x) \, \Lambda^{-1}(x + a\,\hat{\mu}) \quad \text{with} \quad \Lambda \,\in\, SU_c(3) \;. \tag{2.11}$$

Consequently, the trace of any closed loop of link variables is a gauge invariant quantity. The simplest of these loops is a closed loop of four links, the plaquette

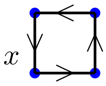

$$\hat{=} \; U_P \equiv U_\mu(n) \, U_\nu(n + a\,\mu) \, U_\mu^+(n + a\,\nu) \, U_\nu^+(n) \;. \tag{2.12}$$

Using this quantity the discretised version of the gauge action can be written as

$$S_G\,[U] = \beta \sum_P \left[1 - \frac{1}{3}\,\mathrm{ReTr}\,(U_P)\right] \tag{2.13}$$

where the sum over P runs over all plaquettes of the lattice. Here β is an *a priori* unknown coupling constant. Using the definitions (2.13) and (2.3) it is easy to verify that

$$\lim_{a\to 0} S_G = -\frac{g_0^2}{24}\,\beta \int_{\Omega_T} d^4x\; \mathrm{Tr}\,(F_{\mu\nu}\,F_{\mu\nu}) + \mathcal{O}(a^2)\;. \tag{2.14}$$

Matching with the continuum action then leads to the relation

$$\beta = \frac{6}{g_0^2}\;. \tag{2.15}$$

Eq. (2.14) further implies that lattice artefacts introduced by the gauge part of the action are of order a^2.

2.2.2 Fermion action

The next step is the discretisation of the fermionic part of the action. Using eq. (1.5) one can write down the lattice version of the covariant derivative in the symmetric form,

$$\nabla_\mu\,\psi(x) \equiv \frac{1}{2a}\left(U_\mu(x)\,\psi(x+a\,\hat{\mu}) - U_\mu^+(x-a\,\hat{\mu})\,\psi(x-a\,\hat{\mu})\right)\;. \tag{2.16}$$

However, the naive substitution of D_μ by ∇_μ leads to a sine function in the nominator of the massless propagator in momentum space which then has 16 poles in the first Brillouin zone. This leads to a 16-fold degeneracy of the fermionic degrees of freedom, an effect known as the fermion doubling problem.

To remove this degeneracy *Wilson* used the freedom to add terms proportional to the lattice spacing to the action without changing the continuum limit [23]. A proper additional term that removes the doublers is the discretised version of the d'Alembert operator

$$\begin{aligned} -\frac{r}{2}\,a\,\bar{\psi}(x)\,\Box\,\psi(x) \quad &= \quad \frac{r}{2\,a}\,\bar{\psi}(x)\;\left[2\,\psi(x) - U_\mu(x)\,\psi(x+a\,\hat{\mu})\right. \\ &\qquad \left. -U_\mu^+(x-a\,\hat{\mu})\,\psi(x-a\,\hat{\mu})\right]\;. \end{aligned} \tag{2.17}$$

Here r is an unphysical constant and the doublers are completely removed as long as $r \neq 0$. In practice, r can be chosen at will as observables in the continuum limit cannot depend on it and it is usually set to 1, as in the rest of this thesis. The result is the Wilson action for fermions given by

$$\begin{aligned} S_F[U,\bar{\psi},\psi] \quad &= \quad a^3 \sum_{x\in\Gamma_T} \bar{\psi}(x)\,(a\,\mathcal{M}_b + 4)\,\psi(x) \\ &\quad -\frac{a^3}{2} \sum_{x\in\Gamma_T} \sum_{\mu=\pm 0}^{\pm 3} \bar{\psi}(x+a\,\hat{\mu})\,(1+\gamma_\mu)\,U_\mu(x)\,\psi(x)\;. \end{aligned} \tag{2.18}$$

The following notation is commonly used, $\gamma_{-\mu} \equiv -\gamma_\mu$ and $U_{-\mu}(x) \equiv U_\mu^+(x)$.

Another convenient form for the fermionic action is the so called hopping parameter representation. The hopping parameter

$$\kappa_f \equiv \frac{1}{2\,a\,m_{b,f} + 8} \tag{2.19}$$

is related to the bare quark mass $m_{b,f}$ of flavour f. One can rescale the fermionic fields according to

$$\psi_f(x) \;\rightarrow\; \sqrt{2\,\kappa_f}\,\psi_f(x) \quad \text{and} \quad \bar{\psi}_f(x) \;\rightarrow\; \sqrt{2\,\kappa_f}\,\bar{\psi}_f(x)\;, \tag{2.20}$$

which allows the fermionic action to be written as

$$S_F[U,\bar{\psi},\psi] = \sum_{x\in\Gamma_T} a^4 \left[\bar{\psi}(x)\,\psi(x) - \frac{\kappa}{a}\sum_{\mu=\pm 0}^{3}\bar{\psi}(x+a\,\hat{\mu})\,(1+\gamma_\mu)\,U_\mu(x)\,\psi(x)\right]\;. \tag{2.21}$$

Here κ is a diagonal matrix with entries $\kappa = \mathrm{diag}(\ldots,\;\kappa_f,\;\ldots)$. It has become standard to refer to κ instead of the bare quark mass in the context of simulations.

An unpleasant feature of the additional term in eq. (2.17) is its explicit breaking of chiral symmetry at nonzero lattice spacing. The two offending terms are

$$\bar{\psi}(x)\,\left(\mathcal{M}_b + \frac{4}{a}\right)\,\psi(x) - \frac{1}{2\,a}\,\bar{\psi}\;(x+a\,\hat{\mu})\;U_\mu(x)\,\psi(x)\;. \tag{2.22}$$

The term proportional to $\mathcal{M}_b$ is the usual mass term while the terms proportional to $4/a$ and $U_\mu(x)$ are due to the insertion of the d'Alembert operator in the action. At finite lattice spacing these two terms lead to a mass shift m_c of the theory which changes with the lattice spacing and is in addition generated dynamically by the coupling term $\bar{\psi}(x{+}a\hat{\mu})U_\mu(x)\psi(x)$. The size of m_c is thus unknown *a priori* and has to be determined in the course of the simulations. The proper bare quark mass for a flavour f on the lattice is then given by

$$\bar{m}_f = m_{b,f} - m_c\;. \tag{2.23}$$

In terms of κ the mass shift m_c corresponds to a critical hopping parameter κ_c and the proper bare quark mass can also be written as

$$\bar{m}_f = \frac{1}{2\,a}\left(\frac{1}{\kappa_f} - \frac{1}{\kappa_c}\right)\;. \tag{2.24}$$

The Wilson term also introduces cut-off effects of order a. This presents a problem for simulations since very fine lattices are eventually needed to ensure sufficiently small lattice artefacts. Nevertheless, the leading lattice artefacts can be removed by an additional term in the action as discussed in the next section.

2.3 Lattice artefacts and $\mathcal{O}(a)$-improvement

One of the most fundamental systematic effects entering quantities measured in lattice simulations are the effects due to finite lattice spacing. A wanted feature of the theory is that lattice artefacts enter only at $\mathcal{O}(a^2)$ since then it is reasonable to perform the continuum extrapolation using only the leading order (a^2) term while the next terms of $\mathcal{O}(a^3)$ can be expected to be small. This is not the case for Wilson fermions where the artefacts enter at order a. In addition, the lattice operators suffer from cut-off effects, which means that even if the main lattice artefacts stemming from the action are of $\mathcal{O}(a^2)$ this must not be the case for the observable of interest. A systematic way to deal with lattice artefacts by means of an effective continuum theory has been introduced by *Symanzik* [86, 87]. The method allows for the construction of improved operators and actions with reduced lattice artefacts. In this section it is briefly reviewed with a focus on $\mathcal{O}(a)$-improvement for Wilson fermions. For a more detailed discussion see [82].

2.3.1 Effective continuum theory

The cut-off Λ^{lat} is the scale at which new continuum physics enters the lattice theory. Starting from the continuum, the theory on the lattice can be seen as an effective low-energy theory with the action [86, 87]

$$S_{\text{eff}} = \int_{\Gamma_T} d^4x \left[\sum_{n=0}^{\infty} \mathcal{L}_n(x)\, a^n \right] \tag{2.25}$$

and the constraint $\mathcal{L}_0 = \mathcal{L}^{\text{cont}}$. The effective lattice fields are similarly given as

$$\Phi_{\text{eff}}(x) = \sum_{n=0}^{\infty} \Phi_n(x)\, a^n \,. \tag{2.26}$$

Here $\Phi(x)$ is any lattice field or any linear combination of fundamental fields and $\Phi_0 = \Phi^{\text{cont}}$ the associated continuum field. The fields $\mathcal{L}_n$ and Φ_n are constrained by dimensionality and symmetry of the lattice fields and redundant operators, related to other operators using field equations and partial integration, can be eliminated. This reduces the number of possible terms significantly.

Important for the measurement of physical quantities are the connected renormalised correlation functions of some composite field Φ. Any of these, e.g. the connected renormalised lattice n-point function of the field Φ [2]

$$G_n(x_1, \dots, x_n) = \mathcal{Z}_\Phi^n \, \langle \Phi(x_1) \, \dots \, \Phi(x_n) \rangle \,, \tag{2.27}$$

---

[2] Here $\mathcal{Z}_\Phi$ is the renormalisation constant of the composite field Φ, as discussed in the next section.

is in the effective continuum theory given by an expansion of the form

$$\begin{aligned} G_n(x_1,\ldots,x_n) \; &= \; \langle \Phi_0(x_1) \, \ldots \, \Phi_0(x_n) \rangle^{\mathrm{cont}} \\ &\quad -a \int_{\Gamma_T} d^4y \; \langle \Phi_0(x_1) \, \ldots \, \Phi_0(x_n) \, \mathcal{L}_1(y) \rangle \\ &\quad +a \sum_{k=1}^{n} \langle \Phi_0(x_1) \, \ldots \, \Phi_1(x_k) \, \ldots \, \Phi_0(x_n) \rangle + \mathcal{O}(a^2) \; . \end{aligned} \tag{2.28}$$

All expectation values are taken with respect to the continuum action and contain connected contributions only. The integral in the second line diverges if y is equal to one of the points x_i. This divergence can be absorbed into a redefinition of the field $\Phi_1(x_i)$ since it is a local effect connected with the correlation between the field $\Phi(x_i)$ and $\mathcal{L}_1(x_i)$. The dependence on a in (2.28) is twofold: the explicit a-dependence and the possible variation of the coefficients included in the composite fields Φ_1 and $\mathcal{L}_1$. The latter will in general be small and can be computed perturbatively (see the extensive review by *Capitani* [88]).

The theory discussed above gives a handle on lattice artefacts and enables systematic improvement by using terms in the action and fields that cancel the leading order terms in eq. (2.28). The details of the necessary improvement terms depend on the action and the associated symmetries.

2.3.2 The Sheikholeslami-Wohlert action

The first task in the $\mathcal{O}(a)$-improvement program for Wilson fermions is the improvement of the action. The term $\mathcal{L}_1$ can be shown to be a linear combination of the operators (see [82, 89, 90])

$$O_1 \equiv i \, \bar{\psi} \, \sigma_{\mu\nu} \, F_{\mu\nu} \, \psi \; , \quad O_2 \equiv \widetilde{m}_G \, \mathrm{Tr} \, (F_{\mu\nu} F_{\mu\nu}) \;\; , \quad O_3 \equiv \widetilde{m}_\psi^2 \, \bar{\psi} \, \psi \; . \tag{2.29}$$

Here the definition $\sigma_{\mu\nu} = \frac{i}{2} \, [\gamma_\mu \, , \, \gamma_\nu]$ is used and $\widetilde{m}_G$ and $\widetilde{m}_\psi$ are coefficients with dimension of mass. The operators O_2 and O_3 are proportional to the operators in the kinetic term for the gluons and the one including the quark mass. In consequence, their coefficients can be absorbed in the renormalisation of the lattice coupling and the quark masses. This of course changes the renormalisation properties of the theory. O_1 is the only relevant operator that explicitly enters the improved action,

$$S_{SW}[U, \bar{\psi}, \psi] \equiv S_F[U, \bar{\psi}, \psi] + c_{SW} \, \frac{a^5 \, i}{8} \sum_{x \in \Gamma_T} \bar{\psi}(x) \, \sigma_{\mu\nu} \, \mathbb{F}_{\mu\nu}(x) \, \psi(x) \; . \tag{2.30}$$

This action has been introduced by *Sheikholeslami* and *Wohlert* in 1985 [35].

In eq. (2.30) $\mathbb{F}_{\mu\nu}$ is a suitable lattice representation of the gluon field strength tensor. Using the same arguments as for constructing the gauge action it is straightforward to show that the operator $\mathbb{F}_{\mu\nu}$ may be written as

$$\mathbb{F}_{\mu\nu}(x) = \frac{1}{8 \, a^2} \, \left(\mathbb{Q}_{\mu\nu}(x) - \mathbb{Q}_{\nu\mu}(x) \right) , \tag{2.31}$$

where $\mathbb{Q}_{\mu\nu}$ is given by a sum of plaquettes in the $\mu\nu$-plane, and a possible graphical representation is

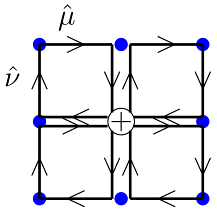

$$\hat{=} \quad \mathbb{Q}_{\mu\nu}(x) \; . \tag{2.32}$$

Here the '$\oplus$' is located at point x and denotes the summation over the four plaquettes. Due to the clover-leaf structure of the operator $\mathbb{Q}_{\mu\nu}$ the Sheikholeslami-Wohlert action that includes this particular improvement term is often referred to as the 'clover' action.

To complete the $\mathcal{O}(a)$-improvement, the clover coefficient c_{SW} has to be tuned appropriately. This is a non-trivial task and can be done perturbatively or non-perturbatively. The latter is naturally the preferred choice at large couplings. The non-perturbative value for c_{SW} was calculated for a large range of β-values in [91,92]. The results are conveniently given in the form of an interpolation formula, i.e. the Padé

$$c_{SW}(g_0) = \frac{1 - 0.454\, g_0^2 - 0.175\, g_0^4 + 0.012\, g_0^6 + 0.045\, g_0^8}{1 - 0.720\, g_0^2} \; , \tag{2.33}$$

which is used as the definition of c_{SW} in the range of $5.2 \leq \beta \leq 12.0$. The other possibility is to use perturbation theory which leads to the one-loop result [93]

$$c_{SW}(g_0)|_{\text{1-loop}} = 1 + 0.267\, g_0^2 \; . \tag{2.34}$$

If the simulations are not designed to take place in the region where c_{SW} is known non-perturbatively, eq. (2.33) should not be used to define c_{SW}. One would then suffer from a non-exact cancellation of $\mathcal{O}(a)$ lattice artefacts that in the worst case might lead to an increase of those. Possibilities to tune c_{SW} below $\beta = 5.2$ are discussed in appendix A.7.

A similar improvement can also be performed for the gauge action (2.13). Two types of improved gauge actions are the tree-level Symanzik [94,95] and the Iwasaki action [96]. However, the leading order lattice artefacts of the plaquette action are of $\mathcal{O}(a^2)$ and in terms of $\mathcal{O}(a)$-improvement it is sufficient for Wilson fermions to use the unimproved action for the simulations.

2.3.3 Improvement of local operators

To ensure an $\mathcal{O}(a)$-improvement for observables constructed from renormalised n-point functions one also has to get rid of the term including the field $\Phi_1(x)$ in the last line of eq. (2.28). To this end, one has to add counterterms to the local operators Φ similar to the counterterm for the Wilson action in the last section.

Of particular relevance for the rest of the thesis is the $\mathcal{O}(a)$-improvement for the vector and axial vector currents from eq. (1.17), as well as for the pseudoscalar density. On the lattice local versions of these operators are given by

$$\begin{aligned} P^a(x) &= \bar{\psi}(x)\,\gamma_5\,\frac{\sigma^a}{2}\,\psi(x) \\ J^a_{V,\mu}(x) &= \bar{\psi}(x)\,\gamma_\mu\,\frac{\sigma^a}{2}\,\psi(x) \\ J^a_{A,\mu}(x) &= \bar{\psi}(x)\,\gamma_\mu\,\gamma_5\,\frac{\sigma^a}{2}\,\psi(x)\;. \end{aligned} \tag{2.35}$$

The analysis [90, 97] shows that no additional operators contribute to $P^a(x)$ at $\mathcal{O}(a)$ and that the improved currents are given by

$$\begin{aligned} (J_{V,I})^a_\mu(x) &= J^a_{V,\mu}(x) + a\,c_V\,\partial_\nu\,T^a_{\mu\nu}(x) \\ (J_{A,I})^a_\mu(x) &= J^a_{A,\mu}(x) + a\,c_A\,\partial_\mu\,P^a(x)\;. \end{aligned} \tag{2.36}$$

Here ∂_μ is the symmetric version of the lattice derivative and $T^a_{\mu\nu}$ is the tensor current

$$T^a_{\mu\nu}(x) = i\,\bar{\psi}(x)\,\sigma_{\mu\nu}\,\frac{\sigma^a}{2}\,\psi(x)\;. \tag{2.37}$$

c_V and c_A are coefficients analogous to c_{SW} and need to be tuned appropriately. The perturbative and non-perturbative results, as far as available, are listed in appendix A.2.

2.4 Renormalisation

When physical quantities are extracted from theoretical computations in quantum field theories there is the inherent need for renormalisation of the bare parameters and fields of the theory (see the reviews by *Weisz* [98] and *Sommer* [99]). This is also true for LQCD simulations where the bare parameters and fields have to be renormalised when the regulator Λ^{lat} is removed. First contact with this procedure has already been made in the context of the bare coupling g_0 in eq. (2.9) where the relation between the coupling and the lattice spacing has been pointed out. This section presents a short review on renormalisation of LQCD with Wilson fermions as far as needed in the course of this thesis. It is important to note that any renormalisation procedure at zero temperature is sufficient to renormalise the theory at non-zero temperature as well [80]. This may be shown within perturbation theory.

2.4.1 Bare parameters

The first step on the way to a renormalised theory is to replace the bare parameters $\{\beta,\ \kappa_f\}$ by renormalised quantities $\{a,\ m_f\}$, where m_f is the renormalised quark mass of flavour f. All dimensionful quantities obtained in a simulation are given in units of the lattice spacing a, which is connected to the bare coupling by the renormalisation group equation (2.9). Since this equation cannot be solved non-perturbatively, due to the incomplete knowledge on the lattice β-function, the relation between the two is not known *ab initio*. A similar relation holds between the subtracted bare quark mass $\bar{m}$ and the renormalised mass m_f for a specific flavour.

Lattice spacing and renormalised quark mass can be determined from a set of observables Q_i that can be measured on the lattice and have a known counterpart in the continuum. This procedure is known as scale setting. It trades the knowledge about the simulation point against the predictivity for the quantities Q_i. This procedure is similar to perturbative renormalisation where the bare parameters have to be related to the physical ones to enable the theory to be predictive. The set of quantities Q_i defines the renormalisation scheme which is apparently not unique. In fact, different schemes might lead to different results at finite lattice spacing while results have to agree in the continuum. A scheme where hadronic quantities are used is known as a 'hadronic' renormalisation scheme. While there are lots of possible schemes, some of them are more appropriate then others in terms of residual systematic effects. However, going into the depths of the different schemes and their advantages and drawbacks is beyond the scope of this thesis. Instead, the following the focuses on the renormalisation of the two-flavour theory, as far as needed in the rest of this thesis. In particular, the renormalisation scheme used in the following is chosen to be mass independent. This means that the renormalisation constants and the lattice spacing are defined via the values they assume for some renormalisation condition in the chiral limit. This leads to a fixed set of renormalisation constants for a particular coupling for all quark masses.

To determine the lattice spacing it is convenient to use a reference scale that is easy to compute with high accuracy in the simulation. A prominent example is the Sommer parameter r_0 [100] which is also used in the course of this thesis. Other examples are the parameters t_0 [101] and the derived quantity w_0 [102]. The problem with these quantities is that they are not accessible for experiment and thus cannot be used to determine the lattice spacing in physical units directly. Instead, their continuum value in physical units has to be extracted from the simulations using a hadronic renormalisation scheme. Once this is done, the measurements for r_0/a, for instance, can be used to determine the lattice spacing. The continuum determination of r_0 for the particular choice of the action and simulation parameters used in this thesis has been performed using two different hadronic renormalisation schemes in [77, 103].

Once the lattice spacing is determined it is necessary to set the mass-scale, i.e. the relative size of the quark masses compared to the physical ones. This is a non-trivial task since the quark masses cannot be extracted directly without the knowledge about renormalisation constants. In addition, the quark masses are not well known from experiment, making it difficult to define the physical point. Furthermore, it is desirable to obtain a prediction for the light quark masses at the physical point from LQCD. To overcome these problems it has now become standard to use the mass of the pion to set the mass scale relative to chiral limit and physical point. The pion mass is related to the masses of the light quarks by eq. (1.25) in χPT to leading order and can be extracted without additional renormalisation. When more than two quarks are included in the simulation their masses have to be determined from additional quantities such as the mass of the Kaon.

2.4.2 Renormalisation of local operators

In addition to the renormalisation of bare parameters, there is the need for the renormalisation of the quark-fields, or equivalently the renormalisation of fermionic bilinears. It is governed by renormalisation group equations, introduced by *Callan* and *Symanzik* [104–106]. Assuming that the fermionic bilinear Φ_i renormalises only multiplicatively, its renormalised version is given by

$$(\Phi_R)_i = \mathcal{Z}^{\mathrm{SC}}_{\Phi_i}(\mu_R, g_0)\, \Phi_i \, . \tag{2.38}$$

Here $\mathcal{Z}^{\mathrm{SC}}_{\Phi_i}$ is the multiplicative renormalisation factor which in general depends on the scale μ_R, the coupling and the renormalisation scheme SC. The renormalisation factors are unknown *a priori* and have to be determined either perturbatively or non-perturbatively. The latter being the preferred choice at low energies. The renormalisation constants in different schemes are then related by an overall conversion factor $X_Q(\mu)$ that can be calculated perturbatively.

Important for this thesis is the renormalisation of the currents in eq. (2.36) and of the pseudoscalar and scalar densities, P^a and

$$S^a = \bar{\psi}(x) \frac{\sigma^a}{2}\, \psi(x) \, . \tag{2.39}$$

The latter is needed for the renormalisation of the chiral condensate at finite temperature. It should be noted that S^a mixes with the identity and is thus subject to additive renormalisation. The subtracted scalar density which only renormalises multiplicatively is defined as

$$\bar{S}^a = S^a - S_c \, . \tag{2.40}$$

The currents are conserved in the continuum and the chiral limit and thus are renormalisation group invariants. Nevertheless, if the naive local currents from eq. (2.36) are used the currents are not conserved at non-zero lattice spacing and thus obtain a coupling dependent renormalisation. In principle it is possible to construct a conserved vector current at finite lattice spacing, since $SU_V(2)$ is conserved for the Wilson action with two degenerate flavours. This is not the case for the axial current since the $SU_A(2)$ symmetry is broken explicitly. The multiplicative renormalisation factors of the local operators are a lattice artefact and thus cannot depend on the renormalisation scale. They can be extracted by imposing particular Ward-Takahashi identities [107, 108] on the lattice. At this point one has to proceed with some care for $\mathcal{O}(a)$-improved Wilson fermions, because in the process of $\mathcal{O}(a)$-improvement additional terms contributing to the renormalisation of the coupling and the quark masses were dropped. These contribute additional terms to the renormalised coupling and quark masses that for two degenerate flavours are given by [90]

$$g_R^2 = \mathcal{Z}^{\mathrm{SC}}_g(\mu_R, g_0)\ (1 + b_g\, a\, \bar{m})\ g_0^2 \quad \text{and} \quad m_R = \mathcal{Z}^{\mathrm{SC}}_m(\mu_R, g_0)\ (1 + b_m\, a\, \bar{m})\ \bar{m} \, . \tag{2.41}$$

Similar factors appear for the local operators so that [90,109]

$$\begin{aligned}(S_R)^a(x) &= \mathcal{Z}_S^{\mathrm{SC}}(\mu_R, g_0)\ (1 + b_S\, a\, \bar{m})\ \bar{S}^a(x) \\ (P_R)^a(x) &= \mathcal{Z}_P^{\mathrm{SC}}(\mu_R, g_0)\ (1 + b_P\, a\, \bar{m})\ P^a(x) \\ (J_{V,R})^a_\mu(x) &= \mathcal{Z}_V(g_0)\ (1 + b_V\, a\, \bar{m})\ (J_{V,I})^a_\mu \\ (J_{A,R})^a_\mu(x) &= \mathcal{Z}_A(g_0)\ (1 + b_A\, a\, \bar{m})\ (J_{A,I})^a_\mu\ . \end{aligned} \tag{2.42}$$

It is important to note that the coefficients b_Φ are artefacts of the $\mathcal{O}(a)$-improvement and thus do not depend on the renormalisation scheme. They only depend on the bare coupling and can be computer either perturbatively or non-perturbatively. A compilation of results from 1-loop perturbation theory as obtained in [97] and non-perturbative results for b_m and $[b_A - b_P]$ from [110] are given in appendix A.2.

In a simulation the renormalisation factors are obtained at non-zero quark mass and, in the mass-independent scheme, correspond to the effective renormalisation factors

$$\left[\mathcal{Z}_\Phi^{\mathrm{SC}}\right]^{\mathrm{eff}}(\mu_R, g_0) = \mathcal{Z}_\Phi^{\mathrm{SC}}(\mu_R, g_0)\ (1 + b_\Phi\, a\, \bar{m})\ . \tag{2.43}$$

In a typical simulation it is difficult to extract $\mathcal{Z}_\Phi^{\mathrm{SC}}(\mu_R, g_0)$ since the simulations have to be carried out at relatively large quark masses. A scheme where the direct determination in the chiral limit becomes possible is the Schrödinger functional (SF) scheme [111]. There the simulations do not suffer from singular quark propagators at zero quark mass. In this formalism μ_R-dependent renormalisation constants can be extracted at a particular physical volume which sets the SF renormalisation scale, i.e. $\mathcal{Z}_\Phi^{\mathrm{SF}}(\mu_R, g_0) = \mathcal{Z}_\Phi^{\mathrm{SF}}(1/(aN_s)^3, g_0)$. This allows contact to perturbation theory if the volume is small enough so that the conversion factors to other schemes can be calculated perturbatively.

In the chiral limit the renormalisation of the subtracted scalar density is equivalent to the inverse of the renormalisation of the subtracted quark mass [112],

$$\mathcal{Z}_S^{\mathrm{SC}}(\mu_R, g_0) = \left[\mathcal{Z}_m^{\mathrm{SC}}(\mu_R, g_0)\right]^{-1}\ . \tag{2.44}$$

This identity will be used in the finite temperature part to renormalise the chiral condensate. Equation (2.44) also implies $b_S = -b_m$.

2.4.3 PCAC and quark masses

A prominent and important example for the renormalisation of physical quantities in LQCD is the renormalisation of quark masses, discussed briefly in this section. For Wilson fermions, where chiral symmetry is broken explicitly, the bare quark mass is not directly proportional to the renormalised one. A good starting point to determine the quark masses is the lattice Ward identity known as the PCAC-relation,

$$\left\langle \partial_\mu (J_{A,R})^a_\mu(x)\, O \right\rangle = 2\, m_f\ \langle (P_R)^a(x)\, O\rangle\ . \tag{2.45}$$

Here $m_f \equiv m_f^{SC}(\mu_R)$ is the renormalised quark mass and O is an operator that has no support at point x. Considering averaged light quarks, i.e. $m_f = m_{ud}$ and $\kappa = \kappa_{\mathrm{sea}}$, solving for m_{ud} and inserting the expressions for the renormalised currents and densities one obtains

$$m_{ud} = \frac{\mathcal{Z}_A}{\mathcal{Z}_P^{\mathrm{SC}}} \, (1 + [b_A - b_P] \; a\bar{m}) \; m_{\mathrm{PCAC}} \; . \tag{2.46}$$

m_{PCAC} is the bare PCAC mass, or bare current quark mass, of flavour f defined by

$$m_{\mathrm{PCAC}} = \frac{\left\langle \partial_\mu (J_{A,I})^a_\mu(x) \, O \right\rangle}{2 \, \langle P^a(x) \, O \rangle} \; . \tag{2.47}$$

When $\mathcal{Z}_P$ is determined from the SF scheme there is a scale-dependent multiplicative factor connecting the renormalised quark mass m_{ud}^{SF} to the quark mass in the $\overline{\mathrm{MS}}$-scheme [113],

$$m_{ud}^{\overline{\mathrm{MS}}}(\mu_R) = X_m^{\overline{\mathrm{MS}},\mathrm{SF}}(\mu_R) \, m_{ud}^{SF} \; , \tag{2.48}$$

which is the standard reference scheme in the literature. For the specific choice of renormalisation factors used in this thesis the factor $X_m^{\overline{\mathrm{MS}},\mathrm{SF}}(\mu_R)$ is given perturbatively to high orders in [114]. In particular, to fourth order in perturbation theory for a renormalisation scale $\mu_R = 2$ GeV it is given by

$$X_m^{\overline{\mathrm{MS}},\mathrm{SF}}(2\;\mathrm{GeV}) = 0.910\,(28) \; . \tag{2.49}$$

2.5 Alternative fermion discretisations

Even though all results in this thesis were obtained with non-perturbatively $\mathcal{O}(a)$-improved Wilson fermions the results are to be compared to results from other collaborations that in general use different fermion discretisations. For the purpose of comparability it is thus necessary to give a short overview of different types of fermion discretisations and their advantages and drawbacks.

Another Wilson-type discretisation used in lattice simulations is the formulation including a chirally twisted mass term of the form

$$i \, a \, \mu_{\mathrm{tm}} \, \bar{\psi}(x) \, \gamma_5 \, \sigma^3 \, \psi(x) \tag{2.50}$$

in the action [115, 116]. This additional term protects the theory from unphysical zero modes and leads to a stabilisation of numerical simulations. In addition, it was realised that the theory is automatically $\mathcal{O}(a)$-improved when the hopping parameter is set to its critical value, $\kappa = \kappa_c(g_0)$ [117]. In this case the quark mass is exclusively defined via the twisted mass parameter μ_{tm}. Except for the enhanced numerical stability, twisted mass LQCD suffers from the same explicit breaking of chiral symmetry as other Wilson fermion formulations. Furthermore, the twisted mass term leads to the breaking of flavour symmetry at non-vanishing lattice spacing and thus to a distorted mass spectrum, which turns out to be a large effect in practice [118]. For a recent review see [119].

Another widely used fermion discretisation is the staggered discretisation [36]. The staggered formulation is obtained in terms of a spinor transformation, disentangling the four components. The resulting four single component Grassmann variables are located at the edges of the hypercubic lattice. As a result the cost for matrix multiplications for staggered fermions is reduced by a factor four and the simulations obtain a speed up by a similar factor. The fermion doublers are thereby reduced to four remaining fermionic degrees of freedom for a single fermion field, called 'tastes'. One of the advantages is the remaining residual chiral $U(1)$ symmetry which protects the mass from additive renormalisation. The drawback of the formulation is that for simulations with less than four fermionic degrees of freedoms one has to use the 'fourth root trick'. This has caused a lot of discussions in the lattice community (see [120–123]). Up to date it is not clear whether the continuum limit of rooted staggered fermions is equivalent to a single fermion flavour in QCD. In particular, *Testa* and *Rossi* recently constructed a zero-dimensional example where rooting fails due to non-perturbative effects [124]. Another systematic effect that has to be controlled in simulations with staggered fermions is taste-breaking (see [125] and [126]) leading to a non-degenerate spectrum. The standard procedure is to refer to the lightest pseudoscalar mass as the pion mass, leading to the possibility to perform simulations even below the physical quark mass. A better estimate for the effective pion mass in the simulations might be given by the averaged pion mass, leading to a significantly larger pion mass in the simulations (see [127]).

All fermion actions discussed above either have a residual number of doublers or break chiral symmetry explicitly. They are special examples for a more general theorem by *Nielsen* and *Ninomyia* [128, 129], which states that one of the following properties, (a) locality, (b) complete removal of the doublers or (c) chiral symmetry, is violated by every discretised theory. It is possible to circumvent this theorem by relaxing the demand for exact chiral symmetry to the demand that its breaking is a lattice artefact. The relaxed condition is known as the Ginsparg-Wilson relation [130]. Indeed, it was shown that any fermion discretisation fulfilling the Ginsparg-Wilson relation obeys an exact symmetry [131] which restores the correct chiral behaviour at finite lattice spacings. To date there are two popular examples for fermion actions that preserve chiral symmetry in terms of the Ginsparg-Wilson relation without residual fermion doublers. These are *Kaplan's* domain wall fermions [37–39] and *Neuberger's* overlap fermions [40, 41]. Both approaches are very costly from the computational point of view and thus not as frequently used in lattice simulations as the fermion discretisations discussed above.

Another approach to preserve chiral symmetry in lattice simulations, which goes back to *Karsten* [132] and *Wilczek* [133], is to keep the exact symmetry, whilst picking up the minimal number of two fermion doublers. The resulting fermion actions are known as minimally doubled fermions. While the general approach is known for quite some time, the topic recently has been revived by *Creutz* who proposed a new type of fermion actions based on a graphene type of lattices [134]. Later it was shown that this action is in fact another realisation of a minimally doubled action [135]. So far no numerical simulations were done with this type of fermions, but first steps towards this goal were reported [136, 137]. The possible advantage of this type of fermions are the presumably cheap simulations compared to overlap and domain wall fermions, but a number of coefficients eventually will have to be tuned.

PART II: Numerics

3 Monte-Carlo simulations

The lattice formulation discussed in the last chapter offers the possibility for numerical simulations in the non-perturbative regime. The purpose of this section is the introduction of the numerical methods. In particular, the hybrid Monte-Carlo method to simulate QCD with fermionic degrees of freedom is discussed with a special emphasis on two flavours of $\mathcal{O}(a)$-improved Wilson fermions. Also discussed are improved algorithms that enable simulations in the chiral regime. The last section contains a summary of the systematic effects that enter the measurements and that need to be controlled. For further reading the reader is referred to the textbooks [75, 81, 83] and the recent review [138].

3.1 Pseudofermionic representation of the fermion determinant

Equation (2.5) is the starting point for the numerical evaluation of the expectation values of observables in full QCD. The basic idea is to calculate the finite dimensional integral via a Monte-Carlo integration. While in principle this is more or less straight forward, some work has to be spent on including the fermionic degrees of freedom $\psi(x)$ in the simulation. These fields are Grassmann-valued and up to date no practical methods exist to directly implement such fields numerically.

The solution to this problem can be achieved by integrating out the fermionic degrees of freedom. Consider a theory with fermion action $S_F[\bar{\psi},\psi,U]$ on a spacetime lattice Γ_T. All types of fermion actions can be written in bilinear form

$$S_F[\bar{\psi},\psi,U] = \sum_{x\in\Gamma_T} \bar{\psi}(x)\, D[U]\, \psi(x)\ . \tag{3.1}$$

The multidimensional matrix $D[U]$ is the Dirac operator, or fermion matrix, of the action. The operator connected with the action (2.18) is known as the Wilson-Dirac operator and denoted by $D_W[U]$. $D[U]$ usually depends on the gauge fields and is a matrix in flavour-, Dirac- and colour-space and connects different lattice points. It is also possible to include the density part of the action $S_\mu[\bar{\psi},\psi]$ in the fermion matrix, which results in an additive contribution of the form $\mu\,\gamma_0$ if μ is the chemical potential connected to the quark number (cf. eq. (1.41)). The inclusion of finite density is a major challenge for numerical simulations since it leads to a complex determinant (see [139]) and the following discussion is limited to the case with $\mu = 0$.

Any operator O can be expressed as a polynomial in the fields $\bar{\psi}$ and ψ and the corresponding functional integral representation of its expectation value (2.5) transforms into a set of additive Gaussian functional integrals over Grassmann-valued fields. It is then possible to integrate out the fermions by using of the common formulae for Gaussian integrals over Grassmann-valued variables. The expectation value is then given by

$$\langle O\rangle = \frac{1}{Z}\int d[U]\ \tilde{O}[U]\ \det(D[U])\, e^{-S_G[U]}\ , \tag{3.2}$$

where $\tilde{O}[U]$ is the summed contribution of the expansion of O in $\bar{\psi}$ and ψ after the integration over the fermionic degrees of freedom. This formula is the starting point for simulations of QCD on the lattice.

Note that up to now the flavour content of the theory is not fixed since $D[U]$ is a matrix in flavour space. If $D[U]$ is diagonal in this space [1] the determinant in eq. (3.2) might also be written as

$$\det(D[U]) = \prod_f [\det(D_f[U])] \ , \tag{3.3}$$

where $D_f[U]$ is the Dirac operator for the specific flavour.

The weight of a given set of link variables $\{U\}$ is now given by $\det(D[U])\exp(-S_G[U])$, so that for the integration of eq. (3.2) one has to calculate the determinant of D for each $\{U\}$. Since D is a large matrix this is clearly not feasible. It is better to treat the fermion determinant stochastically and rewrite it in terms of unphysical bosonic spinor fields $\phi(x)$ and $\phi^+(x)$. Using a matrix $M[U]$ defined by

$$\det(M^+[U]\, M[U]) = \det(D[U]) \ , \tag{3.4}$$

one can rewrite eq. (3.2) as

$$\langle O \rangle = \frac{1}{Z} \int d[U]\, d[\phi^+]\, d[\phi]\, \tilde{O}[U]\, e^{-S_G[U]-S_{PF}[U,\phi^+,\phi]} \ , \tag{3.5}$$

where the pseudofermionic action is given by

$$S_{PF}[U,\phi^+,\phi] = \sum_{x\in\Gamma_T} \phi^+(x)\ \left(M^+[U]\, M[U]\right)^{-1}\ \phi(x) \ . \tag{3.6}$$

Equation (3.4) is easily fulfilled if $D[U]$ includes an even number of equivalent fermion flavours. In this case $\det(D[U])$ is strictly positive and $M[U]$ is simply given by the Dirac operator for half the number of flavours. For a single flavour $\det(D[U])$ is only strictly positive if chiral symmetry is exactly preserved. For Wilson fermions this is not the case which spoils the possibility to use $\det(D[U])$ as a weight in the simulations. Nevertheless, for heavy quarks such as the strange quark, it can be assumed that the configurations with negative determinant have a negligible weight in the functional integral [138] so that these can be dropped in the simulations. For Wilson fermions this is justified by the observation that the Dirac operator has a solid spectral gap for heavy quarks in the presence of gauge fields that are important for the path integral. With this assumption it is then possible to rewrite eq. (3.4) as

$$\det(M^+[U]\, M[U]) = \det\left(\sqrt{Q^+[U]\, Q[U]}\right) \ , \tag{3.7}$$

where $Q \equiv \gamma_5 D$ is the hermitian Dirac operator. In this case the operator M is not directly accessible and it is necessary to approximate the square root in an appropriate way. This can be done by a polynomial [140–142], a complex polynomial [143, 144] or a rational series [145,146]. However, the simulations of this thesis are concerned with two degenerate flavours where this problem does not occur.

---

[1] A Dirac operator where this is not the case is the twisted-mass Dirac operator.

3.2 Concepts of Monte-Carlo simulations

The idea of the statistical evaluation of integrals, known as Monte-Carlo integration, has been known to the mathematics and physics community for a long time. While it is a straight-forward approach for multi-dimensional integration, its unimproved version soon becomes unfeasible when going to more complicated integrands or higher dimensional integrals. A direct numerical evaluation of the integral (3.2), which involves roughly $\mathcal{O}(10^8)$ degrees of freedom for usual lattice sizes, is unfeasible. Instead one has to use optimised importance sampling within the Monte-Carlo integration as discussed in the following.

3.2.1 Importance sampling

The naive way to integrate the expectation value of eq. (3.2) randomly picks N sets of gauge fields $\{U\}_n$ and approximates the integral by

$$\langle O \rangle = \frac{1}{Z} \sum_{n=1}^{N} O[\{U\}_n]\, \rho_n \ , \tag{3.8}$$

where ρ_n is given by

$$\rho_n \equiv \det(D[\{U\}_n])\, e^{-S_G[\{U\}_n]} \ . \tag{3.9}$$

This approximation is exact in the limit $N \to \infty$. It is obvious that a naive integration of this type is inefficient as most parts of the parameter space are unimportant due to the exponential damping in ρ_n.

A more efficient way for performing the integration is achieved when the configurations $\{U\}_n$ are sampled according to ρ_n, the statistical weight of the configuration. The efficiency of the integration is then encoded in the efficiency of the generation of the configurations $\{U\}_n$. This method is known as importance sampling. Using an ensemble of N gauge field configurations obtained in this way, eq. (3.8) reduces to the ensemble average

$$\langle O \rangle = \frac{1}{N} \sum_{n=1}^{N} O[\{U\}_n] \ . \tag{3.10}$$

The main difficulty is the generation of the configurations $\{U\}_n$ with respect to the measure ρ_n. A convenient way is to use a Markov chain, i.e. to construct the configuration $\{U\}_n$ from the last configuration $\{U\}_{n-1}$ with a given probability $P_{n-1,n}$, known as the 'update step'. To make sure that the full space of configurations can be covered the probabilities $P_{n,m}$ have to fulfill the conditions

$$\sum_m P_{n,m} = 1 \quad \forall\, n \quad \text{and} \quad P_{n,m} > 0 \quad \forall\, n, m \ . \tag{3.11}$$

In practice, the second condition is a little to strict [2] and can be relaxed to $P \geq 0$ if the two additional requirements of 'aperiodicity' and 'ergodicity' are added instead (see e.g. section 2.2.1 in [138]).

---

[2] The DD-HMC used for the simulations of this thesis fulfills the relaxed condition instead of eq. (3.11).

For local theories like pure $SU(N)$ gauge theory or the $SU(2)$ Higgs model efficient update procedures can be constructed by successively applying local updates of single link variables (see [26, 148, 149] for pure gauge theory and [150] for the $SU(2)$ Higgs model). For theories including fermionic degrees of freedom the distribution includes non-local interaction terms encoded in the fermion determinant. In this case strictly local updates are unfeasible and a different method is needed. A suitable alternative is to propose a configuration $\{U\}_m$ and accept it as the nth configuration with the probability

$$P_{n-1,m} = \min\left(1, \frac{\rho_m}{\rho_{n-1}}\right) . \tag{3.12}$$

This is known as the Metropolis accept/reject step [147]. Obviously, a random choice of $\{U\}_m$ results in poor acceptance and it is mandatory to find a method to propose configurations that are in the important region of configuration space. The standard method for simulations in field theory is known as the Hybrid Monte-Carlo (HMC) algorithm [151], discussed in the next section.

3.2.2 Representative ensembles

An ensemble is called representative if it fulfills the demand that the number of configurations that are located in an open region $\mathcal{R}$ of configuration space compared to the total number of configurations is approximately as large as the importance of that particular region for the integrand of eq. (3.2) [138]. This demand in principle requires to have a very large number of gauge fields if all regions in configuration space have to be covered. Nevertheless, actual simulations usually use about $100 - 1000$ statistically independent configurations (at least for simulations at $T = 0$) and get relatively small error bars. The possibility to obtain a representative ensemble already with a relatively small number of gauge fields depends on the observable of choice. The more the observable depends on the long-range correlations of the gauge field the more configurations are needed. This is due to the fact that the average of the short distance behaviour of each configuration is similar, while the long distance behaviour might differ for different regions of the phase space. An example where the long range correlations are important are simulations at finite temperature. There the phase transition is driven by the collective dynamics of the gauge field and a lot more statistically independent configurations (typically of order $10^3 - 10^5$) are needed.

Crucial for the generation of a representative ensemble with a Markov chain is that the first configuration already resides in the important region of configuration space. In practice, it is hardly possible to generate such a configuration from scratch. Instead, the simulations are started from a completely random configuration, ‘hot-start’, or a configuration consisting of unit matrices, ‘cold-start’. Due to the statistical process that generates configurations distributed according to ρ, the simulation is then driven to the important regions in configuration space. After a sufficient number of updates the configurations are in the important region of configuration space, indicated by the fluctuations of the observables around a constant expectation value, and are said to be ‘thermalised’. One might then use one of these configurations as the starting point for the ensemble.

3.3 Hybrid Monte-Carlo

As discussed above the basic task for the algorithm is to find a suitable proposal for the new configuration which is accepted with large probability in the accept/reject step. The standard update algorithm for simulations with dynamical fermions is the 'hybrid' Monte-Carlo [151] (HMC) algorithm discussed below.

The basic idea is to evolve the field along the Hamiltonian equations of motion, i.e. along the extrema of the action, which, if the equations of motion are solved accurately, should lead to large acceptance rates. To this end an abstract simulation time τ is introduced and the hamiltonian is taken to be

$$H[U,\Pi,\phi^+,\phi] = \frac{1}{2}\sum_{x\in\Gamma_T}\Pi_\mu(x)\Pi_\mu(x) + S_G[U] + S_{PF}[U,\phi^+,\phi]\ . \tag{3.13}$$

Here $\Pi_\mu(x)$ is the conjugate canonical momentum of the gauge field $U_\mu(x)$. In addition, the expectation value from eq. (3.5) is rewritten as

$$\langle O\rangle = \frac{1}{Z'}\int d[U]\,d[\Pi]\,d[\phi^+]\,d[\phi]\,\tilde{O}[U]\,e^{-H[U,\Pi,\phi^+,\phi]} \tag{3.14}$$

and ρ_n in eq. (3.12) is replaced by

$$\rho_n^{(H)} \equiv \exp\left(-H[U,\Pi,\phi^+,\phi]\right)\ . \tag{3.15}$$

Note that the theory formulated in the hamiltonian formalism leads to equivalent results, since the Gaussian integrals over the momenta cancel between numerator and denominator in eq. (3.14).

The classical evolution of the fields follows the hamiltonian equations of motion

$$\begin{aligned}\frac{d}{d\tau}U_\mu(x) =&\ \Pi_\mu(x) \qquad \text{and}\\ \frac{d}{d\tau}\Pi_\mu(x) =&\ -\frac{\partial}{\partial U_\mu(x)}\left(S_G[U] + S_{PF}[U,\phi^+,\phi]\right)\ .\end{aligned} \tag{3.16}$$

For simulations these have to be integrated numerically. To this end the interval τ is divided into steps of length $\epsilon = \tau/L_\tau$ and for the time step ϵ the numerical integrator $T(\epsilon)$ is introduced. The proposal for the new fields in the update step is then given by

$$(U,\Pi)' = [T(\epsilon)]^{L_\tau}\ (U,\Pi)\ . \tag{3.17}$$

Numerical integrators used in practice belong to the class of symplectic integrators that are reversible and preserve the integration measure.

A simple and widely used integrator is the leapfrog integrator (see [138]), defined by the integration step

$$T_{LF}(\epsilon) \equiv T_\Pi(\epsilon/2)\,T_U(\epsilon)\,T_\Pi(\epsilon/2)\ , \tag{3.18}$$

with the two sub-integrators

$$\begin{aligned} T_U(\epsilon): &\qquad U_\mu(x,\tau+\epsilon) &&= \exp(\epsilon\,\Pi_\mu(x,\tau))\,U_\mu(x,\tau)\\ T_\Pi(\epsilon): &\qquad \Pi_\mu(x,\tau+\epsilon) &&= \Pi_\mu(x,\tau) - \epsilon\ [F_G[U] + F_{PF}[U]]\,(\tau)\ .\end{aligned} \tag{3.19}$$

Here $F_X[U] \equiv \partial S_X[U]/\partial U_\mu(x)$ and exp(...) is a suitable realisation of the exponential function for elements of the Lie-algebra of $SU(3)$ (see e.g. appendix A in [152]). For the leapfrog integrator discretisation errors with respect to the simulation time are of $\mathcal{O}(\epsilon^3)$. An example for an integrator with less discretisation effects is the Sexton-Weingarten integrator [153, 154], a special form of the the second order minimal norm integrator (see [155]).

So far the update is a deterministic procedure along the classical trajectory in configuration space up to discretisation effects and thus does not result in an ergodic procedure. This can be cured by the use of momentum refreshment where the initial momenta in the update are drawn randomly from a Gaussian distribution

$$\rho_\Pi \equiv \exp\left(-\frac{1}{2}\sum_{x\in\Gamma_T} \Pi_\mu(x)\Pi_\mu(x)\right) . \tag{3.20}$$

The result is a random walk through configuration space and restoration of ergodicity. This form of the field evolution is known as molecular dynamics (MD).

If the integrator is exact, the update preserves energy and leads to $\rho'^{(H)}/\rho^{(H)}_{n-1} = 1$. In practice, this is not the case and along the trajectory $\Delta H = H(U', \Pi') - H(U, \Pi) \neq 0$. To generate the desired distribution this energy violation has to be corrected by the inclusion of an accept/reject step with probability

$$P = \min\left(1, \frac{\rho'^{(H)}}{\rho^{(H)}_{n-1}}\right) = \min\left(1, \exp[-\Delta H]\right) . \tag{3.21}$$

This combination of MD with an accept/reject step is the earlier mentioned HMC algorithm. Important for the efficiency of the algorithm is the acceptance rate that should be sufficiently high (mostly around 80-90%) at reasonable numerical cost. The cost grows with the number of integrator applications L_τ and the cost necessary to calculate the forces F_X in the MD evolution.

3.4 Inversion of the Dirac operator

The most expensive part in the computation of the forces in the MD evolution is due to the included inversions of the Dirac operator. In consequence, the numerical cost of the simulations is directly connected to the efficiency of the inversion procedure. In the course of measuring fermionic observables there are actually two different steps in which the inverse of the Dirac operator is needed. In the HMC algorithm used to generate the configurations it is necessary to calculate spinors of the form

$$\varphi(y) = D_n^{-1}(y, x)\,\chi(x) , \tag{3.22}$$

where $\chi(x)$ is a known spinor. The inverse of the Dirac operator also appears in the computation of fermionic observables as discussed in detail in chapter 4. In this case one is interested in an estimator for the full inverse of the Dirac operator, the propagator. In principle it is possible, even though impractical, to calculate the full propagator by the use of the relation

$$D\,D^{-1} = \mathbf{1} \quad \Rightarrow \quad D_{ac}(x,y)\,D^{-1}_{cb}(y,z) = \delta_{ab}\,\delta_{xz}\ , \tag{3.23}$$

where a, b, c are indices in Dirac and colour space. This relation can be split in 12 × (number of lattice points) equations, one for each value of b and z. These can be written as

$$D_{ac}(x,y)\,\varphi_c(y) = \delta_a(x) \quad \Rightarrow \quad D\,\varphi(y) = \delta_a(x)\ , \tag{3.24}$$

where $\varphi_c(y)$ denotes the specific column a, x of the propagator and $\delta_a(x)$ is a point source, i.e. a spinor with all entries set to zero except for the a-component at point x which is set to one. The propagator is then given by

$$\left(D^{-1}_{ca}(y,x)\right) = (\ldots, \varphi_c(y), \ldots) \tag{3.25}$$

with the spinor $\varphi_c(y)$ at position a, x of the columns.

In both cases it is necessary to solve an equation of the form

$$D\,\varphi = \eta\ , \tag{3.26}$$

where η is the source and φ the solution. Equations of this form can be solved efficiently using iterative solvers.

3.4.1 Iterative solvers and the condition number

An iterative solver uses a sequence of approximate solutions $\varphi_1, \varphi_2, \ldots$ of the exact solution $\varphi(y)$ with increasing accuracy. Increasing accuracy is in this case indicated by a decrease in the norm of the residue

$$|\varrho_n| \equiv |\eta - D\,\varphi_n| = \varepsilon\ |\eta|\ . \tag{3.27}$$

ε then reflects the accuracy of the solution. A possible stopping criterion for the solver is given by $\varepsilon < \varepsilon_R$. ε_R then sets a limit on the accuracy for the approximation of the inverse Dirac operator. If φ_n is the approximate solution fulfilling the stopping criterion it can be shown that

$$|\varphi - \varphi_n| < \varepsilon_R\,K(D)\ |\varphi|\ , \tag{3.28}$$

where $K(D)$ is the condition number of the matrix D

$$K(D) = |D|\ \left|D^{-1}\right| = \sqrt{\frac{\lambda_{max}}{\lambda_{min}}}\ . \tag{3.29}$$

Here λ_{max} and λ_{min} are the largest and smallest eigenvalues of $D^{+}D$ respectively. The precision of the inversion limits the possible accuracy on either the molecular dynamics step or the measurement of the propagator and thereby the observable.

Popular algorithms to solve eq. (3.26) are the ‘CG’, ‘BICGstab’ and ‘GCR’ algorithms, as discussed for instance in [156]. These solvers are based on the Krylov space method, as described in detail in [138], combined with iterative improvement where after n iterations the solver is restarted to solve the residual equation [3]

$$\varphi = \varphi_n + \tilde{\varphi} \quad \text{with} \quad D\,\tilde{\varphi} = \varrho_n \,. \tag{3.30}$$

The measures for the efficiency of the solver are its convergence property and the computational effort for the iterative step. The computational effort for the iteration step is a fixed amount that only depends on the algorithm of choice. More crucial is the convergence property of the algorithm, i.e. the behaviour of the residue with the iteration number n. It is mainly influenced by the properties of the spectrum of the matrix D. In particular, it depends on the distribution of the eigenvalues of D in the complex plane. In the ideal case the residue decreases exponentially

$$|\varrho_n| \lesssim e^{-n/K(D)} \,. \tag{3.31}$$

This behaviour can be shown rigorously for the GCR algorithm applied to the Dirac operator under some assumptions (see chapter 1.2.2 in [138]). This property displays one of the main problems for simulations in the chiral regime. There the condition number of the Dirac operator grows due to the appearance of small eigenvalues and a lot more iterations are needed to reach the desired accuracy.

3.4.2 Preconditioning – Schwarz preconditioning and deflation

A possibility to improve the convergence properties of the solver is to use preconditioning techniques. These yields smaller condition numbers for the matrices in the necessary inversions and thereby reduce the necessary numbers of iterations. The starting point is the introduction of two linear operators L and R to rewrite eq. (3.26) as

$$M\,\chi = (L\,\eta)\,, \quad \text{with} \quad \chi \equiv R^{-1}\,\varphi \quad \text{and} \quad M \equiv L\,D\,R\,. \tag{3.32}$$

The solution is then given by $\varphi = R\,\chi$. If the application of R and L is not to costly and the condition number of M is significantly smaller than the one of D, the method might lead to a significant speed-up.

One of the most common and prominent examples is even-odd preconditioning which goes back to *De Grand* [157, 158]. The technique uses the fact that the Dirac operator is a sparse matrix, including only nearest neighbour interactions. This enables a division of the lattice in the sets of ‘even’ and ‘odd’ points and results in two equations for the two different sets. One of the two equations is easily solved, while the other demands a numerical inversion. The condition number of the matrix in the nontrivial equation is usually reduced by more than a factor two compared to the one of D and the method leads to an acceleration by a factor of about 2. The big advantage of the method is its conceptual simplicity which enables the easy combination with other methods.

---

[3] This procedure also offers the starting point for single precision acceleration, where the residual equations are only solved to single precision, while the result might still be computed to double precision.The use of single precision numbers in the intermediate steps might lead to a significant speed up of about a factor two.

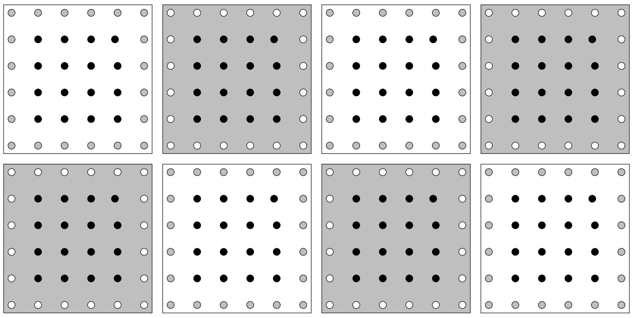

Figure 3.1: Two dimensional sketch of a chessboard cover of a lattice. Taken from [159].

Another efficient preconditioner which tends to project out the high modes, based on the Schwarz alternating procedure [160, 161], has been introduced by *Lüscher* [159]. For this technique the lattice is divided into two sets, Ω_S and Ω_S^*, of non-overlapping domains (blocks) Λ_S and Λ_S^* that form a chessboard cover of the lattice, as shown schematically in figure 3.1. The procedure visits the blocks and updates the estimate $\tilde{\varphi}$ for the solution by

$$\tilde{\varphi} \;\rightarrow\; \tilde{\varphi} + D^{-1}\,\mathcal{P}_{\Lambda_S}\;(\eta - D\,\tilde{\varphi})\;, \tag{3.33}$$

where $\mathcal{P}_{\Lambda_S}$ is the projector on the support of the block Λ_S (here Λ_S might also denote a Λ_S^* block). One such sweep over all blocks of the lattice is called a Schwarz cycle. The residue changes in each step only in Λ_S and its direct neighbours, i.e. on black blocks if Λ_S is a white block or vice versa, because the change of $\tilde{\varphi}$ is transported to the neighbouring blocks only by the Dirac operator. The procedure is thus easily carried out in parallel by first visiting all the white blocks simultaneously and then processing the black blocks. To this end it is beneficial to have at least two blocks on each processor to minimise communication overhead and to avoid sleeping times. A number of cycles of the procedure eliminates the high frequency modes in the operator as they have short wavelengths and thus are coupled to block properties.

The operator which carries out N_{cy} of these cycles is denoted as M_{sap} and might be used as a preconditioner for eq. (3.26) with

$$D\,M_{\mathrm{sap}}\chi = \eta \quad \text{and} \quad \varphi = M_{\mathrm{sap}}\,\chi\;. \tag{3.34}$$

This type of preconditioning is expensive in the sense that some time has to be spent to generate the operator M_{sap} in each application, a cost which is apparently not negligible since inversions are involved. However, the cost can be kept at a moderate rate since $D\,\mathcal{P}_{\Lambda_S}$ only acts on a small subspace of the lattice and is usually well conditioned. In addition, the inversions can be done using a relatively low precision since M_{sap} only acts as a preconditioner and appears at a stage where usually single precision is used. Furthermore, they can be done on a single processor without communication.

A very intuitive way for preconditioning is deflation. In textbook deflation (for reviews see e.g. [138,162]) the exact low-modes of the operator are calculated and used for the exact inversion of the associated part of the operator. Equation (3.26) is then projected to the space orthogonal to these modes which leads to a better conditioned equation due to the smaller ratio of eigenvalues. This procedure soon becomes inefficient for large lattices since the computation of the exact modes is costly and their number below some cut-off increases with the volume [163]. A possible solution is to construct an approximate deflation space from N_D orthogonal spinors ξ_k with strong projection on the low modes [164–166] (for a review see also [167]). Using these spinors one can introduce the projector $\mathcal{P}$ to this approximate deflation space and the associated 'little' Dirac operator A as

$$\mathcal{P} = \sum_{k=1}^{N_D} \xi_k \, \xi_k^{+} \quad \text{and} \quad A \equiv \mathcal{P} \, D \, \mathcal{P} \, . \tag{3.35}$$

As before this projector can be used to obtain separate equations for the deflation space and the orthogonal space. The first equation is readily obtained by using $L = R = \mathcal{P}$, while for the second one might use the two projectors

$$L = 1 - D \, \mathcal{P} \, A^{-1} \, \mathcal{P} \quad \text{and} \quad R = 1 - \mathcal{P} \, a^{-1} \, \mathcal{P} \, D \, . \tag{3.36}$$

Depending on the size of N_D the first equation is relatively easy to solve while the second is usually more demanding. It is important to note that the application of L and R includes the calculation of A^{-1} and is thus more or less costly. The efficiency of the method depends strongly on the numerical cost for the construction of the fields ξ_k and the condition numbers of A and M.

The most crucial part is the construction of the fields ξ_k since they have to be orthogonal with sufficient overlap with the low modes. A very efficient method to construct these modes was introduced in [167] which uses a similar domain decomposition as the Schwarz preconditioner. The method generates the orthogonal fields by projecting a set of global fields with sufficient overlap with the low modes to the blocks where they are orthogonalised. The result is a large approximate deflation subspace at comparably small numerical cost. The new set of spinors still has sufficient overlap with the low modes if the low modes are 'locally coherent', i.e. if they can be approximated locally by a small number of fields. This concept was investigated in [167] and shown to be a good property for the Dirac operator in simulations at zero temperature and for intermediate quark masses.

The combination of this type of deflation and Schwarz preconditioning with a GCR algorithm leads to a very efficient solver, denoted by 'DFL-SAP-GCR'. It has excellent scaling properties with the volume and the quark mass [167] and is the basis for the success of the algorithms discussed in the next section.

3.5 Improved algorithms

The use of a fast solver for the inversions in the HMC algorithm is a first step to speed-up the generation of the gauge ensembles. Further improvement can be achieved if the Dirac operator is preconditioned explicitly within the HMC. This can be realised by a factorisation of the fermion determinant. The consequential appearance of different fermionic forces in the MD and the introduction of multiple timescale integrators usually leads to a further reduction of computational cost.

3.5.1 Preconditioned HMC

The basic idea is to split the Dirac operator in n pieces

$$D = \prod_{i=0}^{n} D_i \,, \qquad \text{so that} \qquad \det(D) = \prod_{i=0}^{n} \det(D_i) \,. \tag{3.37}$$

This decomposition of the determinant is particularly useful if one or more of the matrices D_i are upper or lower triangular since then the determinant is trivial. A factorisation as in eq. (3.37) can be embedded in the HMC algorithm by the introduction of n pseudofermionic fields ϕ_i as described in section 3.1, leading to a pseudofermionic action

$$S_{PF}[U, \phi_i^+, \phi_i] = \sum_{x\in\Gamma_T,\, i=0}^{n} \phi_i^+(x)\, M_i^+[U]\, M_i[U]\, \phi_i(x) \,. \tag{3.38}$$

It is always possible to split the Dirac operator

$$D = \begin{pmatrix} D_{11} & D_{12} \\ D_{21} & D_{22} \end{pmatrix} \tag{3.39}$$

in three parts by the use of the matrices

$$L = \begin{pmatrix} 1 & 0 \\ -D_{21}\, D_{11}^{-1} & 1 \end{pmatrix} \quad \text{and} \quad R = \begin{pmatrix} 1 & -D_{11}^{-1}\, D_{12} \\ 0 & 1 \end{pmatrix} \tag{3.40}$$

and a decomposition similar to the one in eq. (3.32). In that case the determinant of L and R is unity and the matrix M from eq. (3.32) is the Schur complement of the decomposition,

$$M = \begin{pmatrix} D_{11} & 0 \\ 0 & D_{22}\, \overline{M} \end{pmatrix} \,, \quad \text{with} \quad \overline{M} \equiv 1 - D_{22}^{-1}\, D_{21}\, D_{11}^{-1}\, D_{12} \,. \tag{3.41}$$

The fermion determinant is then given by the (symmetric) decomposition [4]

$$\det(D) = \det(D_{11})\, \det(D_{22})\, \det(\overline{M}) \,. \tag{3.42}$$

The method is efficient if the matrices D_{11} and D_{22} have a block diagonal structure with block elements of moderate size. One prominent example is again even-odd preconditioning, where both matrices are diagonal in position space and the inversions and determinant calculations can be done explicitly, i.e. without the use of pseudofermionic fields [170,171].

As a consequence of eq. (3.42) different fermion forces appear in the MD. Usually they are of different magnitude and importance for the movement through phase space. It is then possible to construct an integrator T_{Π} which works with different integration step size for the different forces. Such an integrator is called a multiple-timescale integrator [172,173]. In practice, it turns out that the gauge force F_G is always an order of magnitude larger than the fermionic forces and thus of most importance for the MD. If the fermionic forces

---

[4] There are in fact two possible decompositions, but for practical purpose it turns out that the symmetric version usually leads to more efficient algorithms [168,169].

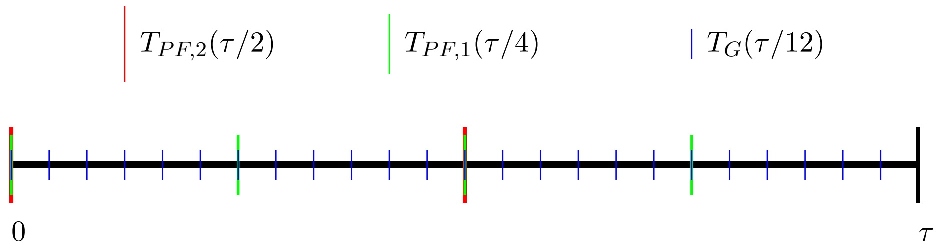

Figure 3.2: Schematic representation of the molecular dynamics evolution in the case of an recursively defined multiple timescale integrator as in eq. (3.43) with $n = 2$ and $L_2 = 1$, $L_1 = 2$ and $L_0 = 3$. For simplicity the application of T_U was left out of this sketch.

$F_{PF,i}$ are ordered according to their magnitude one can use the $n + 1$ recursively defined integrators

$$\begin{aligned} T_0(\epsilon) &\equiv [T_G(\epsilon/2\,L_0)\,T_U(\epsilon/L_0)\,T_G(\epsilon/2\,L_0)]^{L_0} \qquad \text{and} \\ T_i(\epsilon) &\equiv [T_{PF,i}(\epsilon/2\,L_i)\,T_{i-1}(\epsilon/L_i)\,T_{PF,i}(\epsilon/2\,L_i)]^{L_i} \end{aligned} \tag{3.43}$$

and use the integrator $T_{PF,n}$ instead of the leapfrog integrator. Here L_i are integer numbers that define the step sizes and T_G and $T_{PF,i}$ are the integrators defined by

$$\begin{aligned} T_G(\epsilon) \quad &: \quad \Pi_\mu(x,\tau+\epsilon) &= \Pi_\mu(x,\tau) - \epsilon\,(F_G[U])_\mu(\tau) \qquad \text{and} \\ T_{PF,i}(\epsilon) \quad &: \quad \Pi_\mu(x,\tau+\epsilon) &= \Pi_\mu(x,\tau) - \epsilon\,(F_{PF,i}[U,\phi_i^+,\phi_i])_\mu(\tau)\,. \end{aligned} \tag{3.44}$$

Figure 3.2 shows a sketch of a possible distribution of the integrators $T_{PF,i}$ along a MD evolution step. The method leads to a large gain in performance when the numerical cost for the calculation of the terms $F_{PF,i}$ decrease with i since the more expensive terms then have to be computed less often.

To obtain an efficient integrator for the MC evolution the numbers L_i have to be optimised. A suitable and also efficient choice is to tune the L_i so that they obey [173]

$$\left(\prod_{j=i}^{n} L_j\right)^2 |F_{PF,i}| = \left(\prod_{j=1}^{n} L_j\right)^2 L_0^2\,|F_G| = \text{const} \quad \forall\, i\,. \tag{3.45}$$

3.5.2 DD and MP algorithms

Two popular and efficient examples for preconditioning of the HMC are *Hasenbusch's* mass preconditioning [174, 175] (MP) and *Lüscher's* domain decomposition [152, 176] (DD). Both are used for the simulations reported in this thesis and the associated speed up is essential to be able to simulate in the chiral regime.

In the case of mass preconditioning the condition number of the matrices is lowered by using incrementally larger masses in the inversions within the HMC. This can be achieved by splitting the fermion determinant into n parts by using $n-1$ intermediate masses $\bar{m}_i$.

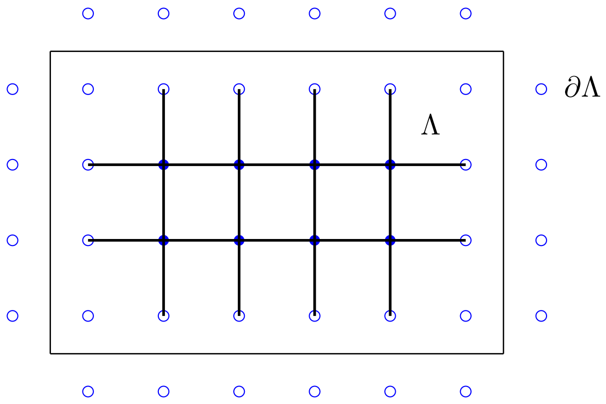

Figure 3.3: Two-dimensional sketch of a 6×4^3 sublattice Λ. The active links are marked by fat solid lines. The open circles outside of the sublattice belong to the exterior boundary $\partial\Lambda$ and therefore to the set $\partial\Omega$ if this block is a 'white' block. The open circles inside of Λ belong to the boundary of the 'black' blocks, i.e. to the set $\partial\Omega^*$.

The resulting decomposition is defined by the matrices

$$D_1 \equiv D + \bar{m}_1 \ , \quad D_i \equiv \frac{D + \bar{m}_i}{D + \bar{m}_{i-1}} \quad \text{for } 1 < i < n \quad \text{and} \quad D_n \equiv \frac{D}{D + \bar{m}_{n-1}} \ , \tag{3.46}$$

where D is the Dirac operator with the target mass. The ordering is also appropriate for the multiple timescale integrator since the influence on the MD evolution of fermions with larger masses is smaller. The procedure combined with even-odd preconditioning is used in a number of large scale simulation projects, for instance by the ETMC collaboration [177]. The method becomes particularly efficient when it is combined with the DFL-SAP-GCR solver since its scaling properties translate directly to the HMC algorithm [178].

Domain decomposition is based on the observation that the high-frequency modes are connected to local properties, while the low-frequency modes correspond to long range interactions. The two types of modes can thus be separated by decomposing the Dirac operator in block operators and the operator for block interactions. In addition to the splitting of the forces, this has the advantage that the high-frequency parts, which have to be evaluated most often, can be treated in parallel without communications. The decomposition can be achieved by using non-overlapping 'white' and 'black' blocks Λ and Λ^* with the associated sets Ω and Ω^* similar to the ones used for Schwarz preconditioning. A sketch of such a block is shown in fig. 3.3. The Dirac operator then assumes the form [152]

$$D = \begin{pmatrix} D_{\Omega} & D_{\partial\Omega} \\ D_{\partial\Omega^*} & D_{\Omega^*} \end{pmatrix} \ . \tag{3.47}$$

Here D_{Ω} and D_{Ω^*} denote the restrictions of D to the individual blocks and includes only hopping terms inside the blocks while $D_{\partial\Omega}$ includes the hopping terms from boundary $\partial\Omega$ to $\partial\Omega^*$ and $D_{\partial\Omega^*}$ the hopping terms from $\partial\Omega^*$ to $\partial\Omega$.

This decomposition is of the form of eq. (3.39) and leads to the decomposition of the determinant

$$\det(D) = \det\left(D_\Omega\right)\,\det\left(D_{\Omega^*}\right)\,\det\left(M_{DD}\right)\ . \tag{3.48}$$

The matrix M_{DD} is defined as

$$M_{DD} \equiv 1 - D_\Omega^{-1}\,D_{\partial\Omega}\,D_{\Omega^*}^{-1}\,D_{\partial\Omega^*}\ . \tag{3.49}$$

The first two matrices are diagonal in block space and their determinants factorise further

$$\det\left(D_\Omega\right)\,\det\left(D_{\Omega^*}\right) = \prod_{\text{all blocks}} \det\left(D_\Lambda\right)\ , \tag{3.50}$$

where D_Λ is the restriction of D to the block Λ. Even though the dimension of D_Λ is significantly smaller than the dimension of D their inversion is still a nontrivial task. It is therefore advantageous to further implement even-odd preconditioning on the blocks. The most complicated and costly part is the inversion of M_{DD}, which actually involves two inversions of the full Dirac operator [152]. These inversions can be accelerated significantly by the use of the DFL-SAP-GCR solver [179].

For the domain decomposition the links that are changed in the course of the MD are conveniently restricted to some subspace of 'active' link variables as described in detail in [152]. To restore ergodicity it is then necessary to shift the gauge field by a random vector after each step of the HMC evolution so that different links are held fixed in different proposals for new configurations. In this case the only parts of the program where communications are needed are applications and inversions of M_{DD} which includes the low frequency part and thus appears in the outer part of the multiple-timescale integrator. Domain decomposition in combination with the DFL-SAP-GCR solver leads to a significant speed up for large lattices and small quark masses. The drawback is the increase in autocorrelations of the configurations due to the restriction to a subset of active link variables in the HMC update. The autocorrelations might be decreased by choosing larger blocks which in turn demand larger local lattices and a smaller number of processors. Furthermore, the blocks in the algorithm have to be arranged so that two blocks are located on each sublattice while at the same time they should be bigger than 0.5 fm to ensure an efficient distribution of low and high frequency modes between the block operators and the Schur complement [152]. This is a major drawback if large scale computing systems should be used for the simulations. On these platforms it is mandatory to use a large number of processors for efficient calculations which is difficult to combine with the restrictions from the DD-HMC.

3.6 Limitations and systematic effects

Simulations are necessarily done at finite volume and non-zero lattice spacing which introduces systematic effects that need to be controlled. Furthermore, when simulations are done at unphysically large pion masses there is the additional need for an extrapolation to the physical point or the chiral limit which is prone to systematic uncertainties. Those aside there are also other less obvious systematic effects affecting the simulations and measurements. This section serves to summarise the main effects and their parameter dependence. Of particular relevance is the approach to the chiral limit where most of the systematic effects are enhanced. The chiral and continuum extrapolations are left out from the discussion in this section as they are the subject of the following parts of this thesis.

The systematic effects can be classified according to:

1. **Discretisation effects:** Discretisation effects, or cut-off effects, are due to non-zero lattice spacing and become problematic when the inverse lattice spacing reaches an energy scale only a few times larger then the energy of the bound states of interest. In this case the extent of the meson or nucleon becomes of the same order of magnitude as the lattice spacing and is not screened accurately. This effect appears as a drastic increase in the size of the coefficients in the effective continuum theory. To keep these effects under control the lattice spacing should fulfill [181]

   $$m_E \ll 1/a \,. \tag{3.51}$$

   where m_E is the typical energy scale for the observable of interest. For hadrons and mesons consisting of light quarks it is thus sufficient to discard all lattices with $a > 0.1$ fm.

   One of the main problems that arises when the lattice spacing is reduced is the corresponding increase in autocorrelations due to the approach to the second order critical point at $\beta \to \infty$. One of the observables that is most affected and thus serves as a good indicator is the topological charge [182]. As noted recently this effects tends to become large at lattice spacings of about $a = 0.03$-0.04 fm for dynamical Wilson fermions [183, 184]. Recently, it has been proposed to solve this problem by the use of open boundary conditions in the temporal direction [185, 186].

2. **Finite volume effects:** These are effects that occur due to the finite size of the box and their size depends on the sensitivity of the particular quantity on long range correlations. For a typical energy scale m_E of the observable of interest this means that

   $$\frac{1}{a\, m_E} \ll \frac{N_s}{a} \,. \tag{3.52}$$

   For mesonic quantities one thus expects that finite size effects are negligible if [180, 181]

   $$m_\pi\, a\, N_s \gtrsim 4 \,. \tag{3.53}$$

   If this is fulfilled, the wavelength of the pion, and thus also of all other states is smaller than the spatial extent of the lattice. This condition has been shown empirically to work for a number of quantities, such as the spectrum of mesons. However, even if this criterion is fulfilled the analysis should be supplemented by an explicit check of the size of finite volume effects to ensure that they are small for the quantity of interest.

3. **Contamination from excited states:** Operators in LQCD project on the whole set of states in a given quantum number channel. The excited states evolve a mass gap ΔE to the ground state and their contributions to correlation functions die out

exponentially with $\exp(-\Delta E\, t)$. Here t is the time separation of the source or sink (cf. section 4.1). Depending on the particular quantity, it is expected that the mass gap decreases with decreasing pion mass. The excited states thus die out significantly slower at small quark masses. In practice, the problem is that neither the mass gaps nor the overlaps between the states are known. One is thus restricted to either decide by eye at which t the excited state might be suppressed sufficiently or to perform a fit including terms modeling the excited state contributions. The limiting effect for the extraction of the observable is then often the bad signal-to-noise ratio for large temporal separations t. A case where this is especially problematic are baryonic quantities, as discussed in detail in [187].

4. **Quenching effects:** These effects arise due to the neglection of the effects of quark loops in the generation of gauge ensembles and their size is difficult to quantify. While the heaviest generation of quarks likely decouples from the dynamics of the light quarks this is not necessarily the case for the quarks of the second generation. At present simulations are usually carried out with two to four dynamical quarks. While the results for quantities connected to mesons and baryons made only of light quarks tend to agree well between simulations with a different number of dynamical quarks (see [29]). This will in general not be the case for quantities that include strange or charm quarks explicitly. Another effect similar to quenching is the effect of iso-spin breaking. In the simulations the light quarks are taken to be degenerate to protect the simulations from the appearance of negative fermion determinants. This of course is only approximately realised in nature. Since measurements in LQCD have started to reach a precision where these effects might become visible they should eventually be included. First attempts have already been reported in [188].

The different effects listed above are of course interrelated. Finite volume effects and excited state contributions increase in the approach to the chiral limit while the others are not affected as much. In the approach to the chiral limit it is thus necessary to enlarge the lattice significantly. In addition, the HMC algorithm slows down due to the increase in the condition number of the Dirac operator and the enhancement in the relative size of the fermionic contribution. The combination of these effects is responsible for the problem to simulate at physical quark masses directly. Today first simulations at physical quark masses are available, made possible by the tremendous increase in the efficiency of algorithms and compute power (see [189–191]).

4 Fermionic observables

The last section focused on the generation of ensembles. The next step to calculate physical quantities is their measurement on the generated configurations. While operators that only depend on link variables are easy to calculate on a given configuration fermionic observables are more difficult. First, fermionic degrees of freedom are integrated out in lattice simulations. In this process the fermionic fields have to be taken into account. This results in the appearance of quark propagators that have to be measured by inverting the Dirac operator. Second, physical quantities have to be extracted in the asymptotic limit in temporal direction of Euclidean correlation functions that suffer from an exponential growth of the noise-to-signal ratio, except for those related to a pion at rest. The purpose of this chapter is the discussion of the methods used to extract fermionic observables and the discussion of the construction of improved estimators that lead to a substantial error reduction. This is of particular importance for simulations in the chiral regime where fluctuations tend to be large.

4.1 Spectral representation of Euclidean correlation functions

Fermionic observables can be expressed in terms of expectation values of n-point functions constructed from gauge invariant fermion operators. In this thesis the focus is on mesonic observables, constructed from local fermionic bilinears of the form $\Phi(x) = \bar{\psi}(x)\,\Gamma\,\psi(x)$ with the quantum numbers of mesons. Γ is a multi-dimensional matrix with Dirac, colour and flavour indices. The common matrices and their relations to mesonic states are listed in table 4.1. The purpose of this section is to explain the connection between n-point functions and masses as well as matrix elements. The next section is devoted to the calculation of those. Note that the identification of particle masses with the exponential decay of the signal in the temporal direction for n-point functions applies to expectation values of QCD at zero temperature. At non-zero temperature mesonic correlation functions are also connected to a spectral function but the groundstate energies are in general not directly related to the masses of boundstates (cf. section 9.4).

Masses and vacuum-transition matrix elements can be extracted from 2-point functions $\big\langle \Phi_2(y)\,\Phi_1^{+}(x) \big\rangle$. Here the hermitian conjugate denotes the creation operator associated with Φ_1. In most applications one is interested in properties of particles or bound states at a particular momentum $\mathbf{p}$. To access these one needs to change from position to momentum space by Fourier transformation, leading to the associated 2-point function

$$C^{2}_{2,1}(y^0, x^0, \mathbf{p}) = \sum_{\mathbf{x},\,\mathbf{y}} e^{i\,\mathbf{p}\,(\mathbf{y}-\mathbf{x})}\,\big\langle \Phi_2(y)\,\Phi_1^{+}(x) \big\rangle \ . \tag{4.1}$$

This expression can be rewritten through the use of the Euclidean time evolution operator $\exp\left(-t\,H\right)$, where $t = x^0$ and H is the Hamiltonian. Inserting unity in the form of

$$\mathbf{1} = \sum_{n} \frac{1}{2\,E_n(\mathbf{p})}\ |\,E_n(\mathbf{p})\rangle\,\langle E_n(\mathbf{p})\,| \tag{4.2}$$

State	Γ	$J^{P(C)}$	$I=0$ particle	$I=1$ particles
Scalar	$\mathbf{1}\ ,\ \gamma_0$	0^{++}	σ	δ
Pseudoscalar	$\mathbf{1}\,\gamma_5\ ,\ \gamma_0\,\gamma_5$	0^{-+}	η	π
Vector	$\gamma_i\ ,\ \gamma_0\,\gamma_i$	1^{--}	ω	ρ
Axial vector	$\gamma_i\,\gamma_5$	1^{++}	f_1	a_1
Tensor	$\gamma_i\,\gamma_j$	1^{+-}	h_1	b_1

Table 4.1: Matrices for mesons used in fermionic bilinears (see [81]) and the associated lightest particle for two flavours. Here J denotes the quantum number of spin and I of iso-spin. The charge conjugation property is for the iso-singlet state only.

the 2-point function is obtained in the spectral representation

$$C^2_{2,1}(t,0,\mathbf{p}) = \sum_n \frac{1}{2\,E_n(\mathbf{p})}\, e^{-t\,E_n(\mathbf{p})}\, \langle 0|\,\Phi_2(\mathbf{p})\,|E_n(\mathbf{p})\rangle\, \big\langle E_n(\mathbf{p})|\,\Phi_1^+(\mathbf{p})\,|0\rangle \ , \tag{4.3}$$

where translation invariance was used to set $x^0 = 0$ and $y^0 = t$. Here $|E_n\rangle\,(\mathbf{p})$ is the eigenstate of the n-th eigenvalue $E_n(\mathbf{p})$ of the Hamiltonian H at momentum $\mathbf{p}$ and it is assumed that the states are ordered according to the size of the eigenvalues, i.e. $E_0(\mathbf{p})$ is the smallest eigenvalue. It is important to note that only states with a non-zero matrix element $\langle 0|\,\Phi_i(\mathbf{p})\,|E_n(\mathbf{p})\rangle$ contribute to the sum, i.e. states with similar quantum numbers as the operators $\Phi_i(\mathbf{p})$.

At large temporal extent the sum is dominated by the term corresponding to the smallest eigenvalue with non-zero overlap E_0 and can be rewritten as

$$C^2_{2,1}(t,0,\mathbf{p}) = \frac{Z_{\Phi_2}(\mathbf{p})\,Z^*_{\Phi_1}(\mathbf{p})}{2\,E_0(\mathbf{p})}\, e^{-t\,E_n(\mathbf{p})} \left(1 + \sum_{n=1}^{\infty} \alpha_{\Phi_2\Phi_1,n}(\mathbf{p})\, e^{-t\,\Delta E_n(\mathbf{p})}\right) \ . \tag{4.4}$$

Here the vacuum transition matrix elements

$$Z_{\Phi_i}(\mathbf{p}) = \langle 0|\,\Phi_i\,|E_0(\mathbf{p})\rangle \tag{4.5}$$

have been defined, the coefficients α are defined as

$$\alpha_{\Phi_2\Phi_1,n}(\mathbf{p}) = \frac{E_0(\mathbf{p})}{E_n(\mathbf{p})}\, \frac{\langle 0|\,\Phi_2\,|E_n(\mathbf{p})\rangle\, \big\langle E_n(\mathbf{p})|\,\Phi_1^+\,|0\rangle}{Z_{\Phi_2}(\mathbf{p})\,Z^*_{\Phi_1}(\mathbf{p})} \tag{4.6}$$

and $\Delta E_n(\mathbf{p}) = E_n(\mathbf{p}) - E_0(\mathbf{p})$ is the energy difference between the n-th excited state and the ground state. Using this form it is possible to extract the vacuum matrix elements and the groundstate energies by a fit to the 2-point function in the region where the contributions from excited states are sufficiently small. In practice, when extracted from the lattice with periodic or anti-periodic boundary conditions in the temporal direction, there are contributions from the backward and forward directions of the lattice. The spectral representation of the 2-point function in the asymptotic regime is then given by

$$C^2_{2,1}(t,0,\mathbf{p}) = \frac{Z_{\Phi_2}(\mathbf{p})\,Z^*_{\Phi_1}(\mathbf{p})}{2\,E_0(\mathbf{p})} \left(e^{-t\,E_0(\mathbf{p})} \pm e^{-(T-t)\,E_0(\mathbf{p})}\right) \ . \tag{4.7}$$

The sign of the second part in the brackets depends on the time reversal properties of the contributing states and $T = a\, N_t$ is the temporal extent of the lattice. Here T should not be confused with a temperature which is conventionally denoted by T as well. The convention is that T will represent the temporal extent in the zero temperature parts and the temperature in the finite temperature parts of the thesis.

Matrix elements with a mesonic state in initial and final state can be extracted using 3-point functions. For a 3-point function of the form $\left\langle \Phi_3(z)\, \Phi_2(y)\, \Phi_1^\dagger(x) \right\rangle$ the analogue to eq. (4.7) is given by

$$\begin{aligned} C^3_{3,2,1}(t_s, t, 0, \mathbf{p}_i, \mathbf{p}_f) \;&=\; \frac{Z_{\Phi_3}(\mathbf{p}_f)\, Z^*_{\Phi_1}(\mathbf{p}_i)}{4\, E_{f,0}(\mathbf{p}_f)\, E_{i,0}(\mathbf{p}_i)}\, \langle E_{f,0}(\mathbf{p}_f)|\, \Phi_2\, |E_{i,0}(\mathbf{p}_i)\rangle \\ &\times\; \Big[\vartheta(t_s - t)\, e^{-E_{i,0}(\mathbf{p}_i)\, t - E_{f,0}(\mathbf{p}_f)\, (t_s - t)} \\ &\quad \pm \vartheta(t_s - t)\, e^{-E_{i,0}(\mathbf{p}_i)\, (T-t) - E_{f,0}(\mathbf{p}_f)\, (t - t_s)}\Big] \;. \end{aligned} \tag{4.8}$$

Here $C^3_{3,2,1}(t_s, t, 0, \mathbf{p}_i, \mathbf{p}_f)$ is the Fourier transformed three-point function

$$C^3_{3,2,1}(t_s, t, 0, \mathbf{p}_i, \mathbf{p}_f) = \sum_{\mathbf{x},\, \mathbf{y},\, \mathbf{z}} e^{i\, \mathbf{p}_f\, (\mathbf{z}-\mathbf{y})}\, e^{i\, \mathbf{p}_i\, (\mathbf{y}-\mathbf{x})}\, \left\langle \Phi_3(z)\, \Phi_2(y)\, \Phi_1^\dagger(x) \right\rangle \;, \tag{4.9}$$

$E_{i,0}(\mathbf{p}_i)$ and $E_{f,0}(\mathbf{p}_f)$ are the lowest energies of the states with non-zero overlap to the operators Φ_1 and Φ_3 respectively, ϑ is the step function and again the sign depends on the quantum numbers of the operators. Translation invariance was used to set $x^0 = 0$ and conventionally $y^0 = t$ and $z^0 = t_s$. A formula for excited states similar to the one of eq. (4.4) for the 2-point function, can be obtained by the inclusion of higher terms of the sums in eq. (4.8) (cf. section 5.4.2). The matrix element $\langle E_{f,0}(\mathbf{p}_f)|\, \Phi_2\, |E_{i,0}(\mathbf{p}_i)\rangle$ is then obtained by using a suitable combination of 3- and 2-point functions.

The magnitude of the contamination from a particular excited state at finite source-sink separation in the n-point function is governed by two quantities, the energy gap ΔE between the excited state and the ground state and the overlap α. While the energy gap does only depend on the quantum numbers of the operator the overlap also depends on its projection properties onto the different states. This offers the possibility to improve the signal by constructing operators with an improved projection onto the ground state, e.g. by *smearing* [192, 193]. The combination of a measurement of a set of operators with different overlaps to different states with a variational method [194–196] allows to further improve the signal for the ground state and allows to extract excited states, too. Further reduction of excited state contributions can be achieved by the use of so called 'summed operator insertions' [197–200]. These methods are advantageous for hadrons heavier than pions or pions with large momenta that suffer from the growths of the noise-to-signal ratio. However, they come at larger numerical cost and for pions at small momenta, the case relevant for this thesis, it is often advantageous to use stochastic sources discussed in section 4.3.

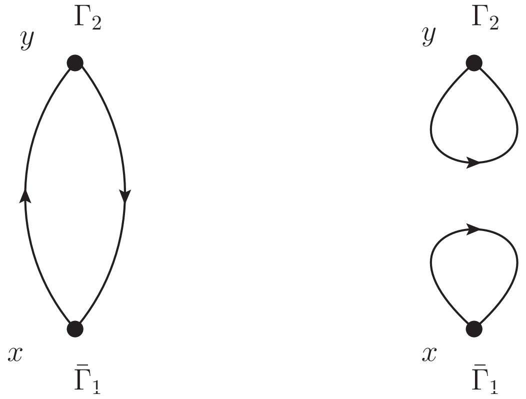

Figure 4.1: Diagrammatic representation of the connected (left) and disconnected (right) part of the 2-point function from eq. (4.11).

4.2 Evaluation of correlation functions

As noted in the beginning of this chapter, the fermionic fields stemming from the n-point functions have to be taken into account when the fermionic fields are integrated out. This section serves to discuss the details of this process and to provide the expressions for the n-point functions that can be calculated numerically.

4.2.1 Wick's theorem and quark disconnected diagrams

Following Wick's theorem, the expectation value of a n-point function is given in terms of the sum over all possible fermion contractions. Following the rules for Gaussian integrals over Grassmann-valued fields, each contraction yields a propagator in the integration, i.e.

$$\wick{\c\psi_f(x) \c{\bar\psi}_{f'}(y)} \;\rightarrow\; D_f^{-1}(x,y)\,\delta_{ff'}\;. \tag{4.10}$$

Here f is the flavour index and D_f denotes the Dirac operator for the specific flavour. The term in the sum is further multiplied by the combinatorial factor $(-1)^P$ where P is the number of commutations of fermionic fields.

For a 2-point function of the form $\left\langle \Phi_2(y)\,\Phi_1^+(x)\right\rangle$ with $\Phi_i(x) = \bar\psi_{f_i'}(x)\,\Gamma_i\,\psi_{f_i}(x)$ the possible contractions are given by

$$\begin{aligned}\left\langle \Phi_2(y)\,\Phi_1^+(x)\right\rangle \;=\;& -\left\langle \mathrm{Tr}\left(D_{f_1'}^{-1}(x,y)\,\delta_{f_1'f_2'}\,\Gamma_2\,D_{f_2}^{-1}(y,x)\,\delta_{f_2f_1}\,\overline{\Gamma}_1\right)\right\rangle \\ & + \left\langle \mathrm{Tr}\left(D_{f_2}^{-1}(y,y)\,\delta_{f_2f_2'}\,\Gamma_2\right)\,\mathrm{Tr}\left(D_{f_1'}^{-1}(x,x)\,\delta_{f_1'f_1}\,\overline{\Gamma}_1\right)\right\rangle\;.\end{aligned} \tag{4.11}$$

Here $\overline{\Gamma}_i$ is a shorthand notation for $\gamma_0\,\Gamma_i^+\,\gamma_0$. Note that for mesonic operators at $N_f = 2$ $\overline{\Gamma} = \pm\Gamma$, depending on the operator. In the language of Feynman diagrams each quark propagator is represented by a quark line. The diagrams corresponding to the two terms in eq. (4.11) are shown in figure 4.1. In the diagrammatic representation of the first

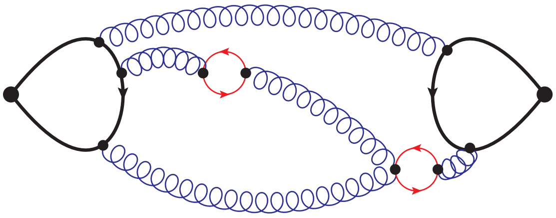

Figure 4.2: Sketch of the disconnected part of the 2-point function from eq. (4.11) with couplings to virtual gluons (blue) and sea-quarks (red).

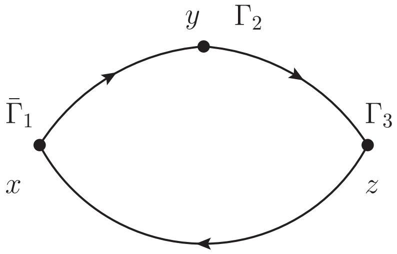

Figure 4.3: Diagrammatic representation of the connected part of the 3-point function.

term all quark lines are connected in contrast to those of the diagram associated with the second term. These two different types of diagrams are called quark-connected and quark-disconnected, respectively. Note that the second term only appears for iso-scalar operators, i.e. operators that project onto iso-spin zero states with $f_i = f'_i$. The quark disconnected diagram is disconnected only with respect to the quark lines associated with the operator whereas the two loops still interact via virtual gluons and quarks. These interactions are effectively generated within the configuration updates and enter through the gauge field configurations used in the ensemble average. Figure 4.2 shows a sketch of the disconnected part of the 2-point function including these virtual interactions.

For 3-point functions Wick's theorem leads to considerably more possible contractions, but only one of them is connected. It is shown in figure 4.3. In practice, most of the disconnected diagrams of the 3-point function will not be present since either some of the quarks are not degenerate or some of the traces will vanish.

The spectral representation from the last section applies to the sum of connected and disconnected parts. The computation of the connected part is discussed below and the disconnected part in principle can be calculated similarly. However, for the disconnected diagram the all-to-all propagator, i.e. the propagator from every point x to every other point y, has to be calculated. This is computationally demanding, even with the methods discussed in the next section, since the corresponding estimate for the all-to-all propagator is usually very noisy. The fermionic observables discussed in this thesis do not include disconnected diagrams and the discussion of the treatment of those is dropped for convenience.

Equations (4.11) for 2-point functions and its equivalent for 3-point functions in principle allow for their computation using point sources and the inversion algorithms from section 3.4. Nevertheless, this would mean that a large number of inversions have to be done. The first step to reduce the number of necessary inversions is to use γ_5-hermiticity,

$$D_f^{-1}(x,y) = \gamma_5 \left(D_f^{-1}(y,x) \right)^+ \gamma_5 \, . \tag{4.12}$$

When inserted in the connected part of the 2-point function from eq. (4.11) this yields

$$\left\langle \Phi_2(y)\, \Phi_1^+(x) \right\rangle_C = \left\langle \mathrm{Tr} \left(\gamma_5 \left(D_{f_1'}^{-1}(y,x) \right)^+ \gamma_5\, \delta_{f_1' f_2'}\, \Gamma_2\, D_{f_2}^{-1}(y,x)\, \delta_{f_2 f_1}\, \overline{\Gamma}_1 \right) \right\rangle \, . \tag{4.13}$$

In this form one has to compute the propagator from x to y only. A similar usage of eq. (4.12) in the connected part of the 3-point function reduces the number of required inversions to two instead of three.

The second step is to use translation invariance in both the temporal and spatial direction. Since one is mainly interested in the exponential decay of the signal in temporal direction it is sufficient to choose a particular time slice, typically the one with $x^0 = 0$, as permitted by translation invariance in the gluonic field [1]. Translation invariance in the spatial directions also allows to single out a specific position, e.g. $\mathbf{x} = 0$. This procedure reduces the necessary inversions to 12 per propagator for point sources. A suitable scheme at moderate numerical cost for the evaluation of 3-point functions is given in terms of extended propagators. It will be discussed in the context of variance reduction in the next section.

4.2.2 Quenching – sea and valence quarks

The quark propagators obtained from a simulation have no distinct flavour index. On this level different propagators are only distinguished by their mass (and later also the twist, see section 4.4). For the measurements the mass is a free parameter and can be chosen at will. Consequently, there are two types of quarks in the computation of fermionic observables. The sea quarks, quarks that are included in the generation of the gauge ensemble via the quark determinant, and the valence quarks, quarks connected to the measurements of the fermionic observables. The difference between the two is that sea quarks are integrated over in the path integral and appear as virtual fermion loops (the red loops in figure 4.2) while the valence quarks are associated with the quarks in the operator (the thick black lines in figure 4.2) and do not appear in the loops. The sea quarks of the simulation are always associated with the lightest quarks because these contribute most to the virtual fermion loops. All other quarks, realised by a different valence quark mass compared to the mass of the sea quarks, are said to appear ‘quenched’. A simulation with two degenerate dynamical quarks is denoted by $N_f = 2$. The extreme case is a completely quenched calculation of fermionic observables where the configurations are obtained using pure $SU(3)$ gauge theory. This corresponds to $\det(D) = 1$ in eq. (3.2) and the neglection of all effects of dynamical quarks. The situation of quenched valence quarks is of course unphysical, since in nature all

---

[1] Note that the antiperiodic boundary conditions of the Dirac operator have to be translated accordingly.

quarks contribute as virtual fermions, and leads to unknown systematic uncertainties in the simulations. However, the importance of the systematic effect due to quenching depends on the observable of choice. For example it is not likely that the effect of a quenched strange quark is of much importance for the mass and form factors of the pion while it can be expected to be of more important for measurements of the properties of Kaons.

4.3 Variance reduction

A possibility to compute propagators is to use a point source. However, for pseudoscalar correlation functions and disconnected diagrams there is a more efficient method using sources with stochastic entries. The purpose of this section is to review the method and its application to 2- and 3-point functions. While the method can be applied to a variety of observables its efficiency depends on the quantity of interest.

4.3.1 Stochastic sources

The basic idea behind the introduction of stochastic sources is, that the unit matrix entering fermionic observables via point sources can be rewritten using random spinors $\eta(x)$ with elements randomly drawn from a group $\mathcal{G}$ [201, 202]

$$\eta_\alpha(x) = z \quad \in \mathcal{G} \; , \tag{4.14}$$

that fulfil

$$\left\langle \eta(x) \; (\eta)^+ \, (y) \right\rangle_{\mathcal{G}} \equiv \frac{1}{Z_{\mathcal{G}}} \int \mathcal{D}\mathcal{G} \, \eta(x) \, \eta^+(y) = \mathbf{1} \; . \tag{4.15}$$

The expectation value of an observable O can then be written as

$$\langle O \rangle = \left\langle \left\langle \eta(x) \, \eta^+(y) \, O \right\rangle_{\mathcal{G}} \right\rangle \; . \tag{4.16}$$

This can be advantageous since the resulting estimates for the observable contain estimates for the quantities stemming from every lattice point supported by the source. For practical purposes it is important to note, that in general the two expectation values are independent and commute, if the additional noise from the finite set of random vectors used is not larger than the gauge noise. Suitable groups are $Z_2 \times Z_2$ and $U(1)$, where the former is generaly preferable [201, 202].

A popular example for the use of stochastic sources is the calculation of the trace of the propagator. It can be obtained by using the solution of the equation

$$D(x, y) \, \varphi(y) = \eta(x) \; , \tag{4.17}$$

via

$$\begin{aligned} \left\langle \sum_y \eta^+(y) \, \varphi(y) \right\rangle_{\mathcal{G}} &= \left\langle \mathrm{Tr} \left(\sum_x D^{-1}(y, x) \, \eta(x) \; (\eta)^+ \, (y) \right) \right\rangle_{\mathcal{G}} \\ &= \mathrm{Tr} \left(D^{-1} \right) \; . \end{aligned} \tag{4.18}$$

Here the trace is taken with respect to space, Dirac and colour indices. The advantage is that the operator inside the trace is an estimate for the all-to-all propagator and thus includes information on the diagonal piece of the Dirac operator from all lattice points and for all Dirac and colour indices. In contrast, an estimate obtained from a point source on a single lattice point obtained from 12 inversions would only contain contributions from that particular lattice point. It is thus natural to assume that the estimate (4.18) leads to a reduction of the noise. Apart from this intuitive argument the error reduction becomes apparent when looking at the variance (see [202]), where the inclusion of the stochastic source forbids certain contractions.

4.3.2 2-point functions and dilution

The method introduced above for the trace of the propagator can be extended to evaluate 2- and 3-point functions. In this case one is not interested in a trace over the temporal indices but in the temporal behaviour of the correlation function. Furthermore, one is usually interested in the correlation function projected to a particular momentum. While the method can be applied to every Fourier momentum it is most easily adopted for zero Fourier momentum. Since for this thesis this is the important case, the following discussion is restricted to this particular choice. The generalisation to other momenta is straight forward.

To gain information about the temporal behaviour of the correlation function it is necessary to have a random vector with support at a particular time slice, e.g. a source which is only non-zero at timeslice $x_0 = 0$ [203, 204]. If this was not the case the result from the inversion at a particular time-slice y_0 would contain contributions from every time-slice of the lattice, spoiling the exponential fall-off of the correlation function. The method is known as time dilution and the associated sources are denoted as ‘wall’ sources. Starting from the connected part of a 2-point function projected to zero momentum it is possible to insert a unit matrix as in eq. (4.15),

$$\begin{aligned}\left[C^2_{2,1}(y^0,x^0)\right]_C \;&=\; \sum_{\mathbf{x},\mathbf{y}} \Big\langle \mathrm{Tr}\Big(\gamma_5\,\left(D^{-1}(y,x)\right)^+\,\gamma_5\,\Gamma_2\,D^{-1}(y,x) \\ &\qquad\qquad \eta(\mathbf{x},x^0)\,\eta^+(\mathbf{x},x^0)\,\overline{\Gamma}_1\Big)\Big\rangle\ , \end{aligned} \tag{4.19}$$

where the expectation value also includes the average over stochastic sources and the momentum argument has been suppressed.

In principle, it is possible to calculate the 2-point function with the spinors $\varphi_1(y) = D^{-1}(y,x)\,\left(\overline{\Gamma}_1\,\gamma_5\right)^+\,\eta(\mathbf{x},x^0)$ and φ, defined by eq. (4.17). Inserting these two spinors leads to

$$\left[C^2_{2,1}(y^0,x^0)\right]_C = \sum_{\mathbf{x},\mathbf{y}} \left\langle (\varphi_1(y))^+\,\gamma_5\,\Gamma_2\,\varphi(y)\right\rangle\ . \tag{4.20}$$

This method is not convenient when more than a single combination of Γ-matrices should be evaluated in the same run since a new inversion for each Γ_1 is required. In this case one would like to have a source that obeys

$$\eta^+(\mathbf{x},x^0)\,\overline{\Gamma}_1\,\gamma_5 = \overline{\Gamma}_1\,\gamma_5\,\eta^+(\mathbf{x},x^0) \tag{4.21}$$

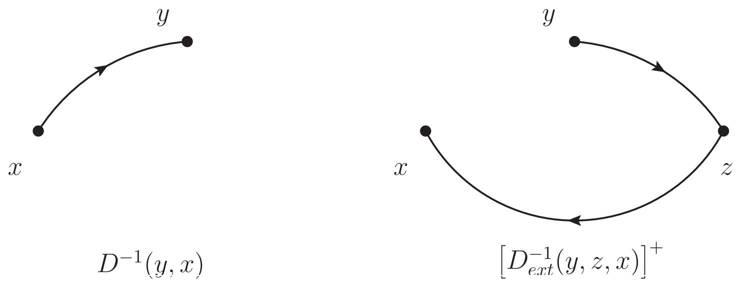

Figure 4.4: Diagrammatic representation of the two parts that can be used to construct the 3-point function.

which allows to bring $\eta^{+}(\mathbf{x},0)$ next to the conjugated propagator in eq. (4.19). Then it is possible to use the solution from eq. (4.17) for both propagators. Equation (4.21) can only be satisfied by η for all matrices Γ_1 if it is matrix valued in Dirac and colour space, at least for the subspace of indices in which the matrix $\overline{\Gamma}_1\,\gamma_5$ is non-diagonal, denoted as the 'relevant subspace' (RS). In this case $\varphi(y)$, the solution of eq. (4.17), is matrix valued as well. It can be calculated by solving a single equation of the type of eq. (4.17) for each of the rows of η. The simplest choice for η that fulfills eq. (4.21) is to chose it to be proportional to the unit matrix in the RS. Denoting the RS-indices by a and b this means

$$\eta_{ab}(\mathbf{x},x^0) = \xi(\mathbf{x},x^0)\,\delta_{ab} \quad \text{with} \quad \xi_\alpha(\mathbf{x},x^0) = z \quad \in \mathcal{G}\,. \tag{4.22}$$

Here α is the index in the residual space in which $\overline{\Gamma}_1\,\gamma_5$ is diagonal. This procedure is known as 'spin dilution' [203–206]. Writing out the Dirac and colour indices in the relevant subspace explicitly, the 2-point function is given by

$$\left[C^2_{2,1}(y^0,x^0)\right]_C = \sum_{\mathbf{x},\mathbf{y}} \left\langle (\varphi(y))^{+}_{ab}\;(\gamma_5\,\Gamma_2)_{bc}\;(\varphi(y))_{cd}\;\left(\overline{\Gamma}_1\,\gamma_5\right)_{da}\right\rangle\,. \tag{4.23}$$

In this way the whole set of 2-point functions of interest can be computed with dim(RS) inversions. If all matrices are diagonal in colour space but non-diagonal in all parts of Dirac space the dimension of the relevant subspace is 4, i.e. 4 inversions are needed to calculate all possible 2-point functions.

In principle a detailed error analysis is necessary to compare the gain of the use of stochastic sources against the cost, for an example see [206]. In some cases the method might be worse than a point source, in particular, if the stochastic noise adds to the gauge noise. However, this is not likely to be the case for the lower lying states, such as for the pseudoscalar, scalar, vector and tensor correlation functions, as shown in [206]. A test of the method for some particular quantities on a subset of the ensembles used in this thesis can be found in [207, 208].

4.3.3 Stochastic evaluation of 3-point functions

The method introduced above is also applicable to the connected part of 3-point functions projected to zero Fourier momentum. The bottomline is the extended propagator method

[209] where the connected part of the 3-point function is rewritten as

$$\left[C^3_{3,2,1}(t_s,t,0)\right]_C = \sum_{\mathbf{x},\mathbf{y},\mathbf{z}} \left\langle \mathrm{Tr}\left(\left\{ D^{-1}(y,z)\,\overline{\Gamma}_3\, D^{-1}(z,x) \right\}^+ \gamma_5\, \Gamma_2\, D^{-1}(y,x)\, \overline{\Gamma}_1\, \gamma_5 \right) \right\rangle \,. \tag{4.24}$$

The first part in the curly brackets is the extended propagator

$$D^{-1}_{\mathrm{ext}}(y,z^0,x) = \sum_{\mathbf{z}} D^{-1}(y,z)\,\overline{\Gamma}_3\, D^{-1}(z,x)\,. \tag{4.25}$$

The 3-point function now consists of two parts shown in figure 4.4. Inserting a unit matrix as in eq. (4.19) with a suitable matrix valued random source and using the commutation relation (4.21) yields

$$\left[C^3_{3,2,1}(t_s,t,0)\right]_C = \sum_{\mathbf{x},\mathbf{y}} \left\langle \mathrm{Tr}\left(\left\{ D^{-1}_{\mathrm{ext}}(y,z^0,x)\,\eta(\mathbf{x},x^0) \right\}^+ \gamma_5\, \Gamma_2\, D^{-1}(y,x)\,\eta(\mathbf{x},x^0)\, \overline{\Gamma}_1\, \gamma_5 \right) \right\rangle \,. \tag{4.26}$$

The 3-point function can be obtained using 2 × dim(RS) inversions by calculating the matrices

$$\varphi(y) = D^{-1}(y,x)\,\eta(\mathbf{x},x^0) \quad \text{and} \quad \varphi_{\mathrm{ext}}(y) = D^{-1}(y,z)\,\overline{\Gamma}_3\,\varphi(z)\,. \tag{4.27}$$

Then the 3-point function is given by

$$\left[C^3_{3,2,1}(t_s,t,0)\right]_C = \sum_{\mathbf{x},\mathbf{y}} \left\langle \{\varphi_{\mathrm{ext}}(y)\}^+_{ab}\, (\gamma_5\,\Gamma_2)_{bc}\, \varphi(y)_{cd}\, \left(\overline{\Gamma}_1\,\gamma_5\right)_{da} \right\rangle \,. \tag{4.28}$$

Note that the use of this scheme demands new inversions for each sink position $z^0 = t_s$ and for each matrix Γ_3.

As for the 2-point function it depends on the particular case as to whether the use of stochastic sources is advantageous or not. Nevertheless, for the 3-point function the analytical analysis of the variance is much more involved and usually does not allow for an unambiguous conclusion. It is thus necessary to perform a numerical check of the efficiency of the method. For 3-point functions with external pseudoscalar fields, the case relevant for this thesis, an analysis has been performed in [206], where it was shown that the method leads to a significant reduction of the noise.

4.4 Twisted boundary conditions

If one is interested in the extraction of form factors and other momentum dependent quantities, one of the most crucial restrictions is the quantisation of the Fourier momenta due to finite volume as discussed in section 2.1. A possible solution is to use twisted boundary conditions [48–50]. The general idea is to introduce a static $U(1)$ background field $\mathbf{B}$ that couples to the quarks via the covariant derivative. The modified covariant derivative $\tilde{D}_\mu$ is then given by

$$\tilde{D}_\mu = D_\mu + i\,B_\mu \quad (\text{with } B_0 = 0)\,. \tag{4.29}$$

It leads to a propagator with a pole shifted to $m+\not{B}$ for zero Fourier momentum [50], corresponding to a particle with momentum $\mathbf{B}$.

The modified covariant derivative in eq. (4.29) is equivalent to the usual covariant derivative for quark fields $\tilde{\psi}(x)$ that are defined as

$$\tilde{\psi}(x) = e^{-i\,\mathbf{B}\,\mathbf{x}}\,\psi(x)\ . \tag{4.30}$$

These can be shown to be equivalent to usual quark fields $\psi(x)$ that satisfy the boundary conditions [50]

$$\psi\left(x + L\,\hat{i}\right) = e^{i\,B_i}\,\psi(x)\ , \tag{4.31}$$

instead of periodic boundary conditions in the spatial directions. These boundary conditions (4.31) are usually referred to as ‘twisted’ boundary conditions. The $U(1)$ field $\mathbf{B}$ is conventionally reformulated in terms of a vector of angles Θ via

$$\mathbf{B} = \frac{\Theta}{N_s}\ . \tag{4.32}$$

The entries θ_i of Θ are denoted as ‘twist angles’.

Sea quarks with shifted momentum demand a new simulation for each momentum. This is obviously not feasible for more than one momentum. Anyhow, in practice one is mostly interested in different momenta for the valence quarks only, corresponding to shifted on-shell momenta. Then it is sufficient to modify the boundary conditions for the Dirac operator in the measurements whilst keeping them periodic during the generation of the configurations. This use of twisted boundary conditions is referred to as ‘partially’ twisted boundary conditions [50]. It allows the computation of various different momenta for particles on the same set of configurations with one additional inversion per momentum.

For twisted boundary conditions written in the form eq. (4.30) the twist of the quark fields cancel in each term of the fermion action except for the spatial hopping terms as the factor $\mathbf{x}$ is different for the two appearing quark fields. This term becomes [210]

$$\left[\bar{\tilde{\psi}}(x-\hat{i})\,e^{i\frac{a\,\theta_i}{L}}\,U_i(x)\,(1-\gamma_i) + \bar{\tilde{\psi}}(x+\hat{i})\,e^{-i\frac{a\,\theta_i}{L}}\,U_i^{+}(x)\,(1+\gamma_i)\right]\,\tilde{\psi}(x)\ . \tag{4.33}$$

In practice, this means that the propagator of a twisted quark can be obtained by performing the inversion using the stored gauge field with the replacement

$$U_i(x) \quad \to \quad e^{i\frac{a\,\theta_i}{L}}\,U_i(x)\ . \tag{4.34}$$

The use of partially twisted boundary conditions potentially leads to additional finite volume effects due to the different boundary conditions for sea- and valence quarks. The form of the finite volume effects can be calculated in the framework of partially quenched χPT and it was shown in [50] that the resulting finite volume corrections remain exponentially small for quantities with at most one meson in the initial and final states. The situation is different for baryonic quantities where large finite volume effects cannot be excluded. An extensive study of twisted boundary conditions for mesonic 2-point functions in pseudoscalar, vector and axial vector channels has been presented in [210]. It has been shown that partially twisted boundary conditions do not introduce notable systematic effects and allow to extract correlation functions at any (not to large) momentum.

Partially twisted boundary conditions have by now become a standard tool to investigate physical quantities at arbitrary momentum in LQCD. In particular, they are fundamental for the extraction of the pion form factor in the regime of low momentum transfer in this thesis and will be used extensively in the following chapters. Just to name two other important applications: They enable fundamental improvements for the extraction of hadronic form factors [51, 211] and allow to stabilise the inter and extrapolation of the hadronic vacuum polarisation, necessary to calculate the hadronic contribution to the anomalous magnetic moment of the muon [212].

PART III: Zero Temperature

5 The electromagnetic form factor of the pion from lattice QCD

Among the most important tasks for lattice QCD is the calculation of properties of quark bound states in the hadronic phase. The relevant energy scale is in the region where the renormalised coupling is large and thus cannot be explored using perturbation theory. Measurements in LQCD are then the preferred tool to extract these quantities. Crucial for a reliable determination of a physical quantity in LQCD is the control of systematic effects. In particular, since most of the simulations are still done at unphysically large quark masses, this includes a chiral extrapolation. One possibility to address systematic effects is to use effective field theories such as χPT which can be extended to include finite volume and lattice spacing, as well as iso-spin breaking effects. In the cases where agreement between LQCD and experiment to date is less satisfactory this is often related to the absence of an adequate effective field theory description or doubts about its applicability for the mass range of interest. This part of the thesis deals with the electromagnetic pion form factor which might serve as a test case for systematic effects entering the form factors of baryons that are more difficult to extract. Note, that in the following discussions about systematic effects iso-spin breaking effects and effects from quenching are excluded, since their examination is beyond the scope of this thesis. Parts of the analysis were already presented in [213–216].

5.1 Form factors of mesons and baryons – Lattice vs experiment

One class of quantities where the agreement between LQCD and experiment is less satisfactory are the form factors of the constituents of nuclear matter, protons and neutrons (see [30] and [217] for recent reviews). These quantities are important since they serve as a benchmark for QCD as the fundamental theory to describe the constituents of nuclear matter. They encode information about basic properties such as the shape of the nucleons with respect to the fundamental charges of the SM that are known from experiment. The extraction of these form factors from LQCD suffers from severe problems like exponential decay of the signal-to-noise ratio in correlation functions and unknown systematic effects, such as finite volume effects and excited state contributions. For a recent study of those in the context of nucleon form factors see [200, 218]. Those aside, one of the main problems for baryons is the absence of an established effective field theory framework to perform chiral and continuum extrapolations.

Mesonic form factors, in particular those of the pion, are computationally simpler than their baryonic counterparts. The form factors of the pseudoscalar iso-vector mesons (e.g. charged pions and kaons) can be obtained with high accuracy due to the possibility to make efficient use of stochastic wall sources, as discussed in section 4.3. In addition, no quark-disconnected diagrams contribute to the 3-point functions in the iso-spin limit. This enables high-precision calculations in LQCD, providing the perfect test case for a study of systematic effects in the computation of form factors.

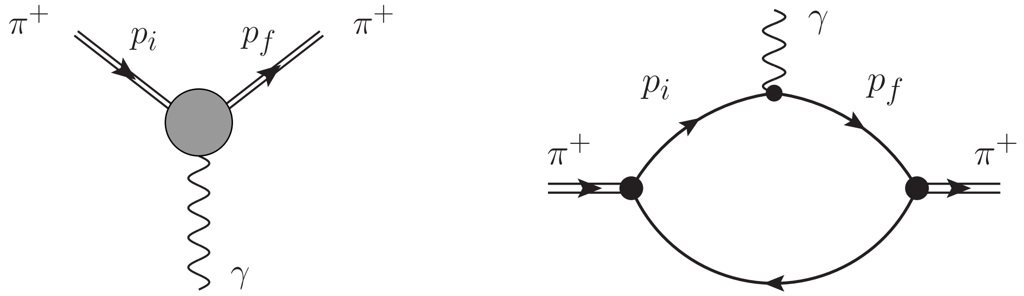

Figure 5.1: Diagram defining the pion electromagnetic iso-vector form factor $f_{\pi\pi}(Q^2)$ at the hadronic level (left) and at the quark level (right).

Form factors are defined in terms of transition matrix elements of the particles with the current associated to the force of interest at a particular momentum transfer

$$q^2 \equiv (p_f - p_i)^2 \equiv -Q^2 \; . \tag{5.1}$$

The corresponding diagram for such a process is shown in figure 5.1 at the hadronic level (left) and at the quark level (right) for the example of the interaction between pions and photons. The associated electromagnetic pion form factor $f_{\pi\pi}(Q^2)$ for $N_f = 2$ is defined by the matrix element

$$\langle \pi^+(\mathbf{p}_f) | \tfrac{2}{3} \bar{u} \gamma_\mu u - \tfrac{1}{3} \bar{d} \gamma_\mu d | \pi^+(\mathbf{p}_i) \rangle = (p_f + p_i)_\mu \, f_{\pi\pi}(Q^2) \; . \tag{5.2}$$

It is known in χPT to next-to-next-to leading order [42–44] (NNLO) and thus allows for a direct test of the applicability of χPT to lattice data. $f_{\pi\pi}(Q^2)$ is known with high precision in the region of small space-like momentum transfer from pion-electron scattering from the NA7 collaboration [45] and in the region of larger Q^2 from high-energy electro production of pions on a nucleon by the JLAB-F_π collaboration [219] (see figure 5.2, left). After some initial quenched studies [220–224] the form factor has been computed in lattice simulations with dynamical fermions in the intermediate Q^2-regime [51, 52, 225–229] and found to be in reasonable agreement with experiment (figure 5.2, right). Here it is important to note that due to the Euclidean signature of spacetime the form factor can only be extracted for space-like momenta, i.e. $Q^2 \geq 0$ [1].

Apart from the intermediate regime there are the regimes of very small and very large Q^2 that are difficult to access both for experiment and LQCD. For the latter one this is due to the inherent quantisation of the momenta at non-zero lattice spacing and finite volume. For the region of large Q^2 where the momentum transfer becomes comparable to the inverse of the lattice spacing a, large cut-off effects are expected. In the region of small Q^2 the lowest non-zero momentum transfer accessible via Fourier momenta is given by $(2\pi)/(N_s a)$, which is typically of order 550 MeV (for a common lattice with $N_s = 32$ and $a = 0.07$ fm) in actual simulations. In the large Q^2 regime it is expected that perturbation theory starts

---

[1] A recent proposal in principle enables the calculation of the electromagnetic form factor of the pion also at time-like momentum transfers, at least in the region $2\, m_\pi \leq q^2 \leq 4\, m_\pi$ [230].

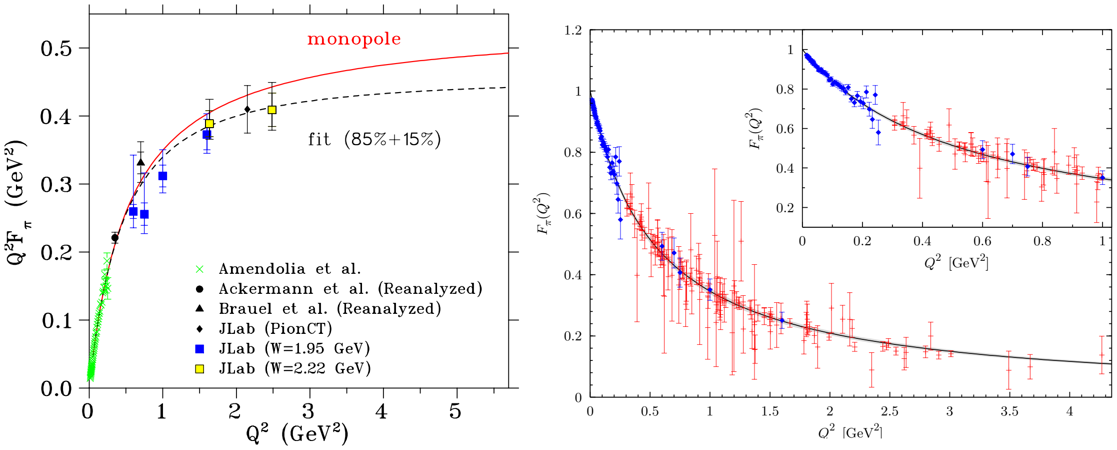

Figure 5.2: Left: Experimental results for the electromagnetic iso-vector pion form factor as presented in [219] in comparison to a monopole ansatz, eq. (5.4). **Right:** Lattice results for $f_{\pi\pi}(Q^2)$ in the intermediate regime, taken from [225].

to become applicable due to the smaller coupling for these relatively large energies and the Q^2 behaviour for $Q^2 \to \infty$ has been worked out [231–236]. To bridge the gap between low and large Q^2 domains a number of effective theories were used (cf. [237–243]).

In this thesis the focus is on the region of small momentum transfers where the Q^2 behaviour of the form factor defines the charge radius $\langle r_\pi^2 \rangle$ and the curvature C_V by

$$f_{\pi\pi}(Q^2) = 1 - \frac{\langle r_\pi^2 \rangle}{6}\, Q^2 - C_V\, Q^2 + \ldots \quad \Rightarrow \quad \langle r_\pi^2 \rangle = 6\, \frac{d\, f_{\pi\pi}(Q^2)}{dQ^2}\bigg|_{Q^2=0} . \tag{5.3}$$

The normalisation $f_{\pi\pi}(0) = 1$ is fixed by the electrical charge of the pion. This regime is only accessible through the use of partially twisted boundary conditions [51, 52], that have been discussed in section 4.4. Other studies have already made use of this technique to determine the form factor below the smallest available Fourier momenta [51, 52, 228, 229]. The potential of the use of partially twisted boundary conditions is demonstrated in figure 5.3 where a compilation of LQCD results is shown in comparison to experimental results in the region typically inaccessible to Fourier momenta. Also visible is the gap to $Q^2 = 0$ for data from both, experiment and lattice. This gap prohibits the direct extraction of $\langle r_\pi^2 \rangle$ and leads to an inherent model dependence in its determination. A commonly used ansatz is the model of vector pole dominance [46, 47] with a Q^2-dependence of the form

$$f_{\pi\pi}(Q^2)\big|_{\mathrm{VPD}} = \left(1 - \frac{\langle r_\pi^2 \rangle_{\mathrm{VPD}}}{6}\, Q^2\right)^{-1} . \tag{5.4}$$

In this model the term $\langle r_\pi^2 \rangle_{\mathrm{VPD}}/6$ corresponds to a pole mass which can be related to the mass of the ρ-meson. Even though the model tends to describe the data well, there is no strict justification for its use. In practice, the state-of-the art results for $\langle r_\pi^2 \rangle$ from experimental data either rely on this functional form or on χPT. The same is true for the

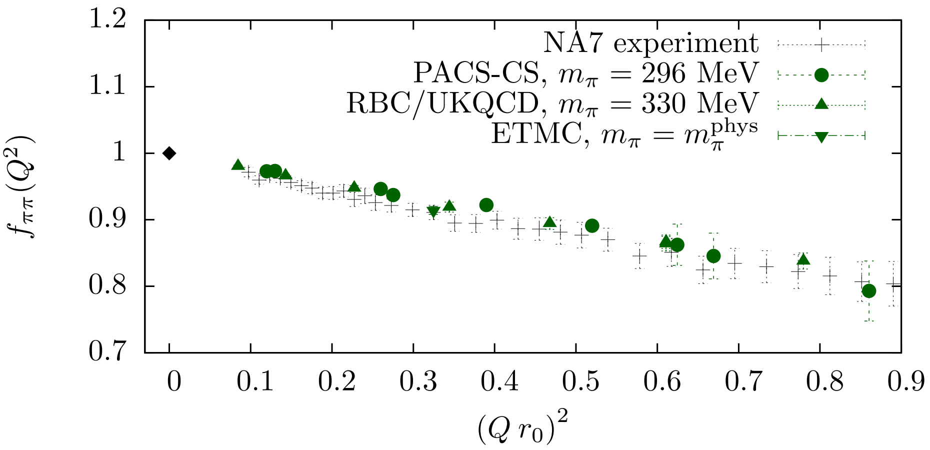

Figure 5.3: Comparison between lattice data from [52,228,229] and experimental results [45] in the region of small Q^2. The momentum transfer depicted on the x-axis is plotted in units of the Sommer parameter r_0 and $r_0 = 0.503\,(10)$ fm, as obtained in [77], is used to convert to physical units.

results from LQCD. For a completely model independent computation of $\langle r_\pi^2 \rangle$ it is necessary to go to much smaller values of Q^2 where the charge radius can be defined in terms of a discretised derivative with respect to Q^2. Such an extraction of $\langle r_\pi^2 \rangle$ can potentially remove the systematic uncertainty. One is then left with controlling the systematics connected to the chiral extrapolation.

5.2 Computational strategy

This section contains the definition of the observables in terms of 2- and 3-point functions. Even though the main goal is the determination of $f_{\pi\pi}(Q^2)$ and $\langle r_\pi^2 \rangle$, it turns out that for the chiral extrapolations in the χPT framework it is crucial to include data for the pion decay constant F_π and the light quark mass m_{ud}.

5.2.1 Matrix elements and correlation functions

For extracting the form factor it is necessary to obtain pion masses and transition matrix elements of a vector current sandwiched between two charged pion states with different momenta. The operator with the correct quantum numbers to create or annihilate a pion is the pseudoscalar density, see table 9.1. To calculate the pion decay constant, defined by the matrix element from eq. (1.19), the matrix element between the vacuum and the pion with the axial vector current are needed as well. These quantities can be extracted from the 2-point functions

$$\begin{aligned} C^2_{PP}(t,\mathbf{p}) &= \sum_{\mathbf{x}} e^{i\mathbf{p}\cdot(\mathbf{x}-\mathbf{x}_i)} \langle\, P(t,\mathbf{x})\, P^+(0,\mathbf{x}_i)\,\rangle\,, \\ C^2_{PA}(t,\mathbf{p}) &= \sum_{\mathbf{x}} e^{i\mathbf{p}\cdot(\mathbf{x}-\mathbf{x}_i)} \langle\, P(t,\mathbf{x})\, (J_{A,I})^+_0(0,\mathbf{x}_i)\,\rangle\,, \end{aligned} \tag{5.5}$$

where $(J_{A,I})_0$ is the zero component of the $\mathcal{O}(a)$-improved axial current from eq. (2.36), and the 3-point function

$$\begin{aligned} C^3_V(t_f,t,\mathbf{p}_i,\mathbf{p}_f) &= \sum_{\mathbf{x}_f,\mathbf{x}} e^{i\mathbf{p}_f\cdot(\mathbf{x}_f-\mathbf{x})} e^{i\mathbf{p}_i\cdot(\mathbf{x}-\mathbf{x}_i)}\, C^3_{P,V,P}(t_f,t,\mathbf{x},\mathbf{x}_f,\mathbf{x}_i) \\ &= \sum_{\mathbf{x}_f,\mathbf{x}} e^{i\mathbf{p}_f\cdot(\mathbf{x}_f-\mathbf{x})} e^{i\mathbf{p}_i\cdot(\mathbf{x}-\mathbf{x}_i)}\, \langle\, P(t_f,\mathbf{x}_f)\, (J_{V,I})_0(t,\mathbf{x})\, P^+(0,\mathbf{x}_i)\,\rangle\,, \end{aligned} \tag{5.6}$$

where $(J_{V,I})_0$ is the zero component of the $\mathcal{O}(a)$-improved vector current. For $(J_{A,I})_0$ the non-perturbative improvement constant from [244] is used as listed in eq. (A.15) in the appendix. The numerical values for $\mathcal{O}(a)$-improvement and renormalisation constants for the ensembles of this study are listed in table 5.1. $\mathcal{O}(a)$-improvement and renormalisation for the vector current is discussed later.

The physical quantities are extracted using the spectral representation discussed in section 4.1. Taking into account only the ground state contributions one obtains

$$\begin{aligned} C^2_{PP}(t,\mathbf{p}) &= \frac{|Z_P|^2}{2\,E(\mathbf{p})}\left(e^{-E(\mathbf{p})\,t} + e^{-E(\mathbf{p})\,(N_t-t)}\right)\,, \\ C^2_{AP}(t,\mathbf{p}) &= \frac{Z_P\,Z_A^*}{2\,E(\mathbf{p})}\left(e^{-E(\mathbf{p})\,t} - e^{-E(\mathbf{p})\,(N_t-t)}\right)\,, \end{aligned} \tag{5.7}$$

and

$$\begin{aligned} C^3_V(t,t_f,\mathbf{p}_i,\mathbf{p}_f) &= \frac{|Z_P|^2}{4\,E(\mathbf{p}_i)\,E(\mathbf{p}_f)}\,\langle\pi(\mathbf{p}_f)|J_{V,0}(0)|\pi(\vec{p}_i)\rangle \\ &\quad\times\Big[\vartheta(t_s-t)\,e^{-E(\mathbf{p}_i)\,t-E(\mathbf{p}_f)\,(t_s-t)} \\ &\qquad -\vartheta(t-t_s)\,e^{-E(\mathbf{p}_i)\,(N_t-t)-E(\mathbf{p}_f)\,(t-t_s)}\Big]\,. \end{aligned} \tag{5.8}$$

Here the pion source is always located at the time slice with $x^0 = 0$ for convenience, t is the temporal position of the insertion of the vector current and t_s the position of the sink. In the following $t_s = N_t/2$ and the corresponding function argument will be dropped. Z_P and Z_A are the ground state matrix elements as defined in eq. (4.5) and the pion decay constant is defined by (cf. eq. (1.19))

$$Z_A = \big\langle \pi(\mathbf{p})\,\big|(J_{A,0})^+(0)\big|\,0\big\rangle = \sqrt{2}\,E(\mathbf{p})\,F_\pi\,. \tag{5.9}$$

β	$\mathcal{Z}_A$ [77,246]	$\mathcal{Z}_P$ [77,114]	c_A [244]	$b_A - b_P$ [110]
5.2	0.771 (6)	0.518 (5)	-0.0641	-0.1079
5.3	0.778 (9)	0.518 (5)	-0.0506	-0.0992
5.5	0.793 (5)	0.518 (5)	-0.0361	-0.0848

Table 5.1: Renormalisation and improvement constants from the lattice used in the analysis. The quantities c_A and $b_A - b_P$ are referenced without error bars, because their value can be seen as a specific choice for the coefficients (and thus to an $\mathcal{O}(a)$-improvement scheme) as in the case of c_{SW}.

5.2.2 Form factor, decay constant and light quark mass

The form factor can be extracted from the correlation functions using the ratios [51]:

$$R_1(t,\mathbf{p}_i,\mathbf{p}_f) = \mathcal{Z}_V^{\text{eff}}\, 4\sqrt{E(\mathbf{p}_i)\, E(\mathbf{p}_f)}\sqrt{\frac{C_V^3(t,\mathbf{p}_i,\mathbf{p}_f)\, C_V^3(t,\mathbf{p}_f,\mathbf{p}_i)}{C_{PP}^2(T/2,\mathbf{p}_i)\, C_{PP}^2(T/2,\mathbf{p}_f)}} \tag{5.10}$$

$$R_2(t,\mathbf{p}_i,\mathbf{p}_f) = 2\sqrt{E(\mathbf{p}_i)\, E(\mathbf{p}_f)}\sqrt{\frac{C_V^3(t,\mathbf{p}_i,\mathbf{p}_f)\, C_V^3(t,\mathbf{p}_f,\mathbf{p}_i)}{C_V^3(t,\mathbf{p}_i,\mathbf{p}_i)\, C_V^3(t,\mathbf{p}_f,\mathbf{p}_f)}} \tag{5.11}$$

$$R_3(t,\mathbf{p}_i,\mathbf{p}_f) = \mathcal{Z}_V^{\text{eff}}\, 4\sqrt{E(\mathbf{p}_i)\, E(\mathbf{p}_f)}\,\frac{C_V^3(t,\mathbf{p}_i,\mathbf{p}_f)}{C_{PP}^2(T/2,\mathbf{p}_f)} \tag{5.12}$$

$$\times\sqrt{\frac{C_{PP}^2(T/2-t,\mathbf{p}_i)\, C_{PP}^2(t,\mathbf{p}_f)\, C_{PP}^2(T/2,\mathbf{p}_f)}{C_{PP}^2(T/2-t,\mathbf{p}_f)\, C_{PP}^2(t,\mathbf{p}_i)\, C_{PP}^2(T/2,\mathbf{p}_i)}}\,.$$

The factor $\mathcal{Z}_V^{\text{eff}}$ is a suitable combination of 2- and 3-point functions that ensures conservation of the electric charge, $f_{\pi\pi}(0) = 1$, for every lattice spacing. Non-perturbatively $\mathcal{Z}_V^{\text{eff}}$ is given by

$$\mathcal{Z}_V^{\text{eff}} = \frac{C_{PP}^2(T/2,\mathbf{0})}{2\, C_V^3(t,\mathbf{0},\mathbf{0})}\,. \tag{5.13}$$

This normalisation for the form factor corresponds to an effective renormalisation condition for the vector current, similar to the one used by the ALPHA collaboration [109, 245] to extract $\mathcal{Z}_V$ in the SF scheme. In practice, $\mathcal{Z}_V^{\text{eff}}$ will be extracted from a fit to the ratio from eq. (5.13) to a constant prior to the multiplication with the rest of the ratio.

Due to the symmetry of the 2- and 3-point functions the results for the ratios in eqs. (5.10) to (5.12) can be combined with the ones from the backward half of the lattice, i.e. in the region $T/2 < t < T$, with suitable replacements for t and $T/2 - t$. Then the ratios in eqs. (5.10)–(5.12) are constant and related to $f_{\pi\pi}(Q^2)$ by

$$R_i(t,\mathbf{p}_i,\mathbf{p}_f) = f_{\pi\pi}(Q^2)\ (E(\mathbf{p}_i) + E(\mathbf{p}_f))\,. \tag{5.14}$$

Here it should be borne in mind that this relation is correct only for the zero-component of the vector current and up to corrections induced by excited state contributions.

The main interest of this study is on the form factor at small momentum transfers. For stochastic sources each Fourier momentum demands an additional inversion. For small momenta it is thus suitable to project all correlation functions to zero Fourier momentum and generate the momenta entirely by the use of twisted boundary conditions as discussed in section 4.4. Then the momentum transfer satisfies [52]

$$Q^2 = -\left[(E_\pi(\Theta_f) - E_\pi(\Theta_i))^2 - \left(\frac{\Theta_f}{L} - \frac{\Theta_i}{L} \right)^2 \right] . \tag{5.15}$$

Here, Θ_i and Θ_f are the vectors of twist angles applied to the quark probed by the electromagnetic current in the initial and final pion respectively, L is the spatial size of the lattice and $E_\pi(\Theta)$ is the energy of the pion with momentum $\mathbf{p} = \Theta/L$.

As discussed earlier it is advantageous to calculate the light quark mass as well. Here its definition in terms of the renormalised and $\mathcal{O}(a)$-improved PCAC mass m_{PCAC} from section 2.4.3 will be used. In terms of the 2-point functions from eq. (5.5) the PCAC mass is given by

$$m_{\text{PCAC}} = \lim_{t \to T/2} \frac{\partial_0 \left\langle C^2_{AP}(t, \mathbf{0}) \right\rangle}{2 \left\langle C^2_{PP}(t, \mathbf{0}) \right\rangle} . \tag{5.16}$$

The renormalisation of m_{ud} is done in the SF scheme as defined by the non-perturbative results for $\mathcal{Z}_A$ and $\mathcal{Z}_P$ from [77,114,246]. The values for $\mathcal{Z}_A$ and $\mathcal{Z}_P$ used in this study are listed in table 5.1 and the value for $[b_A - b_P](g_0)$ is taken from [110]. For κ_c the results from [77], listed in table 5.2, are employed to determine the bare quark mass $\bar{m}$.

5.3 Simulation setup and basic quantities

All computations in this part of the thesis are based on the existing CLS ensembles, generated with two degenerate dynamical flavours of Sheikholeslami-Wohlert fermions. In this section the basic parameters, the error analysis procedure and the results for basic quantities on these ensembles are discussed.

5.3.1 Basic setup and ensemble properties

The gauge ensembles have been generated using the DD-HMC [152, 176, 179] and MP-HMC [178] algorithms as discussed in section 3.5. The associated speed up enables the generation of gauge ensembles at small quark masses down to roughly 190 MeV at lattice sizes up to 128×64^3 and lattice spacings down to 0.048 fm (cf. tables 5.2 and 6.7). The computation of the form factor has so far only be done on the subset of the available ensembles listed in table 5.2. The results are converted to physical units via the Sommer scale r_0 in the chiral limit, which has been computed for the CLS ensembles in [77,247], and its continuum result $r_0 = 0.503\,(10)$ fm obtained in [77]. The latter has been determined by setting the scale via the kaon decay constant and is consistent with the result from scale setting via the Ω-mass from [103] when the updated results for r_0/a are used [248]. It is important to note that all ensembles fulfill the naive conditions from section 3.6 to enable the control of finite size and cut-off effects as $m_\pi L > 4$ and $a < 0.1$ fm. The issue of long

ens.	N_{meas}	$N_t \times N_s^3$	β	r_0/a	κ_c	κ_{sea}	m_π [MeV]	$m_\pi L$
A3	132	64×32^3	5.2	6.15(6)	0.136055(4)	0.13580	455(10)	6.0
A4	175	64×32^3	5.2	6.15(6)	0.136055(4)	0.13590	351(8)	4.7
A5	108	64×32^3	5.2	6.15(6)	0.136055(4)	0.13594	299(7)	4.0
E4	81	64×32^3	5.3	7.26(7)	0.136457(4)	0.13610	552(13)	6.2
E5	119	64×32^3	5.3	7.26(7)	0.136457(4)	0.13625	412(10)	4.6
F6	233	96×48^3	5.3	7.26(7)	0.136457(4)	0.13635	295(7)	5.0
F7	250	96×48^3	5.3	7.26(7)	0.136457(4)	0.13638	254(6)	4.3
N3	98	96×48^3	5.5	10.00(11)	0.1367749(8)	0.13640	625(14)	7.6
N4	117	96×48^3	5.5	10.00(11)	0.1367749(8)	0.13650	534(12)	6.5
N5	189	96×48^3	5.5	10.00(11)	0.1367749(8)	0.13660	424(10)	5.2

Table 5.2: Summary of properties of the gauge ensembles. The results for the Sommer scale r_0/a and for κ_c are taken from [77].

autocorrelations has been addressed on a subset of the ensembles in [184] and they appear to be under control for the ensembles used here.

All 2- and 3-point functions have been computed using stochastic $Z_2 \times Z_2$ wall sources as discussed in section 4.3. To reduce the noise, two hits were done per configuration with a source separated in time by $N_t/2$ in all cases, except for ensemble A5 where four hits separated by $N_t/4$ have been applied. The data sets cover a large range of quark masses and several lattice spacings, thus allowing for a study of the systematic effects from the chiral extrapolation and the continuum extrapolation. In addition, they have large volumes and satisfy $m_\pi L \geq 4$, so that finite size effects can be expected to be small.

The project of the measurement of the pion form factor is conveniently conjoined with the project to calculate the $K \to \pi$ form factor [249] to avoid additional inversions. Following refs. [51, 211] it is possible to tune the twist angles so that the $K \to \pi$ form factor can be computed directly at the phenomenologically relevant point of vanishing momentum transfer. The associated twist angle of the pion is given by

$$|\Theta| = N_s \sqrt{\left(\frac{m_K^2 + m_\pi^2}{2\, m_K}\right)^2 - m_\pi^2}\,, \tag{5.17}$$

when the kaon is at rest. Here the choice is made to introduce a twist only in one of the spatial directions so that the twist angle is fixed by the above condition. Since the bare parameter κ_s for the strange quark is not known from the start, simulations have been performed with four different κ-values eventually surrounding κ_s and thus enabling an interpolation to the correct strange quark mass. Accordingly, four twist angles ($\theta_1 - \theta_4$ in table A.1) for the pion are fixed by the condition in eq. (5.17) and can be computed by the input from initial measurements of m_π and m_K. In addition, the pion form factor has been computed using one additional twist angle θ_5 which has been tuned appropriately to

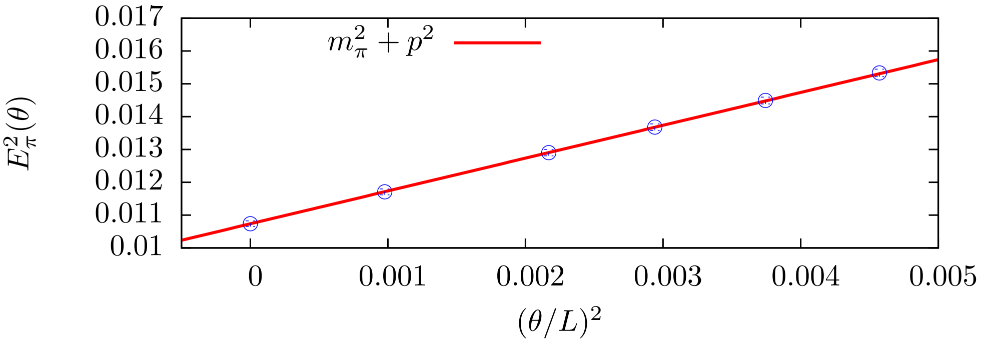

Figure 5.4: The energies of the boosted pions evaluated on the F6 ensemble compared to the continuum dispersion relation, eq. (5.19).

yield a dense set of data points at very small momentum transfers. The complete set of twist angles for all ensembles is listed in table A.1. Each of these twists was used to induce a momentum for the initial (θ_i) as well as for the final pion (θ_f).

Error estimates are obtained using the bootstrap method with 1000 bins in combination with the percentile error estimate, as discussed in appendix A.3. For most of the quantities only the symmetric error is quoted while for final results and quantities with a significant deviation from symmetric errors upper and lower error bars are given. The various observables evaluated on a given gauge field ensemble are correlated. A measure for the degree of correlation is provided in terms of the covariance matrix which can be obtained as a result of the bootstrap (cf. appendix A.3). In a Monte-Carlo simulation the elements of the covariance matrix are known only up to statistical precision and this can cause severe problems when using its inverse in least-square minimisations (see for example [250]). In the analysis for most of the fits the correlation matrix could not be estimated with sufficient precision to reliably compute its inverse. Consequently, all fits are done without taking the correlations into account in the following.

The uncertainties of the renormalisation constants in table 5.1 and that of other quantities, like the Sommer parameter, that are external input for the analysis are taken into account by generating a Gaussian distribution with the width of the quoted uncertainty. For each bootstrap sample one element drawn from the distribution is used. The procedure is discussed in more detail in appendix A.4, including a discussion of checks that were performed for each generated distribution.

5.3.2 Masses, decay constants and kinematics

The energies of the pions are extracted from the corresponding 2-point function $C_{PP}(t, \mathbf{p})$ via an uncorrelated fit to the form of eq. (4.7) where $E_0(\mathbf{p})$ is the corresponding energy and the multiplicative factor is given by $|Z_P(\mathbf{p})|$. Since excited state contributions might

ensemble	$r_0\, m_\pi$	$r_0\, F_\pi$	$r_0\, m_{ud}$	$\mathcal{Z}_V$
A3	1.161 (12)	0.280 (8)	0.090 (3)	0.73228 (7)
A4	0.895 (11)	0.247 (12)	0.052 (3)	0.72885 (12)
A5	0.761 (11)	0.251 (14)	0.040 (2)	0.72731 (10)
E4	1.406 (16)	0.287 (10)	0.128 (5)	0.74962 (8)
E5	1.048 (13)	0.271 (11)	0.078 (4)	0.74461 (8)
F6	0.752 (8)	0.254 (8)	0.041 (2)	0.74119 (4)
F7	0.646 (7)	0.237 (8)	0.029 (1)	0.74030 (5)
N3	1.593 (18)	0.329 (7)	0.188 (5)	0.77162 (3)
N4	1.360 (16)	0.304 (9)	0.139 (4)	0.76855 (3)
N5	1.080 (13)	0.291 (8)	0.091 (3)	0.76543 (3)

Table 5.3: Results for the pion mass, the pion decay constant and the renormalised light-quark mass. Also listed are the results for $\mathcal{Z}_V$ as discussed in section 5.5.1.

not be negligible the result have been checked with a fit including also a three-pion state as first excited state suggested in [251]. For the present analysis both results for the pion masses agree well within error bars. It has also been checked that varying the fitrange did not change the results significantly. m_{ud} is obtained from a fit to a constant for the ratio in eq. (5.16). Also here it has been checked that a variation in the fitrange did not change the results. The renormalisation is done via the renormalisation constants and improvement parameters listed in table 5.1.

The bare pion decay constant can be related to the bare PCAC mass and Z_π using eqs. (2.47), (5.28) and (5.9) by

$$F_\pi^{\text{bare}} = \sqrt{2\ |Z_\pi|^2}\ \frac{m_{\text{PCAC}}}{m_\pi^2}\ . \tag{5.18}$$

A similar relation was used to determine the pion and kaon decay constants in [77]. The renormalised decay constant is then obtained as $F_\pi = \mathcal{Z}_A\ (1 + b_A\, a\, \bar{m})\ F_\pi^{\text{bare}}$ where b_A is the 1-loop result from eq. (A.20). Note the difference in normalisation compared to [77].

The results for m_π, F_π and m_{ud} in units of r_0 are listed in table 5.3. Up to exponentially suppressed finite volume effects, the pion energies obey the dispersion relation

$$E_\pi(\mathbf{p}) = \sqrt{m_\pi^2 + \mathbf{p}^2}\,, \tag{5.19}$$

where $\mathbf{p} = (\Theta_u - \Theta_d)/L$, i.e. the difference of the twist angles applied to the pions valence quarks [50, 210]. To show how well the continuum dispersion relation is reproduced by the data the numerical results for ensemble F6 are shown in comparison to the prediction from eq. (5.19) in figure 5.4. In the remainder of the analysis eq. (5.19) is used to determine the kinematics in terms of the pion energy at rest together with the twist angles.

Using the results for the pion mass, the resulting Q^2-values can be calculated. They are shown in units of r_0 in figure 5.5. The red line in the plot is the lowest momentum

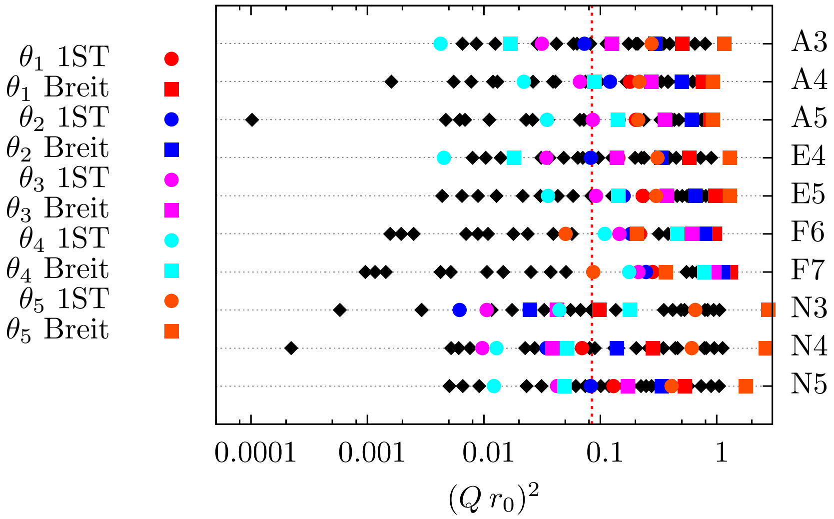

Figure 5.5: Resulting values for Q^2 in units of r_0. The red line is the lowest momentum transfer obtained so far, namely the lowest momentum transfer from [52]. The coloured data points correspond to Q^2-values that result from 3-point functions where either only one of the quarks has a twist (1ST) or $\Theta_i = -\Theta_f$ (Breit) (cf. section 6.2.1). They are the ones used for the final analysis.

transfer obtained so far, namely the lowest Q^2-value from [52]. The plot demonstrates the potential of partially twisted boundary conditions to go to very small momentum transfers.

5.4 Systematic effects I: $\mathcal{O}(a)$-improvement and excited states

Two particular systematic effects that need to be controlled in the simulations are cut-off effects and contaminations from excited states in the computed masses and matrix elements. These are the topics of this section. Cut-off effects split in two different categories, effects of $\mathcal{O}(a)$ and higher order effects. This section addresses $\mathcal{O}(a)$-effects, in particular those of the vector current, that are to be taken into account prior to the analysis in the $\mathcal{O}(a)$-improvement program. Higher order effects are discussed later.

5.4.1 $\mathcal{O}(a)$-improvement of the vector current

To achieve full $\mathcal{O}(a)$-improvement the $\mathcal{O}(a)$-improved current $(J_{V,I})_0$ needs to be inserted in eq. (5.6) given by (cf. eq. (2.36))

$$(J_{V,I})_0(x) = J_{V,0}(x) + a\, c_V\, \partial_i\, T_{0\nu}(x)\ . \tag{5.20}$$

c_V is known to 1-loop order from perturbation theory [93], as given in eq. (A.13), which is used here. It is also known non-perturbatively from quenched simulations [252], albeit

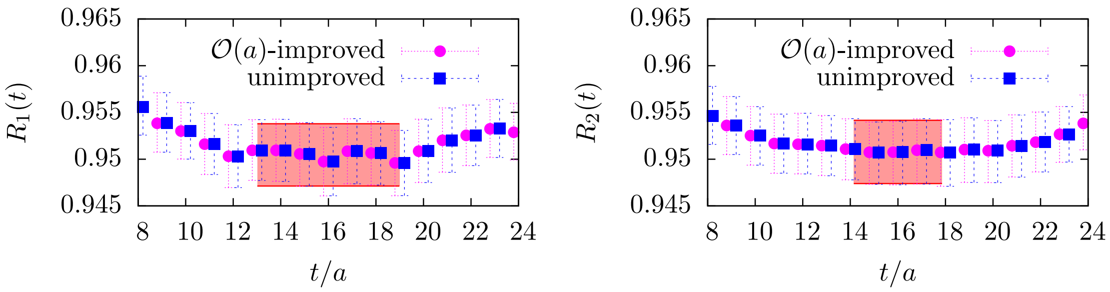

Figure 5.6: Effects of $\mathcal{O}(a)$-improvement of the vector current on the ratios R_1 (left) and R_2 (right) on the A5 ensemble at the coarsest lattice spacing. The data is slightly displaced to enable the visibility of both series of data points.

not in the range of couplings used in this study. When $C^3_{P,T_{\mu\nu},P}$ is the 3-point function with the zero component of the vector current replaced by the tensor current. Then the improvement is accomplished by replacing

$$C^3_{P,V,P}(t,\mathbf{x},\mathbf{x}_f,\mathbf{x}_i) \quad \rightarrow \quad C^3_{P,V,P}(t,\mathbf{x},\mathbf{x}_f,\mathbf{x}_i) + a\, c_V\, \partial_i\, C^3_{P,T_{0i},P}(t,\mathbf{x},\mathbf{x}_f,\mathbf{x}_i)\,. \tag{5.21}$$

in eq. (5.6). When projected to zero Fourier momentum, the additional derivative term vanishes in the absence of twisted boundary conditions which is easily shown by writing out the sum in eq. (5.27). Nevertheless, this is no longer true when twisted boundary conditions are present and the quark fields satisfy eq. (4.31) at the boundaries. The associated boundary terms in the sum from eq. (5.6) then obtain an additional exponential factor and do not cancel. The resulting improvement term reads

$$\begin{aligned} \sum_{\nu=0}^{3}\sum_{\mathbf{x}} \tilde{\partial}_\nu C^3_{P,T_{0i},P}(t,\mathbf{x},\mathbf{x}_f,\mathbf{x}_i) \quad = \quad & \frac{1}{2a}\sum_{k=1}^{3}\sum_{\substack{j=1\\ j\neq i}}^{3}\sum_{x_j=0}^{N_s-1} \\ & \Big\{ \left(e^{i\delta\theta_k}-1\right) C^3_{P,T_{0i},P}(t,\mathbf{x},\mathbf{x}_f,\mathbf{x}_i)|_{x_k=0} \\ & - \left(e^{i\delta\theta_k}-1\right) C^3_{P,T_{0i},P}(t,\mathbf{x},\mathbf{x}_f,\mathbf{x}_i)|_{x_k=N_s-1} \Big\}\,, \end{aligned} \tag{5.22}$$

where $\delta\theta_k$ is the difference of the twist angles in the $\hat{k}$-direction which have been applied to the two quarks defining the vector and the tensor current. Hence, there will only be a correction due to improvement from the directions where a twist-angle has been applied and for which $\delta\theta_i \neq 0$. For the form factor this ensures the correct normalisation at $Q^2 = 0$ since in that case necessarily $\delta\theta = 0$.

To check the size of the additional term it has been computed explicitly on the ensembles with the coarsest lattice spacing ($\beta = 5.20$) and on the lightest ensemble at the intermediate lattice spacing ($\beta = 5.30$) where $\mathcal{O}(a)$-improvement is expected to be most important. In all cases the $\mathcal{O}(a)$-improvement term had a relative size below the per-mille level compared to the vector 3-point function, with changing signs for different time slices. As a further check one can directly look at the ratios with and without $\mathcal{O}(a)$-improvement for the 3-point function. Examples are shown in figure 5.6 for the case of a ratio including 2- and 3-point functions (R_1) and a ratio including only 3-point functions (R_2). Both sets of points agree up to the sub-per-mille level and the deviations are much smaller than the statistical uncertainties. As a consequence, the $\mathcal{O}(a)$-improvement terms can safely be neglected from now on.

5.4.2 Analysis of excited state contributions

Formula (5.14) for the extraction of the form factor is only correct up to the contributions from excited states entering the 2- and 3-point functions. The contamination of the signal can be calculated by including the first excited state in the spectral representation for the correlation functions and inserting the expressions in the ratios, eqs. (5.10)–(5.12). Expanding the resulting expressions around $T/4$ with the assumption that $\Delta E(\mathbf{p}) = 2E(\mathbf{p})$ [251] [2] one obtains

$$\begin{aligned}
R_1(t,\mathbf{p}_i,\mathbf{p}_f) &= R_1^{\text{as.}} \Big[1 + r_{0,i}^{(1)}\, e^{-E(\mathbf{p}_i)\,T} + r_{0,f}^{(1)}\, e^{-E(\mathbf{p}_f)\,T} \\
&\quad + \left(r_{2,i}^{(1)}\, e^{-E(\mathbf{p}_i)\,T/2} + r_{2,f}^{(1)}\, e^{-E(\mathbf{p}_f)\,T/2}\right)(t-T/4)^2 \qquad (5.23)\\
&\quad + \mathcal{O}\left((t-T/4)^3\right) + \mathcal{O}\left(e^{-2\,E\,T}\right)\Big] \\
R_2(t,\mathbf{p}_i,\mathbf{p}_f) &= R_2^{\text{as.}} \Big[1 + r_{0,i}^{(2)}\, e^{-E(\mathbf{p}_i)\,T/2} + r_{0,f}^{(2)}\, e^{-E(\mathbf{p}_f)\,T/2} \\
&\quad + \left(r_{2,i}^{(2)}\, e^{-E(\mathbf{p}_i)\,T/4} + r_{2,f}^{(2)}\, e^{-E(\mathbf{p}_f)\,T/4}\right)(t-T/4)^2 \qquad (5.24)\\
&\quad + \mathcal{O}\left((t-T/4)^3\right) + \mathcal{O}\left(e^{-E\,T}\right)\Big] \\
R_3(t,\mathbf{p}_i,\mathbf{p}_f) &= R_3^{\text{as.}} \Big[1 + r_{0,i}^{(3)}\, e^{-E(\mathbf{p}_i)\,T/2} + r_{0,f}^{(3)}\, e^{-E(\mathbf{p}_f)\,T/2} \\
&\quad + \left(r_{1,i}^{(3)}\, e^{-E(\mathbf{p}_i)\,T/2} + r_{1,f}^{(3)}\, e^{-E(\mathbf{p}_f)\,T/2}\right)(t-T/4) \qquad (5.25)\\
&\quad + \mathcal{O}\left((t-T/4)^2\right) + \mathcal{O}\left(e^{-E\,T}\right)\Big]\ .
\end{aligned}$$

Here $R_i^{\text{as.}}$ is the asymptotic value at $T/4$ in the limit $T \to \infty$ and $r_{j,i/f}^{(k)}$ are the prefactors of the excited state terms and depend on initial (i) and final (f) momentum and the ratio. Note that these are only the leading order terms in $\exp(-ET)$ and higher orders contribute to each order in $(t - T/4)$.

The expressions in eqs. (5.23)–(5.25) have the following important implications:

- There is a constant contribution in the extraction of $f_{\pi\pi}(Q^2)$ which is $\sim \exp(-ET/2)$ for R_2 and R_3 but $\sim \exp(-ET)$ for R_1. Its size depends on the sizes of the prefactors which are not known *ab initio*. For the present values of T and E the exponential

---

[2] To understand this assumption it is important to note that the first excited state in each channel can be expected to be a three-particle state [251]. Then it is obvious that the lightest possible state corresponds to a state with the ground state particle and two additional pions. Here the ground state is also a pion, so that the minimal gap to the next excited state is given by $2\,E(\mathbf{p})$.

		$\beta = 5.20$	$\beta = 5.30$	$\beta = 5.50$
our results	$\mathcal{Z}_V$	0.72331 (14)	0.73766 (7)	0.76083 (4)
	b_V	1.800 (34)	1.685 (21)	1.519 (8)
[245]	$\mathcal{Z}_V$	0.739 (5)	0.750 (5)	0.768 (5)

Table 5.4: Results for $\mathcal{Z}_V$ in the chiral limit using a chiral extrapolation via eq. (5.26) and the results from [245].

factors can be of the size of 2% relative to $R_i^{\text{as.}}$ at most and thus might give a substantial contribution to the form factor. However, since $f_{\pi\pi}(0) = 1$ by definition (which is manifest for R_2), there is a symmetry-based suppression of the constant part of the excited states contribution for small momenta. This can be seen as follows: Effectively, all three combinations of correlation functions $R_{1,2,3}$ contain ratios of 3-pt functions. In the case of R_2 this is immediately obvious. In the case of R_1 and R_3 the 3-pt function in the denominator is absorbed in the definition of $\mathcal{Z}_V^{\text{eff}}$. At zero momentum transfer the unwanted offset of the ground state cancels between the numerator and the denominator and as the momentum increases the offset may start setting in. The current analysis cannot assess the remaining bias quantitatively but the above argument together with the small Q^2-values of the data provides a hint that the additional term might be negligible. Anyhow, one should keep in mind that a systematic study of this effect has not been performed yet.

- For R_1 and R_2 the leading contribution in $(t - T/4)$ is quadratic while for R_3 it is linear. This means that $R_{1,2}$ should evolve a symmetric plateau while R_3 might show a linear behavior in the vicinity of $T/4$. This observation is verified by the data. To account for the contributions from excited states the results for R_3 have been checked using linear fits in addition to the fits to a constant.

5.5 Results for the form factor

5.5.1 Renormalisation of the vector current

As a first step for the computation of the form factor the effective renormalisation constant $\mathcal{Z}_V^{\text{eff}}$ has to be computed using eq. (5.13). The results for the different ensembles are listed in table 5.3. As discussed earlier $\mathcal{Z}_V^{\text{eff}}$ corresponds to the effective renormalisation factor of the vector current at finite quark mass and lattice spacing as given in eq. (2.43). To extract the renormalisation of the vector current in the mass independent scheme one can perform a chiral extrapolation of $\mathcal{Z}_V$ for each lattice spacing by fitting the data to the form

$$\mathcal{Z}_V^{\text{eff}}(\beta, \kappa) = \mathcal{Z}_V(\beta) \left[1 + b_V \left(\frac{1}{\kappa} - \frac{1}{\kappa_c} \right) \right] . \tag{5.26}$$

Here $\mathcal{Z}_V(\beta)$ is the renormalisation factor in the mass-independent scheme, consistent with $\mathcal{O}(a)$-improvement (cf. section 2.4.2, in particular eq. (2.43)). The results in the chiral

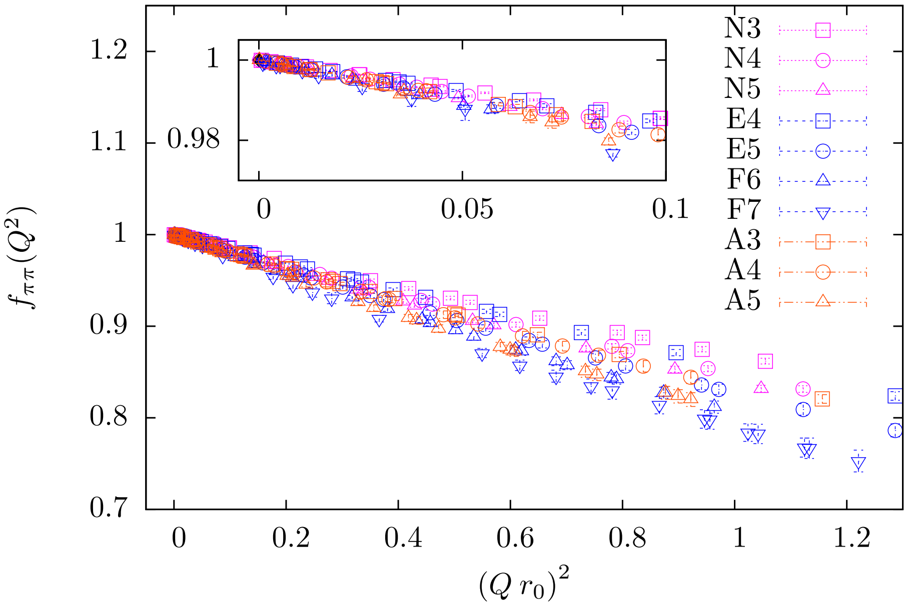

Figure 5.7: Results for the pion form factor for all ensembles. The inlay shows a zoom into the region of small Q^2.

limit are listed in table 5.4. They agree well with the results obtained in a study on nuclear form factors [187] on the same lattices. They are also of similar magnitude as the ALPHA results for $\mathcal{Z}_V$ in the SF scheme [245]. Note, that the determination of $\mathcal{Z}_V$ in the SF scheme works closer to the chiral limit and thus has less systematic effects concerning the chiral extrapolation. Note also, once more, that the particular choice of the renormalisation scheme is not important as long as the scheme is used consistently within the analysis and that results from different schemes will not agree at non-zero lattice spacing. Important for the choice of the renormalisation scheme is only the smooth approach to the continuum with leading lattice artefacts of $\mathcal{O}(a^2)$, which is here ensured by using the physical renormalisation condition $f_{\pi\pi}(0) = 1$ for the form factor. The results for b_V can be compared to perturbation theory and, as expected for these relatively large couplings, the results tend to be significantly larger then the perturbative values from eq. (A.19). However, both results are of similar magnitude and the non-perturbative value rapidly approaches the perturbative one with decreasing coupling. b_V is also known non-perturbatively from simulations of pure gauge theory [109] but only up to $\beta = 6.0$, so that it cannot be compared directly to the results from table 5.4.

5.5.2 Q^2-dependence of the form factor

As discussed in the previous section, excited states give rise to contributions to the time dependence of the ratios. For R_1 and R_2 these contributions are quadratic in $(t - T/4)$ and

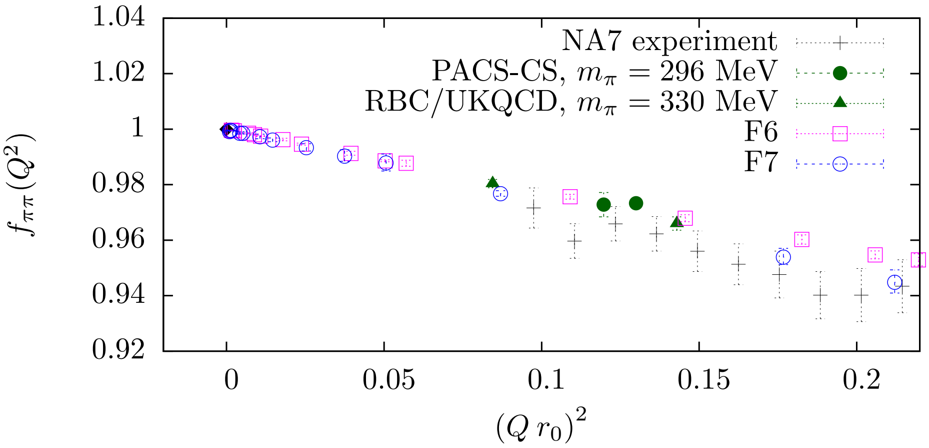

Figure 5.8: Compilation of results for the pion form factor in dynamical LQCD [51, 52, 229] and as determined from the NA7 experiment [45].

it is sufficient to look for a plateau and extract the value for $f_{\pi\pi}(Q^2)$ using a constant fit. For R_3 the leading order correction is linear and in many cases significant. To parametrise these deviations both constant and linear fits were applied, the latter typically allowing for a larger time interval to be fitted. Since the results are fully compatible the constant fit is used from now on for all ratios. The ratios that did not provide a reasonable signal were discarded and not used for the extraction of $f_{\pi\pi}(Q^2)$. In practice, at least one of the three ratios worked for each kinematic point so that no point was left out in the analysis. Examples for ratios that were kept in the analysis and for some that were discarded are shown in figure C.1 in appendix C.2. In the cases where several ratios provided good fits the results from these ratios were combined using a weighted average for each bootstrap sample. The weight factor is given by the diagonal elements of the covariance matrix.

Figure 5.7 shows the results for the form factor on all ensembles. The inlay shows the region of very small Q^2. Figure 5.8 shows the results for the F6 and F7 ensembles in comparison to the experimental measurement and results of other lattice collaborations in the region of small Q^2. The plot illustrates the unprecedented high density of points in the low Q^2 region and demonstrates the accuracy of the data.

5.5.3 A first look at the charge radius

The charge radius of the pion (5.3) is defined as the derivative of the form factor with respect to the momentum transfer at $Q^2 = 0$. In practice, it is extracted in terms of the slope of a phenomenologically motivated function with its coefficients determined from a fit to the form factor data. Until recently, data from both experiment and LQCD did not cover the important region of very low momentum transfers where one would ideally like to extract the slope. Studies of the systematics introduced by the fit-ansatz were therefore

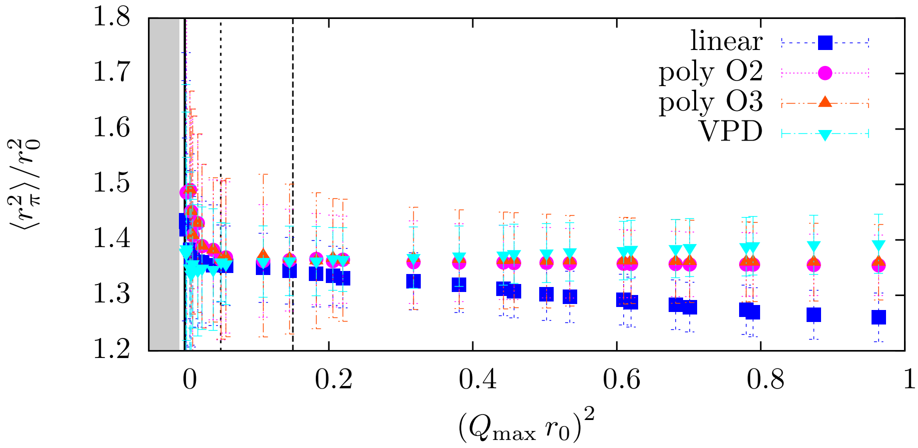

Figure 5.9: Results for $\langle r_\pi^2 \rangle$ obtained from different fit functions including all results for $f_{\pi\pi}(Q^2)$ up to $(Q_{\max}\, r_0)^2$ for the case of ensemble F6. The results with the labels 'poly O2' and 'poly O3' are the results of a polynomial of degree two and three in Q^2 respectively and the results denoted by VPD are the results of a fit to the form of eq. (5.4).

very limited.

The high density of data points for $f_{\pi\pi}(Q^2)$ for $Q^2 \to 0$ for all ensembles, illustrated in figures 5.5 and 5.7, allows to constrain the functional form of the form factor in that region accurately and to reduce the model dependence in the extraction of the charge radius to a minimum. In practice, radii as extracted from

- linear fits to the form
$$f_{\pi\pi}(Q^2)\big|_{\text{lin}} = 1 - \langle r_\pi^2 \rangle_{\text{lin}}\; Q^2 \;, \tag{5.27}$$
- fits to polynomials of degree n,
$$f_{\pi\pi}(Q^2)\big|_{\text{poly O}n} = 1 - \langle r_\pi^2 \rangle_{\text{poly O}n}\; Q^2 - C_V\, Q^4 - \sum_{i=3}^{n} c_i\, Q^{2\,i} \;, \tag{5.28}$$
- a VPD motivated pole-fit to the form of eq. (5.4),

are compared which allows to assess the potential contribution of higher order terms. The pole ansatz was already used in [45] to determine the charge radius from experimental data and in [225–227,229] in its determination from lattice data. The studies in refs. [51,52,228] have also probed the extraction of the charge radius more systematically but were limited by the number of points in the low Q^2-region.

The results for $\langle r_\pi^2 \rangle$ for the different ansätze discussed above on ensemble F6 are shown in figure 5.9. The data has been obtained by a fit to all results for $f_{\pi\pi}(Q^2)$ below $(Q_{\max} r_0)^2$, defining the horizontal axis. As can be seen, the data can roughly be divided in three

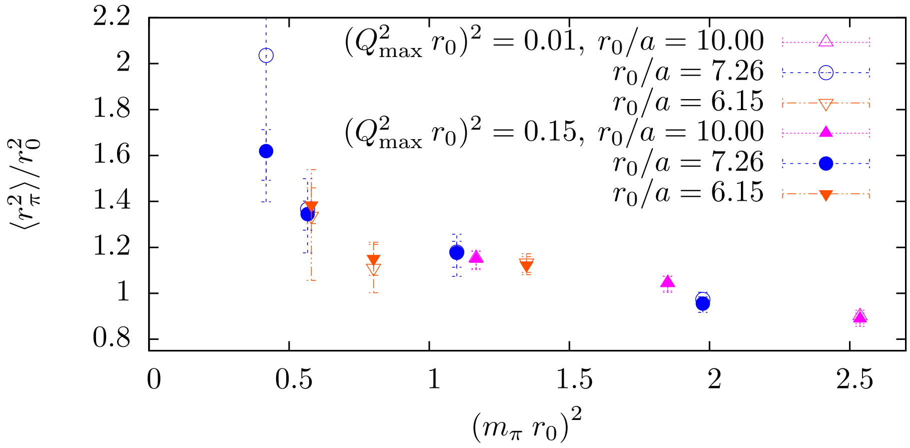

Figure 5.10: Pion mass dependence of the results for $\langle r_\pi^2 \rangle$ in units of r_0 as extracted from linear fits with cuts at $(Q_{\max}\, r_0)^2 = 0.15$ and $(Q_{\max}\, r_0)^2 = 0.01$.

different regimes. In the first regime, roughly up to $(Q_{\max}\, r_0)^2 = 0.05$ (1st dashed vertical line), the results for $\langle r_\pi^2 \rangle$ agree well for the different fits but the results have relatively large uncertainties due to the small number of measurements entering the fit and the resulting sensitivity to fluctuations. In the second regime the results also agree well and the error bars are reasonably small. This is the region where one would like to extract the results. Similar pattern are seen for the other ensembles as well. A possible cut in $(Q\, r_0)^2$ at which fluctuations are under control and agreement between the different fits is still good for all ensembles is indicated by the second dashed vertical line at $(Q_{\max}\, r_0)^2 = 0.15$. In the third regime the results from different models for the Q^2-dependence start to deviate, indicating that the treatment of the higher order terms becomes relevant.

Figure 5.10 shows the results for $\langle r_\pi^2 \rangle$ obtained by a linear fit to $f_{\pi\pi}(Q^2)$ including values up to $(Q_{\max}\, r_0)^2 = 0.15$ in comparison to the results with values up to $(Q_{\max}\, r_0)^2 = 0.01$. The data underlying the plot is listed in table C.3 in appendix C.2. As can be seen from the plot, both results agree well within errors while the error bars are much larger for the more aggressive cut at $(Q_{\max}\, r_0)^2 = 0.01$. This is especially true for the most chiral ensemble, F7, where the error bars increase drastically.

Up to this point most of the systematic effects that appear on the level of the individual ensemble are taken into account. The only effect left out so far, which can be addressed within the scope of this thesis and affects the data on the individual ensemble is the one of finite volume which is discussed in the beginning of the next chapter. It is important to recall that the momenta are introduced via a change in the boundary conditions of the quark fields, i.e. by the use of a finite volume effect. This leads to different finite volume effects for different values of Q^2. In consequence, the extraction of $\langle r_\pi^2 \rangle$ is only free of systematics if these effects are eventually taken into account.

6 Chiral extrapolations for $f_{\pi\pi}(Q^2)$ and $\langle r_\pi^2 \rangle$

After the discussion of the systematic effects for the individual ensembles and the extraction of the results for the form factor, one can now make contact with experiment and extrapolate the data to the continuum and physical quark mass. In this process one can also include the extrapolation to infinite volume. Ideally these extrapolations should be done model-independently. In practice, this is difficult and the present analysis is restricted to probe χPT with the data for the form factor and the charge radius, and to compare the results from χPT for the charge radius at the physical point with the results from polynomial extrapolations.

Since the simulations are done with two degenerate light quark flavours it is natural to compare the quark mass dependence of the data with $SU(2)$ chiral perturbation theory as introduced in section 1.3.2. The formula for the pion form factor to next-to leading order (NLO) has been worked out in [18, 42] and to next-to-next-to leading order (NNLO) in [43]. The expressions for the form factor to NNLO are summarised in appendix A.5 in eqs. (A.48)–(A.50). Later it will turn out that the information from the data for $f_{\pi\pi}(Q^2)$ or $\langle r_\pi^2 \rangle$ alone is not sufficient to constrain the 6 free parameters in the fits. This problem can be overcome by simultaneously performing the chiral extrapolation together with the ones for m_π and F_π that have been worked out in [253–255]. They are also listed in appendix A.5 in eqs. (A.46) and (A.47). To be able to perform the simultaneous chiral extrapolation of the three quantities it is necessary to replace F_π and m_π on the right hand side of the formulae by its NNLO expressions to obtain a set of self consistent formulae. In this process the dependence on m_π is exchanged by the dependence on the renormalised quark mass m_{ud}. The details are discussed in appendix A.6 and the results are given in eqs. (A.57) to (A.63).

The data discussed in the last section implies the existence of residual lattice artefacts and related terms should be included in the analysis to perform the extrapolation to the continuum and to allow for a simultaneous fit to the data from different lattice spacings. Given the fact that $\mathcal{O}(a)$ cut-off effects are either small or explicitly removed from the data the cut-off effects are modeled by adding a^2 terms to the extrapolation ansätze for the pion decay constant and the pion mass. For the form factor the imposed normalisation $f_{\pi\pi}(0) = 1$ allows only for cut-off effects that vanish for $q^2 \to 0$. They are modeled by adding a term $(aq)^2$ to the extrapolation formulae. For the charge radius this translates into adding a simple a^2-term. One could also include higher orders in the lattice spacing but our data does not allow to constrain any further terms. The resulting formulae that can be used to perform a simultaneous extrapolation to chiral and continuum limit are listed in eqs. (A.64) to (A.67).

To get an idea about the reliability of the chiral extrapolation and the effect from choosing a particular ansatz, the extrapolation of the charge radius is also performed using polynomials. The spread of the results then allows to obtain an estimate for the systematic uncertainty.

The chapter starts with a first look at χPT to NLO and its limitations. The second section then contains the discussion of finite volume effects and the final results for the pion charge radius. The last two sections provide the details of the different chiral extrapolations and the final results as well as a discussion of perspectives for further improvement and research.

6.1 A first look at χPT to NLO

If χPT is the correct effective field theory to describe the form factor it should be sufficient to use χPT to NLO when the pion masses are small enough. However, it is not clear up to which pion mass this would be the case. It is possible to check for consistency with the present data by using a fit to the Q^2-dependence of $f_{\pi\pi}(Q^2)$ for each ensemble separately using the formula from eq. (A.48) to $\mathcal{O}(m_\pi^2)$. The resulting fit function has two parameters, F_π and $\bar{\ell}_6$. The renormalisation scale μ is set to $m_\rho \approx 770$ MeV throughout the whole analysis. Here it is sufficient to insert the experimental value for F_π. Another choice for F_π, as for instant the calculated value, corresponds to changing the higher order terms. If χPT to NLO works in some range of pion masses, covered by the ones of this analysis, the fit should produce identical results for $\bar{\ell}_6$, up to statistical precision, in that region. When χPT to NLO is only applicable for some limited range of pion masses then this also translates to a limit for the applicability in Q^2 since both are subject to the same power counting. To avoid an influence of the Q^2-range on the comparability of the results for $\bar{\ell}_6$ one should thus use a low cut in Q^2 for its extraction. For the following the cut is set to $(Q\, r_0)^2 = 0.22$, which corresponds to a cut at $Q^2 = 0.034$ GeV^2 or equivalently $|Q| \approx 190$ MeV. This particular choice has been made since the cut is lower than the lightest pion mass and a similar cut is applied later for the extraction of the charge radius.

The results of the fits are listed in table C.3 in appendix C.2 and are shown in figure 6.1. $\bar{\ell}_6$ is clearly not constant for any range of pion masses, indicating that χPT to NLO does not provide a consistent description of the data (see also [215]). The same is true for the data for $\langle r_\pi^2 \rangle$ as extracted in section 5.5.3, indicating that its chiral extrapolation cannot be done using χPT to NLO. This is true even when only the most chiral ensembles are included. Nevertheless, the m_π-dependence of this effective $\bar{\ell}_6$ can be used to extract information on its value at the physical point and thus on the expected charge radius in NLO there. Note, that this treatment of $\bar{\ell}_6$ as a mass dependent parameter corresponds to a model for the effects of higher order terms in the chiral expansion. A true LEC in χPT is always independent of the pion mass. As a simple ansatz for the extrapolation one can use a second order polynomial, also including a term for a^2-effects,

$$\bar{\ell}_6^{\mathrm{NLO}} = l_0 + l_1\, m_\pi^2 + l_2\, m_\pi^4 + l_a\, \frac{a^2}{r_0^2}\ . \tag{6.1}$$

The results from the fit are listed in table 6.1 together with the results for $\bar{\ell}_6$ and $\langle r_\pi^2 \rangle$ at the physical point. The result for $\langle r_\pi^2 \rangle$ at the physical point is in good agreement with the value extracted from experiment [45] and the result for $\bar{\ell}_6$ is consistent with the estimate from [43]. A more detailed comparison to results from other groups and from experiment and phenomenology is postponed to section 6.4.

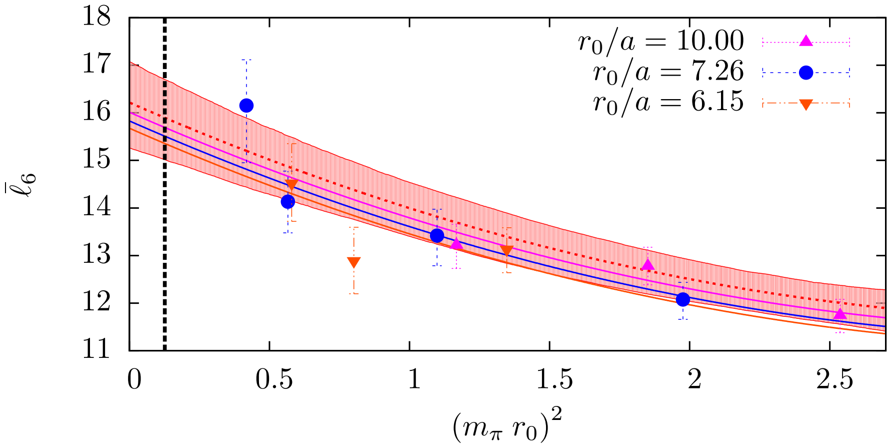

Figure 6.1: Results for the LEC $\bar{\ell}_6$ as extracted from the fit to the form factor data using χPT to NLO. The curves are the ones for different lattice spacings indicated by the colour code as in the key, obtained by a fit to the form of eq. (A.53). The red band represents the continuum extrapolated function.

l_0	l_1	l_2	l_a	$\bar{\ell}_6^{\mathrm{NLO}}\vert_{\mathrm{phys}}$	$\langle r_\pi^2\rangle_{\mathrm{phys}}/r_0^2$	χ^2/dof
16.2 (9)	-2.6 (8)	0.4 (3)	-20 (22)	15.9 (9)	1.70 ($^{+7}_{-9}$)	0.9

Table 6.1: Results for the extrapolation of $\bar{\ell}_6$ with a fit to the form of eq. (A.53).

6.2 Systematic effects II: Finite size effects and the charge radius

Apart from chiral and continuum extrapolations and effects due to the restriction to $N_f = 2$, the only type of systematic effects which have not been taken into account are finite size effects (FSE). Since $m_\pi\, L \geq 4$ for all ensembles one would expect according to empirical evidence that they are small and only contribute a minor effect. Nevertheless, the data for $f_{\pi\pi}(Q^2)$ has error bars that are below the per cent level, which means that even small effects might lead to significant shifts and thus should be included. Furthermore, momenta are introduced via a change in the boundary conditions between sea and valence quarks, i.e. a finite volume effect, which potentially enlarges the effects. In particular, the effect will be Q^2-dependent and thus potentially contribute to $\langle r_\pi^2\rangle$.

6.2.1 Calculation of finite size effects from χPT

FSE can be estimated in χPT. For the pion mass and the pion decay constant the corresponding expressions have been derived in [256, 257]. In fact, the formulae allow the predictions for FSEs at NNLO using only the LECs that contribute to NLO in the usual expansion. For the vector form factor computed with partially twisted boundary conditions FSE have been computed in NLO χPT [258] for the case where either $\Theta_i = 0$ or $\Theta_f = 0$ (1ST) and in [259] for the Breit-frame $\Theta_i = -\Theta_f$ (Breit).

Since the formulae for the FSEs depend on the values of the LECs they in principle have to be included in the chiral fits to the full Q^2-dependence of the form factor. In turn, this procedure cannot be combined with the model independent computation of $\langle r_\pi^2 \rangle$ from the slope. Since the model independent calculation of $\langle r_\pi^2 \rangle$ and its chiral extrapolation is one of the aims of this thesis a slightly different procedure is used. First an estimate for the FSEs is calculated using the values as used in the study on FSEs in [257], namely the ones from [260]. To become independent of this external input and to be able to compute the LECs from present data an iterative procedure is applied. It starts with the first estimate and determines $\langle r_\pi^2 \rangle$ using only data points for which the FSEs are known (see the discussion in the next section). The new data set for $\langle r_\pi^2 \rangle$ is then used to determine new LECs from a global fit to the data for $\langle r_\pi^2 \rangle$, F_π and m_π in χPT to NNLO as discussed in section 6.3.2. These new LECs are then used to reiterate the whole procedure.

The resulting FSEs are small, as expected, and depend only weakly on the exact value for the LECs. Consequently, there is no noticeable effect already after two or three iterations. The results for the FSEs are tabulated in tables C.4 and C.5 in appendix C.3. Even though these effects are small compared to the current error bars the corrections are applied to the data prior to any subsequent analysis. In the following the data for the form factor is restricted to the two kinematic situations, 1ST and Breit-frame, where the FSEs are known. The corrected results for the form factor for these cases are given in table C.2 in appendix C.2. The Q^2 values that result from these two cases are marked with coloured points in figure 5.5. Note that due to the weak dependence of the FSEs on the LECs they can be used for all fits used for the chiral extrapolations. However, one should keep in mind that the values are strictly correct only for the fits to $\langle r_\pi^2 \rangle$ including the data for F_π and m_π.

6.2.2 Final analysis for the charge radius

Now that the FSEs are known, at least for a subset of the kinematic points, the analysis from section 5.5.3 can be redone to obtain the final set of results for $\langle r_\pi^2 \rangle$. Here it is important to note that the restriction to the kinematic points where either $\Theta_i = 0$ or $\Theta_f = 0$, or $\Theta_i = -\Theta_f$ reduces the available number of points in the low Q^2 region significantly. This is especially true for ensemble F7 where only three data points are left below $(Q_{\text{max}} r_0)^2 = 0.22$ or $Q^2_{\text{max}} = 0.034\ \text{GeV}^2$ (cf. figure 5.5).

Figure 6.2 contains the updated plot from figure 5.9, i.e. the results for $\langle r_\pi^2 \rangle$ from different $(Q_{\text{max}}\, r_0)^2$ and fit functions on the ensemble F6 including correction for FSEs. It is interesting to note that the inclusion of FSEs tends to enhance the discrepancy between linear and the other fits. In the following the results from a second order polynomial with $(Q_{\text{max}}\, r_0)^2 = 0.22$ are used. The second order polynomial is preferable since it yields consistent results over a larger range of value for Q^2_{max} which is useful when the analysis is restricted to the limited set of points for which FSEs are known. Also, the error bars are not much increased in comparison to the linear fit or the VPD fit. The results for $\langle r_\pi^2 \rangle$ are listed

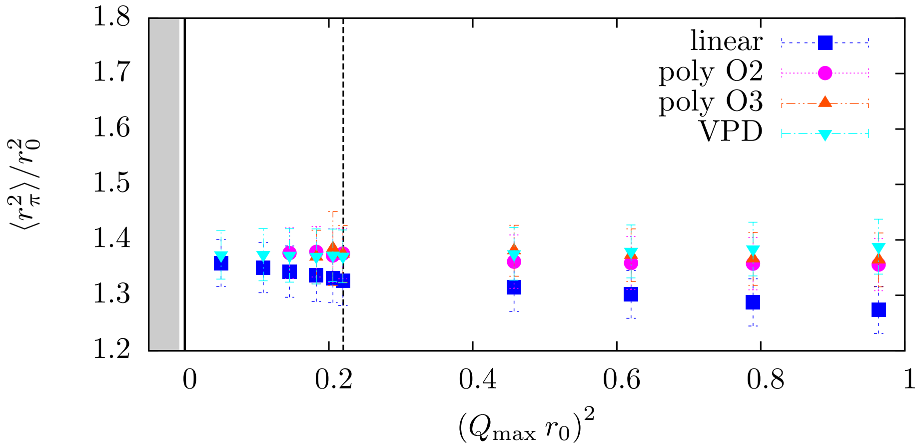

Figure 6.2: Results for $\langle r_\pi^2 \rangle$ obtained from different fit functions including all results for $f_{\pi\pi}(Q^2)$ up to $(Q_{\max}\, r_0)^2$ for ensemble F6 as in figure 5.9. The data is now restricted to the two kinematic schemes discussed in the main text and FSEs are included.

together with the results from the other fits in table 6.2. As can be seen from the table the different fits are in reasonable agreement. An illustration of the pion mass dependence and a comparison to the results from other collaborations is provided in figure 6.3. The data is in good agreement with the measurements from the other collaborations and approaches the experimental point when going to smaller pion masses. The data also indicates possible lattice artefacts which should be included in the chiral extrapolation.

The data suggests that the form factor can be represented very well by a second order polynomial up to values of the momentum transfer which have been probed by the NA7 experiment [45]. For comparison we compute the corresponding value for the fit to this data up to $(Q_{\max} r_0)^2 = 0.22$. For this exercise we ignore the fact that the overall normalisation of the experimental data is unknown and assume $f_{\pi\pi}(0) = 1$. Fitting to the ten experimental data points below $Q^2 = 0.034$ GeV^2 the result is

$$\langle r_\pi^2 \rangle / r_0^2 = 1.98^{+45}_{-41} \quad \left(\text{NA7, } Q^2 \leq 0.034 \text{ GeV}\right) \ . \tag{6.2}$$

Interestingly, this result is significantly larger than the result from the VPD ansatz quoted in [45], of course with a large error attached. This large uncertainty is due to the small number of points with relatively large error bars in the relevant regime.

6.3 Chiral and continuum extrapolations

After the extraction of the charge radius for each ensemble one can eventually examine the chiral extrapolation. The particular form of the extrapolation will depend on the underlying model. Here the systematics stemming from the model dependence is estimated in terms

	$\langle r_\pi^2 \rangle / r_0^2$			
ensemble	linear	VPD	poly O3	poly O2
A3	1.12 (4)	1.13 (4)	1.14 (4)	1.14 (5)
A4	1.16 (6)	1.19 (7)	1.18 (7)	1.18 (7)
A5	1.39 (7)	1.44 (7)	1.49 (8)	1.48 (8)
E4	0.95 (3)	0.96 (3)	0.97 (3)	0.97 (4)
E5	1.17 (5)	1.19 (5)	1.17 (6)	1.17 (6)
F6	1.33 (5)	1.37 (5)	1.37 (6)	1.37 (6)
F7	1.59 (8)	1.64 (9)	—	1.66 (10)
N3	0.89 (3)	0.89 (3)	0.89 (3)	0.89 (4)
N4	1.04 (3)	1.05 (3)	1.01 (4)	1.01 (5)
N5	1.15 (3)	1.16 (3)	1.18 (4)	1.18 (5)

Table 6.2: Results for the charge radius for the different fits as explained in section 5.5.3 with $(Q_{\max} r_0)^2 = 0.22$ including finite size corrections. For the ensemble F7, there are not enough data points below this border to enable a fit to a third order polynomial.

of the spread of results from different ansätzen. Since χPT to NLO did not provide a satisfactory description of the form factor data in the present range of pion masses a logical next step is to try χPT at NNLO. The different types of extrapolations used here are:

- a simultaneous fit to χPT at NNLO for f_π, m_π and $f_{\pi\pi}(Q^2)$,
- a simultaneous fit to χPT at NNLO for f_π, m_π and $\langle r_\pi^2 \rangle$ and
- polynomial fits to $\langle r_\pi^2 \rangle$.

In the latter type of fits $\langle r_\pi^2 \rangle$ is used as determined from the second order polynomial in the last section. The continuum extrapolation is performed by including terms proportional to a^2 in the formulae as listed in eqs. (A.64)–(A.67). In practice, only the leading order term with the coefficient $\alpha_O^{(1)}$ ($O = m,\ f,\ r$) will be used since the data is not sensitive to additional terms. The simultaneous fit to f_π, m_π and $f_{\pi\pi}(Q^2)$ also allows to predict the behaviour of the form factor at the physical pion mass and can be compared to the experimental data directly.

6.3.1 χPT to NNLO for the form factor

The formula for $f_{\pi\pi}(Q^2)$ in χPT to NNLO in its basic form, eq. (A.48) and following, contains five free parameters, the LECs $\bar{\ell}_6$, $\tilde{\ell} = 1/(6\,N)\,(\bar{\ell}_1 - \bar{\ell}_2)$, $\bar{\ell}_4$, r^r_{V1} and r^r_{V2}. The inclusion of the leading order term for lattice artefacts yields another free parameter. The fit to $f_{\pi\pi}(Q^2)$ alone does not constrain the LECs sufficiently, in particular, the LECs $\tilde{\ell}$ and $\bar{\ell}_4$. The later is the LEC which dominantly determines the pion mass dependence of the

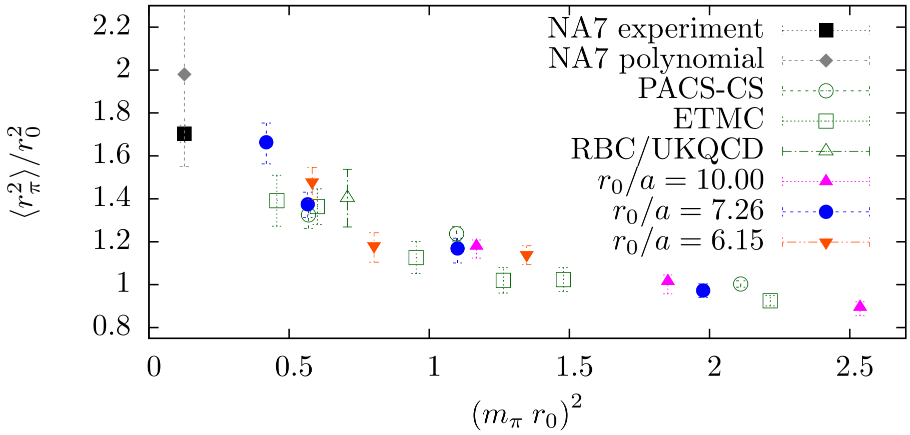

Figure 6.3: Compilation of results for the pion charge radius in dynamical LQCD [51, 52, 228, 229] and as determined from experiment [45]. Most of the lattice data is extracted from a single pole fit except for the data from RBC/UKQCD where the result of a second order polynomial with identical Q^2-cut as in this study is shown. The point denoted by 'NA7 polynomial' is the result from eq. (6.2).

pion decay constant [253–255]. The same formula also includes $\tilde{\ell}$ and a simultaneous fit to the data for F_π can thus be expected to increase the information on these two parameters. Nevertheless, the combination of the two formulae, as discussed in appendix A.6, includes four additional LECs, F, $\bar{\ell}_1$, $\bar{\ell}_3$ and r_f^r where F is the pion decay constant in the chiral limit. While $\bar{\ell}_4$ is mostly related to the chiral extrapolation of F_π, $\bar{\ell}_3$ dominates the dependence of m_π on the average light-quark mass m_{ud} [253–255]. It is thus advantageous to exchange the pion mass dependence for the dependence on m_{ud} and to use the data for the pion mass to further constrain the fits. For m_{ud} one can use the renormalised PCAC quark mass in the SF renormalisation scheme. The particular choice of the scheme for m_{ud} is not important since it exclusively appears in combination with the parameter B (cf. eq. (A.42)). The multiplicative factor associated with a change of the renormalisation scheme thus can be absorbed in B. The full set of equations including the terms modeling the cut-off effects are listed in eqs. (A.64)–(A.67) and have 14 free parameters, the ones listed in table 6.3 and $\tilde{\ell}$ and $\bar{\ell}_1$.

With the current set of data points the 14 fit parameters are again not constrained sufficiently. A possibility to improve the situation is to eliminate some of the LECs that are known from the analysis of experimental data to high accuracy. Here the choice is to eliminate $\bar{\ell}_1$ and $\bar{\ell}_2$ (and thereby $\tilde{\ell}$) by the results obtained from $\pi\pi$-scattering [260]

$$\bar{\ell}_1 = -0.4\,(5) \quad \text{and} \quad \bar{\ell}_2 = 4.3\,(1)\ . \tag{6.3}$$

While the results for the other LECs are sensitive to the particular choice for $\bar{\ell}_1$ and $\bar{\ell}_2$, $\langle r_\pi^2 \rangle$ at the physical point is relatively stable. In fact, the result for the charge radius at

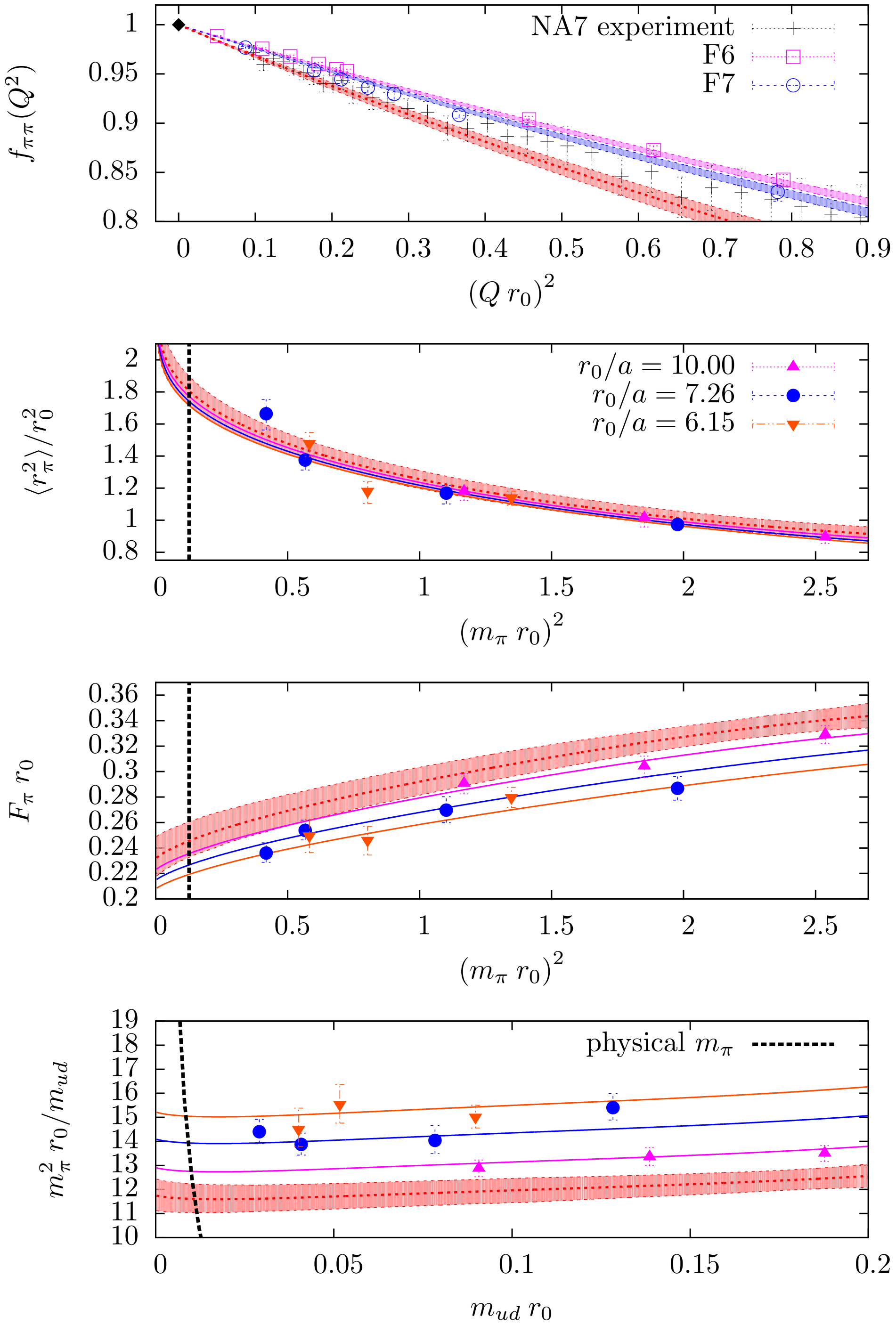

Figure 6.4: Results of the global fit **A** to the data for $f_{\pi\pi}(Q^2)$, F_π and m_π to χPT at NNLO. Shown are the chiral extrapolations for $f_{\pi\pi}(Q^2)$, $\langle r_\pi^2 \rangle$, F_π and m_π (from top to bottom). The plot for $f_{\pi\pi}(Q^2)$ includes the data points from the NA7 experiment [45] and the two lightest ensembles for comparison.

Fit	**T**	**Tc**	**A**	**Ac**	**B**	**Bc**
B	5.9 (4)	6.1 (5)	5.9 (4)	6.1 (4)	5.9 (4)	6.1 (5)
F	0.228 (14)	0.215 (17)	0.232 (17)	0.214 (23)	0.225 (12)	0.213 (15)
$\bar{\ell}_6$	—	—	17.1 (18)	15.3 (22)	16.7 (13)	15.5 (15)
$\bar{\ell}_4$	4.1 (6)	5.3 (7)	4.1 (6)	5.4 (9)	4.2 (6)	5.4 (8)
$\bar{\ell}_3$	2.3 (12)	4.1 (13)	2.2 (12)	4.1 (14)	2.3 (11)	4.1 (13)
- r^r_{V1} 10^4	—	—	1.3 (4)	0.9 (4)	1.2 (3)	1.0 (3)
r^r_{V2} 10^4	—	—	0.7 (3)	0.6 (3)	—	—
r^r_m 10^4	-0.7 (8)	1.2 (11)	-0.8 (8)	1.2 (14)	-0.7 (8)	1.2 (11)
- r^r_f 10^4	0.6 (9)	1.8 (13)	0.7 (10)	1.9 (14)	-0.5 (9)	1.9 (13)
- $\alpha^{(1)}_r$	—	—	5 (3)	5 (3)	6 (4)	5 (3)
- $\alpha^{(1)}_m$	5 (1)	5 (1)	5 (1)	5 (1)	5 (1)	5 (1)
- $\alpha^{(1)}_f$	0.8 (5)	0.9 (6)	0.9 (6)	0.9 (6)	0.7 (5)	0.8 (6)
χ^2/dof	1.6	1.3	1.1	1.1	1.4	1.3

Table 6.3: Results for the LECs from the fits using χPT to NNLO. The fit labels are explained in the text.

the physical point do not change significantly even if $\bar{\ell}_1$ and $\bar{\ell}_2$ are varied by a factor 2.

The results for the fit, denoted as χPT-NNLO fit '**A**', to the data for $f_{\pi\pi}(Q^2)$, F_π and m_π from all ensembles with fixed values for $\bar{\ell}_1$ and $\bar{\ell}_2$ and including lattice artefacts and FSEs are shown in figure 6.4. The resulting LECs and other fit-parameters are summarised in table 6.3. In the figures the χPT curves for $\langle r_\pi^2 \rangle$ and F_π are plotted versus the pion mass as defined through the NNLO formula, while the data points are plotted with their measured value for m_π. This form of the presentation enables comparisons with the polynomial fits that are done with respect to m_π and not m_{ud}. As can be seen from the plots, the data is well described by the fit and produces a reasonable χ^2/dof as listed in table 6.3. The fit also yields results for $\langle r_\pi^2 \rangle$, F_π and m_{ud} at the physical point. These are listed in tables 6.5 and 6.6 in section 6.4. The fits also demonstrate the possible presence of residual lattice artefacts, especially for F_π and m_π, and underline the importance of including cut-off terms in the chiral extrapolation.

The results for the LECs $\bar{\ell}_3$ and $\bar{\ell}_4$ and the impact of the inclusion of F_π and m_π in the chiral extrapolation can be checked by comparing with the results for a similar fit only to the data for F_π and m_π, i.e. χPT to NNLO with $\bar{\ell}_1$ and $\bar{\ell}_2$ fixed and including lattice artefacts. The results for the fit, labeled as χPT-NNLO fit '**T**', are listed in table 6.3, too. The LECs in both fits agree well and the absence of an increase in the error bars for the LECs obtained in fit **T** indicates that the data for F_π and m_π indeed stabilises the fits and dominates the results for $\bar{\ell}_3$ and $\bar{\ell}_4$ in the combined fits.

To probe the pion mass range in which χPT is applicable and to check for associated systematics one is interested in applying mass cuts to the fits and to compare the results. Another reason for such a study is that the statistical uncertainty of the result increases when going to smaller quark masses. This is due to the fact that fluctuations increase and the computations are becoming more expensive so that less statistic is available. It leads to the effect that data points from ensembles with heavier quark masses naturally obtain a larger weight in the fit even though they are *per se* less important for the chiral extrapolation. Thus a precise study of the sensitivity of the fit to the data points at heavier pion masses is a crucial step towards a reliable estimate of systematics concerning the chiral fits. With the current set of ensembles the NNLO fits are only stable when almost all ensembles at hand are included. The only cut which still leads to a stable result is a cut at $m_\pi = 600$ MeV, i.e. a fit including the data from all ensembles except for ensemble N3. This cut is rather high and one is eventually interested to push it towards smaller pion masses. The associated fit is denoted by '**Ac**' and the resulting fit parameters are listed in table 6.3, too. While most of the LECs are not affected by the cut there is a tendency for $\bar{\ell}_3$ and $\bar{\ell}_4$ towards larger values and $\bar{\ell}_6$ shows a decrease. Comparing the results for the LECs to the ones of a fit to χPT to NNLO to the data for F_π and m_π only, fit '**Tc**', shows again the good agreement and a similar trend in the fits between the fits **T** and **Tc**.

6.3.2 χPT to NNLO for the charge radius

To reduce the impact of the functional form assumed for the Q^2-dependence (in the fits above the dependence implied by χPT) in the analysis it is possible to fit the data for $\langle r_\pi^2\rangle$ as obtained in the last section to the functional form given by χPT to NNLO, eq. (A.61). In this way the charge radius is extracted model-independently and the only assumptions left concern the chiral extrapolation. Again it is advantageous to include the data for F_π and m_π in the chiral extrapolation to constrain $\bar{\ell}_4$. The resulting formulae have 11 free parameters when $\bar{\ell}_1$ and $\bar{\ell}_2$ are fixed according to eq. (6.3). The reduction from the form factor to the charge radius saves one parameter but leads to a massive reduction in terms of the number of data points. Anyhow, the strategy might still be advantageous since the data in the low Q^2 region mostly constrain the linear term, i.e. the LECs that are related to the chiral extrapolation of the charge radius. One might thus expect not to suffer too much in terms of information.

The results for this fit, denoted as χPT-NNLO fit '**B**', are illustrated in figure 6.5 and the resulting LECs are listed in table 6.3. As can be seen from the plot the fit describes the data equally well as the fit to the full Q^2-dependence of the form factor and yields compatible results. Also the error bars for the LECs are not larger compared to fit **A** which is in agreement with the expectations that the higher orders in Q^2 are not well constrained by the data. Similar to the fit for the form factor also fits to the charge radius produce stable results only when all ensembles are included with or without a cut at $m_\pi = 600$ MeV. The fit including the cut is denoted as '**Bc**' and the resulting LECs are listed in table 6.3, too. As before for the fit to the form factor there is a tendency for $\bar{\ell}_3$ and $\bar{\ell}_4$ to increase while $\bar{\ell}_6$ decreases when going to a smaller pion mass range. In fact, both sets of LECs agree well for the fits with a cut at $m_\pi = 600$ MeV and the trend for the LECs implies a sensitivity on the cut in m_π.

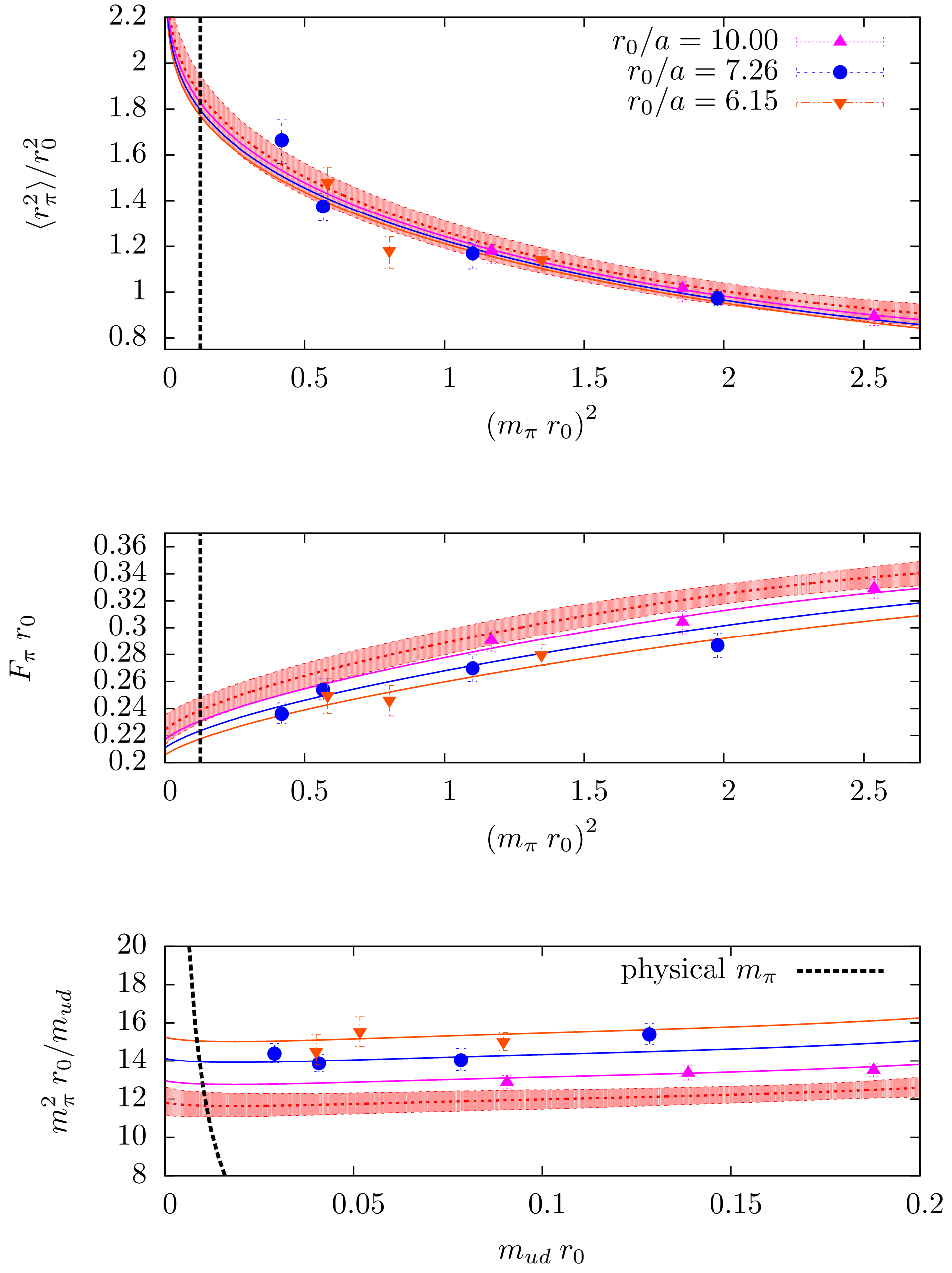

Figure 6.5: Results from the global fit **B** to the data of $\langle r_\pi^2 \rangle$, F_π and m_π (from top to bottom).

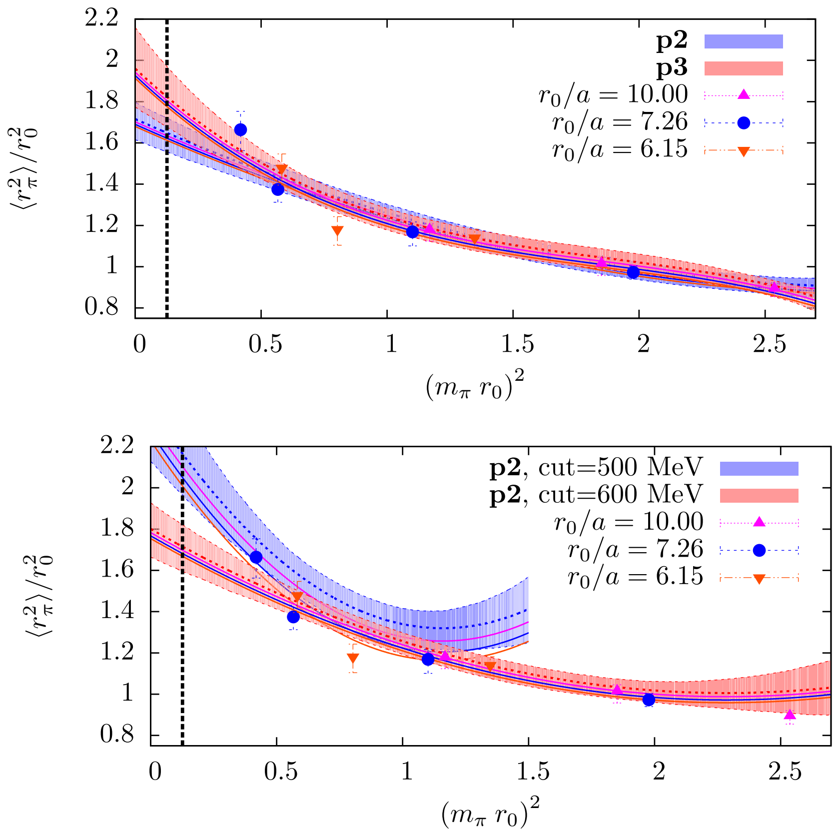

Figure 6.6: Results for the polynomial fits, eq. (6.4), to order two, '**p2**', and three, '**p3**', to all ensembles (top) and with cuts in the range of pion masses (bottom) at $m_\pi = 600$ and 500 MeV for **p2**.

6.3.3 Polynomial extrapolations for the charge radius

To reduce the model dependence even further and to be able to estimate the systematic effect stemming from the use of χPT for the chiral extrapolation, with a range of pion masses where its applicability is uncertain, one should look at a simple ansatz and compare the results with the ones obtained earlier. The simplest functional form for the extrapolation are polynomials to a given order in the squared pion mass [1]. Including cut-off effects, as shown to be mandatory earlier, these polynomials obey the general form

$$\left\langle r_\pi^2 \right\rangle (m_\pi) = \left\langle r_\pi^2 \right\rangle (0) + b_a\, (a/r_0)^2 + \sum_{n=1} b_n\, m_\pi^{2n} \,. \tag{6.4}$$

Note that in contrast to a fit based on χPT there are no symmetries relating the expansion parameters of the different observables in a simple polynomial ansatz. Hence, a global fit to

---

[1] Note that the squared pion mass is proportional to the quark mass which rules out odd powers of m_π in the approach to the chiral limit.

Fit	$\langle r_\pi^2 \rangle$ (0)	b_a	b_1	b_2	b_3	χ^2/dof
p2	1.72 (10)	-1.4 (26)	-0.55 (10)	0.09 (3)	—	1.4
p2$_{c600}$	1.80 (14)	-1.8 (27)	-0.69 (20)	0.15 (8)	—	1.5
p2$_{c500}$	2.25 (28)	-2.8 (36)	-1.81 (58)	0.77 (32)	—	1.0
p3	1.96 (20)	-1.8 (27)	-1.16 (42)	0.53 (29)	-0.09 (6)	1.3
p3$_{c600}$	2.55 (33)	-0.6 (28)	-3.1 (10)	2.37 (90)	-0.60 (24)	0.6

Table 6.4: Resulting parameters for the chiral extrapolation of $\langle r_\pi^2 \rangle$ using polynomials of the form indicated in eq. (6.4) with different mass cuts for the pion mass in MeV indicated by the subscript '$c\{X\}$'.

$\langle r_\pi^2 \rangle$, F_π and m_π makes little sense and only the chiral extrapolation of $\langle r_\pi^2 \rangle$ is considered here.

The simplest polynomial is a linear function, i.e. a polynomial of order one. When looking at the full range of pion masses, the data shows a significant non-linear behaviour and one would not expect the data to be described accurately by a linear ansatz. A linear fit only to the lightest points is also not desirable as it would be dominated by possible small fluctuations in the data. To obtain a reliable extrapolation it is necessary to go to higher order polynomials, namely to second ('**p2**'), and third ('**p3**') order polynomials. The latter is a good crosscheck for higher order terms in the second order polynomial, but one would expect to obtain larger error bars since the data does not indicate strong effects beyond the second order in m_π^2. The results from these two types of fits are shown in comparison in figure 6.6 (top) and the resulting fit parameters are listed in table 6.4. As can be seen from the plot, the behaviour of both polynomials agrees well with the data points and indeed higher orders do not seem to be dominant for this mass range. At the physical point however they yield slightly different results. This could be due to missing terms with chiral logarithms which are present on top of the second order polynomial in m_π^2 in the case of χPT. The effects of these terms might be captured to some extend by the m_π^6 term in the third order polynomial, leading to the stronger upward trend close to the physical point. Anyhow, it is not clear whether this effect is an effect of higher order terms or logarithms rather than an effect of a possible upwards fluctuation of the data point of the F7 ensemble.

As for the chiral extrapolation via χPT it is desirable to check the impact of the ensembles at heavier pion masses on the extrapolation. To this end similar fits with mass cuts at $m_\pi = 600$ and 500 MeV have been performed. For the second order polynomial a comparison of these two cases is shown in figure 6.6 (bottom) and the resulting fit parameters are also listed in table 6.4. While the fit with a mass cut at $m_\pi = 600$ MeV provides an accurate description for most of the data points the fit with a cut at $m_\pi = 500$ MeV shows a strong curvature from a large second order term. In the latter, one can expect a strong influence of the ensembles A4 and F7 due to the small number of points in the fit. The results from these two ensembles seem to be a bit lower/higher then what one might naively expect from the position of the other data points at similar lattice spacing.

The associated fluctuations have a strong influence on the fit results. The impact of the cut at $m_\pi = 600$ MeV is not significant for the second order polynomial but has a stronger impact on the fit with a third order polynomial. This can be expected since the third order polynomial has one additional parameter that has to be fixed which again allows for stronger impact of single ensembles and associated fluctuations. Since the fits $\mathbf{p2}_{c500}$ and $\mathbf{p3}_{c600}$ cannot be regarded to provide reliable results they are discarded from the further analysis. However, they serve as indicators that a model independent chiral extrapolation is difficult and sensitive to small fluctuations in the data, that not necessarily have to display physical effects.

To get an idea of the impact of chiral logarithms these can in principle be included by extending the polynomial to the functional form

$$\langle r_\pi^2 \rangle (m_\pi, \mu) = \langle r_\pi^2 \rangle (0) + c_0 \ln \left(\frac{m_\pi^2}{\mu^2} \right) + b_a \, (a/r_0)^2 + \sum_{n=1} b_n \, m_\pi^{2n} \left[1 + c_n \ln \left(\frac{m_\pi^2}{\mu^2} \right) \right] . \quad (6.5)$$

Here μ plays a similar role as the renormalisation scale in χPT and ideally should be fixed to a similar value to enable direct comparisons. While this form is of course not the most general possibility for the inclusion of logarithmic terms it should capture the main effects. Unfortunately, since the first logarithm already appears in the constant term, even an extrapolation at the first nontrivial order using eq. (6.5) involves two logarithms (as does the χPT formula). This hampers the stabilisation of the fit since the coefficients of the logarithms are not constrained by symmetry. A direct comparison of χPT with a general functional form including logarithms thus strongly depends on the fine tuning between the two coefficients and appears to be difficult without pion masses that are very close to the physical point.

6.4 Discussion and final results

To come to the conclusions it is time to compare the results from different fits to get an idea for the internal consistency and the systematic error connected to the chiral extrapolation. Furthermore, it is interesting to see how the results compare to the experimental ones.

6.4.1 Best estimates and fit comparison

To sum up, the different fits in χPT are mutually consistent. Nevertheless, the LECs show a dependence on the applied cut. From the conceptual point of view the results obtained with the mass cut at $m_\pi = 600$ MeV are more trustworthy then the ones including all data points. It is difficult to compare the parameters directly to the results from the polynomial fits since the χPT formulae include logarithmic terms in the expansion of $\langle r_\pi^2 \rangle$ in both, constant and linear terms. A meaningful comparison can only be made for the term encoding cut-off effects, i.e. for the parameters $\alpha_r^{(1)}$ and b_a, and the charge radius at the physical pion mass and in the continuum. As can be seen from the data in tables 6.3 and 6.4 the coefficient in the term modeling cut-off effects has the same sign and is of the same order of magnitude. Nevertheless, it tends to be bigger for the fits to χPT. The only exceptions are the linear fit and the third order polynomial with a mass cut at $m_\pi = 600$

	ref	N_f	χ-PT	$\langle r_\pi^2\rangle\|_{\text{phys}}/r_0^2$
this study		2	NNLO: **B**	1.86 $\left(^{+\ 9}_{-10}\right)$
			NNLO: **Bc**	1.91 $\left(^{+10}_{-10}\right)$
			NNLO: **A**	1.81 $\left(^{+\ 9}_{-\ 9}\right)$
			NNLO: **Ac**	1.87 $\left(^{+12}_{-10}\right)$
			p2	1.65 $\left(^{+\ 7}_{-10}\right)$
			$\mathbf{p2}_{c600}$	1.72 $\left(^{+11}_{-13}\right)$
			p3	1.82 $\left(^{+15}_{-15}\right)$
			NLO: $\bar{\ell}_6$	1.70 $\left(^{+\ 7}_{-\ 9}\right)$
QCDSF	[225]	2	—	1.74 (8)
ETMC	[228]	2	NNLO	1.80 (16)
JLQCD/TWQCD	[227]	2	NNLO	1.62 (18)
RBC/UKQCD	[51, 52]	2+1	NLO	1.65 (13)
Nguyen et al.	[229]	2+1	NNLO	1.74 (19)
NA7 experiment	[45]	—	—	1.70 (4)
Fit eq. (6.2)		—	—	1.98 $\left(^{+45}_{-41}\right)$
BCT	[43]	—	NNLO	1.73 (7)

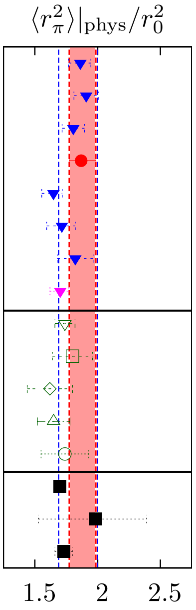

Table 6.5: Results for the charge radius of the pion at the physical point from the fits performed in this study, experiment [45], χPT to NNLO for the experimental data [43] and other LQCD calculations [51, 52, 225, 227–229]. The labels for the fits are explained in the text of the previous section. The figure on the right hand side illustrates the agreement of the results for $\langle r_\pi^2\rangle$. The red band is the statistical error bar for the best estimate and the blue lines indicate statistical and systematic uncertainties added in quadrature.

MeV. As discussed in the last section both are sensitive to possible statistical fluctuations in the small pion mass regime and cannot be trusted.

The data for the charge radius at the physical point is listed in table 6.5 and its consistency displayed on the scatter plot on the right hand side of the table. The fit denoted by 'NLO: $\bar{\ell}_6$' is the result obtained from the chiral extrapolation of $\bar{\ell}_6$ from section 6.1. As can be seen from the plot all fits are mainly consistent even though the results scatter a bit. Looking at the systematics one can identify the χPT fit **Ac** as the best estimate for the charge radius at the physical point. The reason for this is that this fit includes the full information of the data on the LECs that define the chiral extrapolation of three different quantities. This stabilises the fit and ensures that statistical fluctuations do not play a significant rôle. Furthermore, the fit describes the lattice data well, as shown in figure 6.7, and especially captures the Q^2-dependence well in the regime of low Q^2, as can be seen from the comparison of the model independent results for the charge radius. It also captures the behaviour of the experimental points for $f_{\pi\pi}(Q^2)$ in the relevant regime of small Q^2-values. Furthermore, it is consistent with most of the other chiral extrapolations

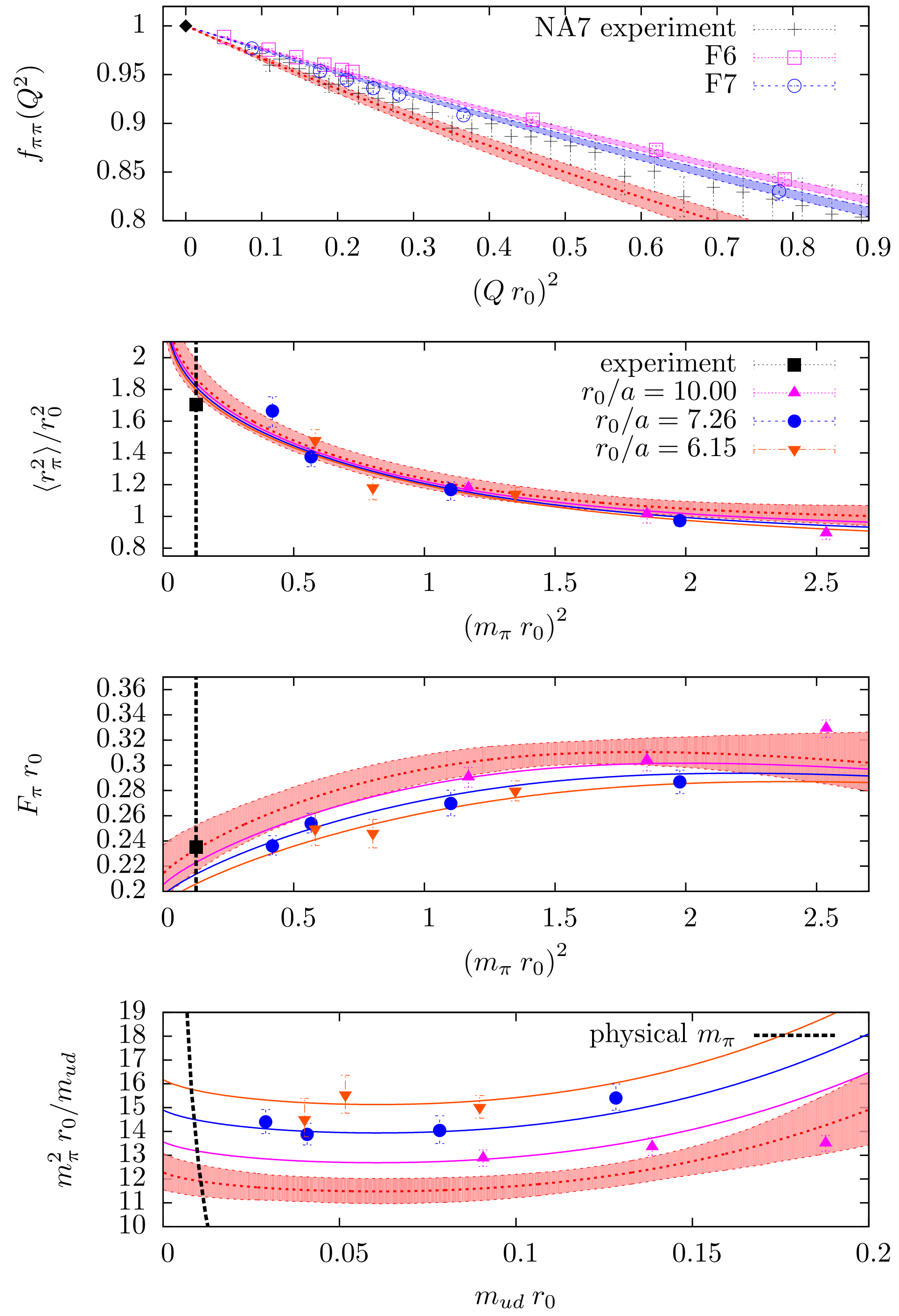

Figure 6.7: Results from the global fit **Ac** to the data of $f_{\pi\pi}(Q^2)$, F_π and m_π to χPT at NNLO. Shown are the chiral extrapolations for $f_{\pi\pi}(Q^2)$, $\langle r_\pi^2\rangle$, F_π and m_π (from top to bottom). The plots also include the data points from the NA7 experiment [45] for $f_{\pi\pi}(Q^2)$ and $\langle r_\pi^2\rangle$ and the experimental value for F_π quoted in [76].

and includes the effect from reducing the range of pion masses to the ones below $m_\pi = 600$ MeV. The best estimate for the charge radius at the physical point is thus given by

$$\left\langle r_\pi^2 \right\rangle^{\rm phys} / r_0^2 = 1.87 \, \left({}^{+12}_{-10}\right) \left({}^{+\,4}_{-15}\right) \quad \text{or} \quad \left\langle r_\pi^2 \right\rangle^{\rm phys} = 0.473 \, \left({}^{+30}_{-26}\right) \left({}^{+10}_{-38}\right) (10) \ \text{fm} \, . \tag{6.6}$$

The second error is systematic and has been estimated from the spread of the different fits excluding the fits **p2** and 'NLO: $\bar{\ell}_6$'. The latter does not include finite size effects and thus does not contain all systematic effects. The third error for the result for $\left\langle r_\pi^2 \right\rangle$ in physical units is the systematic error due to scale setting. **p2** shows a large deviation from the other fits which is most likely due to the strong influence of ensemble N3 which has a small error bar at rather large pion mass. The final result is shown as the red band in the scatter plot in table 6.5 and the error bars including also the systematic uncertainties added in quadrature are indicated by the additional blue dashed lines. Note, that some information about the magnitude of the systematic effect stemming from the range of pion masses included in the fit can be obtained by looking at the differences between the fits **A** and **Ac** and **B** and **Bc** respectively. The effect tends to be notable and is included in the systematic error bars quoted in eq. (6.6).

So far the comparison to the experimental values and other results from LQCD has been deliberately avoided in the discussions and plots in order to permit an unbiased scrutinisation of the different fits. At this point however a comparison seems adequate. To this end the data for the charge radius from experiment [45] and other LQCD calculations [51, 52, 225, 227–229] are listed in table 6.5, too, and are also shown in the scatter plot. Also listed is the value obtained by the polynomial fit to the experimental data from section 6.2.2 and an analysis of the experimental data using χPT to NNLO from [43]. Note, that the data is given in units of r_0 and that the estimate $r_0 = 0.503\,(10)$ fm from [77] has been used to rescale the experimental data and the data from other LQCD calculations. The error on r_0 in physical units was not taken into account in this process. As can be seen from the table and the scatter plot, the extrapolations are mainly compatible with the experimental result and the result from χPT at the physical point, albeit with a much larger statistical error. The data of the present study has the tendency to lie above the results from experiment and other collaborations, even though not significantly given the size of the statistical error bars. The cause of this systematic trend (if it is a true trend) is difficult to identify. It might be an effect of the large number of data points in the low Q^2-region which are not present for all the other calculations. In fact, the charge radius as obtained from the present study shows a curvature in the low Q^2-region which is compatible with the experimental results. This is also reflected in the result from the polynomial fit to the experimental data below $(Q\, r_0)^2 = 0.22$, which yields a much larger value for $\left\langle r_\pi^2 \right\rangle$ even though with a very large error attached. On the other hand the tendency to lie above the other data points might simply be due to statistical fluctuations and/or data points at a large pion mass at which χPT to NNLO is no longer the correct description of the data. In addition, the comparison is difficult, because the results depend on the particular procedure for the chiral extrapolation, indicated by the spread of results from the different extrapolations in table 6.5, and not all other studies have used χPT to NNLO. However, for the present analysis χPT describes the data well even for this relatively large range of pion masses which strengthens the confidence in the chiral extrapolation. Furthermore, the polynomial fits are also in reasonable agreement with the χPT results, even though they tend to yield somewhat smaller results for the form factor at the physical point.

As a byproduct of the chiral extrapolation of the charge radius one obtains estimates for the pion decay constant in the chiral limit F, the decay constant at the physical point F_π^{phys} and the average light quark mass at the physical point m_{ud}^{phys}. Furthermore, one might extract the phenomenologically interesting quantities F_π/F, where F_π is the experimental value for the decay constant (see eq. (1.20)), and the quark condensate in the chiral limit $\langle\bar{\psi}\psi\rangle$ which is related to the LEC B via

$$\langle\bar{\psi}\psi\rangle = F^2\,B\,. \tag{6.7}$$

Equation (6.7) follows from the well known Gell-Mann-Oakes-Renner (GMOR) relation (see [112]). Even though the extraction of these quantities is not the main goal of this study it is still interesting to obtain predictions for them and see how they compare to the results from other studies and experiment. The results for these quantities from the different fits are listed in table 6.6. Note, that the light quark mass and the chiral condensate depend on the renormalisation scheme. For the results in table 6.6 the $\overline{\text{MS}}$-scheme was used at a renormalisation scale of 2 GeV. The conversion factor between the $\overline{\text{MS}}$-scheme and the SF-scheme used for m_{ud} and $\langle\bar{\psi}\psi\rangle$ is given in eq. (2.49). Note that in table 6.6 the results for the third root of $\langle\bar{\psi}\psi\rangle$ are listed as this is convention in the literature. The table also includes results from experiment and global estimates from lattice simulations as obtained in the FLAG review [29] for these quantities if available. As can be seen from the table all results agree well with each other. The best estimate is again taken from fit **Ac** and is listed in the column labeled with ‘BE’ including an estimate for the systematical uncertainty. The systematic error is estimated from the spread of the data in the different fits. It is important to note that there is still some uncertainty due to the pion mass range included in the fit. Until a more elaborate study of the effect of going to lighter pion masses is available one might suspect that the systematic error is possibly underestimated. The results from our fits agree very well with the results from FLAG and experiment.

In addition to the quantities mentioned above, it is also useful to compare the NLO LECs directly to the ones obtained in other studies. This gives an idea of the consistency of the approach to the chiral limit within the lattice community. The only LECs for which such a comparison is meaningful at the moment are $\bar{\ell}_3$, $\bar{\ell}_4$ and $\bar{\ell}_6$ since these are the ones that can be obtained with sufficient accuracy. The FLAG working group at the moment only provides a global average for $\bar{\ell}_3$ which is given by [29]

$$\bar{\ell}_3 = 3.2\,(8)\,. \tag{6.8}$$

Comparing to the results listed in table 6.3 the values are in agreement within the relatively large error bars. For $\bar{\ell}_4$ other collaborations typically find values between $\bar{\ell}_4 = 3.8$ to 4.7 that are also consistent with the findings of the present study, even though there seems to be a tendency towards larger values when the pion mass range is decreased. $\bar{\ell}_6$ has the largest uncertainty since there are not so many measurements available. The typical values are in the range $\bar{\ell}_6 = 12$ to 15 in lattice simulations, while a non-lattice estimate yields

source	$F_\pi^{\rm phys}$ [MeV]	$m_{ud}^{\rm phys}$ [MeV]	$\langle\bar\psi\psi\rangle^{1/3}$ MeV	F_π/F
B	$94\ \binom{+5}{-5}$	$3.9\ \binom{+3}{-3}$	$270\ \binom{+20}{-16}$	$1.05\ \binom{+7}{-6}$
Bc	$91\ \binom{+5}{-6}$	$3.8\ \binom{+3}{-3}$	$263\ \binom{+19}{-16}$	$1.11\ \binom{+9}{-8}$
A	$96\ \binom{+7}{-6}$	$3.9\ \binom{+3}{-3}$	$276\ \binom{+19}{-18}$	$1.01\ \binom{+8}{-8}$
Ac	$92\ \binom{+9}{-8}$	$3.8\ \binom{+3}{-3}$	$265\ \binom{+21}{-18}$	$1.10\ \binom{+13}{-12}$
BE	$92\ \binom{+9}{-8}\ \binom{+4}{-1}$	$3.8\ \binom{+3}{-3}\ \binom{+1}{-0}$	$265\ \binom{+21}{-18}\ \binom{+11}{-2}$	$1.10\ \binom{+13}{-12}\ \binom{+1}{-9}$
FLAG [29]		3.6 (1)(2)	269 (18)	1.073 (15)
other	92.21 (3)(15) [76]			1.072 (6) [256]

Table 6.6: Results for $F_\pi^{\rm phys}$, $m_{ud}^{\rm phys}$, $\langle\bar\psi\psi\rangle$ and F_π/F from the χPT fits to the data of the current study. The light quark mass and the quark condensate are given in the $\overline{\rm MS}$-scheme at a renormalisation scale of $\mu_R = 2$ GeV. Also listed are lattice averages for the $N_f = 2$ theory as collected in the FLAG review [29] and non-lattice estimates, indicated as 'others', where available. The values labeled 'BE' are the best estimates of the current study, i.e. the result from fit **Ac**, and include an estimate for the systematic error.

$\bar\ell_6 = 16.0\,(5)(7)$ [43]. Looking at table 6.3, the results of the present study tend to be larger than 15, albeit with a large error of about 10-15 %. This appears to be more in agreement with the phenomenological results rather then the ones from LQCD. However, there is a tendency towards smaller values for $\bar\ell_6$ when the pion mass range is decreased. Altogether, the results for the LECs seem to be in rather good agreement with other results from LQCD and phenomenology. Nevertheless, the current accuracy does not allow for any fully conclusive statement. Note also that $\bar\ell_1$ and $\bar\ell_2$ where fixed to the values from $\pi\pi$-scattering, eq. (6.3), to stabilise the fits and the final values for the NLO LECs will also depend on the particular choice for these. This introduces a further uncertainty.

6.4.2 Discussion and perspectives

This part of the thesis contains the details of a comprehensive study of the pion electromagnetic iso-vector form factor. In particular, the charge radius of the pion has been extracted from the data in a model-independent way, made possible by the large number of precise data points in the region of low momentum transfer. The main systematic effects such as excited state contaminations and $\mathcal{O}(a)$-lattice artefacts have been discussed extensively and are under control. Finite size effects are included using χPT and subtracted prior to the extraction of the charge radius. In practice, finite size effects are small which confirms the expectations since $m_\pi L \geq 4$ for all ensembles. The chiral extrapolation of the data to the physical point has been carried out using χPT for the form factor and the charge radius. The results for the latter are also compared to polynomial extrapolations, allowing for estimating systematic effects connected to the particular ansatz. The chiral extrapolation is combined with a continuum extrapolation by including terms modeling lattice artefacts of $\mathcal{O}(a^2)$. These turn out to be significant and a meaningful combination of our data from different lattice spacings can only be achieved if lattice artefacts are included in

ens.	$T \times L^3$	β	κ_{sea}	m_π [MeV]	$m_\pi L$
B6	96×48^3	5.2	0.13597	∼200-250	∼4.0
G8	128×64^3	5.3	0.13642	∼190	4.1
N6	96×48^3	5.5	0.13667	∼330	4.0
O7	128×64^3	5.5	0.13671	∼260	4.2

Table 6.7: Additional ensembles available within CLS at smaller pion masses [248].

the fits.

Summing up the results from the chiral extrapolations, the current data seems to be well described by χPT to NNLO in the mass range considered but slight differences appear when the pion mass range is decreased. The present results from the chiral extrapolations are in good agreement with the results from experiment, phenomenology and other LQCD calculations as discussed in the previous section. The results for the charge radius at the physical point tend to be a bit larger than the estimates from other groups. However, the current data set does not allow for a good control of the systematic uncertainty associated with the pion mass range included in the chiral extrapolation. The results from polynomial extrapolations agree with the χPT values but show a trend towards smaller values for $\langle r_\pi^2 \rangle$ for polynomials of lower order without a mass cut (see fit **p2**).

In conclusion, the chiral extrapolation, even though consistent with the findings of other groups, remains the biggest concern regarding systematic effects. The main problem with the chiral fits is the large number of free parameters, rendering the stabilisation of the fit challenging, as was also found in previous studies [228, 229]. The main problem is the lack of data points in the regime of small pion masses. While one might improve the stability with including data points at smaller pion masses, it appears that only very precise measurements with a large number of points close to the physical point have the potential to reliably extract the LECs with high precision. The situation looks better for physical quantities like the charge radius and the quantities listed in table 6.6. They seem to be rather stable under changes in the mass range, as can be seen from the relatively small systematic errors attached. Whether this remains true when lighter ensembles are added to the data is to be seen.

Concerning perspectives, there are still ensembles with lighter dynamical quarks at each lattice spacing within CLS, going down to pion masses of 190 MeV. The parameters are listed in table 6.7. The measurement of the form factor on these ensembles will clearly improve the control over the chiral extrapolation. A milestone would be the measurement of the form factor with the present accuracy at the physical point. Since lattice simulations are enclosing on physical quark masses this might become possible in the near future. The combination of the tools applied in this thesis for the measurement and the analysis of the form factor will then allow for a first calculation of the charge radius which is potentially free of any model dependence. This of course demands a similar or even better control of systematic effects as reached in the present analysis which appears to need a tremendous computational effort even with todays powerful algorithms.

PART IV: Non-Zero Temperature

7 The QCD phase diagram and lattice QCD

Under extreme conditions such as high temperatures and/or large densities hadrons start to 'melt' and quarks and gluons become deconfined and move freely in a new plasma-like state of matter. Since QCD remains strongly coupled up to temperatures above the conjectured transition temperature the plasma and the phase transition can only be studied within a non-perturbative setup and once again numerical simulations of LQCD are the preferred tool for probing the transition. The purpose of this chapter is to introduce the fundamental concepts to address the transition in numerical simulations and to provide an overview of the current understanding of the phase diagram with a special emphasis on the properties of the transition in the chiral limit of two-flavour QCD. Of particular relevance in this context is universal scaling, discussed in section 7.5, as it provides the framework to address the question of the order of the transition in the chiral limit. Valuable information can also be extracted from the strength of the anomalous breaking of the $U_A(1)$-symmetry at the transition point in the chiral limit. $U_A(1)$-symmetry can be probed using mesonic correlation functions and the associated screening masses, discussed in section 7.4.

7.1 Critical phenomena and universality

QCD at non-zero temperature in equilibrium is described in the framework of equilibrium statistics in the grand canonical ensemble and is characterised by its macroscopic properties like temperature T, pressure P and volume V. When changing from one state to another the system passes through a phase of rapid change, known as phase transition. This section serves to introduce the basic concepts of critical phenomena in the vicinity of phase transitions with focus on the parts needed for the understanding of the transition from hadronic matter to the QGP. The discussion is mainly based on the textbooks by *Schwabl* [261] and *Itzykson* and *Drouffe* [262]. For further reading on the numerical and theoretical approach to phase transitions in the different universality classes as well as for numerical results for universal parameters see the review by *Pelissetto* and *Vicari* [263].

The rapid change of the thermodynamic properties of the medium in the course of the transition are characterised by non-analyticities in the derivatives of the thermodynamic potential. Phase transitions are identified to be first order if non-analyticities appear in at least one of the first derivatives of the potential and of second order if all of the first derivatives are analytic. If all higher derivatives are analytic as well the system changes its state smoothly in a broader range and no true transition exists. Such a change of phase is denoted as 'crossover'.

Each true phase transition is accompanied by the spontaneous breaking of an associated symmetry, signaled by the appearance of a non-zero value for the order parameter Θ. In the following the discussion will focus on the grand canonical ensemble and the related free energy F (cf. eq. (1.32)). In the presence of an external field h that breaks the symmetry explicitly the order parameter and its susceptibility χ_Θ are defined as

$$\Theta = -\left(\frac{\partial F}{\partial h}\right)_{T,V} \quad \text{and} \quad \chi_\Theta = \left(\frac{\partial \Theta}{\partial h}\right)_{T,V} , \tag{7.1}$$

where the subscript T, V indicates that the derivative is to be taken at constant temperature and volume. At the transition point the rapid change of the order parameter to a non-zero value is expected to be accompanied by a divergence of its susceptibility for a first order phase transition, or by a significant peak in the case of a second order transition. As a consequence, the order parameter and its susceptibility are ideal tools to determine the transition point. In the case of a crossover there is no order parameter, as there is, in general, no symmetry whose breaking can be related to the transition. Nevertheless, it can be expected that the change of the phase is accompanied by a rapid change for thermodynamic quantities which can be identified as approximate order parameters. The rapid change should then be accompanied by a noticeable change and peak-like structure in the susceptibility, enabling the detection of the crossover region. However, the transition will occur in a broad region so that there is no unique definition for a transition temperature and the estimates for the crossover region obtained from different quantities can differ.

Since the transition is a global effect it has to be accompanied by long range correlations that signal all parts of the system to change from one phase to the other. Thus for a transition of second order the correlation length ξ has to diverge. A similar effect should be present in the case of a first order transition and a crossover where the system internally starts to communicate increasingly between different geometrical regions. This increase in long range correlations implies that the generalised susceptibilities

$$\bar{\chi}(O) \equiv V\ \left[\left\langle O^2\right\rangle - \langle O\rangle^2\right] \tag{7.2}$$

of a thermodynamic observable O diverge or at least show a strong increase at the transition point triggered by the global fluctuations. For the order parameter this generalised susceptibility appears naturally as part of its full susceptibility.

The divergence of the correlation length in the vicinity of the transition also causes the dynamics of the system to be governed by its global symmetries. This allows for the classification of physical systems in universality classes according to their spatial dimension d_{s} and global properties. Different universality classes share a common behaviour in the vicinity of the phase transition indicated by scaling properties of the order parameter and other physical quantities with the reduced temperature

$$\tau \equiv \frac{T - T_C(0,\infty)}{T_C(0,\infty)} \tag{7.3}$$

and the external field h. Here $T_C(h, V)$ is the critical temperature for external field h and volume V. In particular, the order parameter in the vicinity of the critical point fulfils the scaling law

$$\Theta \sim |\tau|^{\beta_{\mathrm{ce}}} \quad \text{and} \quad \Theta \sim h^{1/\delta_{\mathrm{ce}}} \tag{7.4}$$

at $h = 0$ or $\tau = 0$, respectively. Here the critical exponents are marked by the subscript 'ce' to enable the distinction from other quantities. In finite volume the correlation length of the system has a natural upper bound L for $V = L^{d_\mathrm{s}}$. In consequence, quantities that diverge in the thermodynamic limit with ξ are necessarily finite. In the approach of this limit there is thus an associated scaling behaviour with the volume [264, 265], known as finite size scaling (FSS).

A quantity that provides direct information on the universality class is the Binder cumulant B_4 [266]. For the observable O it is defined as

$$B_4(O) = \frac{\langle \delta O^4 \rangle}{\langle \delta O^2 \rangle^2} \quad \text{with} \quad \delta O = O - \langle O \rangle \ . \tag{7.5}$$

When evaluated at the transition point in the limit of infinite volume for any thermodynamic quantity, its value approaches

$$B_4(\Theta) = \begin{cases} 3 & \text{for a crossover ,} \\ 1 & \text{for a 1st order transition ,} \\ 1.604 & \text{for a 2nd order transition } Z_2\text{-universality and} \\ 1.092 & \text{for a 2nd order transition } O(4)\text{-universality .} \end{cases} \tag{7.6}$$

7.2 The phase diagram of QCD

Before moving on to the details of the methods to probe phase transitions in LQCD this section contains a review of the present knowledge of the QCD phase diagram and points out the importance of the chiral limit in the two-flavour case. For reviews on experimental and phenomenological aspects of the phase diagram, see for instance the reviews by *Braun-Munzinger* and *Stachel* [267] as well as *Braun-Munzinger* and *Wambach* [268].

7.2.1 Heavy ion collisions and physical quark masses

The experimental realisation of a thermal system of quarks and gluons demands the existence of a large number of hadrons at sufficient energy densities. These conditions are realised in collisions of ultrarelativistic heavy ions with sufficient overlap and are probed in the extensive experimental programmes at RHIC and the LHC with ions of lead and gold. In the course of such a collision the initial system, made up of partons far away from thermal equilibrium, expands and is driven to a locally equilibrated system of quarks and gluons, the QGP. When expanding further, the system cools down and re-hadronises at the freeze-out point [269, 270]. The resulting spectrum of hadrons is well described by a statistical ansatz [271–274] which yields information on the temperature T_F and the chemical potential μ_F at freeze-out and thus can be converted into a phase diagram. Here it is important to note that the resulting freeze-out curve $(T_F,\ \mu_F)$ in the $(T,\ \mu)$-plane does not necessarily have to coincide with the critical line $(T_C,\ \mu_C)$ associated with the thermal QCD transition. While there are arguments from phenomenology [275] that T_F should be close to T_C in the region of small chemical potential μ, this does not necessarily hold for larger μ.

The region of small but non-vanishing chemical potential is indirectly accessible for simulations of LQCD through the use of various methods (for recent reviews see [33, 276,

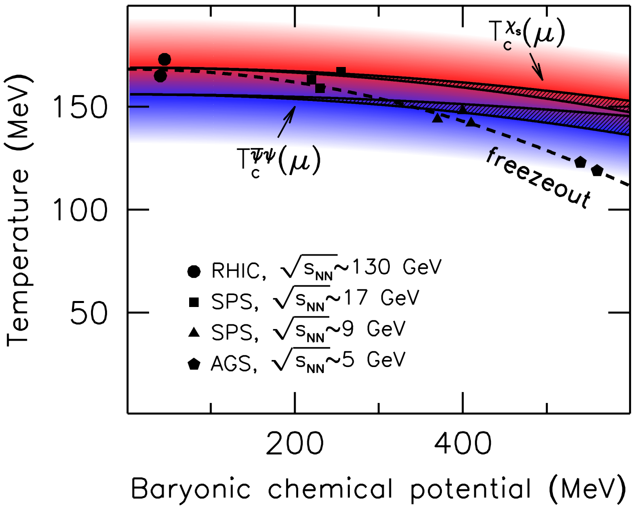

Figure 7.1: Comparison between the freeze-out curve from experiment and the critical line extracted from LQCD, as presented in [278].

277]). While the curvature of the critical line in the μ-direction is found to be smaller than the one from the freeze-out line, both curves agree well in the region close to vanishing chemical potential, as shown in figure 7.1. While these results at small chemical potential can be considered to be reliable this is not the case for results at larger chemical potential. One example is the hunt for a possible critical endpoint in the thermal transition line as indicated in figure In.1 in the introduction. While there appears to be evidence for its existence (cf. [33] for a review on recent results) unknown systematic uncertainties render conclusive statements difficult.

One of the most important lessons learned from heavy ion-collisions is that the evolution of the equilibrated system is well described by ideal relativistic hydrodynamics. This is indicated by the good agreement between the pattern of the elliptic particle flow observed in experiments (cf. the data from STAR [279] and the recent data from ALICE [280]) and the predictions from hydrodynamics [281, 282]. While in general a direct comparison between experiment and LQCD is difficult, this is one of the occasions where LQCD in principle can provide direct input in form of hydrodynamic transport coefficients and other hydrodynamic related quantities (for a review see [283]). One of the most prominent examples is the QCD equation of state which is essential for the hydrodynamic treatment. For a recent review on lattice results see [284].

The region of large chemical potential can neither be explored by LQCD nor by the current experimental programes. For the former this is due to the sign problem, i.e. the appearance of a complex determinant, in the HMC algorithm. Methods to extract information from usual HMC simulations, e.g. Taylor expansions [285, 286] or reweighting [287–289], break down at $\mu/T \lesssim 1$. Alternative methods for performing the Monte-Carlo simulation,

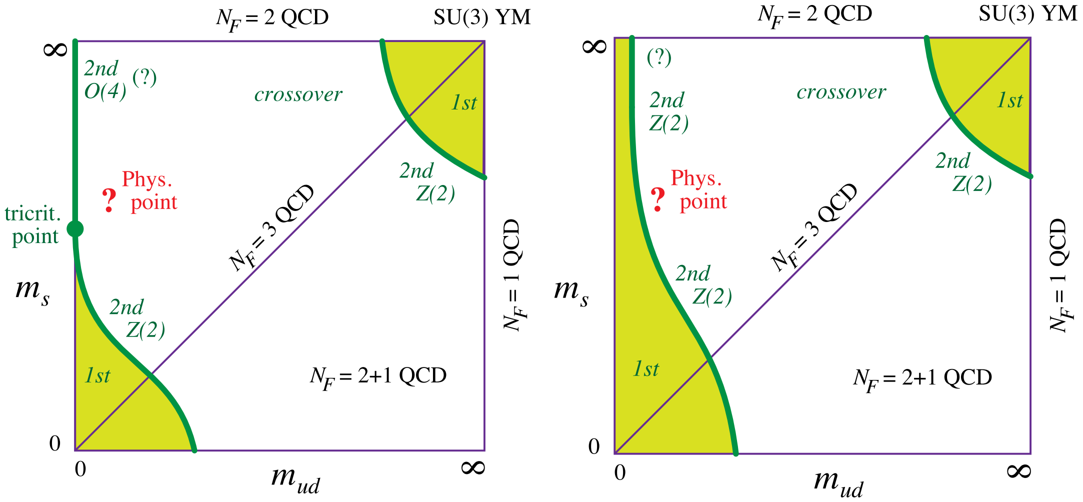

Figure 7.2: The current understanding of the nature of the phase transition at $\mu = 0$ in the enlarged parameter space of degenerate up and down quark masses and an additional strange quark, taken from [32]. The two different diagrams show the two possible scenarios of an second order transition in the $O(4)$ universality class (left) or a first order transition (right) in the chiral limit.

e.g. the Complex Langevin Method [290], which had a revival recently (see [291]), still suffer from algorithmical and conceptual problems when applied to full QCD. For an extensive review on the aforementioned topics see [139]. New experimental results at larger chemical potential are expected from the FAIR facility. Until results from FAIR are available and/or the algorithmic problems described above are under control this regime can only be explored using models or QCD-like theories (for a review consult [24]).

Recently there has also been progress and results from alternative non-perturbative approaches to QCD using the functional renormalisation group [292] or Dyson-Schwinger equations [293]. As already mentioned in the introduction, the effect of the involved assumptions and approximations in the calculations is difficult to quantify and it is unclear whether these methods will be able to yield more than qualitative results in the future.

7.2.2 The QCD phase diagram in lattice QCD: Current status

Directly accessible to lattice simulations is the region with $\mu = 0$ on the left axis in figure In.1. In LQCD the quark masses are free parameters which offers the possibility to simulate at any quark mass and to study the interplay between chiral symmetry restoration and deconfinement in the enlarged parameter space $\{m_{ud},\, m_s,\, T\}$. Of particular interest in this context is the order of the transition. The current knowledge on the nature of the transition in the m_{ud}-m_s plane is shown in figure 7.2. In principle, the parameter space of the phase diagram has to be extended to include the quark masses of the other quark flavours of the SM. However, due to their large physical masses it is unlikely that their contributions changes the qualitative properties of the phase diagram. Nevertheless, the charm quark is light enough to possibly influence plasma properties in the region close to the transition. First studies including the effects of the charm quark on the equation of state have already been reported [294].

In the two opposite limits of pure gauge theory and the limit of massless quarks there are first order transitions, associated to the breaking of center [295] and chiral [34] symmetry, respectively. The regions of first order transitions in the neighbourhood of these two limiting cases are bounded by second order critical lines in the $Z(2)$ universality class [296–298], known as deconfinement and chiral critical lines. The chiral critical line has been mapped out in simulations with staggered quarks on lattices with $N_t = 4$ for small values of m_s below the physical one in [299] and was shown to move closer to the chiral limit when going to finer lattices [300, 301]. These findings show that the transition at the physical point is a crossover as noted already in [302]. The transition temperature at the physical point is found to be between 145 and 160 MeV [127, 303].

The remaining open question in the phase diagram of the m_{ud}-m_s plane at $\mu = 0$ concerns the order of the transition in the chiral limit of two-flavour QCD, i.e. the upper left corner in the phase diagrams from figure 7.2. There are two possible scenarios [34, 304]: In the first scenario, shown in the left panel of figure 7.2, the chiral critical line reaches the $m_{ud} = 0$ axis at some tricritical point m_s^{tc}. Then the transition in the chiral limit at $N_f = 2$ is of second order and the restoration of chiral symmetry belongs to the $SU(2) \times SU(2) \simeq O(4)$ universality class [305]. In the second scenario, depicted in the right panel of figure 7.2, the chiral critical line never reaches the $m_{ud} = 0$ axis and the transition remains first order for all values of the strange quark mass. In [34, 304] it was shown that the realisation of one of the two scenarios can be linked to the strength of the anomalous breaking of the $U_A(1)$-symmetry at the transition point in the chiral limit. If the symmetry is restored at the transition point the transition will be of first order. If on the other hand the breaking is strong the $O(4)$-scenario is favoured. The strength of the anomaly can be probed by looking at scalar and pseudo-scalar screening masses as discussed in section 7.4.

The first initial studies aiming at extracting the transition in the chiral limit at $N_f = 2$ were done with staggered fermions on coarse lattices and neither showed the $O(4)$ [306–308] nor the staggered specific $O(2)$ [309–311] scaling behaviour. The following studies with Wilson fermions at $N_t = 4$ showed consistency with $O(4)$-scaling [312, 313, 332]. All these results were obtained on rather coarse lattices where no continuum behaviour can be expected. More recently a study with staggered fermions at $N_f = 2$ and $N_t = 4$ including an extensive analysis of finite size scaling has been reported [314–316] and shows consistency with first order scaling. On the other hand results from $N_f = 2 + 1$ at finer lattice spacings and at the physical strange quark mass indicate consistency with $O(4)$ scaling [127]. Note that all these results have been obtained using staggered fermions and as already discussed in section 2.5 there are doubts concerning their continuum limit when using the fourth root trick. This especially affects the universality of staggered fermions and the question whether arguments extracted from scaling are reliable (see [32]). For the results at the physical point where the transition is a crossover and the details of the underlying chiral dynamics are not of such fundamental importance they might provide a reasonable description of the QCD dynamics. This is supported by the fact that recent simulations with Wilson fermions at $N_f = 2 + 1$ [317, 318] and quark masses much larger than physical ones find agreement with staggered results. Nevertheless, in the chiral limit the situation is different as the transition is expected to be governed by the restoration of chiral symmetry and in this context the underlying dynamics is essential. As *Creutz* has pointed out it is questionable whether this dynamics is correctly reproduced by rooted staggered fermions in the continuum limit [123, 319].

To extract reliable information about the transition in the chiral limit it is thus important to use alternative fermionic actions. Wilson fermions are an obvious choice since they can be simulated at moderate numerical cost. Studies with Wilson fermions [53, 320–322] show consistency with $O(4)$-scaling. However, the studies suffer from large quark masses, corresponding to pion masses larger then 300 MeV. In particular, it was pointed out in [53] that with the present set of data points no distinction between first and second order scenarios is possible. Furthermore, in the study [320, 321] measurements from different values of N_t and volumes are mixed in the scaling analysis, leading to possibly large uncontrolled systematic effects. In this context one of the main effects which has to be controlled in simulations with Wilson fermions is the explicit breaking of chiral symmetry. This effect obviously will be severe for probing chiral symmetry restoration in the chiral limit as for Wilson fermions at finite lattice spacings chiral symmetry is still not manifestly restored. The effect can be controlled when the simulations are done close enough to the continuum. For Wilson fermions this means that one needs lattices with $N_t \geq 12$ as indicated by a study on cut-off effects for the pressure in the free theory [323]. To come to a conclusive result it is thus necessary to perform a study on large lattices with controlled systematics concerning the size of quark masses and effects of finite volume.

The problem with explicit chiral symmetry breaking can be avoided by using fermion actions that have an exact chiral symmetry on the lattice. First studies with domain wall [324] and overlap [325] fermions for $N_f = 2$ have already been reported. So far both projects are not at a stage that any reliable conclusion can be drawn, concerning the transition in the chiral limit.

7.3 Observables and order parameters

To extract the properties of phase transitions one has to perform scans in the temperature and monitor the behaviour of observables that are sensitive to the transition in the critical region. The observables of choice in the case of the QCD transition are the order parameters for deconfinement and chiral symmetry breaking. In this section possible scan setups and observables are discussed in detail with particular emphasis on non-perturbatively $\mathcal{O}(a)$-improved Wilson fermions with $N_f = 2$.

7.3.1 Temperature scans and the transition temperature

In the presence of an external field which breaks the symmetry associated with the phase transition explicitly there are different ways to cross the transition, each having its advantages and drawbacks. One particular possibility is to keep the external field fixed while varying the temperature. In these temperature scans the physical conditions remain constant except for thermal effects, i.e. the scan is performed along a line of constant physics (LCP). This is the method of choice used in this study.

Concerning the chiral transition in LQCD for $N_f = 2$ the external field is proportional to the renormalised quark mass and the temperature is connected to the inverse temporal extent of the lattice $T = 1/(a\,N_t)$ (cf. eq. (2.2)). In general there are two ways to change the temperature. The first possibility is the fixed scale approach where N_t is changed while all other bare parameters are kept fixed. Since the physical properties other than the temperature do not depend on N_t this is tantamount to a scan along LCPs. In this setup the resolution around T_C and the maximal temperature are limited by the integer nature of N_t. The method is particularly problematic when domain decomposition is used to speed up the simulations. The associated demand that the lattice can be chessboard covered with sublattices not smaller then 4^4 only allows temporal extents of $N_t = 8,\ 12,\ 16,\ \ldots$. The method of choice for these algorithms is to keep N_t fixed whilst varying the lattice spacing a by changing the bare coupling β. This method will be used for the present study. A line of constant renormalised quark mass then has to be realised by changing the bare quark mass with β. As a result, scanning along a LCP is difficult since the condition of a constant renormalised quark mass is not easily realised (see [277]). This is especially true for Wilson fermions where the quark mass also undergoes an additive renormalisation. The details of the computational setup and the expected phase structure for Wilson fermions are discussed in section 9.1.

Furthermore, β-scans are preferable since they enable the use of multi-histogram methods that in principle allow to obtain quasi-continuous results in the transition region [56, 57, 360, 361]. The method has originally been developed for pure gauge theories but is equally applicable for scans at constant κ-values and fermions that have a fermion determinant without explicitly β-dependent terms. However, in this form it cannot be applied to non-perturbatively $\mathcal{O}(a)$-improved Wilson fermions where the improvement coefficient c_{SW} changes with β. More generally this is true for scans along LCPs for any kind of fermion action, since the bare mass in the fermion action has to be changed with β to ensure a constant renormalised quark mass. In chapter 8 an extension of the method will be presented that can also be applied to scans with coupling dependent parameters in the action, provided that their change along the scan is small.

7.3.2 Deconfinement and center symmetry

As quarks and gluons are effectively free in the QGP, one signature of the plasma is the deconfinement of quarks. It is signaled by a finite free energy F_q of a single quark while for confined quarks F_q is infinite. Connected to the free energy of a single quark is the absolute value of the Polyakov loop

$$|L| \equiv \frac{1}{V\,N_t} \left| \sum_{\mathbf{x}} \prod_{x_0} U_4(\mathbf{x}, x_0) \right| \,. \tag{7.7}$$

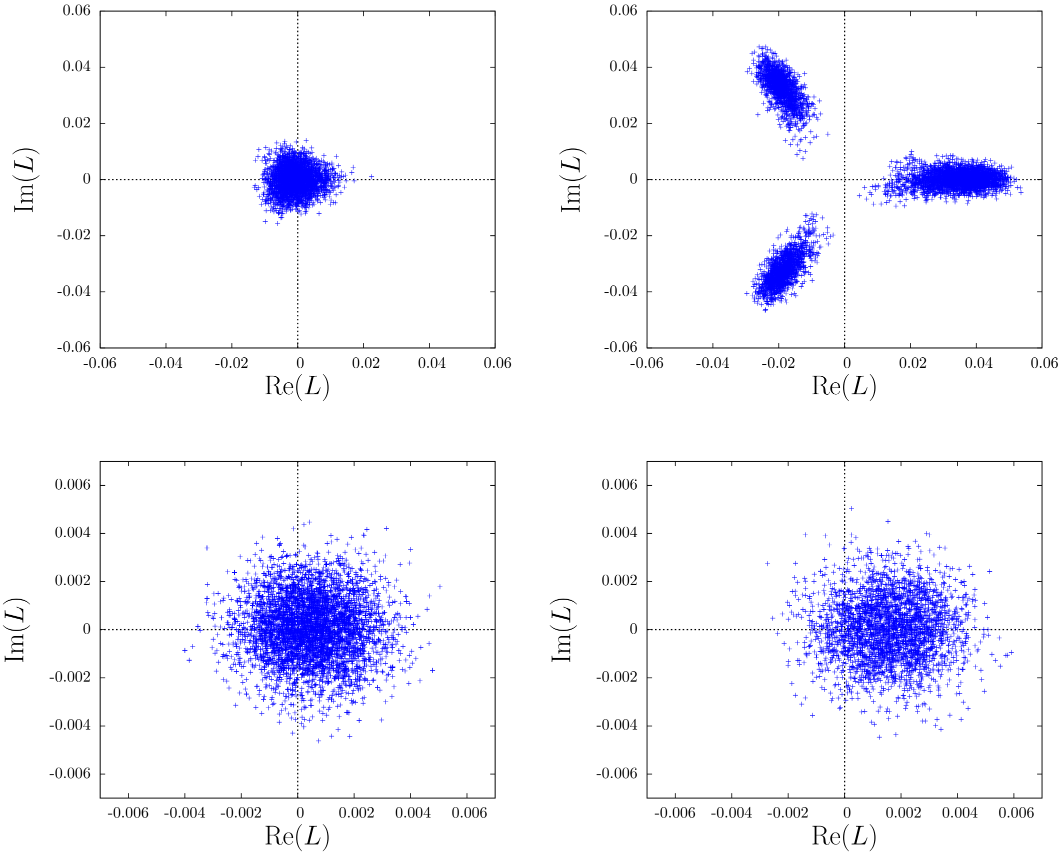

Figure 7.3: Scatter plots for the Polyakov loop close to pure gauge theory (at $\kappa = 0.03$) below (top, left) and above (top, right) the deconfinement transition, obtained from a 8×16^3 lattice and for scan $\mathbf{B1}_\kappa$ from section 9.2 (below) at smaller quark masses.

In the case of pure gauge theory, i.e. for infinitely heavy quarks, it can be shown that the Polyakov loop is connected to F_q by [326]

$$\langle |L| \rangle \sim e^{-\beta\,(F_q - F_0)} \,. \tag{7.8}$$

Here F_0 is the subtraction of the vacuum contribution. For pure gauge theory and confined quarks, $|L|$ vanishes while it obtains a non-zero value in the deconfined phase and thus constitutes a true order parameter. Its susceptibility is given by [1]

$$\chi_L = V \left(\left\langle |L|^2 \right\rangle - \langle |L| \rangle^2 \right) \,. \tag{7.9}$$

---

[1] The susceptibility can be obtained from the usual derivative with respect to κ^{N_t} in eq. (7.1), when heavy quarks are included in the framework of an expansion in the hopping parameter κ.

The symmetry associated with the deconfinement transition in pure gauge theory is center symmetry,

$$U_\mu(x) \quad \rightarrow \quad w\, U_\mu(x) \quad \text{with} \quad w = \mathbf{1}\, e^{i\, 2\, \pi\, n/3} \;, \quad n \in \mathbb{N} \,. \tag{7.10}$$

The center group for $SU(N)$ is defined by

$$C(SU(N)) = \left\{ w \in SU(N) \;\middle|\; \forall\, U \in SU(N) \;:\; w\, U\, w^{-1} = U \right\} \;. \tag{7.11}$$

Since the lattice gauge action is invariant under transformations of the center while the Polyakov loop is not, it is obvious that $\langle |L| \rangle$ is invariant as long as $\langle |L| \rangle = 0$, i.e. in the confined phase. For $\langle |L| \rangle \neq 0$ this is no longer true and the symmetry is broken. Figure 7.3 (top) contains scatter plots for the measurements of the Polyakov loop in the complex plane close to pure gauge theory ($\kappa = 0.03$) below and above the deconfinement transition. In the confined phase the Polyakov loop scatters around $|L| = 0$ while in the deconfined phase $|L|$ acquires a non-zero central value and the Polyakov loop scatters around that value at the three different phases associated to the generators of $C(SU(N))$.

In the presence of dynamical fermions center symmetry is no longer fulfilled. In that case the explicit breaking of center symmetry singles out the direction $n = 0$, i.e. $w = \mathbf{1}$, as shown in the scatter plots in figure 7.3. As a consequence, the Polyakov loop is no longer a true order parameter and acquires a non-zero but small value also in the confined region. In this case it is sufficient to use the real part of the Polyakov loop which will enhance the signal since the fluctuations stemming from the imaginary part (where the expectation value is known to vanish) are not included. In the following the real part of the Polyakov loop is used throughout and the loose notation L will be used to refer to the real part instead of the complex quantity. The Polyakov loop requires a multiplicative renormalisation in order to have a well defined continuum limit [327]. This is not necessary for the extraction of the signal for the thermal transition at a given value for N_t since the renormalisation factor is not sensible to the transition. Nevertheless, the factor needs to be included when Polyakov loops obtained from scans at different cut-offs are to be compared. A suitable renormalisation condition which works without input from simulations at $T = 0$ has been given in [318]. In this scheme the renormalised Polyakov loop $\langle |L| \rangle_R$ is defined by having a fixed value L_0 at a temperature $\tau_0 \equiv (T/T_C)_0$ in units of the critical temperature,

$$\langle |L| \rangle_R (T) = \left(\frac{L_0}{\langle |L(\tau_0\, T_C)| \rangle} \right)^{\frac{\tau_0\, T_C}{T}} \langle |L(T)| \rangle \;. \tag{7.12}$$

This normalisation ensures that the divergent additive term in eq. (7.8) is subtracted properly.

An improved estimator for the thermal transition can be obtained by the use of ‘link smearing’ [328]. Figure 7.4 contains the relative error of the real part of the Polyakov computed with APE smearing [329] and HYP smearing [330] at different smearing parameters. For APE smearing the parameter α multiplies the sum over staples and for HYP smearing α_i are the parameters multiplying the nested staples. For the rest of this thesis 5 levels of APE smearing with $\alpha = 0.5$ are used to compute the smeared version of the

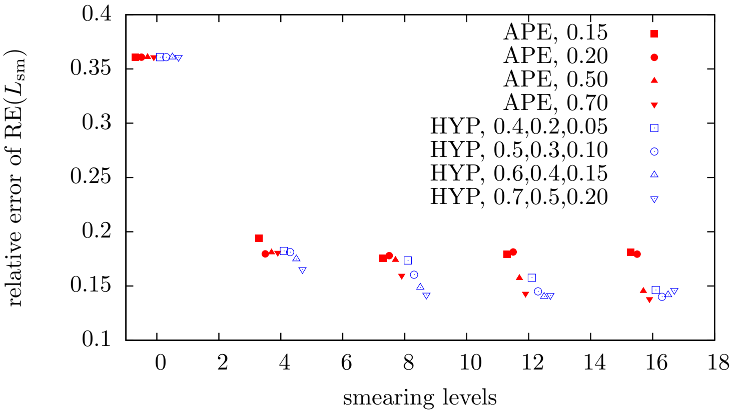

Figure 7.4: Comparison of the relative error for the real part of the Polyakov loop for different smearing procedures and parameters on a test run on a 12×24^3-lattice with $\beta = 5.22$ and $\kappa = 0.1345$. The number in the key for APE smearing corresponds to the parameter α and numbers in the key of HYP smearing to α_1, α_2, α_3 respectively. The data points are displaced on the x-axis to enable an easier comparison.

Polyakov loop L_{sm} as this leads to a satisfactory increase for the signal at $N_t = 16$. Note that smearing does not spoil the symmetry properties of the Polyakov loop since the procedures are gauge invariant. In particular, it does not change the properties of the Polyakov loop under center transformations. The renormalised smeared Polyakov loop can also be obtained with the method from eq. (7.12).

7.3.3 Restoration of chiral symmetry

The spontaneous breaking of chiral symmetry in the chiral limit of the two-flavour theory is connected to a non-zero value for the chiral condensate $\langle \bar{\psi}\, \psi \rangle$ (cf. section 1.3.1). In consequence, $\langle \bar{\psi}\, \psi \rangle$ constitutes the order parameter associated with chiral symmetry restoration and the average light-quark mass m_{ud} constitutes the external field that breaks chiral symmetry explicitly. The two are related by

$$\langle \bar{\psi}\psi \rangle = \frac{T}{V} \frac{\partial \ln(Z)}{\partial m_{ud}} \; . \tag{7.13}$$

On the lattice the condensate is given by the expectation value of the scalar density $\langle S \rangle$. When fermions are integrated out the bare condensate $\langle \bar{\psi}\psi \rangle_{\mathrm{bare}}$ is given by the trace over the inverse of the Dirac operator divided by the lattice volume and can easily be measured by the use of stochastic sources as discussed in section 4.3.1. However, as discussed already in section 2.4.2, the scalar density mixes with the identity and thus suffers from additive renormalisation like the quark mass. The renormalised condensate is given by

$$\langle \bar{\psi}\psi \rangle = \mathcal{Z}_S \, \left(\langle \bar{\psi}\psi \rangle_{\mathrm{bare}} - S_c \right) \; . \tag{7.14}$$

The additional term S_c depends on the coupling and has to be computed non-perturbatively. However, the additive renormalisation does not depend on the temperature and can be canceled by subtracting the zero-temperature condensate at equivalent bare parameters

$$\left\langle\bar{\psi}\psi\right\rangle_{\mathrm{Tsub}} = \left\langle\bar{\psi}\psi\right\rangle_{\mathrm{bare}} - \left\langle\bar{\psi}\psi\right\rangle_{\mathrm{bare}}\Big|_{T=0} \ . \tag{7.15}$$

The multiplicative renormalisation factor in the continuum and chiral limit is equivalent to $\mathcal{Z}_m$ which is known from the renormalisation of the bare quark mass and is given by

$$\mathcal{Z}_m^{\mathrm{SC}}(g_0,\mu_R)\ (1+b_m\, a\bar{m}) = \mathcal{Z}_{\mathrm{PCAC}}(g_0)\ \frac{\mathcal{Z}_A(g_0)}{\mathcal{Z}_P^{\mathrm{SC}}(g_0,\mu_R)}\ (1+[b_A-b_P]\ a\bar{m}) \ . \tag{7.16}$$

At finite lattice spacing $\mathcal{Z}_S$ differs from $\mathcal{Z}_m$ by cut-off effects, even in the chiral limit. However, since one is interested in the transition in the chiral limit and in the continuum, one can use eq. (7.16) also at finite lattice spacings.

The susceptibility of $\left\langle\bar{\psi}\psi\right\rangle$ is defined as

$$\chi_{\langle\bar{\psi}\psi\rangle} = \frac{\partial\left\langle\bar{\psi}\psi\right\rangle}{\partial m} \ . \tag{7.17}$$

Its derivative constitutes two parts, the disconnected part, equivalent to the generalised susceptibility

$$\bar{\chi}_{\langle\bar{\psi}\psi\rangle} = \frac{T}{V}\ \left(\left\langle\mathrm{Tr}\left(D^{-1}\right)^2\right\rangle - \left\langle\mathrm{Tr}\left(D^{-1}\right)\right\rangle^2\right) \ , \tag{7.18}$$

and the connected part

$$\chi^{\mathrm{conn}}_{\langle\bar{\psi}\psi\rangle} = -\frac{T}{V}\ \sum_x \left\langle\mathrm{Tr}\left(D^{-1}(x,0)\ D^{-1}(0,x)\right)\right\rangle \ . \tag{7.19}$$

Studies have shown (see [127, 314]) that the disconnected part is expected to dominate the signal for the thermal transition. When the bare condensate is computed the additive renormalisation contributes a temperature dependent term to the susceptibility. For the identification of the critical temperature this additional term should not be important since it is not related to thermodynamic properties of the theory and thus has a smooth behaviour in the transition region.

An alternative definition of the chiral condensate which removes the additive piece in eq. (7.14) can be obtained by an axial Ward identity [112, 331]. In the form integrated over spacetime the axial Ward identity is given by

$$\frac{V}{N_f\,T}\ \left(\left\langle\bar{\psi}\psi\right\rangle_{\mathrm{bare}} - S_c\right) = 2m_{\mathrm{PCAC}} \int d^4x\, \langle P(0)\ P(x)\rangle - \mathcal{Z}_A \int d^4x\, \partial^\mu_x \, \langle P(0)\ A_\mu(x)\rangle \ . \tag{7.20}$$

At finite quark mass the subtracted condensate can now be defined by the first term on the right hand side as the second term vanishes due to the absence of a true Goldstone boson [112], i.e.

$$\left\langle\bar{\psi}\psi\right\rangle_{\mathrm{sub}} \equiv 2\,\frac{N_f\,T}{V}\ m_{\mathrm{PCAC}} \int d^4x\, \langle P(0)\ P(x)\rangle \ . \tag{7.21}$$

This definition of the condensate vanishes in the chiral limit as $m_{\mathrm{PCAC}} \to 0$. This is not the case for the full expression on the right hand side of eq. (7.20). In the chiral limit the existence of a true Goldstone boson ensures a non-vanishing surface term in the integral over the four-divergence [112]. This form of the condensate has also been applied in the early study [332] and was tested by the tmfT collaboration [53]. Note that there is still the need for multiplicative renormalisation which can be done along the lines of eq. (7.16). Furthermore, there are additional mixing terms at $\mathcal{O}(1/a^2)$. Again these do not depend on the temperature and can be subtracted using the condensate at zero temperature.

A conceptually cleaner but more expensive method to calculate the condensate is to use the Banks-Casher relation [333], which can be used for a direct measurement of the renormalised condensate. However, this approach is computationally demanding and thus remains a project for the future.

7.4 Mesonic correlation functions at finite temperature

Mesonic correlation functions have been known as a valuable probe for the properties of the QGP for a long time [54, 55]. In the vicinity of the phase transition they can be used to investigate the pattern of chiral symmetry restoration by investigating the degeneracies for particular channels. The exponential decay of spatial correlation functions defines the 'screening masses' [54]. They can be interpreted as the inverse length scale on which a test meson in that particular channel is screened. When chiral symmetry gets restored the screening masses also become degenerate. The spectral functions associated with the correlation functions are of particular relevance to study plasma properties [334, 335]. In particular, the spectral function of the correlation function in the vector channel can be used to get information on in-medium properties of quark boundstates [336, 337] and is related to the electrical conductivity of the plasma [338] (for a review see [283]). However, the problem with spectral functions is that they can only be accessed indirectly in lattice simulations [334].

Correlation functions at finite temperature can be calculated on the lattice using the same formalism as for $T = 0$, introduced in section 4.2. However, at finite temperature the temporal extent of the lattice is related to the inverse temperature and thus is necessarily finite. This hampers the extraction of the asymptotic behaviour. The spatial extent of the lattice is not limited and thus in principle allows for the extraction of the correlation function at arbitrary distances. Considering a correlation function in $x^3 \equiv z$-direction in a particular channel X projected to zero momentum,

$$C_X^2(z) \equiv \sum_{\mathbf{z}_\perp} \left\langle \Phi_X(z, \mathbf{z}_\perp)\, \Phi_X^+(0) \right\rangle \ , \tag{7.22}$$

where X is any of the operators from table 4.1 and $\mathbf{z}_\perp$ is the vector of coordinates perpendicular to z. The associated screening mass M_X can be extracted using the formalism developed in section 4.1 with the adjustment $t \to z$ and $T \to L$. In particular, M_X can be extracted from a fit to the correlation function to the form given in eq. (4.7) with a positive sign between the two terms in the brackets.

In practice, this is difficult since screening masses usually have a bad signal-to-noise ratio in all channels except the pseudoscalar ones. For practical purpose it is thus more convenient to define an effective mass M^{eff} which approaches the screening mass M_X in the asymptotic limit. A suitable definition for the effective mass is given by the formula for the inverse cosh,

$$a\, M_X^{\mathrm{eff}}(z) \equiv \ln \left[\frac{C_X^2(z+a) + C_X^2(z-a)}{2\, C_X^2(z)} + \sqrt{\left(\frac{C_X^2(z+a) + C_X^2(z-a)}{2\, C_X^2(z)} \right)^2 - 1} \right] . \tag{7.23}$$

Using eq. (4.7) it is easy to show that for this definition

$$M_X = \lim_{z \to L/2} M_X^{\mathrm{eff}}(z) . \tag{7.24}$$

The strategy is then to look for a plateau in the effective mass and extract the screening mass from the plateau value using a fit to a constant. This has the advantage that a loss of the signal is indicated by a non-constant behaviour of the effective mass in the region around $L/2$.

In this study correlation functions in the pseudoscalar (P), scalar (S), vector (V) and axial vector (A) channels are studied. They can be used to study the chiral symmetry restoration pattern in the vicinity of T_C. In particular, the correlation functions of the vector and axial vector channel are related by [54]

$$SU_A(2): \quad C_V^2 \quad \longleftrightarrow \quad C_A^2 \tag{7.25}$$

and thus provide a valuable probe of the restoration of chiral symmetry. The combination of pseudoscalar and scalar channels is ideally suited to study the anomalous breaking of $U_A(1)$-symmetry. In the pseudoscalar channel the iso-vector particles are the pions π and the iso-scalar particle is the η'. In the scalar channel the two associated particles are the δ or a^0 and the σ. These four states are related by [54, 324, 339, 340]

$$\begin{array}{lcccccccc} SU_A(2): & \pi & \longleftrightarrow & \sigma\,, & & \eta' & \longleftrightarrow & \delta\,, \\ U_A(1) & \pi & \longleftrightarrow & \delta & \text{and} & \eta' & \longleftrightarrow & \sigma\,. \end{array} \tag{7.26}$$

In lattice simulations with two degenerate flavours, iso-scalar and iso-vector correlation functions are distinguished only by the appearance of quark disconnected diagrams (cf. section 4.2.1). Here the focus is on the connected contributions only and the associated iso-vector correlation functions. These are related by

$$U_A(1): \quad C_P^2 \quad \longleftrightarrow \quad C_S^2\,. \tag{7.27}$$

When chiral symmetry is restored above T_C this relation can be used to probe the strength of the anomalous breaking of $U_A(1)$ [54, 339, 341, 342].

The restoration of chiral symmetry can be studied at the level of screening masses. However, in practice it is often better to look at the degeneracies of the correlators directly. One possibility is to consider the difference, or alternatively the ratio, of the effective masses of the two correlators in the channels that are to be probed. A plateau in this quantity then corresponds to the difference or the ratio of the two screening masses, respectively. The advantage of taking the difference or the ratio prior to the fit is that global fluctuations in the propagators cancel which in turn improves the signal. Another possibility is to use hadronic susceptibilities [339, 341]

$$\chi_X^{\mathrm{had}} \sim \sum_z C_X^2(z) \ . \tag{7.28}$$

In the case that only a single state contributes it can be shown that they are related to the inverse mass $\sim 1/M_X^2$ [341]. The susceptibilities are ultraviolet divergent and suffer from contact terms. To get rid of these contributions it is useful to define a subtraction condition. Here the sum on the right hand side will be cut off at $N_t/2$. This rather arbitrary cut will ensure the absence of contact terms and a suppression of the contribution of states with larger (screening) masses. The hadronic susceptibilities used in this study are then defined as

$$\chi_X^{\mathrm{had}} \equiv \sum_{z=N_t/2}^{N_s-N_t/2} C_X^2(z) \ . \tag{7.29}$$

An appealing feature of screening masses and their relation to chiral symmetry restoration for simulations with Wilson fermions is that their extraction does not involve any renormalisation in contrast to the extraction of the chiral condensate. Furthermore, screening masses are particularly easy to extract for Wilson fermions as these have an undistorted particle spectrum in contrast to staggered and maximally twisted mass fermions. They thus provide a direct probe for chiral symmetry restoration.

Screening masses in the high temperature regime $T \gtrsim 3\,T_C$ can be used to make contact with perturbation theory. In particular, they can be used to test the applicability of dimensionally reduced perturbation theory [343] and the accuracy of predictions for the behaviour of the screening masses from re-summed perturbation theory. It is known that in the infinite temperature limit, i.e. the limit of free fields, all screening masses become degenerate and approach a value of $M^\infty = 2\pi\,T$ [344, 345]. The leading order correction from interactions is positive [346, 347]. As a consequence all screening masses should approach the infinite temperature limit from above.

In the literature there are several studies that deal with the behaviour of screening masses close to the transition point up to the high temperature limit. For a review of early results see [341] and for more recent studies [342, 348–352]. All studies so far show restoration of $SU_A(2)$-symmetry close to the transition point, indicated by degenerate vector and axial vector correlators. $U_A(1)$-symmetry on the other hand seems to be restored only at values as large as $\sim 1.3\,T_C$. However, no study so far has examined symmetry restoration in the approach to the chiral limit with $N_f = 2$ and controlled systematics. A recent study has looked at chiral symmetry restoration for $N_f = 2$ with domain wall fermions [324]. It was found that $U_A(1)$ is not restored at T_C but soon after at roughly $1.25\,T_C$. However, so far the study has been done only with a single lattice spacing at small volume and quark masses that correspond to a pion of roughly 200 MeV, so that at the moment no conclusion concerning the chiral limit can be made. In the high temperature phase recent studies with dynamical staggered fermions and $N_f = 2$ [351, 352] and $2+1$ [342, 349, 350] found out that the vector screening mass approaches the infinite temperature limit from above and is consistent with it already around 2 to $3\,T_C$ while the pseudoscalar screening masses remain significantly below this limit (roughly 10 % even at 3 to $4\,T_C$). In quenched simulations it has been found that for Wilson fermions the pseudoscalar screening mass approaches this limit much faster [348]. It is interesting to see whether this remains true in simulations with dynamical Wilson fermions since this would hint at specific events for staggered fermions that lead to a smaller value for the pseudoscalar screening masses even at higher temperatures [353].

7.5 Critical scaling and the order of the transition

As noted already in section 7.1, the order of the transition in a given temperature scan can be extracted by means of a FSS analysis for the peak of the susceptibility of the order parameter [264, 265]. For the transition in the chiral limit this procedure cannot be used directly since simulations at zero quark mass are not possible. To gain information about the limit of vanishing external field h one might look at the scaling of the order parameter and the peak position of its susceptibility with h (see [306]). The scaling can be expected to be dominated by the critical point at vanishing external field, at least in its direct vicinity. The associated universal scaling laws can be derived from the scaling of the free energy

$$F(\tau, h, l) = b^{-d_\mathrm{s}}\, F_\mathrm{sing}\left(b^{1/\nu_\mathrm{ce}}\,\tau,\; b^{\delta_\mathrm{ce}\,\beta_\mathrm{ce}/\nu_\mathrm{ce}}\,h,\; b^{-1}\,l\right) + F_\mathrm{reg}\left(\tau,\; h\right) \tag{7.30}$$

(see also [261–263] for a discussion in a more general framework). Here b is an arbitrary scaling factor and l a dimensionless length scale $l = L/L_0$ with $V = L^{d_\mathrm{s}}$. F_sing is responsible for the singular behaviour of F at the transition while F_reg is analytic. The regular term can be expanded in a series around $(\tau, h) = (0, 0)$ which can be truncated at some order for small values of τ and h. This generates additional terms in the scaling relations, so-called ‘scaling violations’. This section serves to review different scaling methods that can be used to extract information on the order of the transition. Table 7.1 contains a compilation of values for the critical exponents that are relevant for the scaling in the approach to the chiral limit.

7.5.1 Finite size scaling

As mentioned earlier the divergence of the correlation length in the approach to the infinite volume limit leads to a scaling of the susceptibility peak of the order parameter [264, 265]. To examine the scaling behaviour of a scan probing a critical point with the volume, one can fix the parameter b by the condition $bl = 1$ [263]. Then the scaling of a thermodynamic observable O is given by

$$O(\tau, V) = l^{\sigma_\mathrm{ce}/\nu_\mathrm{ce}}\,\Psi_O\left(\bar{\tau}\right) \quad \text{with} \quad \bar{\tau} \equiv \tau\, l^{1/\nu_\mathrm{ce}}\,. \tag{7.31}$$

Here Ψ_O is a universal scaling function and it has been assumed that the system is close enough to the thermodynamic limit so that the correlation length diverges as $|\tau|^{-\nu_\mathrm{ce}}$ at

univ.	ν	γ	β	δ	ref.
Z_2	0.6301 (4)	1.2372 (5)	0.3265 (3)	4.789 (2)	[263]
$O(4)$	0.7479 (90)	1.477 (18)	0.3836 (46)	4.851 (22)	[354]
1st order	1/3	1	0 $\delta\cdot\beta = 1$	∞	[314]

Table 7.1: Critical exponents for the universality classes relevant for this thesis. Note, that there is no true scaling for a first order transition. The coefficients listed above have been extracted from analogy.

the critical point. σ_{ce} determines the behaviour of O in the approach to the critical point, $O \sim |\tau|^{-\sigma_{\text{ce}}}$. As a result of eq. (7.31) the derivative of O with respect to τ in the vicinity of $\tau = 0$ is given by

$$\left.\frac{\partial\, O(\tau, V)}{\partial \tau}\right|_{\tau=0} \sim l^{(\sigma_{\text{ce}}+1)/\nu_{\text{ce}}} \ . \tag{7.32}$$

For small τ this leads to

$$O(\tau, V) l^{-\sigma_{\text{ce}}/\nu_{\text{ce}}} = c_O + s_{O,1}\, \bar{\tau} \ + s_{O,2}\, \bar{\tau}^2 + \dots \ . \tag{7.33}$$

In particular, when looking at the susceptibility of the order parameter χ_Θ,

$$\chi_\Theta(\tau, V) = l^{\gamma_{\text{ce}}/\nu_{\text{ce}}}\ \Psi_O\left(\bar{\tau}\right) \ . \tag{7.34}$$

Its peak defines the transition temperature which means that the maximum of the peak, its width and the temperature scale with the volume like

$$\max\left(\chi_\Theta\right) \sim l^{\gamma_{\text{ce}}/\nu_{\text{ce}}} \ , \quad \sigma\left(\chi_\Theta\right) \sim l^{-1/\nu_{\text{ce}}} \quad \text{and} \quad T_C(h, \infty) - T_C(h, V) \sim l^{-1/\nu_{\text{ce}}} \ . \tag{7.35}$$

For a first order transition the order parameter has a non-analytic behaviour that prevents a scaling law in the limit $V \to \infty$. However, since there are no non-analyticities at finite volume one can expect the existence of an associated FSS in the approach to the thermodynamic limit. In particular, the equivalent relation to eq. (7.35) for a first order transition is given by [355–357]

$$\max\left(\chi_\Theta\right) \sim l^3 \ , \quad \sigma\left(\chi_\Theta\right) \sim l^{-3} \quad \text{and} \quad T_C(h, \infty) - T_C(h, V) \sim l^{-3} \ . \tag{7.36}$$

Comparing eqs. (7.35) and (7.36) one can infer that both types of scaling laws can be expressed by eq. (7.35) if the critical exponents for a first order transition take the values listed in table 7.1. The values for β and δ listed there are also consistent with the absence of a scaling law in the thermodynamical limit when inserted in eq. (7.4).

In practice, the above scaling relations are only valid up to scaling violations. This mostly affects the behaviour of the susceptibility of the order parameter when moving away from the peak position. Furthermore, the infinite volume limit of the critical point, i.e. the point where $\tau = 0$, is not known *ab initio*. In principle it can be obtained by fitting the results for different volumes to the form of eq. (7.35) with $T_C(0, \infty)$ as free parameter.

However, this is only possible when a number of volumes close to the thermodynamic limit are available. To be able to compare two measurements at different volumes with the associated scaling laws one can replace τ by $\tilde{\tau} \equiv \tau - \tau_C(V)$ in eq. (7.33), where $\tau_C(V)$ is the critical reduced temperature for this particular volume.

7.5.2 Scaling of the order parameter and T_C with the external field

For a second order transition in the infinite volume limit one can fix b by $b^{\beta_{\rm ce}\,\delta_{\rm ce}/\nu_{\rm ce}}\;|h| = 1$ in eq. (7.30). Then the scaling of the order parameter is encoded in a universal scaling function (see [127, 261, 332])

$$\Theta \sim |h|^{1/\delta_{\rm ce}}\;\Psi_\Theta\left(|z|\,,\;{\rm sign}(h)\right) \quad \text{with} \quad z \equiv \frac{|\tau|}{|h|^{1/(\delta_{\rm ce}\,\beta_{\rm ce})}}\;. \tag{7.37}$$

The universal scaling function $\Psi_\Theta(z)$ can be studied in spin models. For the important example of the $O(4)$-universality class it has been parametrised in [358] and can be used to compare the behaviour of the order parameter around the transition to $O(4)$ scaling [53, 127, 314, 332, 359]. However, one should keep in mind that scaling violations due to the regular part in eq. (7.30) will occur. An expansion of the regular part in τ and h yields [127, 359]

$$\Theta \sim |h|^{1/\delta_{\rm ce}}\;\Psi_\Theta\left(z,\;{\rm sign}(h)\right) + \left(s_{\Theta,01} + s_{\Theta,11}\,\tau\right)\,h + s_{\Theta,02}\,h^2 + \dots\;. \tag{7.38}$$

The critical temperature is defined by the peak position, i.e. the maximum, of χ_Θ. It can be determined by the constraint [127, 306]

$$\frac{d\,\chi_\Theta}{d\tau} = 0\;. \tag{7.39}$$

With the definition of the susceptibility and the scaling relation (7.38) one obtains

$$|h|^{\frac{\beta_{\rm ce}\,(1-\delta_{\rm ce})-1}{\delta_{\rm ce}\,\beta_{\rm ce}}}\;\left(\frac{\beta_{\rm ce}-1}{\delta_{\rm ce}\,\beta_{\rm ce}}\,\frac{\partial\,\Psi_\Theta}{\partial z} - \frac{1}{\delta_{\rm ce}\,\beta_{\rm ce}}\,\frac{\partial^2\,\Psi_\Theta}{\partial z^2}\right) = 0 + \dots\;. \tag{7.40}$$

The additional term on the right hand side refers to terms stemming from the scaling violations in eq. (7.38). Neglecting them for the moment (assuming that the combined terms in τ and h are small in eq. (7.38)) the condition can only be fulfilled by all values of h if the bracket vanishes. This implies that both derivatives vanish and that z is constant at the transition point, say $z = C$. Using the definition of z it follows that

$$T_C(h) = T_C(0)\;\left[1 + C\;|h|^{1/(\delta_{\rm ce}\,\beta_{\rm ce})}\right]\;. \tag{7.41}$$

For simulations at finite volume $T_C(0, V)$ changes with the volume in the case of a true phase transition. This effect is not expected for a crossover, i.e. it might appear with a different strength for different values of h in the approach to $h = 0$. Taking this into account and using eq. (7.35), the generalisation to finite volume in a first order approximation is given by

$$T_C(h,V) = T_C(0,\infty)\,\left[1 + s_{t,1}\,(l)^{-1/\nu_{\text{ce}}} + \left(C + \bar{s}_{t,1}\,(l)^{-1/\nu_{\text{ce}}}\right)\,|h|^{1/(\delta_{\text{ce}}\,\beta_{\text{ce}})}\right]\,. \qquad (7.42)$$

Since Wilson fermions break chiral symmetry explicitly at finite lattice spacing there will also be additional terms proportional to a^2 that appear in the form of scaling violations.

Note that there are some uncertainties concerning the expected scaling in the scenario of a first order transition in the chiral limit. In this case there is a $Z(2)$-critical endpoint separating first order and crossover regions. Then it is not obvious which type of scaling arises in the approach to the endpoint. In particular, it is questionable whether a first order transition results in a scaling law as in eq. (7.41) since the arguments used to derive it do not apply to a first order transition (see [53]). One would thus expect to observe $Z(2)$-scaling which was also found in the $N_f = 3$ case [296, 299]. Note however that there is no true order parameter connected to the critical endpoint at finite quark mass so that one cannot be sure that the scaling extracted from the pseudo-order parameter will be in agreement with the expectations. These issues will be discussed in more detail in section 9.5.

7.5.3 Finite size scaling of the Binder cumulant

The Binder cumulant can be used to extract the order of the transition directly from its value in the infinite volume limit at the critical point. In this limit the behaviour of the cumulant is discontinuous and it jumps from one critical value to the other. At finite volume the divergences and discontinuities are smeared out and B_4 approaches its critical values on continuous curves governed by universality. At finite volume B_4 can thus be used to locate the critical point by means of a FSS analysis [263, 296]. In this procedure the cumulant is evaluated directly on the critical surface in the vicinity of the critical point which is signified by the intersection point of the scaling curves for the different volumes. In particular, the value at the intersection is given by the value for B_4 in the universality class of the critical point as listed in eq. (7.6). B_4 is a function of the dimensionless ratio $(l/\xi)^{1/\nu_{\text{ce}}}$, where ξ is the correlation length of the system [299]. As mentioned before the correlation length diverges like $|r|^{-\nu_{\text{ce}}}$ in the approach to the critical point where r is the distance to it in parameter space. This means that to first order in the vicinity of the critical point and for large volumes B_4 scales according to [299]

$$B_4 = B_4(l^{1/\nu_{\text{ce}}}\,|r|) \approx b_0 + b_1\,l^{1/\nu_{\text{ce}}}\,|r| + \dots\,. \qquad (7.43)$$

Here b_0 is the universal value for B_4 in the infinite volume limit associated with the universality class of the transition. Using this formula the order of the transition can be extracted from the results for the Binder cumulant with different values of r and l.

8 Multi-Histogram methods

One of the main problems for extracting properties of the transition in a temperature scan is the limited resolution in the region of the critical point. This leads to ambiguities in the definition of the transition temperatures and hampers the extraction of the Binder cumulant directly at the critical point which is essential for a scaling analysis. A way to overcome this problem was introduced by *Ferrenberg* and *Swendsen* [56, 57] and is known as multi-histogram (MH) method. The basic idea is to use the information from a set of measurements in the desired region of bare couplings β for an interpolation of the data. In this way it is possible to obtain a quasi-continuous set of measurements in the vicinity of the phase transition. Today the method has become a standard tool to investigate the critical behaviour of QCD in Monte-Carlo simulations (see [285, 288, 296, 299, 360–362]).

In the standard version the method can only be applied to fermions that do not have an explicit β-dependence in the fermionic part of their action. This is not the case for non-perturbatively $\mathcal{O}(a)$-improved Wilson fermions where the $\mathcal{O}(a)$-improvement coefficient c_{SW} has to be tuned with β to ensure $\mathcal{O}(a)$-improvement. This chapter contains a generalisation of the usual method for β-dependent fermion actions. Furthermore, the method is easily extended to set up a MH-method in an even larger parameter space such as the (β, κ)-plane. Here only the formalism will be developed as the method has not yet been tested. The status of the implementation is discussed in section 8.4. The main ideas have already been published in [363]. Recently, a related method was proposed for a MH method in the plane of bare coupling and chemical potential [364] using an expansion for the fermion determinant introduced by *Ejiri* [365].

This chapter is organised as follows: First the MH method is introduced in the context of pure gauge theories. The second and third sections then contain the formalism for the generalisation to β-dependent fermion actions and details for the computation of particular observables and the estimation of statistical and systematic uncertainties. The chapter closes with a discussion of the status of the implementation for $\mathcal{O}(a)$-improved Wilson fermions.

8.1 The density of states method for pure gauge theory

To introduce the main concepts and fix the notation it is useful to start with the original setup of the method in pure gauge theory [56, 57, 360, 361]. The action can be written as (cf. eq. (2.13))

$$S_G\,[U] = \beta\, H[U] \;, \tag{8.1}$$

where $H[U]$ is independent of β. For the following discussion the explicit form of $H[U]$, i.e. the choice of the gauge action, does not matter. Following eq. (3.2) the expectation value of an observable O at bare parameter β is given by

$$\langle O\rangle_\beta = \frac{1}{Z(\beta)} \int d[U]\; O[U]\; e^{-S_G[U]} \;. \tag{8.2}$$

Changing variables, the expectation value can be rewritten as an integral over a probability distribution ρ for values of the energy $E = H[U]$ and the observable O,

$$\langle O \rangle_\beta = \frac{1}{Z(\beta)} \int dO \, dE \, O \, \rho[O, E; \beta] \; . \tag{8.3}$$

The distribution $\rho[A, E; \beta]$ is defined in terms of a canonical partition function

$$Z[O, E; \beta] \equiv \int d[U] \, \delta\left(O[U] - O\right) \, \delta\left(H[U] - E\right) \, e^{-\beta \, H[U]} \tag{8.4}$$

restricted to the particular values of O and E. It can be written as

$$\rho[O, E; \beta] = \frac{Z[O, E; \beta]}{Z(\beta)} \; , \tag{8.5}$$

where $Z(\beta) \equiv \langle 1 \rangle_\beta$ following eq. (8.3). Making use of the δ-function in eq. (8.4), the β-dependence of $Z[O, E; \beta]$ can be pulled in front of the integral

$$Z[O, E; \beta] \equiv e^{-\beta \, E} \int d[U] \, \delta\left(O[U] - O\right) \, \delta\left(H[U] - E\right) \; . \tag{8.6}$$

The last term is independent of β and measures the probability for a configuration to assume the particular values O and E for the observable and action respectively. It is known as the density of states,

$$\mathcal{D}[O, E] \equiv \int d[U] \, \delta\left(O[U] - O\right) \, \delta\left(H[U] - E\right) \; . \tag{8.7}$$

The expectation value from eq. (8.3) is then given by

$$\langle O \rangle_\beta = \frac{1}{Z(\beta)} \int dO \, dE \, O \, \mathcal{D}[O, E] \, e^{-\beta \, E} \; . \tag{8.8}$$

The advantage of this form of the expectation value is that once $\mathcal{D}[O, E]$ is known, it might be used to calculate $\langle O \rangle$ for each value of β.

An estimate for $\mathcal{D}[O, E]$ can be extracted from a simulation at a given coupling β_a. In practice, the simulation will only contain a finite number of configurations that are in the important region of the configuration space for that particular coupling. The result is, that only a small fraction of all possible combinations of values for O and E will be covered. To extract a useful estimate for the density of states it is thus necessary to approximate $\mathcal{D}[O, E]$ by using a density $\mathcal{D}_{\mathrm{IJ}}$ for the bins E_{I} and O_{J} with a finite size [1],

$$E_{\mathrm{I}} - \frac{\Delta E}{2} \leq E < E_{\mathrm{I}} + \frac{\Delta E}{2} \; , \quad O_{\mathrm{J}} - \frac{\Delta O}{2} \leq O < O_{\mathrm{J}} + \frac{\Delta O}{2} \; . \tag{8.9}$$

---

[1] Note that eq. (8.9) assumes that all bins are of equal size. This is useful for practical purpose but the theory is not restricted to this particular case and can be formulated similarly with bins of different size.

$\mathcal{D}_{\mathrm{IJ}}$ should then agree with $\mathcal{D}[O,E]$ in the limit $\Delta E,\ \Delta O \to 0$. For a simulation at β_a the associated probability $\rho[O_{\mathrm{J}}, E_{\mathrm{I}}; \beta]$ can be approximated by the frequency functions

$$\rho[O_{\mathrm{J}}, E_{\mathrm{I}}; \beta_a] \approx f^a_{\mathrm{IJ}} \equiv \frac{N(E_{\mathrm{I}}, O_{\mathrm{J}}; \beta_a)}{N_a} \ , \tag{8.10}$$

where $N(E_{\mathrm{I}}, O_{\mathrm{J}}; \beta_a)$ counts the configurations with energy and observable belonging to bin I and J, respectively. In the following all quantities approximated by the frequency functions are denoted with a tilde and should agree with their exact counterparts in the limits $\Delta E,\ \Delta O \to 0$ and $N_a \to \infty$. Following eqs. (8.5)–(8.7) the associated estimate for the density of states is given by

$$\widetilde{\mathcal{D}}^a_{\mathrm{IJ}} = f^a_{\mathrm{IJ}}\, e^{\beta_a\,(E_{\mathrm{I}} - F^a)} \ , \tag{8.11}$$

where $F^a \equiv -\beta_a^{-1}\, \ln[\tilde{Z}(\beta_a)]$ is the free energy at simulation point β_a, accounting for the factor $\tilde{Z}(\beta_a)$ in eq. (8.5). With the change to finite binsize, the integrals in eq. (8.8) become a sum over bins I and J and the expectation value and the partition function for β read

$$\langle O \rangle_\beta \ = \ \frac{1}{Z(\beta)} \sum_{\mathrm{IJ}} O_{\mathrm{J}}\, \widetilde{\mathcal{D}}^a_{\mathrm{IJ}}\, e^{-\beta\, E_{\mathrm{I}}} \tag{8.12}$$

$$\tilde{Z}(\beta_a) \ = \ \sum_{\mathrm{IJ}} \widetilde{\mathcal{D}}^a_{\mathrm{IJ}}\, e^{-\beta\, E_{\mathrm{I}}} \ . \tag{8.13}$$

In practice, the data sets are finite and the procedure works only for a sufficient overlap of the measured histograms for E and O with the one at the target β-value. Otherwise the estimate $\widetilde{\mathcal{D}}^a_{\mathrm{IJ}}$ for $\mathcal{D}_{\mathrm{IJ}}$ does not have enough support in the important region and becomes inaccurate. The weight of a configuration with energy E decays exponentially according to $\exp(-\left|\beta - \beta_a\right|\, E)$ and in consequence sufficient overlap will only be available for small differences in β. This is a manifestation of the well known overlap problem. For a set of measurements at couplings $\{\beta_a\}$ it is possible to combine the estimates for $\mathcal{D}_{\mathrm{IJ}}$ from the different measurements to obtain an improved estimate for the range of β-values covered by $\{\beta_a\}$. It can be written as a weighted sum over the densities $\widetilde{\mathcal{D}}^a_{\mathrm{IJ}}$,

$$\widetilde{\mathcal{D}}_{\mathrm{IJ}} = \sum_a w^a_{\mathrm{IJ}}\, \widetilde{\mathcal{D}}^a_{\mathrm{IJ}} \ , \tag{8.14}$$

where w^a_{IJ} are weight factors. The resulting improved estimate for $\langle O \rangle_\beta$ is then obtained by replacing $\widetilde{\mathcal{D}}^a_{\mathrm{IJ}} \to \widetilde{\mathcal{D}}_{\mathrm{IJ}}$ in eqs. (8.12) and (8.13). The validity of the procedure does not depend on the specific choice for the weights, but they enter the error analysis and should be chosen with care to obtain reliable error estimates.

8.2 MH method for β-dependent fermion actions

The method discussed in the last section also applies to the case with a β-independent Dirac operator, to usual Wilson fermions or staggered fermions for instance. In this case the additional fermionic weight factors cancel in the reweighting procedure and can be absorbed in the definition of the density of states, eq. (8.7). This is different to the case of a Dirac operator with an explicit β-dependence which will be considered in the following.

8.2.1 β-dependent density of states

Including a β-dependent Dirac operator $D(\beta)$ the partition function in eq. (8.4) is modified to

$$Z[O,E;\beta] \equiv \int d[U]\,\delta\left(O[U]-O\right)\,\delta\left(H[U]-E\right)\,\det\left[D(\beta)\right]\,e^{-\beta\,H[U]}\ . \tag{8.15}$$

In terms of a simulation at β_a it can be rewritten as

$$\begin{aligned} Z[O,E;\beta] \ &\equiv\ \int d[U]\,\delta\left(O[U]-O\right)\,\delta\left(H[U]-E\right) \\ &\qquad\qquad \times R[U;\beta,\beta_a]\,e^{-(\beta-\beta_a)\,H[U]}\,\det\left[D(\beta_a)\right]\,e^{-\beta_a\,H[U]}\ , \end{aligned} \tag{8.16}$$

where the ratio of two fermion determinants

$$R[U;\beta,\beta_a] \equiv \frac{\det\left[D(\beta)\right]}{\det\left[D(\beta_a)\right]} \tag{8.17}$$

has been introduced. It is again possible to pull the exponential factors in front of the integral and to rewrite the resulting probability distribution, eq. (8.5), as

$$\rho[O,E;\beta] = \frac{Z(\beta_a)}{Z(\beta)}\,e^{-(\beta-\beta_a)\,E}\,\left\langle R(\beta,\beta_a)\right\rangle_{\beta_a;O,E} \equiv \frac{1}{Z(\beta)}\,e^{-\beta\,E}\,\mathcal{D}[O,E;\beta]\ . \tag{8.18}$$

This relation defines a now β-dependent density of states in terms of the expectation value of $R(\beta,\beta_a)$ in the canonical ensemble with fixed E and O. Note, that the explicit β-dependence of the expectation value permits the use of this density of states for a MH reweighting to one specific target coupling only. It is fixed by the determinant ratios that have to be measured in the course of the simulations. Together with the costly evaluation of the ratio this renders the procedure extremely expensive, in particular, if more than one target couplings should be considered.

In the numerical implementation the probability distribution at a simulation point β_a reduces to the frequency functions f^a_{IJ} since $R(\beta_a,\beta_a)=1$ and eq. (8.10) still holds. However, the estimate for the density of states at some other coupling β is not given directly in terms of f^a_{IJ}, but in terms of the expectation value of the determinant ratio evaluated on the appropriate bins

$$\left\langle R(\beta,\beta_a)\right\rangle_{\beta_a;O,E} \approx \left\langle R(\beta,\beta_a)\right\rangle_{\beta_a;\,\mathrm{IJ}}\ . \tag{8.19}$$

The generalisation of eq. (8.11) is then given by

$$\widetilde{\mathcal{D}}^a_{\mathrm{IJ}}(\beta) = \left\langle R(\beta,\beta_a)\right\rangle_{\beta_a;\,\mathrm{IJ}}\ e^{\beta_a\,(E_{\mathrm{I}}-F^a)} \tag{8.20}$$

and in eqs. (8.12) and (8.13) one has to replace $\widetilde{\mathcal{D}}^a_{\mathrm{IJ}} \to \widetilde{\mathcal{D}}^a_{\mathrm{IJ}}(\beta)$. Once again the method can be extended to the use of several histograms at a set of different simulation points $\{\beta_a\}$ by using eq. (8.14). In practice the appearance of the free energies impedes the applicability of the theory for two reasons:

1. Following the procedure from [361] for the calculation of optimised weights, the weights become β-dependent and thus cannot be used to calculate the free energies defined at β_a.
2. The determinant ratios which enter in the calculation of F^b, i.e. the ratios $R(\beta_b, \beta_a)$, have to be known for each value of b each configuration in addition to the ratios $R(\beta, \beta_a)$.

The first problem can be solved by making use of the freedom in the choice for the weights and by simply neglecting the reweighting effect of the determinant in their definition as discussed in subsection 8.2.3. The resulting weights do not depend on β and thus can be used in the computation of the densities for all target couplings of interest. The second problem will be dealt with in the following.

8.2.2 Expansion of the fermion determinant

The main problem so far is the costly evaluation of the determinant ratio for a large number of target couplings β. In addition, the latter have to be specified in advance. This problem spoils most of the good properties of the MH method that one is interested in. As proposed already in [363], a possible method to overcome this problem is to expand the ratio of fermion determinants as a series in $\Delta\beta$ and to measure its prefactors. Similar methods have already been used for single measurement reweighting [285, 365]. In practice, this is possible only if the series can be truncated at some early order, which appears to be the case for several actions. In particular, fermion actions that result from *Symanzik's* $\mathcal{O}(a)$-improvement program are promising since the change of the associated parameters with β are expected to be small (see the discussion from section 2.3).

For the following it is assumed that the fermion matrix can be decomposed as

$$D(\beta) = D_0 + C(\beta)\, D_1 \,, \tag{8.21}$$

where D_0 and D_1 are β-independent matrices with the same dimensions as $D(\beta)$ and $C(\beta)$ is a real number that contains the complete β-dependence of $D(\beta)$. Such a decomposition is not necessarily possible for all fermion matrices but applies to a lot of relevant cases. In particular, it applies to actions that are the result of an application of the $\mathcal{O}(a)$-improvement program to first order.

Given the decomposition in eq. (8.21), $D(\beta)$ can be rewritten as

$$D(\beta) = D(\beta_0) + \Delta C(\beta, \beta_0)\, D_1 \tag{8.22}$$

where $\Delta C(\beta, \beta_0)$ is defined by

$$\Delta C(\beta, \beta_0) \equiv C(\beta) - C(\beta_0) \,. \tag{8.23}$$

Equation (8.16) then reads

$$\begin{aligned} R(\beta, \beta_0) &= \det\left(D^{-1}(\beta_0)\, D(\beta)\right) \\ &= \det\left(1 + \Delta C(\beta, \beta_0)\, D^{-1}(\beta_0)\, D_1\right) \,. \end{aligned} \tag{8.24}$$

At this stage there are two possibilities how to proceed: Evaluate the ratio explicitly by using stochastic sources (cf. appendix B.1) or expand it in the small parameter ΔC. The latter is the choice to overcome the problems discussed above. As a first step it is possible to express eq. (8.24) as

$$R(\beta,\beta_0) = \exp\left\{\mathrm{Tr}\left(\ln\left[1+\Delta C(\beta,\beta_0)\,D^{-1}(\beta_0)\,D_1\right]\right)\right\}\ . \tag{8.25}$$

Expanding the logarithm in ΔC yields

$$R(\beta,\beta_0) = \exp\left\{\sum_{m=1}^{\infty}\frac{(-1)^{m+1}}{m}\,r_m(\beta_0)\ \left(\Delta C(\beta,\beta_0)\right)^m\right\}\ , \tag{8.26}$$

where the coefficients $r_m(\beta_0)$ are given by

$$r_m(\beta_0) = \mathrm{Tr}\left(\left[D^{-1}(\beta_0)\,D_1\right]^m\right)\ . \tag{8.27}$$

Depending on the size of these coefficients it is possible to expand the exponential in eq. (8.26) as well. Using this expansion, the expectation values $\langle R(\beta,\beta_a)\rangle_{\beta_a;\,\mathrm{IJ}}$ are given in terms of the expectation value of the operators $r_m(\beta_a)$ that are independent of the target coupling β which can then be chosen at will after the simulation.

The above discussion is easily generalised to the dependence on a set of parameters $\{C_n(\beta)\}$ with associated matrices D_n as long as a decomposition according to eq. (8.21) is possible. The expansion in eq. (8.26) then has to be done as a multi-dimensional Taylor series. For a MH method with more than one parameter C one should keep track of the mixing terms as they might give a sizable contribution to the reweighting factor [365]. For a linear approximation the systematic effect of the truncation can be monitored by using the data obtained for $r_1(\beta_a)$ which is the derivative of $\ln[R(\beta,\beta_a)]$ with respect to ΔC at point β_a. In consequence, nonlinear results in the exponential should also show up in the behavior of $r_1(\beta)$ with β.

8.2.3 A suitable choice for the weights

There is no restriction concerning the choice of the weights $w^a_{\mathrm{IJ}}(\beta)$ from eq. (8.14) which offers the freedom to optimise the weights with respect to the statistical uncertainty. Following the strategy of *Huang* and collaborators [360, 361] in the case of a β-dependent fermion determinant leads to

$$w^a_{\mathrm{IJ}}(\beta) = \frac{\left(\mathcal{B}^a_{\mathrm{IJ}}(\beta)\right)^{-1}}{\sum_b\left(\mathcal{B}^b_{\mathrm{IJ}}(\beta)\right)^{-1}}\ , \tag{8.28}$$

with [2]

$$\mathcal{B}^a_{\mathrm{IJ}}(\beta) = \frac{2\,\tau^a_O}{N_a}\ \langle R(\beta,\beta_a)\rangle^2_{\beta_a;\,\mathrm{IJ}}\ e^{2(\beta_a-\beta)\,(E_{\mathrm{I}}-F^a)}\ . \tag{8.29}$$

---

[2] Note the ambiguity in the definition of the integrated autocorrelation time τ_O. In the convention used in this thesis two measurements are completely uncorrelated if $\tau_O = 0.5$ which differs from the normalisation used in [360, 361].

The problem with this choice for the weights is that the F^a's, computed via

$$\begin{aligned} \widetilde{Z}(\beta_a) &= \sum_{\mathrm{IJ}} \widetilde{\mathcal{D}}_{\mathrm{IJ}}(\beta_a)\, e^{-\beta\, E_{\mathrm{I}}} \\ &= \sum_{\mathrm{IJ},b} w^b_{\mathrm{IJ}}(\beta_a)\; \langle R(\beta_a,\beta_b)\rangle_{\beta_b;\,\mathrm{IJ}}\; e^{-(\beta_a-\beta_b)\,E_{\mathrm{I}}}\; e^{-\beta_b\,F^b}\ , \end{aligned} \tag{8.30}$$

depend on different uncomputed weights $w^b_{ij}(\beta_a) \neq w^b_{ij}(\beta)$. This results in an ill-posed problem and hampers the calculation of $w^a_{\mathrm{IJ}}(\beta)$.

The solution is to make use of the fact that the choice for the weights is arbitrary and neglect the effect of the fermion determinant. In this case the weights are equivalent to the ones for the pure gauge case, given by eq. (8.28), with

$$\mathcal{B}^a_{\mathrm{IJ}}(\beta) \;\to\; \overline{\mathcal{B}}^a_{\mathrm{IJ}} = \frac{2\,\tau^a_O}{N_a}\, f^a_{\mathrm{IJ}}\, e^{2(\beta_a-\beta)\,(E_{\mathrm{I}}-F^a)}\ . \tag{8.31}$$

In practice, the numerically more stable choice for the weights in the pure gauge case is obtained if one uses the approximation $f^a_{\mathrm{IJ}}\, e^{\beta_a\,(E_i-F^a)} = \widetilde{\mathcal{D}}^a_{\mathrm{IJ}} \approx \widetilde{\mathcal{D}}_{\mathrm{IJ}}$, where here $\widetilde{\mathcal{D}}$ denotes the pure gauge approximation for the density of states. The resulting weights are then given by

$$w^a_{\mathrm{IJ}} = \frac{N_a\ (2\,\tau^a_O)^{-1}\ e^{-\beta_a\,(E_{\mathrm{I}}-F^a)}}{\sum_b N_b\ \left(2\,\tau^b_O\right)^{-1}\ e^{-\beta_b\,\left(E_{\mathrm{I}}-F^b\right)}}\ , \tag{8.32}$$

which is the generalisation of the weights used in [56, 57] (see also the discussion on this point in [360]).

The drawback of this approximation is the possibly larger statistical error and it might be worth including at least parts of the effect of the fermion determinant. To this end one might choose one particular β-value β_W in the region of the measurements for which the weights are optimised.

8.3 Observables and error estimation

For observables that are primary quantities the MH method is straightforward using the apparatus introduced in the last section. However, the formalism for one of the major tasks, the estimation of the error bars at the target couplings, is still missing. Furthermore, it is desirable to apply the method to more complicated observables like susceptibilities and Binder cumulants. These special topics are discussed in this section.

8.3.1 Susceptibilities

The generalised susceptibility $\bar{\chi}_O$ of the operator O as defined in eq. (7.2) is a secondary quantity since the expectation value of O has to be known to evaluate it. Its expectation value at target coupling β is given by

$$\langle\bar{\chi}(O)\rangle_\beta = \frac{1}{\widetilde{Z}(\beta)}\, V \sum_{\mathrm{IJ}} \Big(O_{\mathrm{J}} - \langle O\rangle_\beta\Big)^2\, \widetilde{\mathcal{D}}_{\mathrm{IJ}}(\beta)\, e^{-\beta\, E_{\mathrm{I}}}\ . \tag{8.33}$$

It is thus essential to first know the expectation value $\langle O\rangle_\beta$ in order to calculate $\langle\bar{\chi}(O)\rangle_\beta$. In fact, once the expectation value is known the susceptibility can be traced back to the pseudo-primary observable $(\delta O)^2$ from eq. (7.5). Then the only difference to the observable itself is that the size of a bin for $\bar{\chi}(O)$ defined by

$$\bar{\chi}_{\mathrm{J}}(O) \equiv \Big(O - \langle O\rangle_\beta\Big)^2_{\mathrm{J}} \,, \tag{8.34}$$

is different from the binsize of O_{J}, however there is a one-to-one mapping between the two. Due to the non-linear relation the bins $\bar{\chi}_{\mathrm{J}}(O)$ are not even of equal size for different J. However this is not a problem for the applicability of the method. It only has to be kept in mind when estimating the systematic uncertainties.

8.3.2 Statistic and systematic uncertainties and Binder cumulants

Important for the MH method is a reliable estimation of the statistical uncertainties at the target coupling β. One possibility to estimate the statistical error of the expectation value

$$\langle O\rangle_\beta = \frac{1}{Z(\beta)} \sum_{\mathrm{IJ}} O_{\mathrm{J}}\, \widetilde{\mathcal{D}}_{\mathrm{IJ}}(\beta)\, e^{-\beta\, E_{\mathrm{I}}} \tag{8.35}$$

is to use Gaussian error propagation. The quantities prone to statistical uncertainties are the canonical expectation values $\langle R(\beta,\beta_a)\rangle_{\beta_a;\mathrm{IJ}}$. In practice, the associated error cannot be estimated reliably from the measurements since the statistic for most of the bins IJ will be insufficient. For theories with β-independent fermion action the canonical expectation value reduces to f^a_{IJ} and thus is expected to obey a Poisson distribution [360, 361] for which the error is known to be f^a_{IJ}/N_a. This argument will not hold for fermions with a β-dependent fermion action since the full expectation value of course will obey a normal distribution for infinite statistic. One possibility would be to make a very crude assumption about the expected error on $\langle R(\beta,\beta_a)\rangle_{\beta_a;\,\mathrm{IJ}}$ for a particular bin by assuming that it obeys a Poisson distribution to a first approximation with some systematic uncertainty on top stemming from the reweighting factor. However, the resulting error estimate will be subject to systematic uncertainties. Furthermore, for secondary quantities such as Binder cumulants the estimation of the statistical uncertainty should ideally be done using jackknife or bootstrap error estimates. These methods can not be applied to the reweighted data directly since there is no prescription of how to perform the binning whilst keeping track of the weights.

An alternative is to set up the full MH analysis in a bootstrapped framework by randomly picking the data points from the individual simulation points that enter the MH analysis for each bootstrap sample. In this way the results from each sample can be treated like a usual bootstrap sample for a secondary quantity. Furthermore, this also allows to measure the impact of the poorly sampled bins directly and thus provides a solid estimate for the statistical uncertainties.

The first type of systematic effects entering the MH analysis is due to finite binsize for

E and A. As pointed out in [361] the effect can contribute an error

$$(\mathrm{E}\left[O,\beta\right])^2_{sys,Q} \leq \sum_{\text{bins}} \left| \frac{\partial \left\langle O \right\rangle_\beta}{\partial Q_n} \right| \frac{\Delta Q_n}{2} \tag{8.36}$$

at most, for a quantity Q binned in bins labeled with n of size ΔQ_n. For the bins of the observable O this upper bound is given by (see also [361])

$$(\mathrm{E}\left[O,\beta\right])^2_{sys,O} \leq \frac{1}{\widetilde{Z}(\beta)} \sum_{\mathrm{IJ},a} \left\langle R(\beta,\beta_a) \right\rangle_{\beta_a;\,\mathrm{IJ}} \; e^{-(\beta-\beta_a)\,E_\mathrm{I}} \; e^{-\beta_a\,F_a} \, \frac{\Delta O_\mathrm{J}}{2} \;, \tag{8.37}$$

which reduces to

$$(\mathrm{E}\left[O,\beta\right])^2_{sys,O} \leq \frac{\Delta O}{2} \tag{8.38}$$

if all bins are of equal size. For the energies with equivalent binsizes one obtains

$$\begin{aligned}(\mathrm{E}\left[O,\beta\right])^2_{sys,E} \quad &\leq \quad \frac{1}{\widetilde{Z}(\beta)} \sum_{\mathrm{IJ},a} \left| O_\mathrm{J} - \left\langle O \right\rangle_\beta \right| \, \left|\beta - \beta_a\right| \, \left\langle R(\beta,\beta_a) \right\rangle_{\beta_a;\,\mathrm{IJ}} \\ &\qquad\qquad \times e^{-(\beta-\beta_a)\,E_\mathrm{I}} \; e^{-\beta_a\,F_a} \, \frac{\Delta E}{2} \;.\end{aligned} \tag{8.39}$$

In addition, there are also systematic effects connected with the finite number of measurements and thus the finite extent of the histograms in the space of E and O. The systematics in the case of a single measurement and the corresponding extrapolation are discussed in detail in [360, 361] and are also valid for the truncated theory with the usual modifications. For the MH analysis with multiple measurements there are two different cases: (a) β is not inside of the interval of values β_a; (b) β is included in the interval. Case (a) corresponds to an extrapolation and can be treated similarly to the case of a single measurement. Case (b) is the interesting case for the MH analysis. In this case two neighbouring measurements might have an insufficient overlap in the histograms to ensure a reliable estimate for the density $\mathcal{D}_{ij}$. The result would then deflect to a mixture of the two asymptotic results from the neighbouring measurements. Despite the fact that this might lead to peculiar spikes in the behaviour of the reweighted points, this will also lead to the domination of noise in the histogram of the observable at a point in the critical region, the histogram 'decays'. This effect can thus be detected by looking at the histograms at the target couplings and its deviation from Gaussian distributions.

8.4 Application to non-perturbatively $\mathcal{O}(a)$-improved Wilson fermions

Concerning this thesis, the primary interest is to apply the method for two degenerate flavours of non-perturbatively $\mathcal{O}(a)$-improved Wilson fermions with the plaquette gauge action in the case of scans at constant κ or along LCPs. The Dirac operator connected with the action (2.30) is given by

$$D_{SW}\,\mathbf{1}_f = D_0\,\mathbf{1}_f + m_q\,\mathbf{1}_D\,\mathbf{1}_f + c_{SW}\;M_{SW}\,\mathbf{1}_f \;, \tag{8.40}$$

where D_0 is the massless Wilson Dirac operator associated with the action (2.18), $\mathbf{1}_f$ is the unit matrix in flavour space, $\mathbf{1}_D$ is the unit matrix in the space of the one-flavour Dirac operator and M_{SW} is the matrix associated to the additional term in eq. (2.30). Even if κ, or equivalently the bare mass m_q, remains constant, the Dirac operator has an explicit β-dependence encoded in the tuning of $c_{SW} = c_{SW}(\beta)$. For the gauge part of the plaquette action, eq. (2.13), the term $H[U]$ is given by

$$H\left[U\right] = \sum_P \left[1 - \frac{1}{3}\,\mathrm{ReTr}\left(U_P\right)\right] . \tag{8.41}$$

8.4.1 Expansion for scans with constant κ

First scans at a constant κ-value are considered. In this case the second term in eq. (8.40) remains constant and the complete β-dependence in D_{SW} is encoded in c_{SW}. The associated operators for the expansion in eq. (8.26) are given by

$$r_m(\beta_a)[U] = N_f\,\mathrm{Tr}\left(\left[D_{SW}^{-1}[U,\beta_a]\,M_{SW}[U]\right]^m\right) . \tag{8.42}$$

They can be measured using stochastic sources as discussed in section 4.3.1.

The first step towards a working MH method is the test of the expansion of the ratios of fermion determinants in the truncated form and its agreement with the full ratio. To this end the reweighting factor from eq. (8.17) has been computed stochastically using the method from [366], summarised in appendix B.1. To test the method an 8×24^3 lattice has been generated at $\beta = 5.82$ and $\kappa = 0.11$. The details of the scan are listed in appendix D.1. The determinant ratio has been calculated for β-values in the range of $5.75 \leq \beta \leq 5.87$ using 100 hits of Gaussian sources for each of the 300 configurations. At the same time the first 5 operators r_m have been measured using 10 hits of stochastic $Z_2 \times Z_2$ sources. The results for the ratios are listed in table D.2.

A good measure for the effect of the reweighting due to the fermion determinant is the relative size of the reweighting factor compared to the one stemming from the gauge action. For pure gauge theory the decrease in overlap between two β-values is controlled by the prefactor E in front of the difference $\beta - \beta_0$. When fermions are included an extra term is added in the exponential which effectively increases or decreases the β-value with equivalent overlap, depending on the sign in front of the additional term. Of course the size of this effect depends on the particular bin, but as it turns out the fluctuations in the reweighting factor for different configurations and thus different bins are small. Figure 8.1 (left) shows the relative size of the average fermionic term for the full determinant and the truncations of the series at first to third order, compared to the average gauge term in the exponential of the full reweighting factor. The plot shows that the effect of the fermion determinant remains at a level of roughly 5 % of the gauge reweighting term over the whole region of β-values and effectively decreases the overlap between different β-values. In particular, the difference between the full determinant and the truncated series only presents a minor effect at the sub-percent level. Peculiar is the fact that the inclusion of higher orders beyond the second does not improve the agreement between the truncated

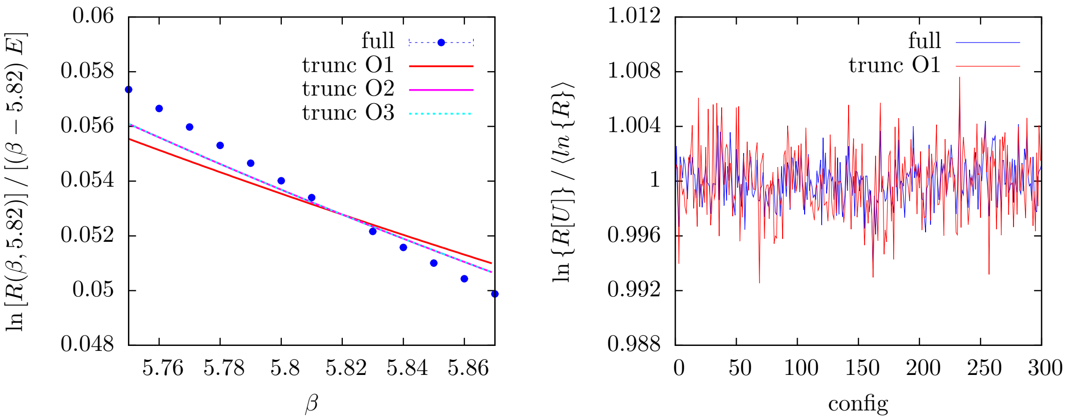

Figure 8.1: Left: Relative contribution of the fermionic term in the exponential of the reweighting factor to the contribution of the gauge action for different values of $\beta - \beta_0$. The results labeled with 'full' are the results from the stochastic estimate for the full ratio of the determinants while the results labeled with 'trunc On' are the results for the series from eq. (8.26) truncated at order n. **Right:** Monte-Carlo history of the 'full' term in the exponential of the fermionic reweighting factor and the result obtained from the truncated series to first order normalised to their expectation value.

series and the full determinant ratio. This indicates a small radius of convergence for the expansion. However, for a difference in β of about 0.01 both agree very well. In general, the effect seems to be at the per mille level and is likely negligible until the relative error on the observables shrinks to the sub-percent level.

Essential for the weight of the individual configuration is the value of the reweighting factor in comparison to its averaged value. This means that if both estimates for the reweighting factors, full and truncated ones, would lead to similar estimates for the relative reweighting factor for a particular bin, they have to agree in relative magnitude compared to their average on each configuration. This can be examined by looking at the fluctuations of the two estimates for the ratio along the Monte-Carlo history. If they show correlated fluctuations, both will give a similar relative weight for the different bins. The histories for the full determinant and the one truncated at first order, normalised to their mean value are shown in figure 8.1 (right). As can be seen, the fluctuations in the Monte-Carlo history of the two quantities are not identical. However, the fluctuations are in general small. Keeping in mind that the quantities are estimated stochastically, it is difficult to conclude whether these small fluctuations result from the stochastic measurement or whether they indicate true differences. Note that most of the peculiar spikes are reproduced by both reweighting factors, indicating that parts of the fluctuations should indeed be due to the properties of the configurations and are captured by both methods equivalently. However, a true test of the equivalence of the results can only be obtained by comparing results from the MH method with the two different methods to compute the determinant ratios. This

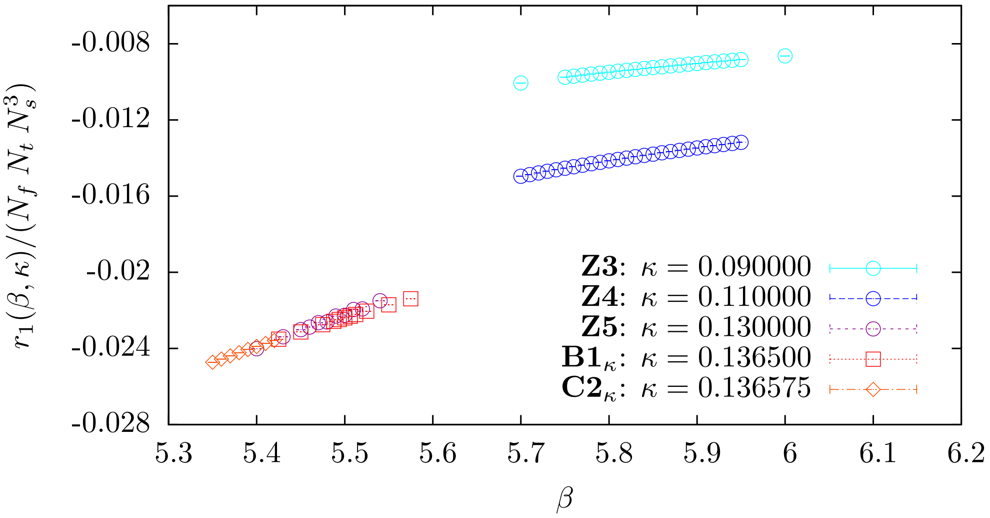

Figure 8.2: Results for the operator $r_1(\beta, \kappa)$ normalised by the lattice volume obtained for different scans at constant κ from section 9.2 and appendix D.1.

can be done for a few target β-values at moderate numerical effort.

So far the whole discussion has been done at a single point in bare parameter space with very heavy quarks at $\kappa = 0.11$. To get an idea of how the influence of the fermionic part changes when going to lighter quark masses one can have a look at the results for the operator $r_1(\beta, \kappa)$ for different values of β and κ. The results for $r_1/(N_f\ N_t\ N_s^3)$ in the scans from sections 9.2 together with the results from scans at larger quark masses as listed in appendix D.1 are shown in figure 8.1. When going to lighter quark masses the size of the operator increases by roughly a factor of two in comparison to its value in the discussion above. The importance for the fermionic part of the reweighting can be expected to increase by a similar factor. This means that for light quark masses the effect of the fermionic reweighting factor can be expected to be of order 10 %. In addition, the plot shows that for each scan the linear operator changes only slightly and approximately linearly with β. As noted earlier, this indicates that higher order terms will be small in the expansion of the determinant ratio since the derivative of $r_1(\beta, \kappa)$ with respect to β is related to the summed contribution of the higher order terms.

8.4.2 Scans along lines of constant physics

The final goal is to perform a MH analysis for scans along LCPs. In this case both parameters c_{SW} and m_q in eq. (8.40) change with β as the bare quark mass has to be tuned so that a constant renormalised quark mass is achieved. The operators associated with the expansion in Δc_{SW} remain unchanged and the ones for the expansion in Δm_q are

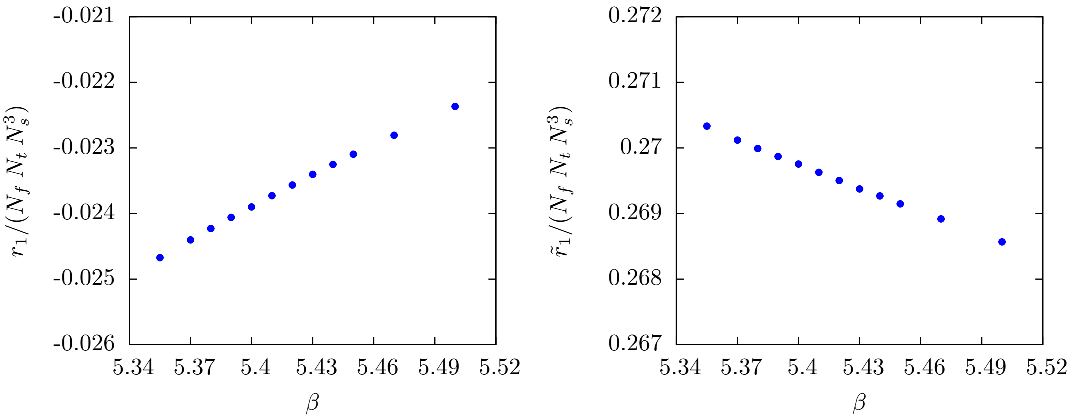

Figure 8.3: Behaviour of the two linear operators $r_1/(N_f\,N_t\,N_s^3)$ (left) and $\tilde{r}_1/(N_f\,N_t\,N_s^3)$ (right) from the double expansion in Δc_{SW} and Δm_q. The results are from scan **C1** (cf. section 9.3.2) which is done along a line of constant physics for a renormalised quark mass of 14.5 MeV.

given by

$$\tilde{r}_k(\beta_a)[U] = N_f\ \mathrm{Tr}\left(\left[D_{SW}^{-1}[U,\beta_a]\right]^k\right)\ . \tag{8.43}$$

The linear operator $\tilde{r}_1$ is equivalent to the chiral condensate summed over the volume. Note, that the two linear operators can be calculated with only a single inversion when the cyclic property of the trace is used. At second order, mixing terms appear due to the mixed derivatives in the expansion. The only mixing term that appears at second order in Δc_{SW} and Δm_q takes the form

$$\tilde{r}_{11}(\beta_a)[U] = N_f\ \mathrm{Tr}\left(D_{SW}^{-2}[U,\beta_a]\ M_{SW}[U]\right)\ . \tag{8.44}$$

In typical β-scans Δc_{SW} and Δm_q are both of order 10^{-2} and thus contribute equally to the terms in the expansion. The importance of the different terms thus depends strongly on the size of the operators.

The behaviour of the two linear operators r_1 and $\tilde{r}_1$ in the scan along a LCP at a renormalised quark mass of 14.5 MeV (or $m_\pi \approx 290$ MeV) from section 9.3.2 are shown in figure 8.3. As can be seen from the plot, the operator $\tilde{r}_1$ is an order of magnitude larger than r_1 and thus will dominate the fermionic part of the reweighting. In particular, the term from the reweighting factor can be expected to be of similar size to the reweighting factor due to the gauge action. It is then questionable whether the truncation of the series for the ratios of the fermion determinants is a valid approximation. The problem is that the truncation error might yield a sizeable effect, since it can be of the size of a few percent of the full reweighting factor. To get an accurate estimate for the truncation error of the expansion in Δc_{SW} and Δm_q it is necessary to make a similar comparison to measurements of the full determinant as done in the previous section for reweighting with constant κ. Since the computational cost for the inversions and thereby the evaluation of the fermion determinant increases drastically when going to lighter quarks this has not been done so far for scan **C1**.

8.4.3 Numerical implementation and perspectives

In principle, the numerical implementation of the method is straightforward, both for pure gauge theory and in the modified version including the fermionic reweighting factor. The only issue which involves some more thought is the calculation of the weights. As noted in section 8.2.3 the formula for the computation of optimised weights involves the computation of $Z(\beta)$ which itself depends on the weights. Thus the weights have to be determined using an iterative procedure. The details are discussed in appendix B.3. The major problem that occurs in a naive implementation is the appearance of large numbers due to the exponential factors in eqs. (8.12) and (8.26). In practice, these are numbers of the order e^{1000} and have to be summed over, rendering them much too large for usual 8-byte `double` numbers where the maximal value is approximately $\sim e^{307}$.

A method to circumvent this problem in pure gauge theories is to cancel the factor $\exp(-(\beta - \beta_a)\, E_{\text{min}})$. It appears in each term of the sum, the normalisation factor in the expectation values (8.12) and equivalently in the two terms of the exponential in the definition of $\widetilde{\mathcal{D}}^a_{\text{IJ}}$ from eq. (8.11). Here E_{min} is the minimal value for $H[U]$ that appears within the simulations. In consequence, the exponential factors only include numbers of the size $(\beta - \beta_a)\,(E - E_{\text{min}})$ that are smaller then 300 for typical values of $(\beta - \beta_a)$. In an analysis including a fermionic reweighting factor this is still possible for the gauge part of the reweighting, but not for the fermionic part where no overall factor for the densities from different β_a's is present.

This particular problem currently hampers the implementation of the extended method. A possible way to overcome it would be to use libraries that are able to deal with variables of arbitrary precision and in turn arbitrary large exponents, like the freely available CLN library [367] or the 'GNU Multiple Precision Arithmetic Library' [368]. Anyhow, with larger precision standard operations like multiplications and summations need more floating point operations and thus become computationally more expensive. This is in particular problematic if the analysis has to be done within a bootstrap where the calculation of the weights has to be done in the order of a thousand times and the convergence usually takes a few hundred iterations (in the pure gauge case). The next step is to implement one of these libraries in the program and to see if the performance of the resulting analysis code is sufficient.

9 Approaching the $N_f = 2$ phase diagram

This chapter contains the current status of the project that probes the thermal transition in the chiral limit for two degenerate flavours using Wilson fermions. Parts of the very time consuming simulations are still ongoing, so that the question of the nature of the transition in the chiral limit could not be settled yet. The chapter starts with a detailed presentation of the simulation setup. The second section contains tests of the setup and provides useful input for the simulations in the approach to the chiral limit. The following sections then present the current status concerning scans along LCPs in the approach to the chiral limit. The final section contains a short summary and discussion, a detailed account on the strategy for a future scaling analysis and research perspectives. Parts of the results presented in this chapter were already published in [363, 369].

9.1 Computational setup

9.1.1 Phase structure of Wilson fermions

The plane of bare parameters (β, κ) for two degenerate flavours of Wilson fermions is split in two domains by the line where the hopping parameter takes its critical value κ_c and the quark mass is zero. Above this line there is a region of unphysical negative mass. In the region of small β-values the critical line opens into a parity violating phase, the Aoki phase [370, 371], which has been investigated for $\mathcal{O}(a)$-improved Wilson fermions in detail in [332] using the Iwasaki gauge action. While the location of the Aoki phase depends on the gauge action its existence does not, as it is a general feature of Wilson fermions. Figure 9.1 shows a sketch of the phase structure for improved Wilson quarks with the plaquette gauge action. For this particular choice of the action the exact location of the Aoki phase is not known, but no sign of the Aoki phase has been found in simulations above $\beta = 5.20$ so far. These phases are general features of Wilson fermions for all temperatures so that the critical line $\kappa_c(\beta)$ is equivalent for $T = 0$ and non-zero temperatures.

At non-zero temperature there is an additional phase boundary associated with the thermal phase transition, $\kappa_T(\beta)$. As the temperature is given by $T = 1/(a\,N_t)$ the critical line will depend on the temporal extent N_t and, in principle, also on the volume. As there is no strict argument from theory that the deconfinement transition and chiral symmetry restoration have to take place at the same temperature there can in principle be two separate lines for each of them. However, lattice simulations indicate that both transitions occur at the same temperature [53, 320, 332]. Furthermore, at sufficiently large quark masses the transition is a broad crossover rather than a true transition. This renders the definition of the transition ambiguous as the transition takes place in a wide region rather than a well defined singular point. In consequence, estimates for the transition point from different observables do not necessarily have to yield identical results. Figure 9.1 also includes a sketch of a thermal transition line with associated 'hot' $(T > T_C)$ and 'cold' $(T < T_C)$ regions. It is important to note that there is a curvature in the thermal phase

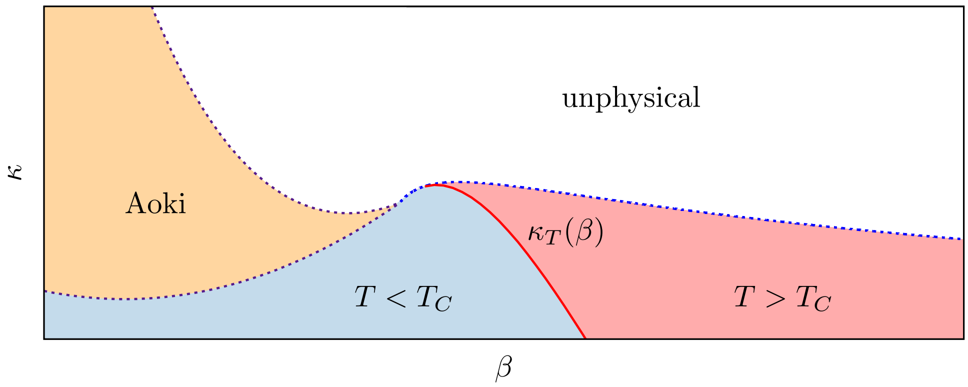

Figure 9.1: Sketch of the phase structure of (improved) Wilson fermions at $N_f = 2$ in the plane of bare parameters (β, κ). The figure is based on the study of the Aoki phase from [332] and the experience gathered in the course of the present study.

boundary that leads to a maximum for larger values of N_t. This was found to appear for N_t-values larger than 10 [320] at least. This 'cusp' at $(\beta_{\mathrm{cu}}, \kappa_{\mathrm{cu}})$ of the critical line signals the point in bare parameter space where a change in β at fixed κ no longer leads to a crossing of the phase boundary due to a change in temperature. Instead, the crossing happens due to a lowering of the pion mass and the associated decrease of the transition temperature. For the tuning of bare parameters this means that it is essential to choose κ carefully so that $\kappa < \kappa_{\mathrm{cu}}$. In practice, this is difficult as the precise location of the cusp is not known *a priori*.

9.1.2 Scan setup

In this study the thermal transition is probed using scans in the temperature by varying the bare coupling β at fixed N_t and fixed hopping parameter κ or along LCPs. The latter is the preferred choice but the tuning of κ to ensure constant renormalised quark mass is difficult. The algorithms used for the simulations are the DD-HMC and MP-HMC algorithms that were also used for the simulations at $T = 0$. As the spectrum of the Dirac operator changes with the temperature some tuning has to be done to ensure that the algorithm also works well at finite temperatures. The associated tuning and the performance of the algorithm is discussed in detail in appendix D.3. When going to smaller quark masses the simulations become more difficult as expected from the discussion in chapter 3. This is especially true in the confined region, where configurations with very small eigenvalues of the Dirac operator appear on occasion on which the solver has problems to converge. This problem can be cured to some extent by carefully tuning the parameters of the DFL-SAP-GCR solver (cf. appendix D.3).

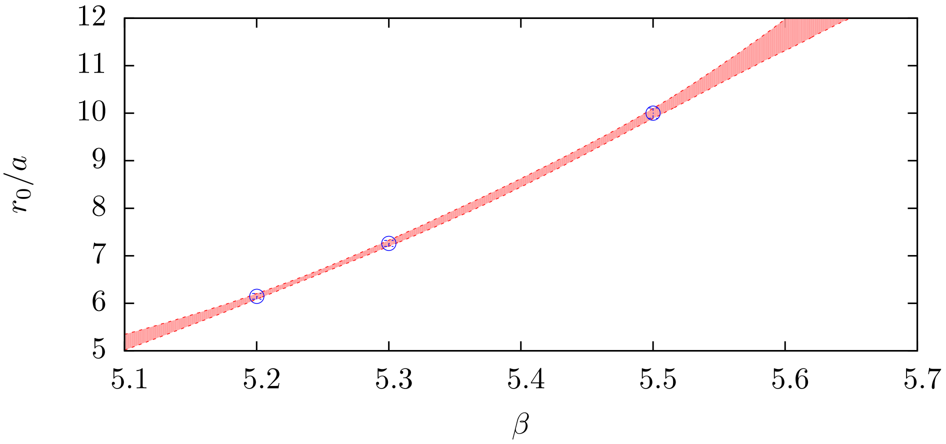

Figure 9.2: Results for the interpolation of the results for r_0/a from table 5.2 with the phenomenological ansatz from eq. (9.2). The fit parameters are listed in table D.3 in the appendix.

The measurements of the quantities relevant for the phase transition are done 'on-the-fly', i.e. during the generation of the gauge ensembles. This procedure provides the possibility to keep the number of configurations that have to be stored on disk low and thereby saves on the limited disk space. The inline measurements are conventionally performed with a measurement frequency $f_{\text{meas}} = 4$ MDU unless stated otherwise. Every measurement contains the computation of bare and APE-smeared Polyakov loops and bare and subtracted chiral condensates. The condensates are measured with a $Z_2 \times Z_2$ volume source and four hits per configuration. This setup enables one to use a different hit for each appearance of $\delta\langle\bar{\psi}\psi\rangle$ (cf. eq. (7.5)) in the susceptibility and the Binder cumulant. This results in improved and unbiased estimates for these quantities. The error analysis is done using 1000 bootstrap samples obtained from binned data. External quantities are, as before, included using pseudo-bootstrap bins (cf. appendix A.4).

In the approach to the chiral regime all simulations are performed with lattices of a temporal extent of $N_t = 16$. This particular choice has the following advantages: $N_t = 16$ (which defines the inverse lattice spacing at the critical point) is sufficiently large, so that experience from other simulations at non-zero temperature on much coarser lattices implies that cut-off effects will be small. Also the explicit breaking of chiral symmetry as an $\mathcal{O}(a^2)$-effects can then be expected to be small. Furthermore, it is possible to get close to the chiral limit without needing to go below $\beta = 5.20$ (where $T \approx 150$ MeV). Finally, the use of $N_t = 16$ is advantageous for DD-HMC and MP-HMC algorithms in combination with the DFL-SAP-GCR solver as it results in more flexibility in the tuning of the included block sizes (see appendix D.3). To control finite volume effects, aspect ratios of $N_s/N_t = 3$ to 4 (or even larger) are necessary. For this setup this means that one has to simulate large lattices such as 16×48^3 or 64^3. Here the excellent scaling properties of the algorithms with the volume are particularly useful since they keep the computational effort at a modest level. To control finite size effects and to be able to perform a FSS analysis the aim is to obtain a final set of scans with three different volumes, 32^3, 48^3 and 64^3, corresponding to aspect ratios of $N_s/N_t = 2, 3, 4$ respectively.

9.1.3 Scale setting

The lattice spacing is determined using the Sommer parameter in the chiral limit as in the analysis at $T = 0$. To determine the renormalised quark mass one can use the PCAC mass with the same renormalisation scheme as for $T = 0$. Since the temporal direction is short it is convenient to use one of the spatial directions, here the x^3-direction, for the extraction of the PCAC mass from the operator identity in eq. (2.45).

The remaining task for the scale setting is to provide a prescription for the interpolation of the r_0/a-values from [77] as listed in table 5.2. To leading order in the lattice β-function the solution for the renormalisation group equation for the bare coupling, eq. (2.9), is given by (see [372])

$$a(g_0) \sim \exp\left(-\frac{1}{\sqrt{12}\, b_0}\,\beta\right) , \quad \text{with} \quad b_0 = \frac{11}{4\,\pi^2} \, . \tag{9.1}$$

Higher orders of the β-function mainly modify the expression in the exponential. Following the strategy in [372] it is thus suitable to parameterise the β-dependence of r_0/a from [77] using the phenomenological ansatz

$$\frac{r_0}{a}(\beta) = \exp\left(\bar{a}_0 + \bar{a}_1\,\beta + \bar{a}_2\,\beta^2 + \ldots\right) \, . \tag{9.2}$$

The resulting interpolation formula for the three values for r_0/a is shown in figure 9.2. The error bars are obtained from the bootstrap samples for the parameters. The details of the interpolations are given in appendix D.2. To check for the dependence of the interpolation on the functional form the results have been compared to a parametrisation in terms of a conventional polynomial. Both agree almost perfectly for the whole region of interest.

It is also useful to have an interpolation formula for the critical hopping parameter. The results for this interpolation are discussed in appendix D.2 as well. For convenience the quark mass can also be related to an effective pion mass using χPT to NNLO via the formulae from appendix A.6 and the LECs from fit **Ac** from table 6.3. This allows for an easier comparison with other results in the literature since it is standard to set the mass scale via the zero temperature pion mass.

9.2 Testing the setup

Before the simulations in the chiral regime can be started it is necessary to test the algorithm, its tuning and the implemented inline measurements. In addition, it is necessary to gain experience with the signals, check its quality and get a first idea where the phase transition might be located in the two-dimensional bare parameter space. The latter enables the accurate estimate of possible transition points. This section contains an account of the results obtained in this phase of testing.

scan	Lattice	DD	κ	β-range	τ_{U_P} [MDU]	MDU
$\mathbf{A}_\kappa$	12×24^3	6^4	0.135950	$5.270 - 5.320$	~ 60	~ 50000
$\mathbf{B1}_\kappa$	16×32^3	8^4	0.136500	$5.355 - 5.750$	~ 10	~ 20000
$\mathbf{B3}_\kappa$	16×64^3	8×4^3	0.136500	$5.481 - 5.513$	~ 46	~ 16000
$\mathbf{C2}_\kappa$	16×48^3	8^4	0.136575	$5.350 - 5.420$	~ 12	~ 16000

Table 9.1: Set of scans at $N_t = 12$ and $N_t = 16$ and at constant κ. The runs where done using the DD-HMC algorithm and the column labeled DD gives the size of the associated blocks. Also listed are the integrated autocorrelation time of the plaquette at the estimate for the transition point τ_{U_P} and the number of MDUs used in the analysis. More details about the scans such as run-parameters and detailed lists for each β-values as well as the results for quantities controlling the algorithm performance are given in tables D.6 to D.9 in appendix D.4.

It is useful to first check the algorithm and the inline measurements at a known critical point in bare parameter space for a computationally cheaper lattice. Here a suitable test case is the critical point $(\beta, \kappa) = (5.29, 0.13650)$ for $N_t = 12$, known from the scans performed by the QCDSF/DIK collaboration [320]. The scan $\mathbf{A}_\kappa$ from table 9.1 is designed to probe this transition point in the framework of β-scans that are complementary to the scans in κ used in [320]. The results for this scan have already been published in [363,369] and are shown in figure 9.3. The grey band corresponds to the estimate for the transition region, $5.293 \leq \beta \leq 5.304$. Here the critical region is extracted naively using the position of the peak and the spread of the nearest neighbouring points up to the point where the susceptibility shows the onset of the rise in the approach to the high temperature regime. A more systematic way to extract the transition region will be used for the scans in the chiral regime (cf. section 9.3.2). As expected for this weak crossover at large quark mass, the signal of the transition is weak. However, the real part of the Polyakov loop shows the expected increase together with an increase and a peak in its susceptibility. For this scan the chiral condensate has not been measured. The resulting estimate for the transition region tends to lie a bit above the expected value but not significantly, given the size of the uncertainties, the weak signal and the fact that the transition is a broad crossover. The associated transition temperature in physical units is given by

$$T_C(m_\pi \approx 600\,\text{MeV}) = 236\,(1)(7)\,\text{MeV}\ . \tag{9.3}$$

Note that this result differs slightly from the one quoted in [369] since the estimate for the scale has changed with the new estimates from [77].

The rescaled results between bare and smeared Polyakov loop agree well and show an identical behaviour in the vicinity of the transition. This confirms that the use of smearing does not change the thermodynamic properties of the operator. The susceptibility of the smeared Polyakov loop usually shows a more pronounced signal, already at lower statistics, as expected from the findings in [328]. Peculiar is the appearance of relatively large autocorrelation times compared to the ones from scan $\mathbf{B1}_\kappa$ discussed later. These are

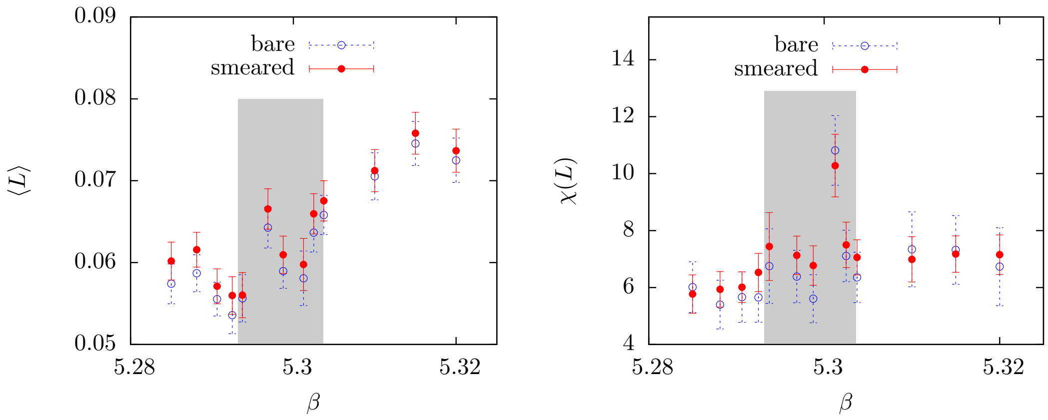

Figure 9.3: Results for the real part of the bare and the APE-smeared Polyakov loop (left) and their susceptibilities (right) for scan $\mathbf{A}_\kappa$. The results for the bare Polyakov loop are rescaled by a factor 8 to fit in a single plot together with the APE-smeared results.

mostly due to the use of the DD-HMC algorithm with a small DD block size of 6^4. This limits the number of active link variables to roughly 20 %. A significant gain in terms of autocorrelation times can thus be expected when going to larger DD blocks of 8^4 that will be used at $N_t = 16$. There the number of active links is already increased to approximately 33 %. Furthermore, in the MP-HMC algorithm all links are active which can be expected to yield a decrease by a factor of 3 in the autocorrelations compared to the DD-HMC algorithm with a block size of 8^4. Apart from the relatively large autocorrelation times the algorithm works stable and fast.

The next step is to start the simulations at $N_t = 16$. Note that $N_t = 16$ is the largest temporal extent used for temperature scans with dynamical fermions so far. Even with cheaper staggered fermions there is only one collaboration that reported scans on these lattice sizes [303]. A good performance of the algorithm is thus essential for this step. The first scan at $N_t = 16$ is done with two volumes, denoted by $\mathbf{B1}_\kappa$ and $\mathbf{B3}_\kappa$ in table 9.1. The location of the simulation points in the (T, m_{ud})-plane are shown in figure 9.4. From now on the $\overline{\text{MS}}$-scheme at a renormalisation scale of $\mu = 2$ GeV is conventionally used for the quotation of quark masses. The DD-HMC algorithm performs well for small lattices and allows to simulate 16×32^3 lattices on 64 processors on small cluster architectures at low computational cost. The larger 16×64^3 lattices have to be done on larger clusters where the MP-HMC algorithm works better. The details of the performance tests are reported in appendix D.3.

The results for L_{SM}, the bare chiral condensate and their susceptibilities for scans $\mathbf{B1}_\kappa$ and $\mathbf{B3}_\kappa$ are shown in figure 9.5 (upper four plots). The chiral condensate has been measured on the stored configurations for the 16×32^3 lattice only and thus has limited statistics. Again the grey area marks the estimate for the transition region estimated from the behaviour of L_{SM}. The estimate for the transition point is listed in table 9.2. The bare

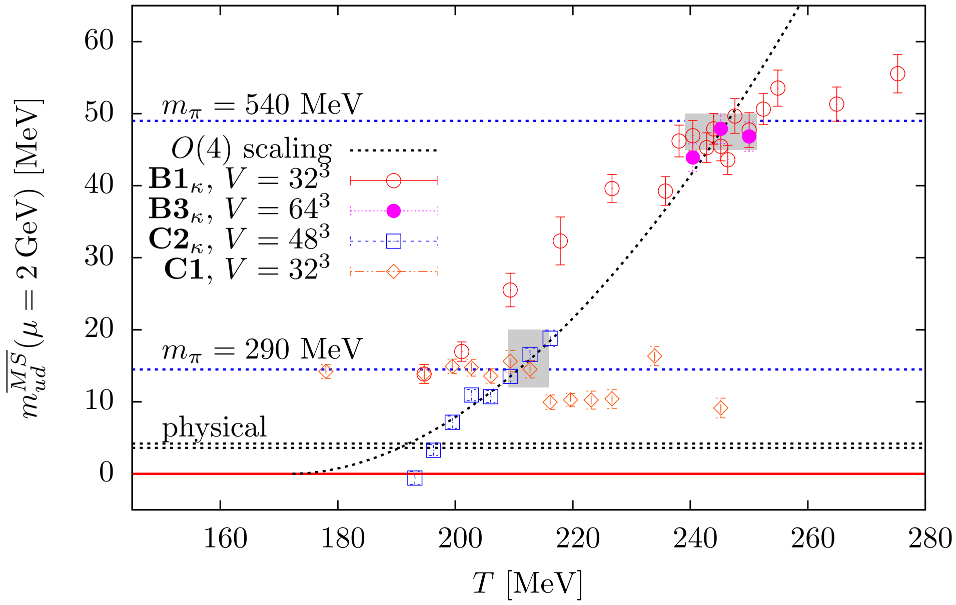

Figure 9.4: Simulation points in the (T, m_{ud})-parameter space. The black dashed line results from a naive test of $O(4)$-scaling for the two transition temperatures using eq. (7.41). It gives a first impression on the possible behaviour of the location of the critical line.

condensate also shows a peak in the crossover region. Again, the signal of the transition is weak in general, which can be expected due to the broad crossover, and for this large quark mass the signal of the Polyakov loop is stronger than the signal from the chiral condensate. The signal in the susceptibility of the condensate will become more pronounced when going closer to the chiral limit. Furthermore, the signals can be expected to be enhanced for scans along LCPs where the angle in which the transition is crossed is larger than for scans at constant κ (cf. figure 9.4). The results of the larger volume, scan **B3**$_\kappa$, seem to indicate a slightly smaller value for the transition point. To clarify the picture additional simulations at smaller temperatures would be necessary. However, since the runs on the large lattices are rather expensive and the exact transition temperature of the scan at this large quark mass is only of minor importance for the approach to the chiral limit these will not be done. The important output is, the possibility to get accurate results from scans on the large 16×64^3 lattices on acceptable timescales.

After settling the algorithmic issues, checking the measurements and the signals one has to obtain further information on the behaviour of the critical line. An obvious next step is to lower the pion mass to about 300 MeV at the transition point. This is on the edge of the desired chiral regime. The associated scan is denoted as scan **C2**$_\kappa$ and is done on a 16×48^3 lattice. As can be seen from the plot, the quark masses in the scan reach down to the chiral limit. In consequence, the scan serves as a benchmark for the algorithm

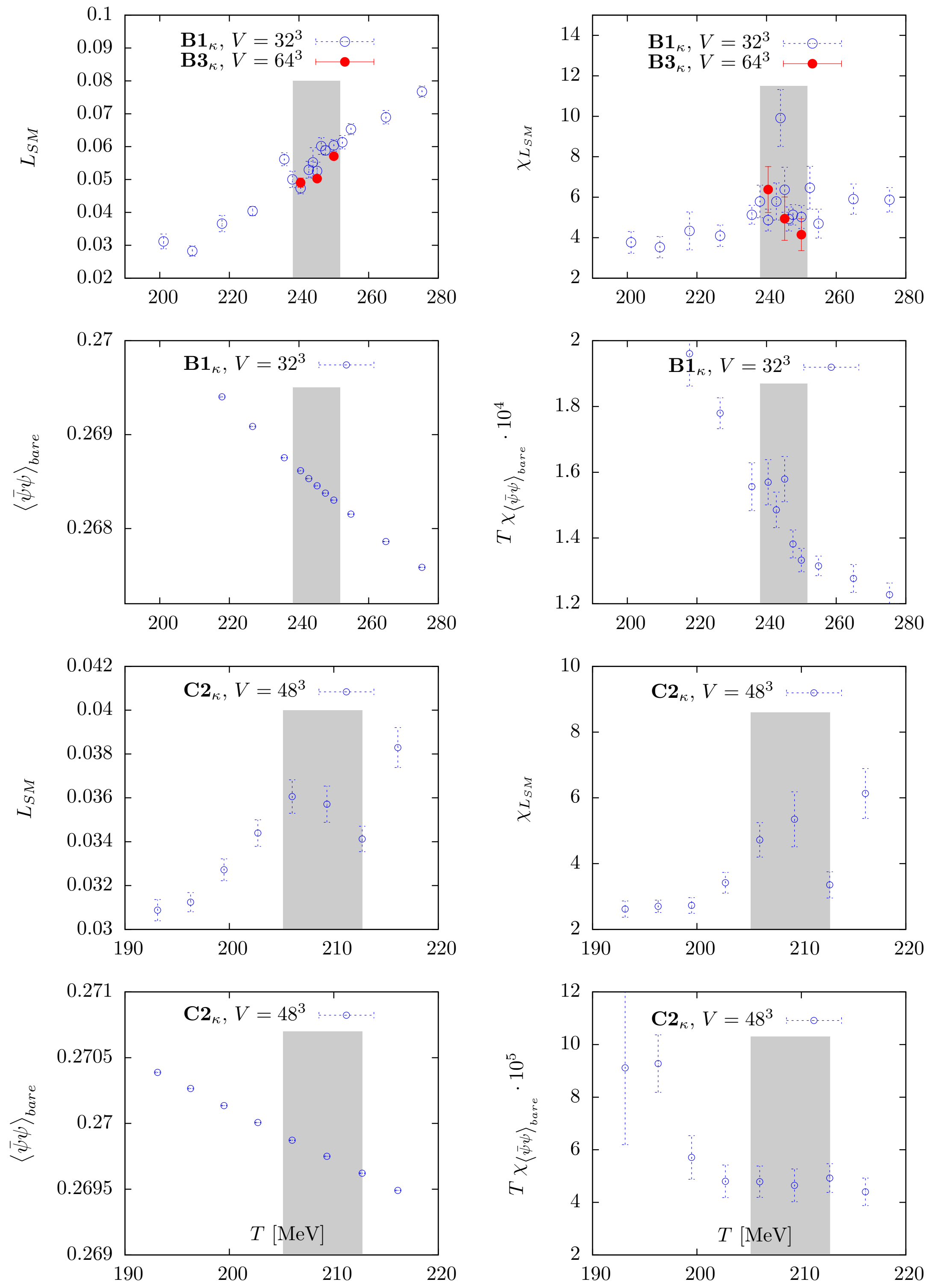

Figure 9.5: Results for the smeared Polyakov loop L_{SM} and the bare chiral condensate $\langle\bar\psi\psi\rangle_{\mathrm{bare}}$ (left) and their susceptibilities (right) for scans **B** (top four plots) and scan $\mathbf{C}_\kappa$ (lower four plots). The grey areas indicate the estimate for the transition region.

scan	T_C [MeV]	$m_{ud,C}$ [MeV]	$m_{\pi,C}$ [MeV]
$\mathbf{B1}_\kappa$ and $\mathbf{B3}_\kappa$	245 (7)(6)	45 (2)(2)	512 (30)(15)
$\mathbf{C}_\kappa$	209 (4)(5)	14 (3)(1)	280 (30)(11)

Table 9.2: Estimates for the transition points for scans $\mathbf{B}_\kappa$ and $\mathbf{C}_\kappa$ extracted from the behaviour of the Polyakov loop. The first error bar reflects the uncertainty due to the extraction of the peak position. For the estimates for the masses this means that half of the spread of the masses in the peak region has been used to estimate this uncertainty. The second error denotes the uncertainty due to scale setting and renormalisation.

at small quark masses. Again the details of the benchmark are discussed in the appendix. The main result is that the algorithm proves stable and shows a good performance down to physical quark masses.

The results for the observables are shown in figure 9.5 (lower four plots). The Polyakov loop shows the expected rise, accompanied by a peak structure in its susceptibility and the grey band shows the corresponding estimate for the crossover region as listed in table 9.2. There are some fluctuations both for the expectation value and the susceptibility which leave some doubt about the interpretation of the signal. The rise in the Polyakov loop is by almost an order of magnitude smaller as what one would have expected from the signals from scan $\mathbf{B1}_\kappa$. Furthermore, the susceptibility of the chiral condensate shows no peak. The reason for this becomes apparent when looking at a naive analysis of the two estimates from the transition points, discussed below. The analysis implies that the scan effectively scans along, or at least close to, the phase boundary (see the position of the data points in comparison to the black dashed line in figure 9.4). In other words this means that $\kappa \approx \kappa_{\text{cu}}$. This explains the weak signal in the observables but at the same time leaves some doubt about the correctness of the extracted transition point. This point will be probed again by the scan along an LCP in the next section.

To perform the first naive scaling analysis mentioned above, one can make use of the knowledge from [53, 320] that eq. (7.41) with $O(4)$-critical exponents describes the behaviour of the transition temperatures reasonably well, at least for larger quark masses. This is helpful for two reasons: It helps to estimate transition points for future runs at smaller quark masses and it allows one to extract the approximate location of the cusp of the thermal critical line in bare parameter space. The result for the naive scaling of the two available transition points is shown as the black dashed line in figure 9.4. Note that it yields a very rough estimate of $T_C \approx 172$ MeV for the transition temperature in the chiral limit. This of course is by no means a reliable estimate but it is reassuring that it lies already in the region of what is expected [53, 320, 321].

To sum up, the algorithm works as expected and seems to be capable to perform simulations close to the physical point at acceptable numerical cost. For scan $\mathbf{B}_\kappa$, where one can be sure to cross the phase boundary, there is a weak but clear signal for a transition which is in agreement with the fact that for these quark masses the transition can be expected to be a broad crossover. The problems observed for scan $\mathbf{C2}_\kappa$ are probably due

z_0	z_1	z_2	χ^2/dof
55 (37)	-20 (14)	1.8 (13)	0.2

Table 9.3: Results for the fit parameters for a fit to the $T = 0$ data for the bare PCAC-mass to the form of eq. (9.5) neglecting the quadratic term and using the ansatz from (9.6) for $\mathcal{Z}_{\mathrm{PCAC}}(\beta)$.

to the fact that it is done approximately at κ_{cu}. This also indicates that scans at smaller quark masses have to be done along LCPs since scans at constant κ demand a fine tuning between the thermal and the chiral critical line in the high temperature region.

9.3 Towards the chiral regime

After the preparatory work this section contains first results for scans along LCPs in the inquest of the chiral regime. Before discussing the results of the scan at a quark mass of $m_{ud} \approx 14.5$ MeV the first part of this section gives an account of the parameter tuning to realise LCPs.

9.3.1 Parameter tuning for lines of constant physics

LCPs can be estimated by using the data from simulations at zero temperature. A very simple method to obtain an estimate for the bare parameters for an LCP at some given quark mass is to first interpolate the κ values in m_{ud} of the known $T = 0$ lattices to the quark mass of interest at each β-value separately. The resulting κ values can then be interpolated using a quadratic polynomial in β. This version of tuning has been used to estimate the current LCP at $m_{ud} \approx 14.5$ MeV, or at a pion mass of $m_\pi \approx 290$ MeV. Note, that the run parameters have been estimated before the values for r_0 and the quark masses have been updated in [77]. In consequence, the LCP is imperfect above $\beta = 5.41$ as can be seen from the associated points in figure 9.4.

For a more systematic way to tune the parameters for future scans it is preferable to have an analytic relation between m_{ud}, β and κ that provides accurate results in the whole region of interest. For Wilson fermions where chiral symmetry is broken explicitly the bare mass obtains an additive renormalisation. The renormalised PCAC mass from eq. (2.46) and the renormalised subtracted bare quark mass $\bar{m}$ from eq. (2.41) are both equivalent to the renormalised quark mass m_{ud} if both are renormalised in the same scheme. This implies that the PCAC mass and the bare quark mass are related by [110]

$$m_{\mathrm{PCAC}} = \mathcal{Z}_{\mathrm{PCAC}} \; (1 + [b_m + b_P - b_A] \; a\bar{m}) \; \bar{m} \; . \tag{9.4}$$

Here the factor $\mathcal{Z}_{\mathrm{PCAC}}$ accounts for the difference between the PCAC and the bare quark mass and the term in the brackets ensures consistency with $\mathcal{O}(a)$-improvement. It is important to note that the factor $\mathcal{Z}_{\mathrm{PCAC}}$ depends on the action and the bare coupling but

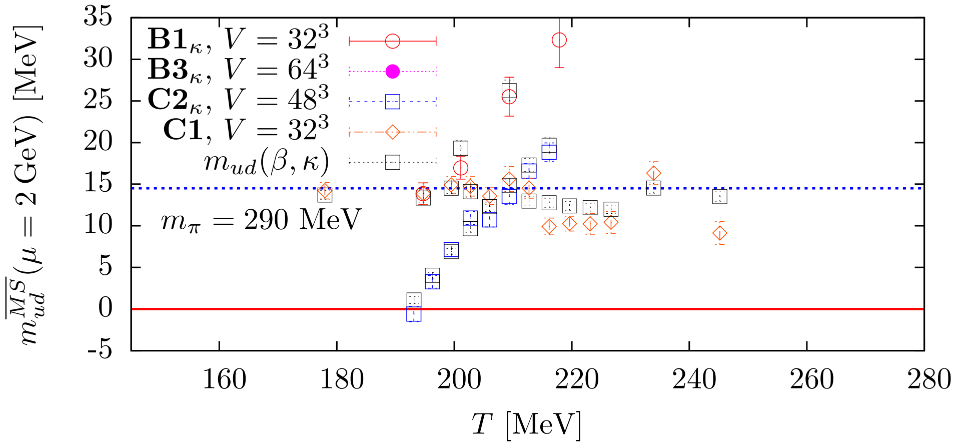

Figure 9.6: Comparison between the predictions obtained from the relation $m_{ud}(\beta, \kappa)$ described in the text and the simulation results for m_{ud} for small quark masses.

relates two scheme independent quantities and thus has to be scheme independent as well. Inserting eq. (2.24) for $\bar{m}$ one obtains

$$m_{\text{PCAC}}(\beta, \kappa) = \frac{\mathcal{Z}_{\text{PCAC}}(\beta)}{2}\left(\frac{1}{\kappa} - \frac{1}{\kappa_c(\beta)}\right) + \mathcal{Z}_2(\beta)\left(\frac{1}{\kappa} - \frac{1}{\kappa_c(\beta)}\right)^2 + \dots\,, \tag{9.5}$$

where $\mathcal{Z}_2(\beta)$ contains the terms in the brackets from eq. (9.4). To first order in perturbation theory the prefactor of the second term is small as can be seen from the expressions for b_m, b_P and b_A in appendix A.2. For small renormalised quark masses $\bar{m}$ is small as well and the second term will most likely be negligible. For $\kappa_c(\beta)$ one can use the interpolation formula (D.3) with the parameters from table D.3. The remaining task is to obtain the factor $\mathcal{Z}_{\text{PCAC}}(\beta)$. Here the ansatz

$$\frac{\mathcal{Z}_{\text{PCAC}}(\beta)}{2} = z_0 + z_1\,\beta + z_2\,\beta^2 \tag{9.6}$$

is used to fit eq. (9.5) to the data from $T = 0$ for the bare PCAC mass listed in table D.4 in appendix D.2. The fit works well and produces a small χ^2/dof of 0.2. The resulting fit parameters are listed in table 9.3. Using this relation between β, κ and m_{PCAC} the renormalised quark mass is obtained using eq. (2.46). The renormalisation and improvement constants are the same as in the $T = 0$ case (cf. table 5.1 and the formulae in appendix A.2).

To check the predictability of the method one can look at the associated predictions for the quark masses for the current set of scans and compare them to the results from the simulations at $T \neq 0$. This comparison is shown in figure 9.6. As can be seen from the plot the agreement between the predictions and the simulations is quite good. The points obtained in the simulation scatter around the predictions with a maximal deviation

scan	Lattice	DD	m_{ud} [MeV]	T-range [MeV]	τ_{U_P} [MDU]	MDU
C1	16×32^3	8^4	14.5 (45)	$175 - 250$	~ 14	~ 12000

Table 9.4: Parameters of the available scan along an LCP. The error on the quark mass is given by the full spread of quark masses along the scan. Note that this does not reflect the uncertainty for the quark mass at a particular simulation point. More details can be found in appendix D.4.

of 20 %. The only exception are the points at a temperature of ~ 245 MeV. There the PCAC masses between the runs at finite temperature and zero temperatures do not agree that well. However, future scans will be located at temperatures between 150 to 230 MeV where the agreement between predictions and the results is good. The associated runs at higher temperatures then might require some further tuning. In the following analysis the analytic relation $m_{ud}(\beta, \kappa)$ is used to define the quark mass in the normalisation of quantities (such as the subtracted condensate) in order to avoid fluctuations in the quark mass obscuring the signal of the normalised observables.

9.3.2 Extraction of the transition point and first results

Table 9.4 contains the parameters for the scan along a LCP at $m_{ud} \approx 14.5$ MeV (or $m_\pi \approx 290$ MeV). As before, the estimates for the transition temperature can be obtained from the peaks in the susceptibilities of the approximate order parameters. As the order of the transition in the chiral limit can be obtained from the scaling of the transition temperature with the quark mass, it is desirable to have a reproducible and systematic definition for the estimate of the transition temperature for a particular observable at a given quark mass. One possibility is to model the behaviour of the susceptibility in the transition region by a Gaussian and extract the transition temperature by the position of the maximum. This method has also been used by the QCDSF/DIK and tmfT collaborations [53, 320]. Here this ansatz will be used as well. However, one should keep in mind that the method relies on the approximation of the peak with a Gaussian shape. As a conservative estimate for the uncertainty of the transition temperature the width of the points included in the fits is used to estimate the error bars.

The increase of long-range correlations in the vicinity of the phase boundary also leads to an increase in the autocorrelation times of the HMC algorithm. This is mainly due to the fact that the update of the infrared modes is not as efficient as for ultraviolet modes (cf. section 3.2.2). When the main HMC parameters (besides solver parameters) are constant this means that the integrated autocorrelation times also provide information about the transition point (see also [53]). For the present scan this is the case for the simulations close to the transition point. Note however that the HMC parameters had to be changed when moving away from the transition in order to ensure an optimal algorithm performance.

The main observables for the determination of the transition temperature are the susceptibilities and integrated autocorrelation times of the smeared Polyakov loop and the

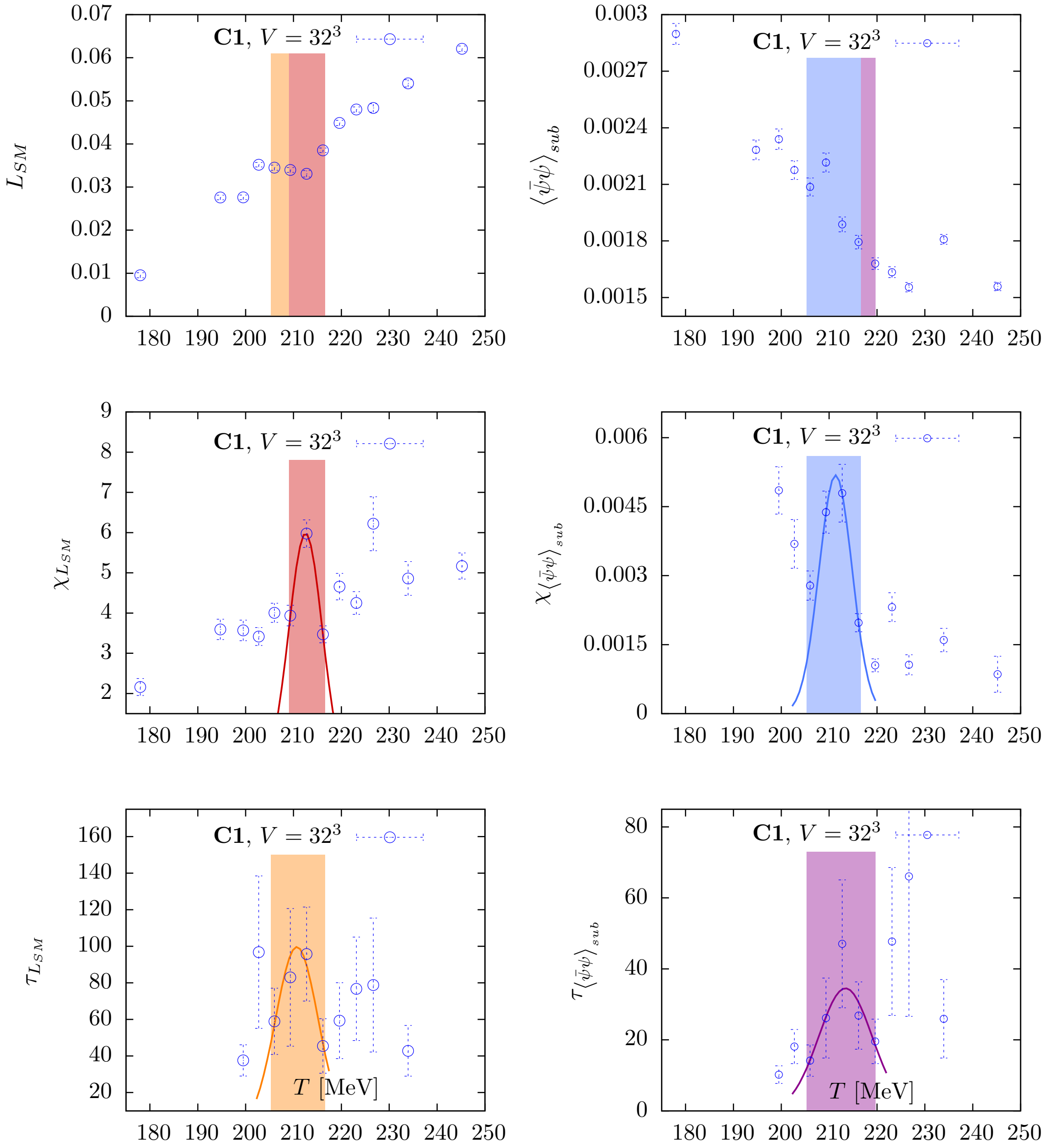

Figure 9.7: Results for the smeared Polyakov loop L_{SM} (left) and the subtracted chiral condensate $\langle\bar{\psi}\psi\rangle_{\mathrm{sub}}$ (right), their susceptibilities and the autocorrelation times (from top to bottom) for scan **C1**. The coloured areas are the transition regions extracted from the associated quantity (for the expectation value both estimates are shown). The curves are the Gaussian fits used to define the transition point as explained in the text.

Obs	$\chi_{L_{\mathrm{SM}}}$	$\tau_{L_{\mathrm{SM}}}$	$\chi_{\langle\bar{\psi}\psi\rangle_{\mathrm{sub}}}$	$\tau_{\langle\bar{\psi}\psi\rangle_{\mathrm{sub}}}$
T_C [MeV]	213 (4)(3)	211 (5)(3)	211 (5)(3)	213 (7)(3)
m_{ud} [MeV]	14.5 (20)(13)			
m_π [MeV]	287 (25)(13)			

Table 9.5: Transition temperatures extracted from Gaussian fits. The first error is the uncertainty of the extraction of the transition region from the spread of the points included in the fit. The quoted uncertainty for quark and pion masses is estimated from the spread of masses in the transition regions. The second set of error bars reflect the uncertainty from scale setting.

subtracted condensate. The uncertainties are estimated using 1000 bootstrap samples generated from bins of 10 measurements each. The results for these quantities are shown in figure 9.7 and the estimates for the transition temperatures as obtained from the Gaussian fits are listed in table 9.5. The plots for the integrated autocorrelation times display only results obtained with equivalent parameters in the HMC algorithm. Note, that the results for the critical temperatures are in good agreement with results found by the tmfT collaboration [53] but somewhat larger then the results obtained by QCDSF/DIK collaboration [320]. The detailed results for the fit parameters including the results for the bare Polyakov loop and the chiral condensate, which can be use to check the improved quantities, are listed in the table in appendix D.6. The Gaussians adaptations are also shown in figure 9.7. As can be seen from the plots, the Gaussian does not provide a good description of the data in all cases. This is also signified by the fact that in the case of the Polyakov loop only three points are consistently described by it. Ideally, one would like to extract the transition point from the data without any assumptions. The MH-method, described in chapter 8, allows for such an extraction by looking at the location of the peak position in the reweighted data. So far the method still suffers from the numerical overflow, as discussed in section 8.4.3. Once this problem is solved the MH-method provides an unambiguous definition of the transition point.

The susceptibilities and the autocorrelation times exhibit pronounced peak structures at similar temperatures. This is reflected in the fully consistent estimates for the transition temperatures obtained from different observables within the statistical uncertainties. The observables connected to the subtracted condensate show particularly good signals (for the bare condensate this is similar), which is especially striking in comparison to the weak signals for the condensate reported in section 9.2. This signal enhancement is in agreement with the expectations of the signal of chiral symmetry restoration becoming stronger in the approach to the chiral limit.

The results for the Binder cumulant for the smeared Polyakov loop and the bare condensate are shown in figure 9.8. For the subtracted condensate the Binder cumulant is too noisy to extract useful information. For a crossover the cumulant is expected to fluctuate around three in the whole transition region. For the smeared Polyakov loop B_4 shows a dip at the transition point. This might signal the onset of a scaling behaviour for the

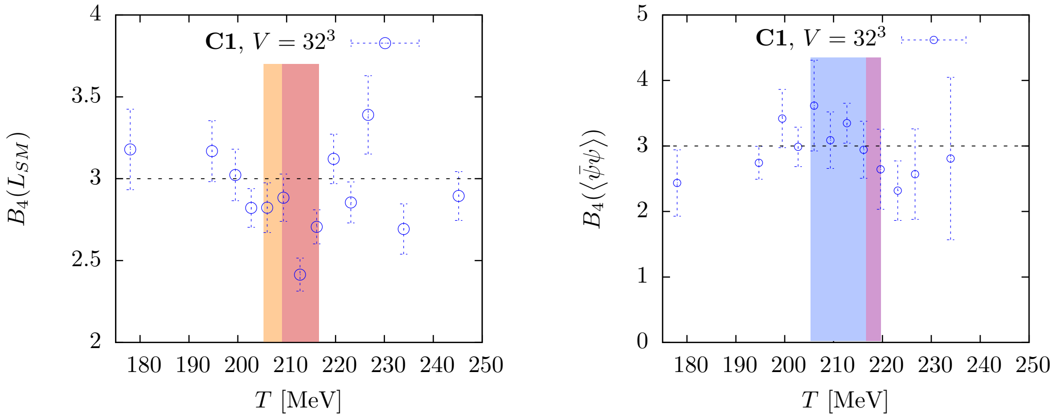

Figure 9.8: Results for the Binder cumulant of the smeared Polyakov loop L_{SM} (left) and the chiral condensate $\langle\bar{\psi}\psi\rangle$ (right) for scan **C1**. The coloured areas are the transition regions as shown in figure 9.7.

cumulant. Nevertheless, this signal has to be checked by comparison to results from larger volumes and by eventually gathering more statistics for this scan in the transition region. For the condensate the cumulant is consistent with three over the whole region, but with larger error bars compared to those from the Polyakov loop. Since the scaling of the Binder cumulant is universal and does not depend on the correct identification of the order parameter, one would expect to see a signal in both cumulants. Future runs will clarify the situation by either showing a signal for both observables or by falsifying the signal in the Polyakov loop.

9.4 Screening masses and chiral symmetry restoration

Further information on the chiral symmetry restoration pattern can be extracted from screening masses. Note however that the current scan is performed at a relatively small volume with $N_s/N_t = 2$ and it was found [348,373] that above T_C screening masses have a linear volume dependence in contrast to the exponential suppressed finite volume effects for usual hadron masses at $T = 0$ [180]. The transition from exponentially suppressed finite volume effects and the linear dependence on the volume happens around T_C [348, 373]. Since the current scan is in the direct vicinity of T_C only, the effect will probably not be too large. Once scans at larger volume become available finite volume effects can be addressed directly. Lattice artefacts, on the other hand, are proportional to $1/N_t^2$ and for $N_t = 16$ likely negligible for the current precision of the data [348]. In the following T_C is given by the result extracted from the peak in the susceptibility of the chiral condensate, $T_C = 211\ (5)(3)$ MeV, since this is expected to be the relevant value for chiral symmetry restoration.

The correlation functions in pseudoscalar (P), scalar (S), vector (V) and axial vector (A) channels have been measured on the stored configurations (separated by 40 MDU) of

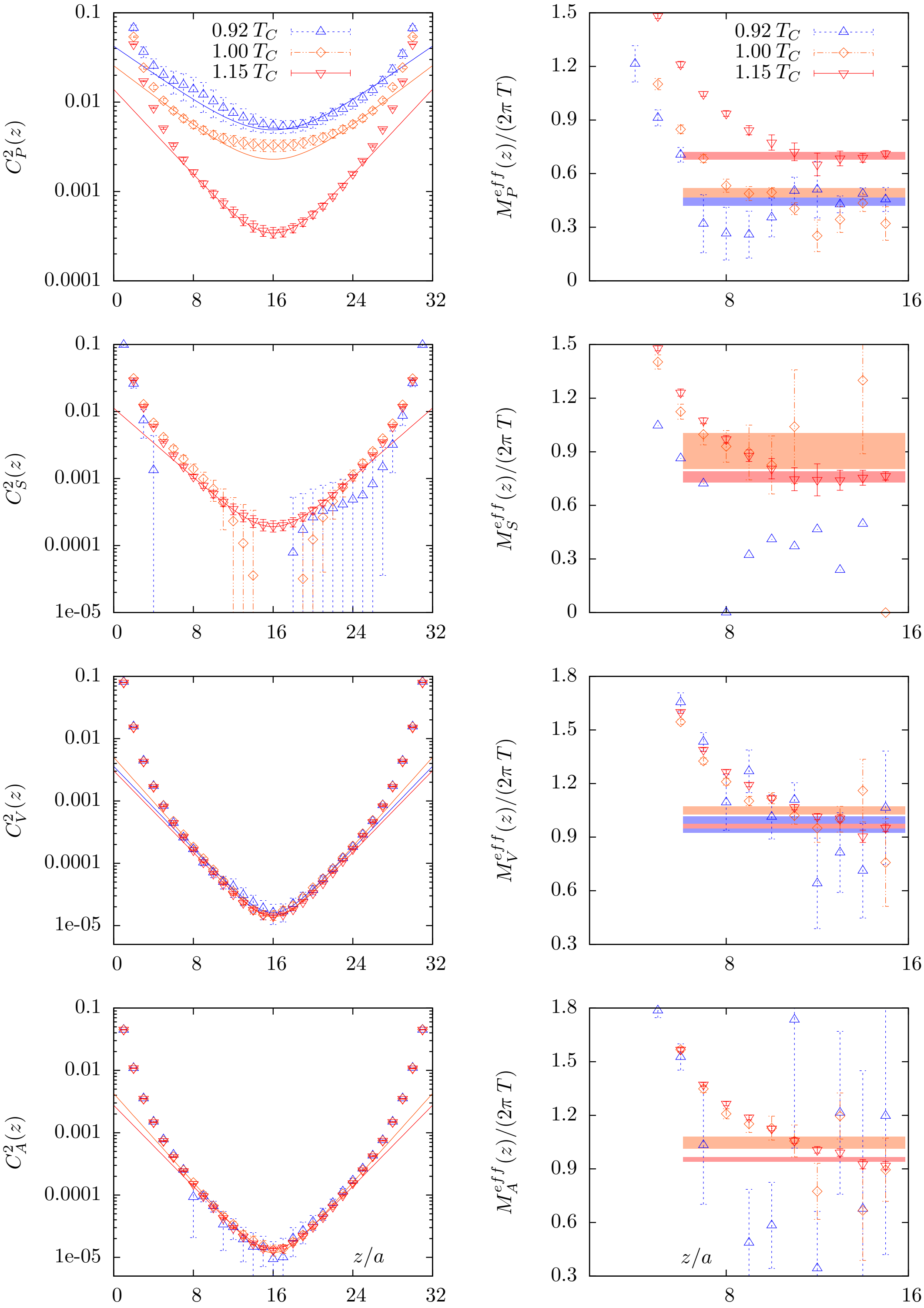

Figure 9.9: Results for the mesonic correlation functions (left) and the effective masses (right) in the P, S, V and A channels (from top to bottom). The filled areas in the effective mass plots indicate the extracted plateau value (the length of the area does not indicate the fitrange) and the lines in the correlator plots represent the associated correlator behaviour. When a value for the effective mass is missing then the signal has been considered as too bad to extract a result.

scan **C1** from the last section using a point source. The available numbers of configurations at each simulation point are listed in table D.10. As before the uncertainties have been estimated using 1000 bootstrap samples. For the vector and the axial vector channel all four components have been included in the measurements. However, the focus lies on the operators polarised in transverse direction and orthogonal to the shorter temporal direction, i.e. on the operators with matrices γ_1 and γ_2 (see [374–376] for discussions of the impact of the 'short' dimension at finite temperature on the screening spectrum above T_C in the case of pure gauge theories). The screening masses have been extracted from a fit to a constant to the data for the effective masses from eq. (9.8). While this usually works reasonably well for P and V-channels, the correlation functions in S and A-channels in the region close to and below T_C in some cases do not show a signal. This is in particular true for the S-channel. Above T_C both channels obtain a stable signal. Examples for the results of the correlation functions below, at and above T_C and the associated effective masses for the different channels are shown in figure 9.9. The coloured areas in the effective mass plots indicate the results for the screening mass extracted from a constant fit [1]. The lines in the left plots show the associated behaviour of the correlator.

The temperature dependence of the screening masses in the different channels is shown in figure 9.10 (top) and a full list of results is given in table D.14. The screening masses in the low temperature region at $0.84\,T_C$ show the expected splittings associated with the splitting of the zero temperature masses of the corresponding mesons. The pseudoscalar screening mass starts from a value of $M_P/(2\pi\,T) = 0.33\,(2)$, which is a bit larger than the value associated with the pion mass, $m_\pi/(2\pi\,T) = 0.26\,(2)$. This is consistent with the expectation that the screening masses approach the zero temperature hadron masses for $T \to 0$ [54,341,342]. Around T_C it then starts to rise. At $1.16T_C$ the value of M_P is roughly 30 % smaller than the asymptotic value of $2\pi\,T$. This is in agreement with what has been found in [348] for screening masses with the Wilson action on pure gauge configurations at finite volume. Note, that the value is larger than what was found in simulations with staggered quarks [342,352]. Nevertheless, considering the differences in volume and quark mass, as well as the limited temperature range, it is at this point not possible to draw any conclusions about contradictions to results from staggered calculations.

Below T_C the pseudoscalar screening mass is expected to obey the scaling law [377,378]

$$M_P^2(\tau) \sim m_{ud}\,\tau^{\beta_{\rm ce}-\nu_{\rm ce}}\ . \tag{9.7}$$

To test the agreement of the present data with this scaling prediction one can fit the results for M_P below T_C to this form with constant m_{ud} and using the values for the critical exponents as listed in table 7.1. The only remaining parameters are two constants in this very naive setup. The result for $O(4)$-scaling is shown in figure 9.10 (top). Note, that the exponents for the different cases are so similar that $O(4)$, $Z(2)$ and first order scaling curves cannot be distinguished. However, the data seems to be in good agreement with the expected scaling behaviour.

---

[1] Note, that for V and A-channels the averaged fit results from both polarisations are shown, while the data points are from the γ_1 correlation function. At $0.92\,T_C$ it was not possible to extract signals in S and A-channels and accordingly there are no fit results shown in the plot.

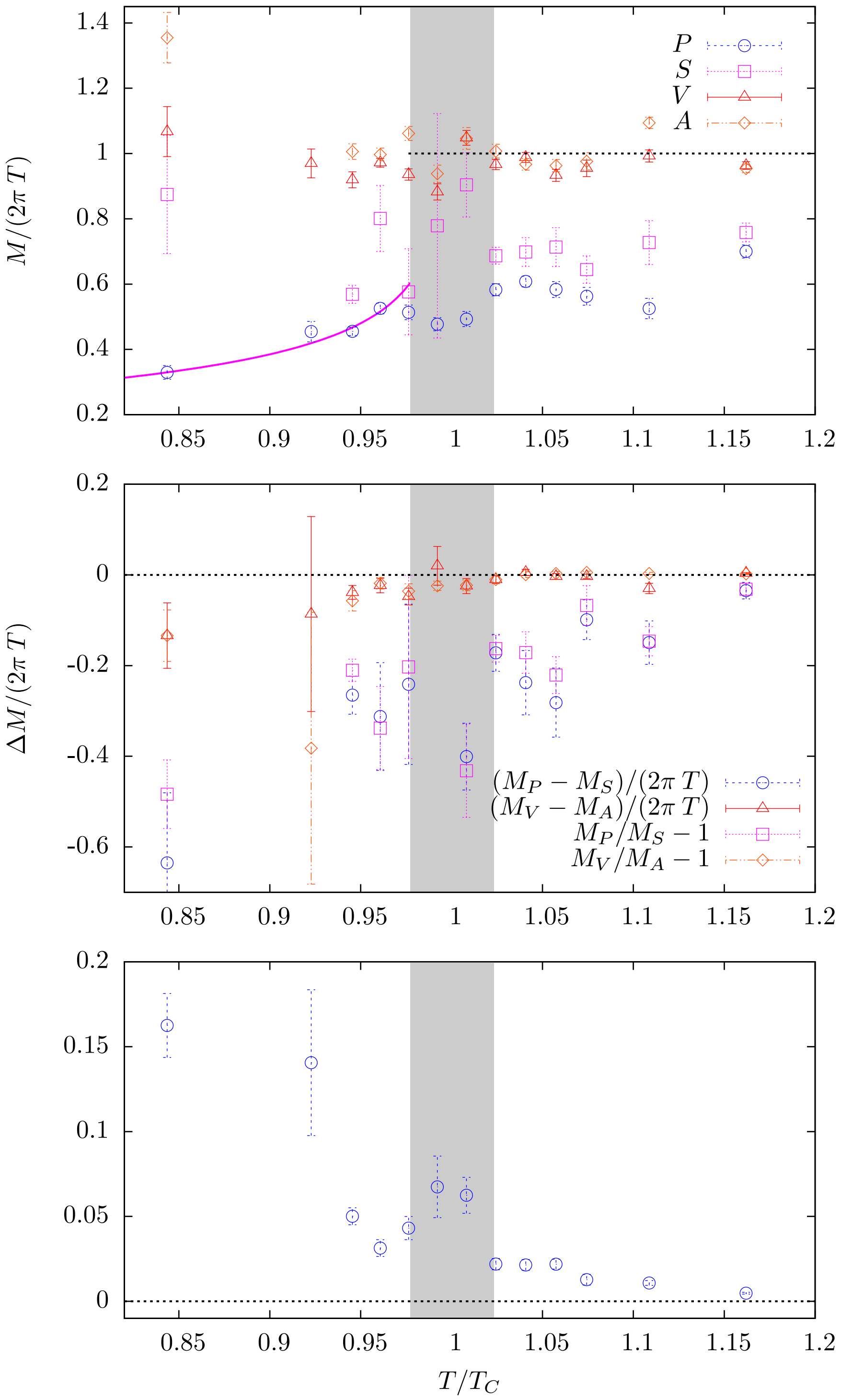

Figure 9.10: Temperature dependence of the screening masses in P, S, V and A channels (top), screening mass differences and ratios for (P, S) and (V, A)-channels (middle) and susceptibility differences (bottom). In the upper plot the dashed line corresponds to the asymptotic value of $M^{\infty} = 2\pi T$ while for the lower two plots the line indicates symmetry restoration. The magenta line in the upper plot is the scaling curve from eq. (9.7) with $O(4)$-critical exponents.

For the screening mass in the S-channel there are large fluctuations below and at T_C which make any definite statement on its behaviour in this regime difficult. What can be taken from the plot is that it first seems to drop when approaching the transition region and then starts to rise again together with the pseudoscalar screening mass above T_C. This is consistent with the findings from [342]. In V and A-channels the results seem to suffer from the, still, relatively large quark masses since the results are already in agreement with the asymptotic result in the region of the transition. Both are not degenerate below T_C and show independent fluctuations. Above T_C they become degenerate and fluctuate simultaneously.

To study symmetry restoration in more detail one can look at the mass differences or ratios directly rather then at the differences of the extracted screening masses. This has the advantage that possible global fluctuations in the correlators are canceled and the resulting estimates might show an improved signal. Here two different quantities are used to study symmetry restoration: The first one is an estimate for the difference between two masses obtained from the effective mass of the ratio of the two correlation functions. The ratio of the two correlation functions is indeed more stable than the individual correlation functions but the application of the effective mass from eq. (9.8) occasionally leads to negative numbers in the logarithm due to fluctuations. Thus for all of these estimates the naive effective mass

$$a\, M_X^{\mathrm{eff}}(z) \equiv \ln\left[\frac{C_X^2(z)}{2\, C_X^2(z+a)}\right] \tag{9.8}$$

has been employed. The second method is the usage of the ratio of the effective masses of the two channels,

$$\lim_{z\to N_s/2} \frac{M_X^{\mathrm{eff}}(z)}{M_Y^{\mathrm{eff}}(z)} = \frac{M_X}{M_Y}\,. \tag{9.9}$$

In fact, $M_X/M_Y - 1$ should be equivalent to the mass difference normalised by $2\pi\, T$.

The results for these two quantities in $(X,Y) = (P,S)$ and (V,S)-channels are shown in figure 9.10 (middle) and are listed in table D.15 in the appendix. The results for the mass differences and the mass ratios of both channels show the expected agreement. In the (V,A)-channel at $0.84\, T_C$ the mass splitting between the two channels is significantly different from zero. In the approach to T_C the results approach zero and become equivalent to zero at T_C or slightly above, signaling restoration of chiral symmetry. In the (P,S)-channel the situation is different: The results approach zero below T_C but remain almost constant in the region of T_C up to roughly $1.05 T_C$. This indicates that the $U_A(1)$-symmetry is not restored at the transition point. Following the data one would expect the symmetry to be restored only in the region close above $1.16\, T_C$. These findings are in agreement with earlier studies on the subject, see e.g. [324,341,342,350] even though they show a tendency to earlier $U_A(1)$-restoration.

More information can be obtained by looking at the difference of the hadronic susceptibilities as defined in eq. (7.28). The differences in the (P,S)-channel are shown in figure 9.10 (bottom). It shows the expected decrease when going into the high temperature region and is non-zero at the transition temperature, indicating that $U_A(1)$-symmetry is not restored. Note that the peak in χ_P^{had} at the transition point is expected as it is a

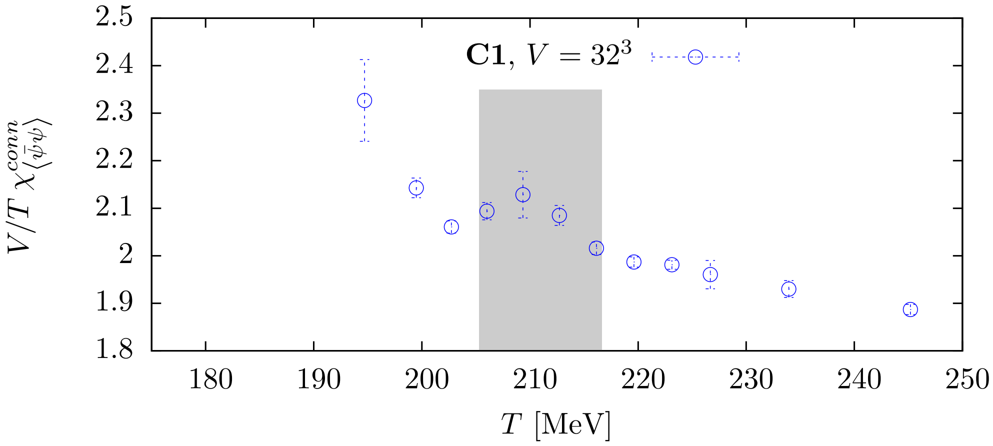

Figure 9.11: Results for the connected susceptibility of the chiral condensate.

remnant of the connected chiral susceptibility since $\chi_P^{\text{had}} = T/V\ \chi^{\text{conn}}_{\langle\bar\psi\psi\rangle}$ when the cut in eq. (7.28) is set to zero (cf. eq. (7.19)). The associated connected susceptibility $T/V\ \chi^{\text{conn}}_{\langle\bar\psi\psi\rangle}$ is shown in figure 9.11.

To sum up, the extraction of the screening masses turns out to be challenging at small volumes with $N_s/N_t = 2$. This is especially true for the S and A-channels below T_C where the signal in the correlation function is weak and even gets lost in some cases. The P channel shows the expected rise and the magnitude of the results are mostly consistent with the ones obtained in [348], however a bit larger than the ones obtained with staggered fermions [342,352]. The V and A-channels are already very close to the asymptotic value of $2\pi\,T$ below T_C and thus mainly fluctuate around this value in the whole interval. The results indicate that M_V and M_A fluctuate independently below T_C and become degenerate above T_C, in consistence with chiral symmetry restoration. This is also reflected in the behaviour of the results for the mass differences and ratios shown in figure 9.10. Concerning the anomalous breaking of the $U_A(1)$-symmetry, the data indicates that the symmetry is not restored up to at least $1.16\,T_C$ in agreement with results from other collaborations [324,341,342,350].

9.5 Summary and perspectives

In this chapter a detailed overview of the current status of the project to extract information about the order of the transition in the chiral limit has been presented. A number of tests of the algorithm have been reported and the setup for the tuning of the parameters in the approach to the chiral limit has been discussed. It was found that DD-HMC and MP-HMC algorithms show good performance also at finite temperature and deflation seems to work well. In particular, it also appears to be feasible to go down to almost physical pion masses. The only source for concern is the occasional appearance of configurations with small eigenvalues, leading to problems with the solver convergence. However, a change in the setup of the DFL-SAP-GCR solver usually helps. The tuning of the parameters for scans along LCPs works accurately and it is possible to estimate parameters for future runs deeper in the chiral regime. First results from a scan at a constant quark mass of roughly 14.5 MeV (or $m_\pi \approx 290$ MeV) in the $\overline{\text{MS}}$-scheme ($\mu = 2$ GeV) on a 16×32^3 lattice have been reported. The scan shows clear peaks in the susceptibility and the autocorrelation time of the subtracted chiral condensate signaling chiral symmetry restoration. The results for screening masses also show the expected chiral symmetry restoration pattern. In particular, the $U_A(1)$-symmetry appears to be still broken at T_C. The measured correlation functions also allow to extract quark number susceptibilities that are connected to the deconfinement transition. They can be used to supplement the analysis of the Polyakov loop. To conclude, everything is set for simulations deeper in the chiral regime. In fact, the generation of first ensembles at quark masses of about 7 ($m_\pi \approx 200$ MeV) and 4 MeV ($m_\pi \approx 140$ MeV) has already started.

When addressing the perspectives for a future scaling analysis it is elementary to clarify what one would expect in the two different cases. For the $O(4)$-scenario the expectations are the following: The critical point which dictates the scaling will be at $m_{ud} = 0$ and the scaling analysis for the transition temperatures using either eq. (7.41) or eq. (7.42) will show consistency with $O(4)$-scaling if the transition temperatures are in the scaling region. Note however that a distinction between $O(4)$ and $Z(2)$-scaling can be expected to be difficult as the critical exponents are very similar. A conclusive comparison might be possible by combining the analysis whit the FSS analysis for the Binder cumulant. The comparison of the behaviour of the chiral condensate with $O(4)$-scaling using eq. (7.38) can provide additional evidence for the $O(4)$-scenario [53, 127].

In the case of a first order transition the situation is more complicated. In this scenario the chiral critical line will continue all the way up to the two-flavour limit where it occurs in form of a critical endpoint in the $Z(2)$-universality class. One thus might expect that the scaling towards this endpoint is guided by $Z(2)$-critical exponents. However, the endpoint is located at some finite non-zero quark mass m_{ud}^{Z2} so that the correct scaling relation between the transition temperatures and the quark masses is given by

$$T_C(h) = T_C(0)\,\left[1 + C\,\left|m_{ud} - m_{ud}^{Z2}\right|^{1/(\delta_{\rm ce}\,\beta_{\rm ce})}\right]\ . \tag{9.10}$$

As a consequence of the non-zero value for the quark mass at the critical endpoint the chiral condensate no longer constitutes an order parameter and one cannot be certain that the peak position extracted from it shows the correct scaling behaviour. However, as the critical endpoint belongs to the chiral critical line one might expect to see a similar scaling as for the $Z(2)$-endpoint on the $N_f = 3$ line where $Z(2)$-scaling for the temperatures has been observed [379]. In this case a combined scaling analysis using $Z(2)$-scaling for the transition temperatures and a simultaneous FSS scaling analysis of the Binder cumulant is particularly promising. Both share the critical endpoint as a free parameter and a combined fit to the data might lead to a significantly non-zero result for it, which would approve the first order scenario. To be able to perform the FSS analysis it is necessary to have the two larger volumes with $N_s/N_t = 3$ and 4 since smaller volumes might lead to an inconclusive signal for the cumulant (see [380]).

Distinguishing between the two types of scalings in the approach to the chiral limit is an ambitious goal. In particular, since accurate results at small quark masses and large volumes are needed. This requires a lot of computer time and algorithms that have a good scaling behaviour with both, volume and quark mass. Considering the accuracy of the data reported in the last sections, the study started within this thesis appears to be capable of producing the results with the required accuracy down to physical quark masses, given the necessary computational resources.

Apart from the obvious perspectives for future research there are also a lot of other options to make use of the generated ensembles. Ensembles at small lattice spacings and large volumes are ideal to study finite temperature observables that are difficult to extract on smaller lattices and that are known to suffer from large discretisation effects. One type of observables are temporal vector current correlation functions and their associated spectral density (see [338]). It can be related directly to the thermal dilepton rate and allows for extracting the electrical conductivity of the QGP. These correlation functions are known to suffer from large cut-off effects, and $N_t = 16$ appears to be at the lower edge where one might expect to be able to extract reliable results. Furthermore large volumes are needed to ensure small finite size effects. A first study of these quantities is already on the way [381]. Other possibilities for future research include the extraction of the density of the low eigenmodes and the associated measurement of the chiral condensate via the Banks-Casher relation [333] and the extraction of other transport coefficients using energy-momentum tensor correlators (see [382, 383]).

Conclusions

This thesis contains a study on the potential of todays state-of-the-art lattice simulations to obtain results in the chiral regime with controlled systematics at zero and non-zero temperature. Particular emphasis has been devoted to study the chiral extrapolations to the physical point and the chiral limit. The thesis focuses on two particular cases in the two different fields of the computation of hadronic form factors at zero temperature and the examination of the QCD phase diagram: The computation of the iso-vector electromagnetic form factor of the pion and a study of the chiral transition in the chiral limit of two-flavour QCD. Both studies were done using two degenerate flavours of non-perturbatively $\mathcal{O}(a)$-improved Wilson fermions. They are numerically more expensive than staggered fermions but have the advantage of a continuum limit which is theoretically well understood. Simulations of Wilson fermions have obtained a significant speed up in the last decade due to the invention of new algorithms (cf. sections 3.4 and 3.5) and today's simulations are closing in on physical quark masses.

The first part of this thesis has been devoted to the introduction of the fundamental concepts of QCD in the continuum and on the lattice. This has been followed by a review of the numerical methods in the second part. Special emphasis has been given to the numerical improvements that enable efficient simulations at small quark masses and large volumes, in particular, domain decomposition and deflation methods. Of particular relevance for the inquest of the chiral regime is the control of systematic effects. These have been discussed as well. Furthermore, an outline of developments for the computation of fermionic observables has been given in chapter 4 with emphasis on stochastic sources and twisted boundary conditions that are essential for the computation of the pion form factor. The focus in both parts has been on the lattice formulation using non-perturbatively $\mathcal{O}(a)$-improved Wilson fermions.

The presentation of new results has started in part III which contains an extensive study of the electromagnetic pion form factor. The main discussion and summary of the results have already been presented in section 6.4. The form factor has been extracted with unprecedented accuracy from a subset of the ensembles generated within the CLS effort, covering three different lattice spacings between 0.08 and 0.05 fm with multiple pion masses each, ranging between 650 and 250 MeV. This setup allows to perform controlled chiral and continuum extrapolations. The details have been discussed in chapter 5. The optimised use of partially twisted boundary conditions has allowed for the extraction of the form factor at momentum transfers close to $Q^2 = 0$ in a previously unexplored regime. This enables the model-independent extraction of the charge radius from the data which has not been possible for previous studies neither in LQCD nor in phenomenology. The systematic effects that can be addressed within the $N_f = 2$ setup at finite lattice spacing and a particular quark mass have been discussed extensively and are fully under control.

Subsequent to the analysis for each individual ensemble the data has been used to probe χPT to NNLO for the chiral extrapolation of the form factor and the charge radius in chapter 6. The chiral extrapolation of the latter has also been compared to polynomial extrapolations. The data appear to be in reasonable agreement with χPT but the information from the data for the form factor and the charge radius alone is not sufficient to constrain the fit parameters. The combination with the chiral extrapolation of the pion decay constant and the pion mass leads to further constrains for the fit parameters and results in reliable fits, at least if all lattices up to pion masses of 600 MeV have been included. The resulting LECs still have large error bars and one would expect that in this setup only an analysis including a large number of simulation points close to the physical point will allow for their accurate extraction. For a decisive conclusion concerning the applicability of χPT in a particular mass range it will clearly be necessary to study the sensitivity of the extrapolation on cuts in the range of pion masses in more detail. However, the extracted result for the charge radius at the physical point appears to be stable and is in good agreement with the results from polynomial fits. The final result is ($r_0 = 0.503\,(10)$ fm [77])

$$\left\langle r_\pi^2 \right\rangle^{\text{phys}} / r_0^2 = 1.87 \left({}^{+12}_{-10}\right) \left({}^{+\,4}_{-15}\right) \quad \text{or} \quad \left\langle r_\pi^2 \right\rangle^{\text{phys}} = 0.473 \left({}^{+30}_{-26}\right) \left({}^{+10}_{-38}\right) (10) \text{ fm} \,,$$

which agrees well with the results from other calculations in LQCD and experiment. Note, that this is the first continuum extrapolated result for the charge radius which has been extracted from measurements of the form factor in the region of small momentum transfers below the lowest accessible Fourier momentum. the study reported in this thesis is the first that combines the chiral extrapolation with χPT to NNLO with an extrapolation to the continuum with controlled systematics. The chiral extrapolation has also provided numbers for other observables at the physical point such as for the averaged light quark mass m_{ud}, the pion decay constant and the chiral condensate. These estimates are listed in table 6.6 and are in good agreement with other results from LQCD and phenomenology as well.

The chiral extrapolation is still the biggest source for concern regarding systematic effects. The main reason for this is the large number of parameters in the fits combined with the modest variation of the results with the pion mass that hampers the reliability of the fit. Note, that if this is true for the pion form factor, where the effective field theory framework is believed to be on relatively solid footing, this will even be worse for baryonic form factors where a consistent effective field theory framework is absent. Furthermore, baryonic form factors have much larger error bars, rendering the comparison to effective field theories yet more difficult. The reliability of the chiral extrapolation can be improved by adding more data points in the region of small pion masses to the analysis. Furthermore, one can include the chiral extrapolation for the scalar form factor in the global fits, which shares some of the LECs but demands the accurate measurements of disconnected diagrams. First results for this quantity have already been reported [384] and a full set of results can be expected to be available soon. One can also ask whether standard χPT includes all the necessary dynamics that governs the chiral extrapolation of the form factor. In particular, the mass of the ρ-meson might be small enough to contribute significantly to the chiral extrapolation [385]. An extension to standard χPT including vector mesons is available [386, 387] and the form factor has been calculated to NLO. However, the associated formulae include even more free parameters so that a comparison to the data will only be possible once additional lattices close to the physical point are available. The model independent extraction of the charge radius at non-physical quark masses presents a first step towards a completely model-independent computation of a quantity connected to hadron structure, which would present an important step for QCD phenomenology. As the chiral extrapolation still has an inherent model dependence this can only be accomplished by simulating at the physical point directly. Even though the simulations are closing in on the physical point, the control of the remaining systematic effects demands large volumes and statistic and in consequence large computational effort. Thus it appears that this remains a project for the future.

In part IV the discussion has turned to the project to determine the order of the thermal phase transition in the chiral limit. Chapter 7 has presented a detailed discussion of the fundamental concepts to address this question within LQCD and has given an account of the current knowledge about the QCD phase diagram. Particular attention has been given to the different types of scaling analyses that can be used to extract information on the transition in the chiral limit from simulations at non-zero quark masses. Further, the relation between the chiral transition and the restoration of the anomalously broken $U_A(1)$-symmetry has been outlined and it was discussed how it can be explored using mesonic correlation functions. In chapter 7 a novel generalisation of the standard MH-method to β-dependent fermions has been presented. Once implemented, this method will allow for the optimised analysis of data obtained in a temperature scan and eventually to extract quasi-continuous data in the transition region. While the theoretical concepts are available, the implementation of the method suffers from numerical overflows, discussed in section 8.4.2. However, first results for the expansion operators connected to the approximation for the ratios of fermion determinants from a test scan at large quark mass $\kappa = 0.11$ have been reported and the associated results compared to stochastic measurements. The agreement was found to be good when the difference in β is small, in the region of $\Delta\beta = 0.01$. With increasing difference in β the difference between the two increases as well and at $\Delta\beta \approx 0.07$ the difference of the associated terms in the exponential is in the region of 5 %. However, this difference is only a tiny effect compared to the reweighting factor stemming from the gauge part of the action and might be negligible in the MH method, at least for this large quark mass.

Finally, chapter 9 contains the setup and the current status on the inquest to the chiral regime. The setup has been discussed in section 9.1. The scans are done on large lattices with $N_t = 16$ and $N_s/N_t = 2,\ 3$ and 4 which reduces the effect of explicit chiral symmetry breaking and allows to get a handle on finite volume effects. Furthermore, the number of different volumes allows for systematic FSS studies. Note that these lattice sizes are unprecedented in simulations with Wilson fermions at finite temperature. Since the project has been started with the begin of the work for this thesis, a detailed account of the reasoning for the choice of parameters has been given. In fact, the optimisation of the setup and the tuning of the simulation algorithms is highly non-trivial and was one of the fundamental tasks in this part of the thesis. The strategy and algorithmical setup as well as the measurements of the observables have been put to an extensive test, reported in section 9.2. The DD-HMC algorithm and the DFL-SAP-GCR solver have been used for finite temperature simulations for the first time and a detailed discussion of tuning and performance at finite temperature is contained in appendix D.3. The algorithms show the expected good performance and in particular seems to be capable of simulations even at physical pion masses. Sections 9.3 and 9.4 present results for the first scan in the chiral regime along a line of constant quark mass of $m_{ud} \approx 14.5$ MeV (or $m_\pi \approx 290$ MeV). The susceptibilities of the chiral condensate and the Polyakov loop show a very good and clean signal. The transition temperature extracted from the chiral condensate is given by

$$T_C(m_{ud} = 14.5\,(20)\text{ MeV}) = 211\,(5)(3)\text{ MeV}\ ,$$

which is compatible with the results of the tmfT-collaboration [53] but somewhat larger than the typical results obtained by the QCDSF/DIK-collaboration [320]. Here the quark mass is given in the $\overline{\text{MS}}$-scheme at a renormalisation scale of $\mu_R = 2$ GeV. As additional observables to study the pattern of chiral symmetry restoration mesonic correlation functions and the related screening masses have been studied. In particular the iso-vector correlation functions in the pseudoscalar, scalar, vector and axial vector channels have been extracted. The pseudoscalar screening mass rises from a value close to the zero-temperature pion mass at $0.84\,T_C$ towards the asymptotic value of $2\pi\,T$. At $1.16\,T_C$ it differs roughly 30 % from this limit. This is in agreement with the results for screening masses extracted from pure gauge theory with Wilson fermions [348], but significantly larger then the results found in simulations with staggered fermions [342, 352]. The results show the expected degeneracy for vector and axial vector channels around and above T_C, signaling chiral symmetry restoration. At the same time, the $U_A(1)$-symmetry still appears to be broken, indicated by non-degenerate scalar and pseudoscalar screening masses.

Since only a single scan in the chiral regime is available at the moment there can be no conclusions concerning the order of the transition in the chiral limit. Nevertheless, the scene is set for additional scans at smaller quark masses and, given the good performance of the algorithms, scans down to physical quark masses appear feasible. First simulations at a pion mass of approximately 200 MeV have already been started. Thus in the long term one can expect further results much closer to the chiral limit, that eventually might allow to provide first conclusions about the order of the chiral transition. Promising strategies for scaling analyses to probe the two different scenarios have been discussed in section 9.5. The project will benefit greatly from the different volumes as it opens up new possibilities for scaling analyses and will enable the extraction of screening masses with much better precision. In addition to this, the study offers a lot of perspectives for other projects such as the extraction of plasma properties from vector correlation functions following the strategy from [338]. First studies in this direction are already on the way [381]. They profit from the large lattices that lead to small cut-off effects, which are one of the main limitations for the reliable extraction of spectral functions. Another interesting project is the extraction of the density of low eigenmodes. It provides direct information on possible spectral gaps for the Dirac operator with direct impact on chiral symmetry restoration (see [324]). Furthermore, it allows to extract the renormalised and subtracted condensate by the use of the Banks-Casher relation [333]. Additional projects include the extraction of other transport coefficients using energy-momentum tensor correlators (see [382, 383]).

To sum up, the status of the two projects with respect to the aims of this thesis, the first aim, the comparison of the form factor data with chiral perturbation theory, has been accomplished successfully and the form factor has been extracted at the physical point.

Nevertheless, a final conclusion about the range of applicability of χPT was not possible with the current set of ensembles. The study has shown that with today's algorithms it is indeed possible to extract quantities related to the structure of hadrons with control over systematic effects in the chiral regime. This is true at least for mesons.

For the second project the aims were to provide a tested setup for future runs including a strategy for the scaling analyses and to provide first results in the chiral regime. Both goals have been reached within this thesis. Given the limited time and the fact that the simulations at finite temperature are computationally intensive, especially for the large lattices used in this study, only a single simulation point in the chiral regime is available so far. Conclusive results will eventually be available in the next few years. The results obtained so far are encouraging. It seems to be indeed feasible with state-of-the-art algorithms to go to physical pion masses for simulations at finite temperature even with Wilson fermions.

Appendix

A Remarks on theoretical aspects

A.1 Conventions

Natural units:

The thesis applies natural units, i.e.

$$\hbar \equiv c \equiv k_B \equiv 1 \; . \tag{A.1}$$

A conversion to other system of units can be done with [76]

$$\begin{aligned} c &= 299792458 \, \mathrm{m \; s^{-1}} \\ \hbar c &= 197.326968(17) \, \mathrm{MeV \; fm} \\ k_B &= 8.617343(15) \cdot 10^{-5} \, \mathrm{eV \; K^{-1}} \; . \end{aligned} \tag{A.2}$$

Therefore temperatures of 100 MeV corresponds to 10^{12} K.

Minkowski, Euclidean spacetime and Wick rotation:

For numerical simulations it is necessary to work in Euclidean spacetime that is connected to Minkowski spacetime by a Wick rotation $t \to -i\, x^0$. Here t is the temporal coordinate of Minkowski space and x^0 denotes the temporal coordinate connected to Euclidean space. The four-vectors in the two different spacetimes obey:

$$\text{Minkowski:} \qquad x = (t, \mathbf{x}) \; , \qquad x^\mu \, x_\mu = t^2 - \mathbf{x}^2 \tag{A.3}$$

$$\text{Euclidean:} \qquad x = (x^0, \mathbf{x}) \; , \qquad x_\mu \, x_\mu = (x^0)^2 + \mathbf{x}^2 \tag{A.4}$$

with

$$x_\mu \, x_\mu = -x^\mu \, x_\mu \; . \tag{A.5}$$

In Euclidean spacetime it is convenient to use the Euclidean version of the γ-matrices γ^E_μ, connected to the usual γ-matrices by

$$\gamma_0 = \gamma^E_0 \quad \text{and} \quad \gamma_i = i \, \gamma^E_i \; . \tag{A.6}$$

The two sets of γ-matrices satisfy the anticommutation relations:

$$\{\gamma_\mu \, , \, \gamma_\nu\} = 2 \, \eta_{\mu\nu} \quad \text{and} \quad \left\{\gamma^E_\mu \, , \, \gamma^E_\nu\right\} = 2 \, \delta_{\mu\nu} \tag{A.7}$$

The right hand side of both equations is thus proportional to the metric of the corresponding space. The superscript E is conventionally dropped throughout this thesis.

Matrix conventions

The vector of Pauli matrices σ^μ is defined by:

$$\sigma^0 = \begin{pmatrix} 1 & 0 \\ 0 & 1 \end{pmatrix} , \quad \sigma^1 = \begin{pmatrix} 0 & 1 \\ 1 & 0 \end{pmatrix} , \quad \sigma^2 = \begin{pmatrix} 0 & -i \\ i & 0 \end{pmatrix} , \quad \sigma^3 = \begin{pmatrix} 1 & 0 \\ 0 & -1 \end{pmatrix} \tag{A.8}$$

The generators of $SU(3)$ are the Gell-Mann matrices. A particular representation for them is:

$$\begin{aligned} \lambda^1 &= \begin{pmatrix} 0 & 1 & 0 \\ 1 & 0 & 0 \\ 0 & 0 & 0 \end{pmatrix} , \quad \lambda^2 = \begin{pmatrix} 0 & -i & 0 \\ -i & 0 & 0 \\ 0 & 0 & 0 \end{pmatrix} , \quad \lambda^3 = \begin{pmatrix} 1 & 0 & 0 \\ 0 & -1 & 0 \\ 0 & 0 & 0 \end{pmatrix} , \\ \lambda^4 &= \begin{pmatrix} 0 & 0 & 1 \\ 0 & 0 & 0 \\ 1 & 0 & 0 \end{pmatrix} , \quad \lambda^5 = \begin{pmatrix} 0 & 0 & -i \\ 0 & 0 & 0 \\ i & 0 & 0 \end{pmatrix} , \quad \lambda^6 = \begin{pmatrix} 0 & 0 & 0 \\ 0 & 0 & 1 \\ 0 & 1 & 0 \end{pmatrix} , \\ \lambda^7 &= \begin{pmatrix} 0 & 0 & 0 \\ 0 & 0 & -i \\ 0 & i & 0 \end{pmatrix} , \quad \lambda^8 = \frac{1}{\sqrt{3}} \begin{pmatrix} 1 & 0 & 0 \\ 0 & 1 & 0 \\ 0 & 0 & -2 \end{pmatrix} . \end{aligned} \tag{A.9}$$

In this thesis the chiral basis for the Euclidean γ-matrices is used which is also implemented for the calculations within the DD-HMC algorithm. In that basis the γ-matrices are represented by:

$$\begin{aligned} \gamma_0 &= \begin{pmatrix} 0 & -\sigma^0 \\ -\sigma^0 & 0 \end{pmatrix} , \quad \gamma_1 = \begin{pmatrix} 0 & -i\sigma^1 \\ -i\sigma^1 & 0 \end{pmatrix} , \\ \gamma_2 &= \begin{pmatrix} 0 & -i\sigma^2 \\ i\sigma^2 & 0 \end{pmatrix} , \quad \gamma_3 = \begin{pmatrix} 0 & -i\sigma^3 \\ -i\sigma^3 & 0 \end{pmatrix} . \end{aligned} \tag{A.10}$$

The matrix γ_5 is then given by

$$\gamma_5 \equiv \gamma_0\gamma_1\gamma_2\gamma_3 = \begin{pmatrix} \sigma^0 & 0 \\ 0 & -\sigma^0 \end{pmatrix} . \tag{A.11}$$

A.2 Improvement coefficients and renormalisation factors

This section of the appendix lists known results for the $\mathcal{O}(a)$-improvement coefficients and the renormalisation factors. When available perturbative and non-perturbative results are listed. The non-perturbative results are mostly given in the form of an interpolation. In the following C_F is defined as

$$C_F = \frac{(N^2-1)}{2\,N} \tag{A.12}$$

where N is the number of colours.

Improvement coefficients:

[93] $$c_V(q_0)|_{\text{1-loop}} = -0.01225(1)\,C_F\,g_0^2 \tag{A.13}$$

[97] $$c_A(q_0)|_{\text{1-loop}} = -0.005680(2)\,C_F\,g_0^2 \tag{A.14}$$

[244] $$c_A(q_0)|_{\text{NP}} = -0.00756\,\frac{1-0.4485\,g_0^2}{1-0.8098\,g_0^2} \tag{A.15}$$

[97] $$b_m|_{\text{1-loop}} = -\frac{1}{2} - 0.07217(2)\,C_F\,g_0^2 \tag{A.16}$$

[110] $$b_m|_{\text{NP}} = (-0.5-0.09623\,g_0^2)\,\frac{1-0.3737\,g_0^{10}}{1-0.5181\,g_0^4} \tag{A.17}$$

[97] $$b_P|_{\text{1-loop}} = 1+0.11484(2)\,C_F\,g_0^2 \tag{A.18}$$

[97] $$b_V|_{\text{1-loop}} = 1+0.11492(4)\,C_F\,g_0^2 \tag{A.19}$$

[97] $$b_A|_{\text{1-loop}} = 1+0.11414(4)\,C_F\,g_0^2 \tag{A.20}$$

[97] $$b_A|_{\text{1-loop}} = 1+0.11414(4)\,C_F\,g_0^2 \tag{A.21}$$

[110] $$b_A - b_P|_{\text{NP}} = -0.00093\,g_0^2\,\frac{1+23.59\,g_0^2}{1-0.6235\,g_0^2} \tag{A.22}$$

Renormalisation constants:

[245] $$\mathcal{Z}_V(g_0)|_{\text{NP}} = \frac{1-0.6715\,g_0^2+0.0388\,g_0^4}{1-0.5421\,g_0^2} \tag{A.23}$$

[77, 246] $$\mathcal{Z}_A(g_0)|_{\text{NP}} = 1-0.116458\,g_0^2+0.0116\,g_0^4-0.0721\,g_0^6 \tag{A.24}$$

$$\mathrm{E}\,[\mathcal{Z}_A]\,(g_0)|_{\text{NP}} = \sqrt{3\;10^{-4}\;\left(0.74\,g_0^8-1.5\,g_0^{10}+0.79\,g_0^{12}\right)} \tag{A.25}$$

[110] $$\mathcal{Z}_{\text{PCAC}}(g_0)|_{\text{NP}} = (1+0.090514\,g_0^2)\,\frac{1-0.3922\,g_0^4-0.2145\,g_0^6}{1-0.6186\,g_0^4} \tag{A.26}$$

$\mathcal{Z}_P^{\text{SF}}(\mu_R, g_0)$ was found to be approximately constant in the β-region of interest at a renormalisation scale of $g_R^2\,(1/V) = 4.484$,

$$\mathcal{Z}_P^{\text{SF}}(\mu_R, g_0) = 0.5184(53) \quad \text{for} \quad 5.2 \leq \beta \leq 6.0\;. \tag{A.27}$$

A.3 Error analysis

The following discussion of the estimation of statistical errors is an abridged version and does not include all details. For further reading it is referred to the extensive review by *Lüscher* [138].

To calculate the expectation value $\langle O \rangle$ of an observable O an associated stochastic estimator O^{st} is measured on the gauge field configuration. If O^{st} is a valid estimator the statistical expectation value $\left\langle O^{\mathrm{st}} \right\rangle$ has to agree with the real expectation value of the operator, here simply denoted by O, in the limit $N \to \infty$,

$$O = \lim_{N\to\infty} \left\langle O^{st} \right\rangle \ . \tag{A.28}$$

Relevant for the error analysis are two different types of estimators, here loosely referred to as observables, 'primary' observables A, i.e. observables that have a well defined value on each configuration $A_n = A[\{U\}_n]$, and 'secondary' ones, that are defined by the expectation value of one or more primary observables, $F[\{\left\langle A^i \right\rangle\}]$. Here the superscript i labels the different observables that contribute to the secondary observable F.

Primary and secondary observables:

For A each individual value A_n can be seen as a statistical measurement. Consequently, its statistical error is given by the second moment, i.e. the standard deviation

$$\mathrm{E}\,[A]^2 = \frac{2\,\tau_A}{N\,(N-1)} \sum_{n=1}^{N} [A_n - \langle A \rangle]^2 \ . \tag{A.29}$$

τ_A is the integrated autocorrelation time, a measure for the autocorrelations of the different configurations introduced by the Markov-process in the Monte-Carlo simulation. It describes the exponential decay of the autocorrelation function

$$\Omega_A(n-m) \equiv \langle (A_n - \langle A \rangle)\ (A_m - \langle A \rangle) \rangle \ . \tag{A.30}$$

For N measurements suitable estimates for the two quantities are given by [152]

$$\Omega_A(h) = \frac{1}{N-h} \sum_{n=1}^{N-h} (A_n - \langle A \rangle)\ (A_{n+h} - \langle A \rangle) \tag{A.31}$$

with $h = |n-m|$ and

$$\tau_A = \frac{1}{2\,\Omega_A(0)} \sum_{m=-W}^{W} \Omega_A(m) \ . \tag{A.32}$$

Here the cutoff W, the 'window' of the summation, is introduced to cut off the region where the noise dominates over the exponential decay in Ω_A.

For a secondary quantity F the error is given by the square root of the FF element of the covariance matrix C_{GH} defined by

$$C_{GH} = \frac{1}{N} \sum_{i,j} \frac{\partial\, G}{\partial \left\langle A^i \right\rangle} \frac{\partial\, H}{\partial \left\langle A^j \right\rangle} \left\langle A^i\, A^j \right\rangle \ . \tag{A.33}$$

The main goal for the error analysis of secondary quantities is thus the estimation of the elements of C_{GH} from the existing data. One possibility which allows for very accurate estimates of the uncertainties is the Γ-method introduced by *Wolff* [388]. However, for practical purpose it is often better to use so called 'binning' methods such as the jackknife or the bootstrap method (see [389]) as introduced in the following.

The jackknife method:

The basic idea of the jackknife method is to replace the set of N measurements by a new set of N_B statistically independent measurements constructed by an inverse binning procedure. These inverse bins $\bar{A}_m$ of size M are defined by

$$\bar{A}_m = \frac{1}{N-M} \left(\sum_{n=1}^{N} A_n - \sum_{k=1}^{M} A_{M\,(m-1)+k} \right) . \tag{A.34}$$

The advantage of these new estimators is that they are statistically independent if M is significantly larger than τ_A and that they are themselves already averaged over a large number of measurements and thus serve as improved estimators directly for the expectation value. The error for the primary quantity A is then given by

$$\mathrm{E}\,[A]^2 = \frac{N_B - 1}{N_B} \sum_{m=1}^{N_B} \left[\bar{A}_m - \langle A \rangle \right] . \tag{A.35}$$

The reliability of the jackknife error depends on the proper choice of the binsize M. A suitable method for its tuning is to plot the relative error of the quantity of interest against M. At some value of M the relative error then develops a plateau and starts to fluctuate around that plateau value. The plateau value then defines the proper statistical error while the size of the fluctuations represent the error on the jackknife error.

The important advantage of the method is its direct applicability to secondary quantities. Here it is important to note that the secondary quantity as computed for a particular jackknife bin

$$\bar{F}_m = F[\{\bar{A}^i_m\}] \tag{A.36}$$

is a stochastic estimator for the observable F. Consequently the covariance matrix is given by

$$C_{GH} = \frac{N_B - 1}{N_B} \sum_{m=1}^{N_B} \left(\bar{G}_m - \langle G \rangle \right) \left(\bar{H}_m - \langle H \rangle \right) . \tag{A.37}$$

The bootstrap method:

Another method which uses binning is the bootstrap method. In this method the data are binned in N/M bins a_m of size M and then for each bootstrap sample $\bar{A}_k$ a random bin is left out from the analysis. This method is convenient for practical purpose since the number of bootstrap bins N_B can be chosen at will and yields a set of statistically independent estimators for the expectation value of A. The error for A can then be estimated by the standard deviation from eq. (A.29) with $A_n \to \bar{A}_n$, $N \to N_B$ and $\tau_A = 1/2$.

The same is true for the the so defined estimators $\bar{F}_k$ for the secondary quantity F and the corresponding covariance matrix is given by

$$C_{GH} = \frac{1}{N_B} \sum_{m=1}^{N_B} \left(\bar{G}_m - \langle G \rangle\right) \left(\bar{H}_m - \langle H \rangle\right) \ . \tag{A.38}$$

The big advantage of the method is that it enables the easy combination of data from different ensembles in a single secondary quantity since each of the N_B samples can be seen as a statistical measurement for the quantity F. The combination of different runs can then be done as for a set of N_B measurements of primary quantities if N_B is chosen to be equivalent for all simulations. This is not necessary possible for the jackknife procedure where the number of bins is fixed by the number of measurements and the binsize.

For non-symmetric distributions of the secondary quantity the bootstrap method has the further advantage that it might be combined with the percentile error estimate. In this procedure the upper and lower value of the distribution at which 16.7 % are cut on both sides of the distribution defines the lower and upper error. This can be of particular advantage if the secondary quantity is obtained by a strong non-linear procedure such as e.g. a non-linear fit where the distributions of the secondary quantities are not necessarily symmetric.

Fitting of correlated data with jackknife and bootstrap methods:

Both error procedures can be used for more and more complicated quantities, also for example for the results for fit parameters. In this case the fit parameters C_i of a fit to the correlated data $F(X)$, where both F and X can be multi-dimensional secondary quantities obtained by one or more simulations, to the functional form $H(X)$ are obtained by the minimisation of the χ^2-functional (see [390])

$$\chi^2 = \sum_{X,X'} \left(H(X) - F(X)\right) \left[C_{F(X),F'(X')}\right]^{-1} \left(H(X') - F'(X')\right) \ . \tag{A.39}$$

This procedure can be done for each jackknife or bootstrap bin which yields an associated result for the fit parameters of each bin. These can then be treated in the usual way as secondary quantities.

The difficulty arises in the treatment of the covariance matrix. In principle, it has to be recalculated for each jackknife or bootstrap bin separately to ensure a consistent statistical treatment. In practice, it might be easier to calculate $\left[C_{F(X),F'(X')}\right]^{-1}$ once for the mean value and keep it fixed for all bins. Both methods are valid to include the correlations while the latter might introduce a bias if the statistics is insufficient [138]. Anyhow, both methods might lead to wrong results if the covariance matrix is not estimated with sufficient accuracy, which leads to a singular matrix in the inversion [250]. This can be detected by looking for obviously wrong results which misses all points in the fit while producing a reasonable χ^2-value. In this case it is necessary to neglect the correlations between the data points and work only with the diagonal part of the covariance matrix. This procedure is denoted as ‘uncorrelated’ fitting.

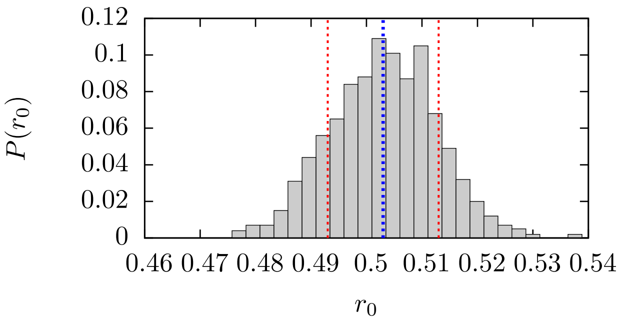

Figure A.1: Pseudo bootstrap distribution for $r_0 = 0.503\,(10)$ fm (blue line) as computed in [77]. The width of the distribution, i.e. the associated statistical error, is indicated by the red lines.

A.4 Pseudo bootstrap distributions

In the course of the analysis the data needs to be combined with results from other simulations, or from experiment, that are known up to some statistical uncertainty. Within the bootstrap method as discussed above the simplest method is to include the error on these quantities in the bootstrap distributions directly. This can be done by generating a pseudo bootstrap distribution that reproduces the variance. For a quantity O with expectation value $\langle O \rangle$ and a purely statistical error $\mathrm{E}\,[O]$ this can be achieved by assuming a normal distribution of the bins $\bar{O}_i$ of the form

$$P(\bar{O}_i) \sim \frac{1}{\mathrm{E}\,[O]\,\sqrt{2\,\pi}} \exp\left[\frac{1}{2}\left(\frac{\bar{O}_i - \langle O \rangle}{\mathrm{E}\,[O]}\right)^2\right] . \tag{A.40}$$

This is in agreement with the standard assumption that statistical measurements in the limit of a large number of measurements obey a normal distribution. The numbers $\bar{O}_i$ can be obtained by the use of a generalised Box-Müller method [391]

$$\bar{O}_i = \mathrm{E}\,[O]\,\sqrt{-2\,\ln\left(1 - r_1\right)}\,\cos\left(2\,\pi\,r_2\right) + \langle O \rangle \tag{A.41}$$

where the r's are uniformly distributed random numbers in the box $(0:1]$. In practice an independent second number can be obtained by replacing the cosine by a sine function. An example for a distribution obtained in this way is shown in figure A.1.

To make sure that the use of the pseudo bootstrap distributions does not introduce systematic effects in the estimation of the error bars for the secondary quantities it is necessary to check its correlation with the bootstrap distributions of the measured quantities, e.g. with some quantity A. This can be done by comparing the bootstrap error for $O \cdot A$ to the error obtained by Gaussian error propagation. If both results agree well the distributions can be considered to be uncorrelated to the ones from the calculated data. A typical quantity which is used for this comparison in our simulations is the pion mass since its error bars are of the typical size around a percent. Table A.1 includes the details for the quantities for which a pseudo bootstrap samples have been generated.

O	$\langle O\rangle$	$\mathrm{E}\,[O]$	$\sigma_{\mathrm{PB}}(O)$	$\sigma_{\mathrm{PB}}(O\cdot m_\pi)$	$\sigma_{\mathrm{EP}}(O\cdot m_\pi)$
$r_0/a\|_{\beta=5.20}$	6.15	0.06	0.060	0.0111	0.0115
$r_0/a\|_{\beta=5.30}$	7.26	0.07	0.064	0.0066	0.0068
$r_0/a\|_{\beta=5.50}$	10.00	0.11	0.108	0.0123	0.0123
r_0 [fm]	0.503	0.010	0.0096	0.00088	0.00089
$\mathcal{Z}_A\|_{\beta=5.20}$	0.771	0.006	0.0058	0.0013	0.0013
$\mathcal{Z}_A\|_{\beta=5.30}$	0.778	0.006	0.0059	0.00066	0.00066
$\mathcal{Z}_A\|_{\beta=5.50}$	0.793	0.005	0.0050	0.00062	0.00062
$\mathcal{Z}_P$	0.518	0.005	0.0052	0.00053	0.00053
$\langle r_\pi^2\rangle^{\mathrm{phys}}$ [fm]^2	0.439	0.008	0.0079	0.00073	0.00074
$\sqrt{2}\,F_\pi^{\mathrm{phys}}$ [GeV]	0.13041	0.00021	0.00022	0.000072	0.000070
m_π^{phys} [GeV]	0.139570180	$3.5\ 10^{-7}$	$3.63\ 10^{-7}$	0.000072	0.000072
$\bar\ell_1$	-0.4	0.6	0.61	0.054	0.054
$\bar\ell_2$	4.3	0.1	0.10	0.0096	0.0093

Table A.1: Properties of the pseudo bootstrap samples generated for the quantities needed in this thesis. O is the quantity, σ_{PB} denotes the bootstrap error of the data including the pseudo bootstrap sample and σ_{EP} denotes the error obtained by Gaussian error propagation. For all quantities the bootstrap sample for the ensemble with the lightest pion mass was used as the reference. For the quantities that are defined in the continuum this means that the pion mass of ensemble F7 was used, while for the quantities that are defined for a specific β-value the pion mass from the lightest ensemble with this particular β value has been used.

A.5 χPT to NNLO for $f_{\pi\pi}(Q^2)$, F_π and m_π

This appendix reviews the formulae for m_π, F_π and $f_{\pi\pi}(Q^2)$ in $SU(2)$-χPT to NNLO from [43]. To keep things simple the notation from [43] is adopted, except for $\hat m \to m_{ud}$, by defining the quantities

$$x_2 \equiv \frac{m_\pi^2}{F_\pi^2} \qquad \bar q^2 \equiv \frac{q^2}{m_\pi^2} \tag{A.42}$$

together with the definitions from eqs. (1.25) and (1.27)–(1.29). Note that in the following the tilde atop the quantities $\tilde N$, $\tilde L$ and $\tilde\gamma_i$ is dropped for convenience. The anomalous dimensions γ_i should not be confused with the γ-matrices. Furthermore, the shorthand notation

$$k_i \equiv (4\,\ell_i^r - \gamma_i\,L)\ L \tag{A.43}$$

is introduced together with the functions

$$\begin{aligned}
J(\bar{q}^2) &\equiv \frac{\sqrt{z}}{N}\,\ln\left(\frac{\sqrt{z}-1}{\sqrt{z}+1}\right)+\frac{2}{N}\\
K_1(\bar{q}^2) &\equiv z\,h^2(\bar{q}^2)\\
K_2(\bar{q}^2) &\equiv z^2\,h^2(\bar{q}^2)-\frac{4}{N^2}\\
K_3(\bar{q}^2) &\equiv \frac{N\,z}{\bar{q}^2}\,h^3(\bar{q}^2)+\frac{\pi^2\,h(\bar{q}^2)}{N\,\bar{q}^2}-\frac{\pi^2}{2\,N^2}\\
K_4(\bar{q}^2) &\equiv \frac{1}{\bar{q}^2\,z}\left(\frac{1}{2}\,K_1(\bar{q}^2)+\frac{1}{3}\,K_3(\bar{q}^2)+\frac{1}{N}\,J(\bar{q}^2)+\frac{(\pi^2-6)\,\bar{q}^2}{12\,N^2}\right)\,,
\end{aligned} \tag{A.44}$$

with

$$z\equiv 1-\frac{4}{\bar{q}^2}\quad\text{and}\quad h(\bar{q}^2)\equiv\frac{1}{N\,\sqrt{z}}\,\ln\left(\frac{\sqrt{z}-1}{\sqrt{z}+1}\right)\,. \tag{A.45}$$

Using these quantities the pion mass and the pion decay constant to NNLO are given by

$$m_\pi^2=m_0\,\left\{1+x_2\,\left[m_\pi\right]_1+x_2^2\,\left[m_\pi\right]_2\right\}\quad\text{and}\quad F_\pi=F\,\left\{1+x_2\,\left[F_\pi\right]_1+x_2^2\,\left[F_\pi\right]_2\right\} \tag{A.46}$$

where

$$\begin{aligned}
\left[m_\pi\right]_1 &\equiv 2\,\ell_3^r+\frac{1}{2}\,L\\
\left[m_\pi\right]_2 &\equiv \frac{1}{N}\left(\ell_1^r+2\,\ell_2^r-\frac{13}{3}\,L\right)+\frac{163}{96\,N^2}-\frac{7}{2}\,k_1-2\,k_2-4\,(\ell_3^r)^2+4\,\ell_3^r\,\ell_4^r\\
&\quad -\frac{9}{4}\,k_3+\frac{1}{4}\,k_4+r_m^r\\
\left[F_\pi\right]_1 &\equiv \ell_4^r-L\\
\left[F_\pi\right]_2 &\equiv \tfrac{1}{N}\,\left(-\tfrac{1}{2}\,\ell_1^r-\ell_2^r+\tfrac{29}{12}\,L\right)-\tfrac{13}{192\,N^2}+\tfrac{7}{4}\,k_1+k_2-2\,\ell_3^r\,\ell_4^r\\
&\quad +2\,(\ell_4^r)^2-\frac{5}{4}\,k_4+r_f^r
\end{aligned} \tag{A.47}$$

Here r_m^r and r_f^r are constants stemming from the $\mathcal{O}(p^6)$-Lagrangian after minimal subtraction and F is the pion decay constant in the chiral limit. For the form factor the expansion is written as

$$f_{\pi\pi}(\bar{q}^2)=1+x_2\,\left[f_{\pi\pi}\right]_1+x_2^2\,\left(P_V^{(2)}+U_V^{(2)}\right)\,. \tag{A.48}$$

Here $[f_{\pi\pi}]_1$ is given by

$$\left[f_{\pi\pi}\right]_1\equiv\frac{1}{6}\,\left(\bar{q}^2-4\right)\,J(\bar{q}^2)+\bar{q}^2\left(-\ell_6^r-\frac{1}{6}\,L-\frac{1}{18\,N}\right) \tag{A.49}$$

and $P_V^{(2)}$ and $U_V^{(2)}$ are the polynomial and dispersive NNLO pieces respectively,

$$
\begin{aligned}
P_V^{(2)} &= \bar{q}^4 \left[\frac{1}{12}\, k_1 - \frac{1}{24}\, k_2 + \frac{1}{24}\, k_6 \right. \\
&\qquad \left. + \frac{1}{9\,N} \left(\ell_1^r - \frac{1}{2}\, \ell_2^r + \frac{1}{2} \ell_6^r - \frac{1}{12}\, L - \frac{1}{384} - \frac{47}{192\,N} \right) + r_{V2}^r \right] \\
&+ \bar{q}^2 \left[-\frac{1}{2}\, k_1 + \frac{1}{4}\, k_2 - \frac{1}{12}\, k_4 + \frac{1}{2}\, k_6 - \ell_4^r \left(2\, \ell_6^r + \frac{1}{9\,N} \right) \right. \\
&\qquad \left. + \frac{23}{36}\, \frac{L}{N} + \frac{5}{576\,N} + \frac{37}{864\,N^2} + r_{V1}^r \right] \\
U_V^{(2)} &= J(\bar{q}^2) \left[\frac{1}{3}\, \ell_1^r \, \left(-\bar{q}^4 + 4\,\bar{q}^2\right) + \frac{1}{6}\, \ell_2^r \, \left(\bar{q}^4 - 4\,\bar{q}^2\right) + \frac{1}{3}\, \ell_4^r \, \left(\bar{q}^2 - 4\right) \right. \\
&\qquad + \frac{1}{6}\, \ell_6^r \, \left(-\bar{q}^4 + 4\,\bar{q}^2\right) - \frac{1}{36}\, L \, \left(\bar{q}^4 + 8\,\bar{q}^2 - 48\right) \\
&\qquad \left. + \frac{1}{N} \left(\frac{7}{108}\, \bar{q}^4 - \frac{97}{108}\, \bar{q}^2 + \frac{3}{4} \right) \right] + \frac{1}{9}\, K_1(\bar{q}^2) \\
&+ \frac{1}{9}\, K_2(\bar{q}^2) \left(\frac{1}{8}\, \bar{q}^4 - \bar{q}^2 + 4 \right) + \frac{1}{6}\, K_3(\bar{q}^2) \left(\bar{q}^2 - \frac{1}{3} \right) - \frac{5}{3}\, K_4(\bar{q}^2) \,.
\end{aligned}
\tag{A.50}
$$

r_{V1}^r and r_{V2}^r are again from the $\mathcal{O}(p^6)$-Lagrangian.

A.6 Reformulation of χPT for global fits

For the fits intended in chapter 6 it is necessary to reformulate the χPT expressions since the right hand sides depend on the quantities m_π and F_π that are in this context subject to χPT themselves. For the fits including $f_{\pi\pi}(Q^2)$ it is convenient to define the new fit parameter

$$
\tilde{\ell} \equiv \ell_1^r - \frac{1}{2}\, \ell_2^r = \frac{1}{6\,N} \, \left(\bar{\ell}_1 - \bar{\ell}_2\right) \tag{A.51}
$$

which eliminates the fit parameters ℓ_1^r and ℓ_2^r completely in eq. (A.50). In the following $\tilde{\ell}$ is used instead of ℓ_2^r also in the expressions for m_π and F_π.

For the reformulation one has to replace m_π and F_π in each formula with the expressions in eq. (A.46) and to keep all terms to $\mathcal{O}(x_2^2)$. It necessary to replace m_π and F_π with its NLO expressions in each NLO term only. In the course of this replacement the parameters

$$
x_2 \,, \quad L \,, \quad \bar{q}^2 \,, \quad \text{and} \quad J(\bar{q}^2) \,. \tag{A.52}
$$

have to be modified and similar parameters appear with the leading order parameters m_0 and F instead of m_π and F_π. These new parameters are defined in analogy to eq. (A.42) and are given by

$$\begin{aligned} \hat{x}_2 &\equiv \frac{m_0}{F^2}\ , & \hat{q}^2 &\equiv \frac{q^2}{m_0}\ , \\ \hat{L}\ ; &\equiv \frac{1}{N}\ \ln\left(\frac{m_0}{\mu^2}\right)\ , & \hat{k}_i &\equiv \left(4\,\ell_i^r - \gamma_i\,\hat{L}\right)\ \hat{L}\ , \\ \hat{J}(\hat{q}^2) &\equiv \frac{\sqrt{\hat{z}}}{N}\ \ln\left(\frac{\sqrt{\hat{z}}-1}{\sqrt{\hat{z}}+1}\right) + \frac{2}{N}\ , & \hat{z} &\equiv 1 - \tfrac{4}{\hat{q}^2}\ . \end{aligned} \tag{A.53}$$

In the functions K_i only the arguments are replaced signaling that it remains the same functions but with $\bar{q}^2 \to \hat{q}^2$ and $z \to \hat{z}$. Using the shorthand notation

$$\Delta_m \equiv 2\,\ell_3^r + \frac{1}{2}\,\hat{L} \quad \text{and} \quad \Delta_f \equiv \ell_4^r - \hat{L}\ , \tag{A.54}$$

m_π^2 and F_π get replaced by

$$m_\pi^2 \ \to\ m_0\ (1 + \hat{x}_2\,\Delta_m) \quad \text{and} \quad F_\pi\ \to\ F\ (1 + \hat{x}_2\,\Delta_f) \tag{A.55}$$

for all quantities in eq. (A.52).

Most of the replacements are straight-forward. The only more complicated replacement is the one which takes place in the function $J(\bar{q}^2)$, since it is a somewhat complicated function of z. The final result can be written in the useful form

$$J(\bar{q}^2) = \hat{J}(\hat{q}^2) - \hat{x}_2\,\frac{\Delta_m}{\hat{q}^2 - 4}\,\left(2\,\hat{J}(\hat{q}^2) - \frac{\hat{q}^2}{N}\right)\ . \tag{A.56}$$

The final expressions for m_π^2 and F_π are given by

$$m_\pi^2 = m_0\,\left\{1 + \hat{x}_2\ [m_\pi]_1 + \hat{x}_2^2\,\left([m_\pi]_2 + \Delta_m\ [\Delta_m - 2\,\Delta_f] + \frac{\Delta_m}{2\,N}\right)\right\}\ , \tag{A.57}$$

and

$$F_\pi = F\,\left\{1 + \hat{x}_2\ [F_\pi]_1 + \hat{x}_2^2\,\left([F_\pi]_2 + \Delta_f\ [\Delta_m - 2\,\Delta_f] - \frac{\Delta_m}{N}\right)\right\}\ , \tag{A.58}$$

where $[m_\pi]_1$, $[m_\pi]_2$, $[F_\pi]_1$ and $[F_\pi]_2$ are defined as in eq. (A.47) with all quantities replaced by their '^'-version from eq. (A.53). For $f_{\pi\pi}(\hat{q}^2)$ one obtains

$$\begin{aligned} f_{\pi\pi}(\bar{q}^2) \ &=\ 1 + \hat{x}_2\ [f_{\pi\pi}]_1 + \hat{x}_2^2\,\left(P_V^{(2)} + U_V^{(2)}\right) \\ &+\ \hat{x}_2^2\,\Big[-\Delta_m\,\hat{J}(\hat{q}^2) \\ &\qquad -2\,\Delta_f\,\left(\tfrac{1}{6}\,\left(\hat{q}^2 - 4\right)\,\hat{J}(\hat{q}^2) - \hat{q}^2\,\left[\ell_6^r + \tfrac{1}{6}\hat{L} + \tfrac{1}{18\,N}\right]\right)\Big] \end{aligned} \tag{A.59}$$

where again the replacements are implied in $[f_{\pi\pi}]_1$, $P_V^{(2)}$ and $U_V^{(2)}$.

The result for the charge radius is obtained by computing the partial derivative of $f_{\pi\pi}(q^2)$ with respect to q^2 and setting $q^2 = 0$ afterwards. In the course of this process it is necessary to evaluate the value of derivative of $\hat{J}(\hat{q}^2)$ in the limit $\hat{q}^2 \to 0$, which is given by

$$\left.\frac{\partial\,\hat{J}(\hat{q}^2)}{\partial \hat{q}^2}\right|_{q^2=0} = \frac{1}{6\,N}\ . \tag{A.60}$$

The rest of the computation is straight forward and the result is

$$\langle r_\pi^2 \rangle = \frac{1}{m_0}\left\{\hat{x}_2\ \left[\langle r_\pi^2\rangle\right]_1 + \hat{x}_2^2\left(\left[\langle r_\pi^2\rangle\right]_2 - 2\,\Delta_F\ \left[\langle r_\pi^2\rangle\right]_1 - \frac{\Delta_m}{N}\right)\right\} \tag{A.61}$$

where $\left[\langle r_\pi^2\rangle\right]_1$ is the NLO part as given in [43],

$$\left[\langle r_\pi^2\rangle\right]_1 = -\left(6\,\ell_6^r + \hat{L} + \frac{1}{N}\right)\ , \tag{A.62}$$

and $\left[\langle r_\pi^2\rangle\right]_2$ the usual NNLO part,

$$\left[\langle r_\pi^2\rangle\right]_2 = -12\hat{L}\tilde{\ell} - \frac{1}{2}k_4 + 3k_6 - 12\ell_4^r\ell_6^r + \frac{1}{N}\left(-2\,\ell_4^r + \frac{31}{6}\,\hat{L} + \frac{13}{192} - \frac{181}{48\,N}\right) + 6r_{V1}^r\ . \tag{A.63}$$

Note that all the results above are in full agreement with the ones obtained in [228].

To model cut-off effects a^2-terms are added to the χPT expressions. For the form factor the normalisation $f_{\pi\pi}(0) = 1$ allows only for cut-off effects that vanish for $q^2 \to 0$. They are modeled by adding a term proportional to $(aq)^2$ to the extrapolation formulae. For the charge radius this translates into adding a simple a^2-term. Adding also terms that correspond to a^2-effects in the logarithmic terms, the extended formulae are given by

$$\begin{aligned}
\left(m_\pi\left[1 + \alpha_m^{(1)}\frac{a^2}{r_0^2}\right]\right)^2 &= (A.57) + \alpha_m^{(2)}\frac{a^2}{r_0^2}\,\hat{x}_2\,\hat{L}\ ; \qquad\qquad\qquad\quad (A.64)\\
F_\pi &= (A.58) + \alpha_f^{(1)}\frac{a^2}{r_0^2} + \alpha_f^{(2)}\frac{a^2}{r_0^2}\,\hat{x}_2\,\hat{L}\ ; \qquad\qquad (A.65)\\
f_{\pi\pi}(\hat{q}^2) &= (A.59) + \alpha_r^{(1)}\frac{a^2}{r_0^2}\,\frac{m_0\,\hat{q}^2}{6} + \alpha_r^{(2)}\frac{a^2}{r_0^2}\,\hat{x}_2\,\hat{L}\,\frac{\hat{q}^2}{6}\ ; \quad (A.66)\\
\langle r_\pi^2\rangle &= (A.61) + \alpha_r^{(1)}\frac{a^2}{r_0^2} + \alpha_r^{(2)}\frac{a^2}{r_0^2}\,\frac{1}{F^2}\,\hat{L}\ . \qquad\qquad (A.67)
\end{aligned}$$

Note that for m_π the lattice artefacts are expected to be of $\mathcal{O}(a^2)$ for the mass itself and thus should be included on the left hand side. The second term however is an effect of $\mathcal{O}(a^2)$ for the LECs and thus has to be included on the right.

A.7 The c_{SW} recursion algorithm

The β-region where c_{SW} is known non-perturbatively ends at $\beta = 5.20$. Below this point the padé from eq. (2.33) should not be used to define c_{SW} since it might lead to an insufficient cancellation of lattice artefacts. In the case of the study of the phase diagram the demand $\beta \geq 5.20$ proves a substantial limitation for simulations. Since $r_0/a = 6.15$ at that point in the chiral limit the minimal temperature for $N_t = 8,\ 12,\ 16$ is given by $T = 303,\ 202,\ 151$ MeV respectively. This means, if one assumes a transition temperature of $T \approx 156$ MeV as obtained in simulations with staggered fermions (cf. section 7.2.2) then one has to go to $N_t = 16$ at least to be able to push the simulations to the chiral point. Thereby the computational cost increases by roughly a factor of 20 or so compared to simulations at $N_t = 8$.

Apart from algorithmical problems that might appear below $\beta = 5.20$, the problem discussed above could be overcome if one is able to find another way to reliably estimate the value for c_{SW}. Since the questionable regime is in the region of strong coupling it is apparent that a weak coupling expansion is not expected to give reliable results. Furthermore, the weak coupling expansion of c_{SW} in the mean field improved version depends on the value for the critical hopping parameter κ_c and the expectation value of the plaquette U_P that are both unknown in that regime as well. In turn, both of the other weak coupling expansions depend on these two quantities, making it difficult to extract any of the quantities from perturbation theory. Anyhow, one might think about possibilities to overcome this problem. In this appendix two procedures are compared to non-perturbative and perturbative results to see if one of them reproduces the non-perturbative results and thus might be used to define c_{SW} below $\beta = 5.20$.

Setup of the two methods:

c_{SW} is known from meanfield perturbation theory in its tadpole improved version [392] to 1-loop order,

$$c_{SW} = U_P^{-\frac{3}{4}} \left[1 + \left(c_{SW}^1 - \frac{2}{3} \left[2\, C_F + \frac{1}{N} \right] T_{MF} \right) g_0^2 \right] . \tag{A.68}$$

Here C_F is defined as in eq. (A.12), $T_{MF} = 1/8$ is the meanfield factor [393] and c_{SW}^1 is given by [392]

$$c_{SW}^1 = 0.26858825\,(1)\ . \tag{A.69}$$

for the plaquette gauge action. To be able to calculate c_{SW} it is thus essential to know the expectation value of the plaquette which, without approximations, can only be calculated in a dynamical simulation within the fully $\mathcal{O}(a)$-improved theory.

The first possibility to overcome this problem is to approximate the expectation value of the plaquette by the expectation value as obtained by the same value of g_0 in the pure gauge theory. Of course there is no reason why both would have to be the same. Nevertheless, naively one would expect the value as obtained by a non-perturbative simulation, even without dynamical quarks, to be closer to the exact non-perturbative case in the region of strong coupling. Results obtained with this method using the plaquette expectation value as obtained on a 12^4-lattice are shown in figure A.2.

The second possibility is to use the perturbative expansion for the plaquette [394] as listed in eq. (A.70). The expansion coefficients themselves depend on c_{SW} and the hopping parameter κ. Since the $\mathcal{O}(a)$-improvement program is conventionally set up in the chiral

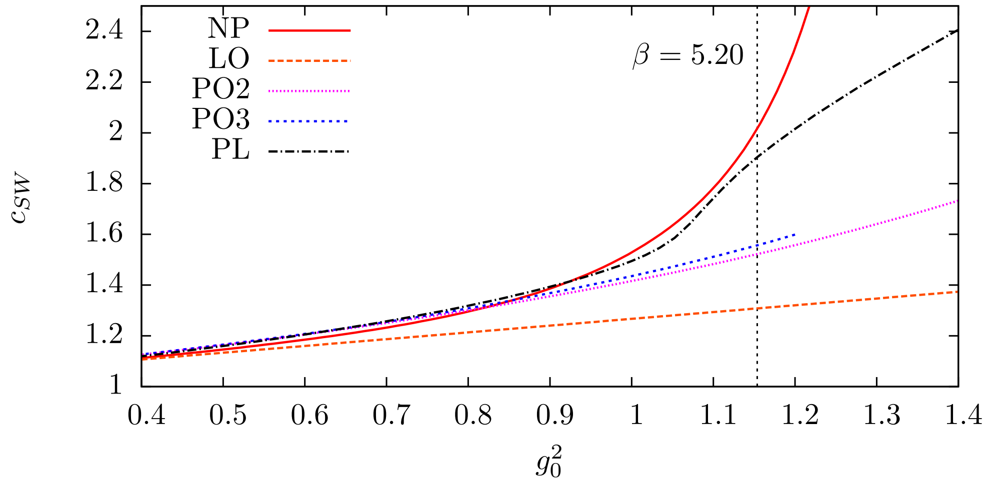

Figure A.2: Results of the different methods to estimate c_{SW}. The labels are as explained in the text.

limit [90–93] one has to set $\kappa = \kappa_c$ in the expansion for the plaquette. Again κ_c has to be calculated perturbatively with the expansion from [395, 396] as listed in eq. (A.74). Again the coefficients of the expansion depend on c_{SW}. In consequence, the calculation of c_{SW} has to be done using an iterative procedure, which can be set up as follows:

1. Start with some initial value $c_{SW}(0)$, e.g. the perturbative value in the free theory $c_{SW}(0) = 1$.
2. Use $c_{SW}(n)$ to calculate $\kappa_c(n+1)$ via the expansion of eq. (A.74).
3. Use $c_{SW}(n)$ and $\kappa_c(n+1)$ to calculate $U_P(n+1)$ via eq. (A.70).
4. Use $U_P(n+1)$ to calculate $c_{SW}(n+1)$ via eq. (A.68).
5. Go to 2 with $n \to n+1$.

If this procedure converges this gives an estimate for c_{SW}. In fact, the convergence properties are quite good and the method converges in all cases after two to five iterations.

Results of the method and comparison to non-perturbative results:

Figure A.2 shows the results as obtained from the different methods discussed earlier. The results denoted with ‘PO2’ and ‘PO3’ are obtained with the plaquette expansion to $\mathcal{O}(g_0^4)$ and $\mathcal{O}(g_0^6)$ respectively. For PO3 the iterative procedure does not work below $\beta = 5.00$ since κ_c is outside of the region where the coefficients for the plaquette are known The results denoted as ‘PL’ are the results from pure gauge theory as calculated on a 12^4 lattice using 1000 heathbath [26, 148, 149] sweeps combined with 3 overrelaxation sweeps [397–399] after thermalisation. Also shown is the line from eq. (2.33), denoted by ‘NP’ and the ‘LO’ perturbative line, eq. (2.34), together with the border at $\beta = 5.20$ below which c_{SW} is not known non-perturbatively.

Up to $g_0^2 = 0.9$ the results from the iterative methods and the ones with the pure gauge plaquette agree well with the non-perturbative results. For larger couplings the iterative results lie significantly below the non-perturbative results while the agreement with the data using the plaquette from pure gauge theory is good up to $\beta = 5.20$. The latter thus appears to be the favourable choice. Note that the numerical cost for the calculation of the plaquette is small and the plaquette can be calculated on a standard processor within an hour.

Weak coupling expansions:

For the plaquette the perturbative expansion has been worked out in [394] and is given by:

$$\begin{aligned} U_P &= N\,(1 - E_G) \\ E_G &= c_1\, g_0^2 + c_2\, g_0^4 + c_3\, g_0^6 \\ c_n &= c_n^G + c_n^F \end{aligned} \tag{A.70}$$

The coefficients c_n^G for the gauge sector are known from [400]:

$$\begin{aligned} c_1^G &= \frac{N^2-1}{8\,N} \\ c_2^G &= \left(N^2-1\right)\left(0.0051069297 - \frac{1}{128\,N^2}\right) \\ c_3^G &= \left(N^2-1\right)\left(\frac{0.0023152583(50)}{N^3} - \frac{0.002265487(17)}{N} + 0.000794223(19)\,N\right) \end{aligned} \tag{A.71}$$

The coefficients c_n^F depend on c_{SW} and can be written in the form:

$$\begin{aligned} c_1^F &= 0 \\ c_2^F &= \left(N^2-1\right)\frac{N_f}{N}\,h_2 \\ c_3^F &= \left(N^2-1\right)\left(N_f\,h_{30} + \frac{N_f}{N^2}\,h_{31} + \frac{N_f^2}{N}\,h_{32}\right) \\ h_2 &= h_2^0 + h_2^1\,c_{SW} + h_2^2\,c_{SW}^2 \\ h_{3i} &= h_{3i}^0 + h_{3i}^1\,c_{SW} + h_{3i}^2\,c_{SW}^2 + h_{3i}^3\,c_{SW}^3 + h_{3i}^4\,c_{SW}^4 \end{aligned} \tag{A.72}$$

The coefficients h_2^j and h_{3i}^j depend on the hopping parameter κ. This dependence is not known analytically but numerical values exists in the range $\kappa = 0.122169 - 0.167500$ [394]. In that region the value for the coefficients for a given value of κ might be extracted using numerical interpolation. Here a standard polynomial interpolation is used [390].

For κ_c the perturbative expansion is taken from [395, 396]:

$$\begin{aligned}
\kappa_c &= \frac{1}{2\,m_C+8} \\
m_C &= m_1\,g_0^2 + m_2\,g_0^4 \\
m_1 &= \frac{N^2-1}{N}\,(-0.16285705871085(15) + 0.04348303388205\,c_{SW} \\
&\qquad +0.01809576878142(1)\,c_{SW}^2) \qquad\qquad (\text{A.73}) \\
\frac{m_2}{N^2-1} &= -0.017537(3) + 0.016567(2)\,\frac{1}{N^2} + 0.00118618(8)\,\frac{N_f}{N} \\
&+ \left(0.002601(2) - 0.0005597(7)\,\frac{1}{N^2} - 0.0005459(2)\,\frac{N_f}{N}\right)\,c_{SW} \\
&+ \left(-0.0001556(3) + 0.0026226(2)\,\frac{1}{N^2} + 0.0013652(1)\,\frac{N_f}{N}\right)\,c_{SW}^2 \\
&+ \left(-0.00016315(6) + 0.00015803(6)\,\frac{1}{N^2} - 0.00069225(3)\,\frac{N_f}{N}\right)\,c_{SW}^3 \\
&+ \left(-0.000017219 + 0.000042829(3)\,\frac{1}{N^2} - 0.000198100(7)\,\frac{N_f}{N}\right)\,c_{SW}^4
\end{aligned}$$

B Remarks on algorithmical aspects

B.1 Measurement of reweighting factors

To measure the reweighting factor from eq. (8.17) in the case of two degenerate flavours one can use the method outlined in [366]. The reweighting factor for each configuration can be written as

$$\begin{aligned} R(\beta,\beta_a) &= \det\left[\frac{D^{+}(\beta)\,D(\beta)}{D^{+}(\beta_a)\,D(\beta_a)}\right] \\ &= \det\left\{\left[(D^{+}(\beta))^{-1}\,D^{+}(\beta_a)\,D(\beta_a)\,(D(\beta))^{-1}\right]^{-1}\right\}\;. \end{aligned} \tag{B.1}$$

Following section 4.3 the determinant can be computed using stochastic sources. In particular it is convenient to use sources that are Gaussian distributed with action $S_\eta = \eta^{+}\eta$ [366]. Using the same arguments as in section 3.1 the expectation value for R can be written as

$$\langle R(\beta,\beta_a)\rangle = \left\langle \frac{1}{Z_\eta}\int d[\eta]\;\exp\left\{\eta^{+}\eta - \varphi^{+}\varphi\right\}\right\rangle\;. \tag{B.2}$$

with

$$\varphi \equiv D(\beta_a)\,(D(\beta))^{-1}\,\eta\;. \tag{B.3}$$

In practice, the integral over the stochastic sources can be evaluated using some finite number of sources for each configuration. This combination of the stochastic and gauge average then leads to a sufficient approximation for the exact reweighting factor.

B.2 Weak starts

Apart from a 'hot' start, i.e. a start from a completely random configuration, it is also possible to start from a fully ordered configuration, consisting of unit matrices. This so called 'cold' start uses the free theory as a starting point. The second starting point is useful to test the ergodicity of the algorithm and to start in a different regime for simulations at finite temperature.

In practice, a start from the unit gauge configuration can be problematic since in the free case the critical hopping parameter is given by $\kappa_c = 1/8$ which means that for typical κ-values the mass becomes negative. This usually leads to problems with the solver convergence for the necessary inversions in the HMC. There are some ways to overcome this problem. The first possibility is to start with $\kappa < 1/8$ and then gradually increase it to the desired value in the course of the thermalisation process. This procedure works well in practice but has the disadvantage that it needs additional time until the thermalisation with the desired κ-value starts. Another possibility is to use a start from a configuration consisting of $SU(3)$ matrices that are close to the free case but with included small fluctuations in the off-diagonal elements. This is what is here referred to as a 'weak' start. The consequence of this procedure is that the gauge fields attain a certain 'temperature' that shifts the critical hopping parameter to larger values, so that the mass is no longer negative at the first few configurations. The task at hand is thus to construct random $SU(3)$-matrices that have small non-diagonal contributions.

There are two ways to realise such matrices:

1. **$SU(3)$-generator representation:**
   Any $SU(3)$ matrix U can be written in terms of the Gell-Mann matrices λ^a as defined in eq. (A.9) via
   $$U = u_0\, \mathbf{1} + \sum_{a=1}^{7} u_a\, \lambda^a\ . \tag{B.4}$$
   A unit matrix in this representation is given by the coefficients $u_0 = 1$ and $u_i = 0$ for $i = 1, \ \ldots\ , 7$. Any small deviation from a unit matrix can now be readily generated by randomly choosing the coefficients $u_i = 0$ uniformly distributed in the interval $[0, \delta_W]$, where δ_W is a small number $\sim 10^{-3}$ to 10^{-1} which limits the maximal deviation from unity of the $SU(3)$ matrices in the configuration. The factor u_0 is then obtained by the constraint $\det(U) = 1$.

2. **Construction via $SU(2)$ subgroups:**
   Another possibility is to use the $SU(2)$ subgroups of $SU(3)$ that are also used in the Cabbibo-Marinary heathbath update [149]. In this case, one might obtain any $SU(3)$ matrix by multiplying the three $SU(3)$ matrices $U_{2,i}$ that contains the i'th $SU(2)$ subgroup,
   $$U = \prod_{i=1}^{3} U_{2,i}\ . \tag{B.5}$$
   To obtain a matrix that has a small deviation from unity the $SU(2)$ matrices contained in the subgroup have to be close to unit $SU(2)$ matrices. They can be obtained by writing the $SU(2)$ sub-matrices $\mathcal{U}_{2,i}$ as
   $$\mathcal{U}_{2,i} = u_0\, \mathbf{1} + \sum_{j=1}^{3} u_j\, \sigma^j\ . \tag{B.6}$$
   If the coefficients u_j are again randomly distributed in the interval $[0, \delta_W]$ then u_0 is simply obtained by $\det(\mathcal{U}_{2,i}) = 1$, i.e.
   $$u_0 = \sqrt{\sum_{j=1}^{3} u_j^2}\ . \tag{B.7}$$
   It is straight forward to show that such a choice for the matrices $U_{2,i}$ leads to a $SU(3)$ matrix which is close to the unit matrix.

Here the second method is used to perform weak starts. The tunable parameter is the interval length δ_W which is chosen to be equivalent for all coefficients u_j. In practice, δ_W often has to be quite large to allow for safe inversions.

B.3 Calculation of the weights in the MH method

Essential for the implementation for the MH method from chapter 8 is the calculation of the weights. Once these are known the computation of all other quantities is straight forward. A suitable choice for the weights is given in eq. (8.32). The formula for the calculation of the weights depends on the free energies F^a, that in turn depend on the weights themselves via eq. (8.30). As a consequence, both sides of eq. (8.32) are mutually dependent and the weights have to be computed using an iterative procedure. A possible starting point are uniform weights, $w^a_{\mathrm{IJ}} = N^{-1}_{\mathrm{meas}}$, where N_{meas} is the number of simulation points. This first set of weights can then be used to obtain the F^a's that in turn are used to compute new weights via eq. (8.32), and so on. A suitable stopping criterion is to demand that

$$\delta \equiv \frac{\sum_{\mathrm{IJ},a} \left[(w^a_{\mathrm{IJ}})_{\mathrm{new}} - (w^a_{\mathrm{IJ}})_{\mathrm{old}}\right]^2}{\sum_{\mathrm{IJ},a} (w^a_{\mathrm{IJ}})^2_{\mathrm{new}}} \tag{B.8}$$

is small, say $\delta < 10^{-10}$, for two consecutive iteration steps old → new.

C Simulation details I: Zero temperature

C.1 Twist angles

set	θ_0	θ_1	θ_2	θ_3	θ_4	θ_5
A4	0.0000	±2.2658	±1.8438	±1.3582	±0.7745	±2.5000
A5	0.0000	±2.4380	±2.0281	±1.5544	±0.9777	±2.5000
E4	0.0000	±1.6799	±1.2748	±0.8195	±0.2969	±2.5000
E5	0.0000	±2.1728	±1.7866	±1.3476	±0.8344	±2.5000
F6	0.0000	±3.2455	±2.9371	±2.6028	±2.2355	±1.5000
F7	0.0000	±3.7892	±3.5196	±3.2323	±2.9231	±2.0000
N3	0.0000	±0.7538	±0.3777	±0.4935	±1.0146	±4.0000
N4	0.0000	±1.2730	±0.8936	±0.4726	±0.5443	±3.9000
N5	0.0000	±1.7513	±1.3942	±0.9945	±0.5311	±3.2000

Table C.1: The choice of twist angles for the ensembles from table 5.2.

C.2 Extraction of $f_{\pi\pi}(Q^2)$ and $\langle r_\pi^2 \rangle$

This appendix collects some results for quantities that are important for the discussion of the extraction of $f_{\pi\pi}(Q^2)$ and $\langle r_\pi^2 \rangle$.

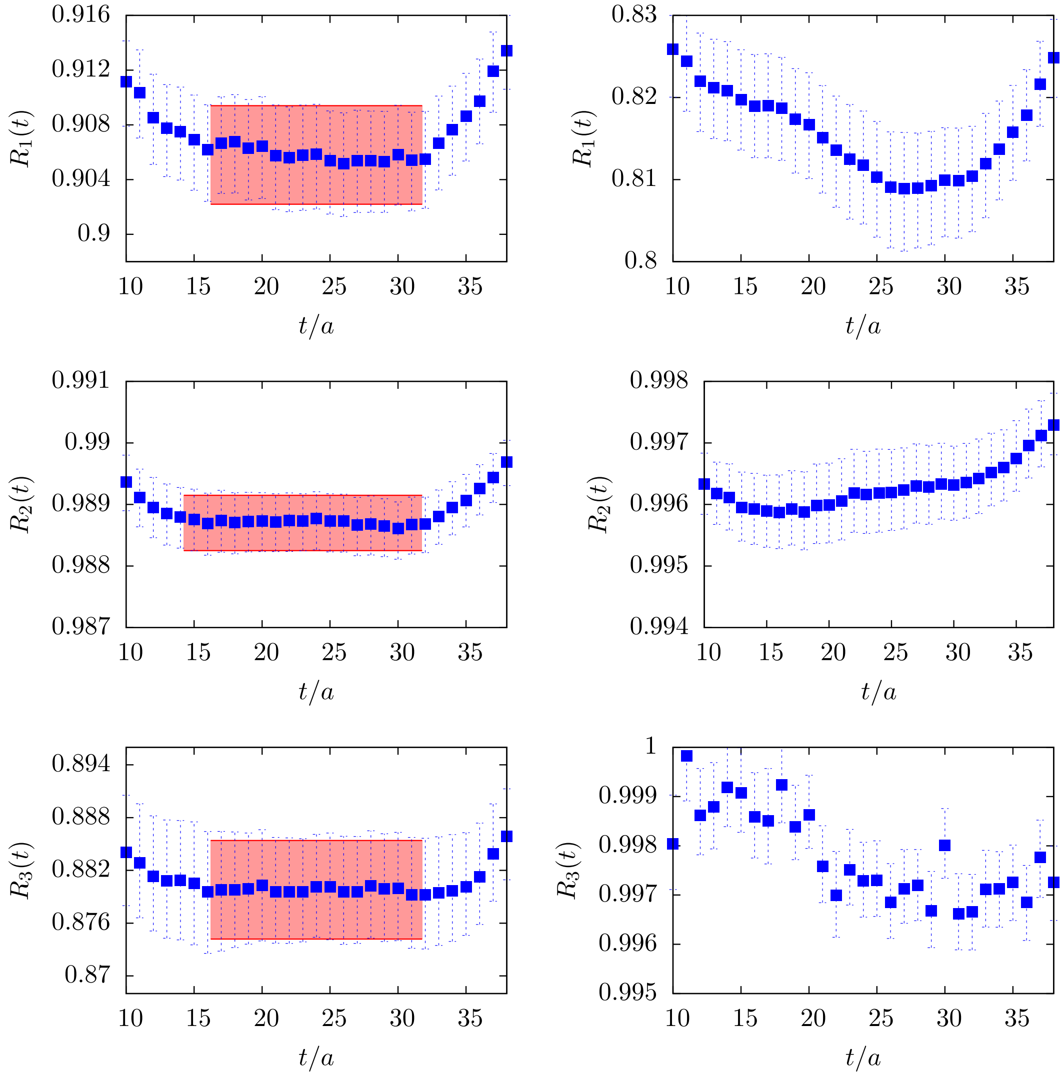

Figure C.1: Typical example for the behaviour of the different ratios R_1–R_3 (from top to bottom) for one of the Q^2-values where the ratio has been included in the analysis (left) and another Q^2-value where it has been left out. The criterion is the quality of the plateau around $T/4 = 24$ as explained in section 5.5.2.

A3		A4		A5	
$(Q\,r_0)^2$	$f_{\pi\pi}(Q^2)$	$(Q\,r_0)^2$	$f_{\pi\pi}(Q^2)$	$(Q\,r_0)^2$	$f_{\pi\pi}(Q^2)$
0.0042	0.99919 (3)	0.0220	0.9957 (3)	0.0347	0.9915 (5)
0.0170	0.9968 (2)	0.0666	0.9870 (8)	0.0859	0.9798 (9)
0.0314	0.9941 (2)	0.0885	0.9827 (9)	0.1410	0.9664 (17)
0.0730	0.9864 (5)	0.1208	0.9766 (13)	0.1429	0.9673 (16)
0.1238	0.9771 (7)	0.1793	0.9658 (19)	0.2016	0.9549 (25)
0.1262	0.9766 (8)	0.2159	0.9592 (24)	0.2112	0.9529 (26)
0.2751	0.9506 (14)	0.2721	0.9487 (26)	0.3564	0.9205 (34)
0.2961	0.9466 (16)	0.5015	0.9094 (44)	0.6067	0.8733 (52)
0.5066	0.9121 (26)	0.7573	0.8686 (58)	0.8767	0.8284 (71)
1.1564	0.8208 (48)	0.9219	0.8446 (66)	0.9219	0.8212 (75)

E4		E5		F6		F7	
$(Q\,r_0)^2$	$f_{\pi\pi}(Q^2)$	$(Q\,r_0)^2$	$f_{\pi\pi}(Q^2)$	$(Q\,r_0)^2$	$f_{\pi\pi}(Q^2)$	$(Q\,r_0)^2$	$f_{\pi\pi}(Q^2)$
0.0045	0.99927 (2)	0.0355	0.9931 (3)	0.0503	0.9886 (4)	0.0870	0.9768 (11)
0.0181	0.99709 (9)	0.0915	0.9821 (7)	0.1090	0.9756 (9)	0.1767	0.9537 (30)
0.0344	0.9945 (2)	0.1433	0.9722 (11)	0.1456	0.9679 (13)	0.2120	0.9445 (43)
0.0828	0.9870 (4)	0.1585	0.9691 (12)	0.1826	0.9602 (17)	0.2469	0.9362 (55)
0.1382	0.9782 (7)	0.2308	0.9555 (19)	0.2058	0.9548 (15)	0.2811	0.9296 (61)
0.1426	0.9775 (7)	0.3010	0.9427 (24)	0.2196	0.9528 (23)	0.3659	0.9084 (36)
0.3095	0.9518 (15)	0.3738	0.9295 (26)	0.4572	0.9037 (32)	0.7817	0.8302 (92)
0.3345	0.9483 (15)	0.6570	0.8809 (41)	0.6197	0.8727 (44)	0.9558	0.7983 (103)
0.5809	0.9130 (24)	0.9718	0.8316 (56)	0.7892	0.8424 (55)	1.3323	0.7670 (112)
1.2865	0.8240 (48)	1.2865	0.7867 (71)	0.9636	0.8119 (68)	1.3135	0.7372 (125)

N3		N4		N5	
$(Q\,r_0)^2$	$f_{\pi\pi}(Q^2)$	$(Q\,r_0)^2$	$f_{\pi\pi}(Q^2)$	$(Q\,r_0)^2$	$f_{\pi\pi}(Q^2)$
0.0062	0.99907 (7)	0.0097	0.99838 (7)	0.0122	0.99762 (7)
0.0106	0.99842 (8)	0.0128	0.99782 (8)	0.0425	0.9918 (2)
0.0246	0.9963 (2)	0.0345	0.9940 (2)	0.0490	0.9906 (3)
0.0248	0.9963 (2)	0.0388	0.9932 (2)	0.0829	0.9842 (4)
0.0423	0.9937 (2)	0.0514	0.9910 (3)	0.1295	0.9756 (6)
0.0445	0.9934 (2)	0.0697	0.9879 (3)	0.1717	0.9675 (8)
0.0987	0.9855 (4)	0.1386	0.9761 (6)	0.3375	0.9382 (15)
0.1788	0.9739 (6)	0.2813	0.9524 (11)	0.4087	0.9270 (22)
0.6525	0.9088 (25)	0.6099	0.9017 (28)	0.5325	0.9060 (22)
2.7778	0.6984 (63)	2.6406	0.6719 (59)	1.7778	0.7440 (57)

Table C.2: Results for $f_{\pi\pi}(Q^2)$ on the different ensembles restricted to the 1ST and Breit-frame for which FSEs are known. The data given in the tables already includes those effects. Here the error bars on Q^2 are not quoted.

ensemble	$\left\langle r_\pi^2 \right\rangle_{\text{lin}} / r_0^2$ $(Q_{\text{max}}\, r_0)^2 = 0.15$	$\left\langle r_\pi^2 \right\rangle_{\text{lin}} / r_0^2$ $(Q_{\text{max}}\, r_0)^2 = 0.01$	$\bar{\ell}_6^{\text{NLO}}$ $(Q_{\text{max}}\, r_0)^2 = 0.22$
A3	1.12 (4)	1.13 (4)	13.1 (5)
A4	1.15 (8)	1.11 (11)	12.9 (7)
A5	1.38 (8)	1.34 (25)	14.5 (9)
E4	0.95 (4)	0.97 (4)	12.1 (4)
E5	1.18 (6)	1.18 (10)	13.4 (6)
F6	1.34 (7)	1.37 (17)	14.1 (7)
F7	1.62 (11)	2.04 (48)	16.2 (11)
N3	0.89 (3)	0.90 (3)	11.7 (4)
N4	1.04 (4)	1.04 (4)	12.8 (4)
N5	1.15 (4)	1.15 (4)	13.2 (5)

Table C.3: Results for $\left\langle r_\pi^2 \right\rangle$ (2nd and 3rd columns) extracted from linear fits to the full data set for $f_{\pi\pi}(Q^2)$ with cuts of $(Q_{\text{max}} r_0)^2 = 0.15$ and $(Q_{\text{max}} r_0)^2 = 0.01$. The last column includes the results for $\bar{\ell}_6$ obtained from fits to χPT at NLO with a cut at $(Q_{\text{max}} r_0)^2 = 0.22$. For the quantities listed here FSEs are not subtracted.

C.3 Finite size effects

The FSEs are calculated in χPT with the expressions given in [256, 257] for the pion mass and the pion decay constant and in [258] for the 1ST case and in [259] for the Breit-frame (cf. section 6.2.1). The FSEs for the form factor are given as a fraction of the quantity

$$g_{\pi\pi}(Q^2) = \frac{f_{\pi\pi}(Q^2) - 1}{Q^2} \,, \tag{C.1}$$

while for the pion mass and the decay constant the value is given in terms of the fraction of the quantity itself.

ensemble	$\Delta_V m_\pi / m_\pi$	$\Delta_V F_\pi / F_\pi$
A3	0.000194	-0.000477
A4	0.000964	-0.002617
A5	0.002133	-0.006003
E4	0.000181	-0.000390
E5	0.001233	-0.003169
F6	0.000459	-0.001337
F7	0.000966	-0.002903
N3	0.000027	-0.000051
N4	0.000112	-0.000251
N5	0.000563	-0.001445

Table C.4: FSEs for the pion mass and the pion decay constant.

θ_i	A3		A4		A5	
	1ST	Breit	1ST	Breit	1ST	Breit
1	-0.0005	-0.0011	+0.0006	-0.0029	+0.0042	-0.0048
2	-0.0009	-0.0013	-0.0011	-0.0037	+0.0007	-0.0063
3	-0.0013	-0.0015	-0.0029	-0.0045	-0.0031	-0.0078
4	-0.0016	-0.0016	-0.0046	-0.0051	-0.0070	-0.0090
5	+0.0005	-0.0005	+0.0016	-0.0024	+0.0047	-0.0045

θ_i	E4		E5		F6		F7	
	1ST	Breit	1ST	Breit	1ST	Breit	1ST	Breit
1	-0.0006	-0.0010	+0.0003	-0.0032	+0.0030	-0.0004	+0.0093	+0.0010
2	-0.0009	-0.0012	-0.0014	-0.0040	+0.0022	-0.0010	+0.0082	+0.0001
3	-0.0012	-0.0013	-0.0031	-0.0047	+0.0012	-0.0015	+0.0068	-0.0008
4	-0.0014	-0.0014	-0.0047	-0.0053	+0.0002	-0.0021	+0.0052	-0.0019
5	+0.0001	-0.0006	+0.0017	-0.0025	-0.0019	-0.0031	-0.0002	-0.0046

θ_i	N3		N4		N5	
	1ST	Breit	1ST	Breit	1ST	Breit
1	-0.0003	-0.0004	-0.0007	-0.0009	-0.0011	-0.0024
2	-0.0004	-0.0004	-0.0009	-0.0010	-0.0019	-0.0028
3	-0.0004	-0.0004	-0.0010	-0.0010	-0.0026	-0.0031
4	-0.0003	-0.0003	-0.0010	-0.0010	-0.0032	-0.0033
5	+0.0003	+0.0000	+0.0009	+0.0001	+0.0024	-0.0004

Table C.5: Finite size effects for the pion form factor in the 1ST and Breit frame for the different twist angles θ_i from table C.1, given in units of $g_{\pi\pi}$ from eq. (C.1).

D Simulation details II: Non-zero temperature

D.1 Test scans for the MH method

scan	Lattice	κ	β-range	N_β	τ_{U_P}	kMDU
Z3	8×24^3	0.09	5.70–6.00	23	~ 20	240
Z4	8×24^3	0.11	5.70–5.95	26	~ 45	240
Z5	8×24^3	0.13	5.40–5.54	11	~ 45	80

Table D.1: Run parameters for the additional runs with heavy dynamical quarks to test the MH method.

			truncated	
β	$\ln[R(\beta, 5.82)]$	1st order	2nd order	3rd order
5.75	-1099.429 (5)	-1065.886 (6)	-1075.376 (6)	-1075.395 (6)
5.76	-930.963 (3)	-905.976 (5)	-913.569 (5)	-913.581 (5)
5.77	-766.547 (5)	-749.409 (4)	-754.604 (4)	-754.610 (4)
5.78	-606.887 (3)	-595.133 (3)	-598.409 (3)	-598.413 (3)
5.79	-449.067 (3)	-443.101 (3)	-444.917 (3)	-444.918 (3)
5.80	-295.8492 (9)	-293.265 (2)	-294.061 (2)	-294.061 (2)
5.81	-146.2415 (7)	-145.5797 (7)	-145.7758 (8)	-145.7758 (7)
5.83	143.85652 (2)	143.5175 (7)	143.3270 (7)	143.3270 (7)
5.84	282.514 (2)	285.015 (2)	284.264 (2)	284.264 (2)
5.85	419.058 (3)	424.534 (2)	422.867 (2)	422.868 (2)
5.86	552.483 (3)	562.114 (3)	559.191 (3)	559.194 (3)
5.87	682.975 (3)	697.795 (4)	693.291 (4)	693.296 (4)

Table D.2: Results for the logarithm of the ratios of fermion determinants. The three rightmost columns contain the results from the truncations to order 1, 2 and 3 respectively.

D.2 Interpolation of $T = 0$ quantities

In this section the interpolations for the Sommer parameter r_0/a and the critical hopping parameter are collected. As already discussed in section 9.1.2 the interpolation for the Sommer parameter from [77] can be done using an ansatz of the form (cf. eq. (9.2))

$$\frac{r_0}{a}(\beta) = \exp\left(\bar{a}_0 + \bar{a}_1\,\beta + \bar{a}_2\,\beta^2 + \ldots\right) \ . \tag{D.1}$$

The results of this parametric ansatz for the results for r_0/a from zero temperature are shown in figure 9.1 (top) and the results for the parameters are listed in table D.3. Note that the large error bars on the parameters do not reflect the uncertainty for the interpolation in the region $5.20 \le \beta \le 5.50$. The form of the interpolation curve is sufficiently constrained,

quantity	ansatz	$\bar{a}_0$	$\bar{a}_1$	$\bar{a}_2$
r_0/a	(D.1)	-13 (16)	3.9 (62)	-0.21 (58)
	(D.2)	-184 (120)	-79 (45)	8.6 (42)
κ_c	(D.3)	-0.82 (4)	10.2 (4)	-29.0 (9)
	(D.4)	-4.09 (2)	-2.967 (8)	-4.70 (2)

Table D.3: Parameters for the interpolation of the zero temperature parameters.

as can be seen from the plot. To check the model dependence of the interpolation one can compare the results to those of an interpolation using a polynomial of the form

$$\frac{r_0}{a}(\beta) = \bar{a}_0 + \bar{a}_1\,\beta + \bar{a}_2\,\beta^2\ . \tag{D.2}$$

The results for the parameters are also listed in table D.3 and the two curves are shown in comparison in figure D.1 (top). As can be seen from the plot the agreement between the two curves is excellent and the systematic error connected with the particular ansatz will be small.

For the purpose of renormalisation and the tuning of the parameters for lines of constant physics it is also convenient to have an interpolation of κ_c. Here the interpolation is done using a padé of the form

$$\kappa_c(\beta) = \frac{1}{8}\,\frac{1+\bar{a}_0/\beta+\bar{a}_1/\beta^2}{1+\bar{a}_2/\beta}\ , \tag{D.3}$$

where the normalisation $\kappa_c(\beta) \to 1/8$ for $\beta \to \infty$ has been built in. The results are shown in figure D.1 (bottom) and the parameters are listed in table D.3. Again the model dependence of the interpolation can be checked by using a polynomial of the form

$$\kappa_c(\beta) = \frac{1}{8} + \frac{\bar{a}_0}{\beta} + \frac{\bar{a}_1}{\beta^2} + \frac{\bar{a}_2}{\beta^3}\ . \tag{D.4}$$

The comparison in figure D.1 shows that both curves agree well in the region of $5.20 \leq \beta \leq 5.50$. The biggest discrepancy appears in the region $5.35 \leq \beta \leq 5.45$. However, the systematic uncertainty will likely be below the statistical uncertainties for most of the quantities of interest. This can be checked directly by looking at the difference in the predictions stemming from the two different interpolation formulae.

To determine the relation between κ and m_{ud} with the method described in section 9.3.1 some input for m_{PCAC} for different values of the bare parameters from the simulations at finite temperature is necessary. The input for m_{PCAC} from the CLS ensembles is listed in table D.4.

D.3 Algorithm tuning and performance at $T \neq 0$

At finite temperature the major part of the simulation time is needed for the generation of the gauge ensembles. As a consequence, choosing a suitable algorithm and its proper tuning

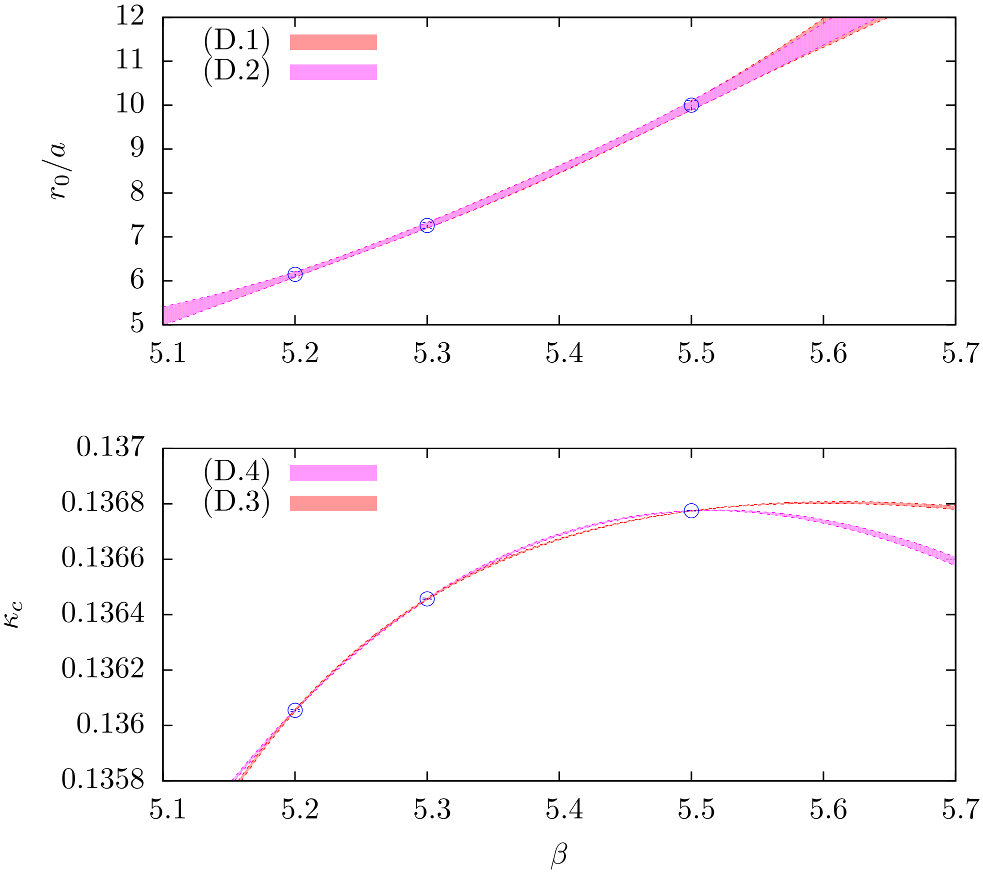

Figure D.1: Results for the interpolations of the results for r_0/a (top) and κ_c (bottom) from table 5.2 for the ansätze (D.1) to (D.4). The fit parameters are listed in table D.3.

are fundamental. This appendix discusses the tuning involved in running the DD-HMC [152, 176] and MP-HMC [174, 175, 178] algorithms (cf. section 3.5) at finite temperatures and reports on their performance.

Algorithm tuning:

The first parameter of the algorithm which has to be fixed is the length of a trajectory τ in molecular dynamic units (MDU). It defines the step size in configuration space to the next proposal for a configuration in the accept/reject step. For finite temperature one important demand is that the step size is large enough to enable an efficient crossing of the phase boundaries, separating configuration relevant for the 'hot' and 'cold' phases. The probability of such a crossing grows with the step size, so that it is more efficient to use larger values for τ [401]. In practice, this increase has to be balanced against an increased number of solver iterations needed to maintain a high acceptance rate. A suitable setup is to use an acceptance rate between 70 and 80 % with a step size of $\tau = 2$ [401]. Note,

ensemble	β	κ	$a\, m_{\mathrm{PCAC}}$
A2	5.20	0.13565	0.0158 (2)
A3		0.13580	0.0098 (3)
A4		0.13590	0.0057 (4)
A5		0.13594	0.0044 (2)
E5	5.30	0.13625	0.0072 (3)
F6		0.13625	0.00375 (11)
F7		0.13638	0.00267 (9)
N4	5.50	0.13650	0.0091 (2)
N5		0.13660	0.0059 (2)
N6		0.13667	0.00343 (12)
O7		0.13671	0.00213 (6)

Table D.4: Results for the bare PCAC mass in lattice units for the CLS lattices. The results for ensembles A2, N6 and O7 are taken from [77].

that the fluctuations in acceptance along the HMC evolution can be substantial. This is particularly true in the region close to T_C where the system often changes its phase in the course of the Markov chain, and thereby the properties of the Dirac operator. To avoid large gaps between successful configuration updates it is convenient to tune the parameters so that the acceptance rate for each bin of 100 successive configurations remains larger than 70 %.

Next, one has to tune the parameters controlling the splitting of infrared and ultraviolet modes and the iteration numbers in the multiple-timescale integrator. In the case of the DD-HMC algorithm this means that one has to tune the domain decomposition block sizes. It has been found that a lower bound for the optimal block size is approximately 0.5 fm in each direction [152, 176]. For simulations at finite temperature this means that a block size of $N_t/2$ is close to optimal because $T_C \approx 200$ MeV and therefore $a\, N_t \approx 1$ fm. This particular choice for the block sizes is used for the simulations in this thesis. The only cases where an exception is necessary are the 16×64^3 lattices that have to be run on a large number of cores. In this case it was necessary to use a block size of 8×4^3. The optimal choice for the 3 iteration numbers in the multiple-timescale integrator, associated with the integrators T_G, T_Λ and T_{DD} for the gauge force, the block force and the force of the Schur complement, have been found to be mostly independent of the block size and the quark mass [152]. The first two can be set to $L_G = 4$ and $L_\Lambda = 5$ while the tuning of L_{DD} controls the acceptance rate. The tuning of the intermediate masses in the MP-HMC is a bit more involved. For the MP-HMC it is suitable to fix the inner iteration numbers to unity, since the evaluation of the fermionic forces is more costly than in the case of the DD-HMC [402] [2]. The intermediate masses can be tuned by demanding that the associated forces obey eq. (3.45).

---

[2] Note, that the implementation of the MP-HMC algorithm uses a Sexton-Weingarten integrator instead of a leapfrog. This automatically leads to an additional factor of two in the step sizes.

After the basic setup the algorithm performance is governed by the parameters of the DFL-SAP-GCR solver. The main parameters which have to be tuned are the block sizes of the Schwartz preconditioner and the deflation blocks, as well as the size of the deflation subspace. The blocks for the Schwartz preconditioning should fit in the cache of the processor, i.e. their size typically should be between 4^4 to 8^4 on current processors. At the same time they limit the size of the blocks connected with the deflation subspace and thus should not be to small to leave some freedom for the tuning. In practice, it turns out that a suitable starting point for the tuning of the solver parameters in the regime of light quarks is a setup with Schwartz blocks of size $8^2 \times 4^2$, a deflation space with blocks of size 4^4 and a number of $N_D = 16$ approximate low modes. To tune the solver one can then vary the parameters and look for a minimum in the computational cost for a trajectory. For the runs of this thesis the typical sizes of the deflation blocks are 4^4 and $8^2 \times 4^2$ with $N_D = 16$ and 26 respectively. This has proven optimal for pion masses down to 290 MeV. For smaller masses it is beneficial to increase the number N_D from 16 to 20 for a block size of 4^4 and similarly for other block sizes. Most of the other solver parameters can be kept fixed and assume the values suggested in [159, 167]. Two additional parameters which have to be increased to assure the stability when going to pion masses below 290 MeV are the size of the Krylov space and the number of solver iterations for the minimal-residual algorithm, used for the inversions of the block operators.

Algorithm performance:

The averaged time per trajectory and the associated quark masses for the different runs are listed in tables D.6 to D.10. The runs use the DD-HMC algorithm and have been distributed over a number of computational facilities, namely the HPC-cluster ‘Wilson’ at the Institute for Nuclear Physics in Mainz, the HPC-cluster ‘Fuchs’ at the Center for Scientific Computing in Frankfurt, the HPC-cluster ‘JUROPA’ and the blue-gene P ‘JUGENE’ at the Forschungszentrum Jülich. The first three host the 16×32^3 and 16×48^3 lattices, since these can be simulated efficiently on a smaller number of processors. Typical parallelisations for the different lattices sizes are listed in table D.5. The 16×64^3 lattices need a larger number of processors and should be done on large scale machines, for instance on JUGENE. To be able to compare the timings for the runs on the different platforms the timings on Wilson are used as the standard reference for the runs on the smaller lattices. To convert the timings into run times for Wilson one can use the empirically obtained relations

$$t_{\text{Wilson}} \approx 2 \times t_{\text{JUROPA}} \approx 0.8 \times t_{\text{Fuchs}} \,. \tag{D.5}$$

Since all runs for the 16×64^3 lattices have been done on JUGENE the timings for those are given in these units directly. The timings are quoted with respect to the numbers of processors for the particular lattice sizes from table D.5.

The timings for the different runs reported in tables D.6 to D.10 illustrate that the DD-HMC algorithm performs well. In particular, a 16×32^3 lattice, which is already quite large for the purpose of simulations at finite temperature, can be simulated efficiently on 64 processors and yields the typically necessary 20000 MDU for a pion mass of 290 MeV in about 120 days. The timings also reveal a significant difference for the simulation time

Lattice	12×24^3	16×32^3	16×48^3	16×64^3
processors	32	64	216	4096

Table D.5: Typical parallelisations for the different lattice sizes.

in hot and cold phases. Below T_C the eigenvalues of the Dirac operator are only bounded from below by the mass of the light quarks. Once the quark mass is small, there are modes with small eigenvalues and the simulations suffer from a significant slowing down. The appearance of small eigenvalues also increases the fluctuations in ΔH and leads to smaller acceptance rates. Above T_C the spectrum of the Dirac operator develops an ultraviolet cut-off which stabilises the simulations. Note, that a percentage of 3 to 4 for the number of spikes with $\Delta H > 10$ is a typical value, also at $T = 0$ for simulations with an acceptance rate of 85 to 90 % [403].

The integrated autocorrelation times of the plaquette also takes values that are in the region of what one would expect from simulations at zero temperature for similar block sizes, at least at temperatures away from the critical one. At the critical point the autocorrelations increase as discussed in section 9.3.2. However, as long as the blocks are larger than 8^4 the autocorrelations are acceptable. Their size increases drastically for smaller block sizes. This is in particular problematic for the 16×64^3 lattices that have been done on JUGENE where the use of a large number of processors is requested. For these lattices block sizes of 8×4^3 have been used and the autocorrelations increase by roughly a factor 3 compared to what one would expect from the autocorrelation times of the 16×32^3 and 16×48^3 lattices. For the runs on JUGENE, or similar systems, it is thus advisable to use the MP-HMC algorithm which has no inactive links and thus does not suffer from larger autocorrelations for finer parallelisations.

Stability in the approach to the chiral regime:

Some algorithmic difficulties appear in the approach to the chiral regime in the region close to and below T_C where the Dirac operator suffers from the appearance of small eigenvalues. The problem is that the condition number of the diagonal matrices in the even-odd block preconditioned ‘little’ Dirac operator (see the notes on the solver for the little system in the appendix of [167] for the definitions) becomes to large to enable a safe inversion via the Householder triangulation method. A reason for this might be that the subspace of modes that are included in the little system covers a wide range of eigenvalues. This can happen when there are very small eigenvalues in the Dirac operator with a gap to the next larger ones, for instance. Another reason might be an accidental inclusion of higher modes in the little subspace due to inexact deflation. However, to confirm either of the two possibilities one would have to perform a designated study on the problem which is beyond the scope of this thesis. A simple solution to the problem is to change the size of the deflation subspace for a few configurations. This automatically changes the condition number for the little Dirac operator and thereby solves the problem. Note, that this neither breaks the Monte-Carlo chain nor presents any problem for the generated ensemble, since the solver parameters have no influence on the solution to the Dirac equation up to the precision set for the solver. Anyhow, one should notice that the deflation subspace is generated stochastically, i.e. a change in the subspace changes the random numbers that appear in the MD after the next construction of the deflation subspace. Again this does not present a problem as such, but one should keep in mind that by changing the deflation subspace one also changes the trajectory of the Monte-Carlo chain in configuration space.

Conclusive statements:

The DD-HMC algorithm has proven to be a powerful algorithm also for simulations at finite temperature and enables fast simulations also on small scale clusters. Nevertheless, the fact that the autocorrelation times are drastically increased when small DD blocks are used is a severe drawback for simulations on a larger number of processors. Future simulations will therefore use the MP-HMC algorithm. The occasional appearance of configurations where the solver does not converge, so called exceptional configurations, is a source for concern and the frequency of their appearance increases in the approach to smaller quark masses. However, a fine-tuning of the solver parameters usually helps. Furthermore, the appearance of exceptional configurations seems to be rare, not more then once per 1000-2000 MDUs, even for the smallest pion masses simulated so far.

D.4 Simulation details of the test scans

This section contains the simulation parameters for the test scans reported in section 9.2. The listed parameters are the bare parameters, the number of molecular dynamics units after thermalisation, MDU, the number of stored configurations N_{cnfg}, and temperature, quark mass in the $\overline{\text{MS}}$-scheme with $\mu_R = 2$ GeV and pion mass in MeV. The second table contains the outer iteration number for the multiple timescale integrator, the time per trajectory of length $\tau = 2$, the integrated autocorrelation time of the plaquette, the acceptance rate, the expectation value of $e^{-\Delta H}$ and the percentage of cases where ΔH was bigger than 10.

β	κ	MDU	N_{cnfg}	T [MeV]	m_{ud} [MeV]	m_π [MeV]
5.270000	0.135950	27000	45	226 (5)	56 (3)	624 (26)
5.275000		20700	23	228 (5)	50 (3)	572 (25)
5.285000		52800	88	232 (5)	59 (3)	647 (29)
5.288130		49800	83	233 (5)	59 (3)	639 (29)
5.290630		49200	82	234 (5)	60 (3)	653 (31)
5.292500		52800	88	234 (5)	65 (3)	691 (36)
5.293750		36000	60	235 (5)	64 (3)	681 (48)
5.296880		32400	54	236 (5)	63 (4)	676 (35)
5.298750		52200	87	237 (5)	67 (3)	707 (41)
5.301250		61200	102	238 (5)	67 (3)	709 (40)
5.302500		56400	94	238 (5)	69 (4)	723 (49)
5.303750		54000	90	239 (5)	72 (4)	752 (54)
5.310000		38400	64	241 (6)	73 (4)	756 (54)
5.315000		31200	52	243 (6)	72 (4)	753 (57)
5.320000		25200	42	245 (6)	79 (5)	818 (77)

β	L_{DD}	t_{traj} [sec]	τ_{U_P} [MDU]	acc [%]	$\langle e^{-\Delta H} \rangle$	$\Delta H > 10$ [%]
5.270000	22	190	95 (24)	73	0.966 (10)	3.3
5.275000	22	200	95 (32)	62	0.953 (14)	3.7
5.285000	22	170	92 (20)	76	0.972 (6)	1.9
5.288130	22	180	72 (12)	78	0.974 (6)	1.8
5.290630	22	180	83 (16)	78	0.986 (5)	1.3
5.292500	22	180	71 (13)	78	0.978 (5)	1.5
5.293750	22	170	60 (9)	78	1.010 (28)	1.4
5.296880	22	170	70 (11)	80	0.986 (7)	1.3
5.298750	22	170	55 (7)	80	0.993 (6)	0.8
5.301250	22	170	58 (7)	80	1.095 (107)	1.0
5.302500	22	170	71 (12)	82	0.984 (4)	0.6
5.303750	22	170	55 (7)	82	0.997 (4)	0.7
5.310000	22	170	74 (13)	83	0.990 (6)	1.0
5.315000	22	160	58 (10)	83	0.994 (4)	0.6
5.320000	22	160	58 (10)	83	0.994 (4)	0.6

Table D.6: Run parameters for run $\mathbf{A}_\kappa$ from table 9.1.

β	κ	MDU	N_{cnfg}	T [MeV]	m_{ud} [MeV]	m_π [MeV]
5.375000	0.136500	9000	45	201 (5)	17.0 (14)	313 (14)
5.400000		11000	55	209 (5)	25.5 (24)	381 (19)
5.425000		20200	101	218 (5)	32.3 (34)	429 (24)
5.450000		20600	103	227 (5)	39.6 (20)	477 (15)
5.475000		21600	108	236 (5)	39.3 (20)	472 (15)
5.481250		20200	101	238 (5)	46.2 (22)	520 (16)
5.487500		19600	98	240 (6)	46.9 (21)	524 (15)
5.493750		21400	107	243 (6)	45.3 (21)	512 (15)
5.496875		16200	81	244 (6)	47.9 (22)	530 (15)
5.500000		21600	108	245 (6)	45.5 (20)	513 (14)
5.503125		16600	83	246 (6)	43.6 (21)	500 (15)
5.506250		21000	105	248 (6)	49.7 (25)	542 (17)
5.512500		21600	108	250 (6)	47.7 (24)	528 (17)
5.518750		19800	99	252 (6)	50.6 (22)	548 (16)
5.525000		19400	97	255 (6)	53.5 (25)	568 (20)
5.550000		19200	96	265 (7)	51.3 (24)	550 (17)
5.575000		12200	61	275 (8)	55.6 (27)	579 (22)

β	L_{DD}	t_{traj} [sec]	τ_{U_P} [MDU]	acc [%]	$\langle e^{-\Delta H} \rangle$	$\Delta H > 10$ [%]
5.375000	60	650	26 (5)	91	0.978 (6)	1.8
5.400000	45	630	56 (8)	81	0.969 (16)	4.1
5.425000	35	460	32 (4)	80	0.944 (12)	3.5
5.450000	35	490	20 (2)	82	0.966 (11)	2.4
5.475000	37	410	22 (3)	89	0.993 (4)	0.5
5.481250	35	500	18 (2)	88	1.000 (6)	0.5
5.487500	35	450	21 (3)	89	0.996 (5)	0.2
5.493750	35	440	19 (3)	90	1.000 (4)	0.3
5.496875	35	410	16 (2)	89	0.998 (4)	0.4
5.500000	37	450	19 (2)	88	0.988 (6)	0.7
5.503125	35	360	16 (2)	91	1.000 (3)	0.1
5.506250	35	410	17 (2)	89	0.993 (3)	0.3
5.512500	35	370	17 (2)	90	0.989 (3)	0.5
5.518750	35	430	14 (1)	90	0.997 (4)	0.1
5.525000	37	400	17 (2)	91	0.999 (3)	0.3
5.550000	37	350	14 (2)	93	0.997 (3)	0.0
5.575000	37	370	13 (2)	94	0.996 (2)	0.0

Table D.7: Run parameters for run $\mathbf{B1}_\kappa$ from table 9.1.

β	κ	MDU	N_{cnfg}	T [MeV]	m_{ud} [MeV]	m_π [MeV]
5.487500	0.136500	16000	100	240 (6)	43.9 (19)	503 (14)
5.500000		16160	101	245 (6)	47.9 (21)	530 (15)
5.512500		16160	101	250 (6)	46.8 (21)	521 (14)

β	L_{DD}	t_{traj} [sec]	τ_{U_P} [MDU]	acc [%]	$\langle e^{-\Delta H} \rangle$	$\Delta H > 10$ [%]
5.487500	65	370	70 (12)	89	0.996 (3)	0.2
5.500000	65	340	93 (20)	90	0.998 (4)	0.2
5.512500	65	330	53 (8)	92	1.000 (3)	0.1

Table D.8: Run parameters for run $\mathbf{B3}_\kappa$ from table 9.1.

β	κ	MDU	N_{cnfg}	T [MeV]	m_{ud} [MeV]	m_π [MeV]
5.350000		12200	305	193 (5)	-0.5 (9)	0
5.360000		19800	495	196 (5)	3.3 (8)	141 (17)
5.370000		15400	385	199 (5)	7.2 (9)	205 (13)
5.380000		15800	395	203 (5)	10.9 (8)	252 (10)
5.390000		15600	390	206 (5)	10.7 (9)	249 (11)
5.400000		16800	420	209 (5)	13.5 (10)	278 (11)
5.410000		16600	415	213 (5)	16.6 (9)	307 (9)
5.420000		13000	325	216 (5)	18.8 (12)	326 (11)

β	L_{DD}	t_{traj} [sec]	τ_{U_P} [MDU]	acc [%]	$\langle e^{-\Delta H} \rangle$	$\Delta H > 10$ [%]
5.350000	160	1750	29 (6)	92	0.953 (16)	3.6
5.360000	160	2000	25 (4)	90	0.959 (9)	3.9
5.370000	140	1500	21 (3)	92	0.970 (5)	2.6
5.380000	120	1400	19 (3)	91	1.060 (82)	2.6
5.390000	120	1240	24 (3)	93	0.975 (4)	2.0
5.400000	120	1300	19 (2)	93	0.988 (4)	1.5
5.410000	120	1300	19 (3)	93	0.987 (4)	1.5
5.420000	90	1100	24 (4)	90	0.977 (5)	1.9

Table D.9: Run parameters for run $\mathbf{C2}_\kappa$ from table 9.1.

D.5 Simulation details and Monte Carlo data for scan C1

This section collects the simulation details for scan **C1** from table 9.4, with a constant quark mass of $m_{ud} \approx 14.5$. The quantities that are listed in the tables are the same as in the last section. The runs have been done on Wilson at the university of Mainz, Fuchs at the university of Frankfurt and JUROPA at Jülich. Also listed are results for the real part of the bare and APE-smeared Polyakov loop and for the bare and subtracted condensate.

β	κ	MDU	N_{cnfg}	T [MeV]	m_{ud} [MeV]	m_π [MeV]
5.300000	0.136356	5360	134	178 (4)	14.2 (10)	293 (11)
5.355000	0.136500	13080	327	195 (5)	13.9 (14)	282 (11)
5.370000	0.136523	12560	314	199 (5)	14.9 (10)	294 (11)
5.380000	0.136545	12280	307	203 (5)	14.7 (12)	292 (12)
5.390000	0.136565	12280	307	206 (5)	13.6 (10)	280 (11)
5.400000	0.136575	12080	302	209 (5)	15.6 (15)	299 (15)
5.410000	0.136603	12320	308	213 (5)	14.5 (12)	287 (13)
5.420000	0.136619	12080	302	216 (5)	9.9 (11)	238 (13)
5.430000	0.136635	12480	312	220 (5)	10.3 (9)	242 (11)
5.440000	0.136649	12160	304	223 (5)	10.2 (13)	241 (15)
5.450000	0.136662	6720	168	227 (5)	10.4 (14)	242 (16)
5.470000	0.136668	6680	167	234 (5)	16.3 (14)	301 (14)
5.500000	0.136700	12520	313	245 (6)	9.1 (14)	225 (17)

β	L_{DD}	t_{traj} [sec]	τ_{U_P} [MDU]	acc [%]	$\langle e^{-\Delta H} \rangle$	$\Delta H > 10$ [%]
5.300000	80	920	19 (3)	80	0.973 (42)	6.2
5.355000	65	930	34 (7)	84	0.931 (14)	5.6
5.370000	65	600	19 (3)	90	0.973 (7)	2.2
5.380000	55	600	25 (4)	87	0.952 (12)	3.1
5.390000	55	540	20 (3)	87	1.015 (56)	3.8
5.400000	55	540	24 (5)	85	0.940 (13)	3.6
5.410000	55	540	31 (5)	88	0.957 (15)	3.3
5.420000	55	520	23 (4)	89	0.963 (10)	2.7
5.430000	55	540	22 (4)	93	0.984 (5)	1.4
5.440000	55	540	15 (2)	90	0.958 (18)	3.0
5.450000	55	580	15 (2)	95	0.997 (3)	0.7
5.470000	55	500	20 (4)	92	0.992 (11)	1.5
5.500000	65	500	14 (2)	97	0.998 (2)	0.3

Table D.10: Run parameters for run **C1** from table 9.4.

β	$\langle L \rangle\ 10^4$	χ_L	τ_L	$\langle L_{\mathrm{SM}} \rangle\ 10^2$	$\chi_{L_{\mathrm{SM}}}$	$\tau_{L_{\mathrm{SM}}}$
5.300	2.1 (5)	0.89 (4)	1.05 (9)	0.95 (6)	2.2 (2)	55 (29)
5.355	4.9 (3)	0.85 (3)	1.10 (9)	2.76 (6)	3.6 (3)	59 (18)
5.370	4.8 (4)	0.90 (3)	1.47 (20)	2.76 (6)	3.6 (3)	38 (9)
5.380	5.7 (4)	0.88 (3)	1.12 (10)	3.52 (6)	3.4 (3)	97 (42)
5.390	5.7 (4)	0.90 (3)	1.01 (7)	3.45 (6)	4.0 (3)	59 (19)
5.400	5.4 (4)	0.94 (3)	1.25 (11)	3.40 (6)	3.9 (3)	83 (38)
5.410	5.5 (4)	0.94 (3)	1.66 (21)	3.31 (8)	6.0 (4)	96 (26)
5.420	6.9 (4)	0.88 (3)	1.02 (9)	3.85 (6)	3.5 (2)	45 (15)
5.430	7.8 (4)	0.96 (3)	1.24 (12)	4.49 (7)	4.7 (4)	59 (21)
5.440	8.1 (4)	0.93 (3)	1.10 (9)	4.80 (7)	4.2 (3)	77 (29)
5.450	8.4 (5)	0.90 (4)	0.94 (8)	4.83 (10)	6.2 (7)	79 (37)
5.470	9.2 (4)	0.97 (4)	0.87 (7)	5.41 (9)	4.9 (5)	43 (14)
5.500	11.6 (4)	0.92 (3)	1.09 (8)	6.21 (7)	5.2 (4)	66 (28)

Table D.11: Results for the real part of the Polyakov loop L and its APE-smeared version L_{SM} for scan **C1**.

β	$\langle \bar\psi\psi \rangle_{\mathrm{bare}}$	$\chi_{\langle \bar\psi\psi \rangle_{\mathrm{bare}}}$	$\tau_{\langle \bar\psi\psi \rangle_{\mathrm{bare}}}$	$\langle \bar\psi\psi \rangle_{\mathrm{sub}}\ 10^3$	$\chi_{\langle \bar\psi\psi \rangle_{\mathrm{sub}}}\ 10^3$	$\tau_{\langle \bar\psi\psi \rangle_{\mathrm{sub}}}$
5.300	0.271104 (4)	13.5 (14)	2.7 (6)	2.90 (6)	19.9 (27)	3 (29)
5.355	0.270331 (3)	12.1 (9)	8.9 (28)	2.28 (6)	9.0 (11)	8 (18)
5.370	0.270120 (3)	8.8 (7)	3.4 (6)	2.34 (6)	4.9 (6)	10 (9)
5.380	0.269991 (3)	10.9 (8)	5.8 (14)	2.18 (5)	3.7 (6)	18 (42)
5.390	0.269869 (2)	6.7 (7)	3.5 (8)	2.09 (5)	2.8 (4)	14 (19)
5.400	0.269754 (3)	8.0 (7)	4.2 (10)	2.22 (5)	4.4 (5)	26 (38)
5.410	0.269627 (3)	9.4 (7)	19.1 (8)	1.89 (4)	4.8 (7)	47 (26)
5.420	0.269503 (2)	6.3 (5)	5.2 (13)	1.79 (4)	2.0 (2)	27 (15)
5.430	0.269375 (2)	5.2 (5)	1.9 (3)	1.68 (3)	1.0 (2)	20 (21)
5.440	0.269267 (2)	6.3 (6)	5.6 (16)	1.63 (3)	2.3 (4)	48 (29)
5.450	0.269140 (2)	4.9 (6)	1.3 (2)	1.55 (3)	1.1 (3)	66 (37)
5.470	0.268909 (2)	4.5 (6)	1.5 (3)	1.81 (3)	1.6 (3)	26 (14)
5.500	0.268564 (2)	3.8 (5)	1.0 (1)	1.56 (3)	0.9 (4)	14 (28)

Table D.12: Results for the bare chiral condensate $\langle \bar\psi\psi \rangle_{\mathrm{bare}}$ and the subtracted condensate $\langle \bar\psi\psi \rangle_{\mathrm{sub}}$ for scan **C1**.

β	$B_4(L)$	$B_4(L_{\text{SM}})$	$B_4(\langle\bar{\psi}\psi\rangle_{\text{bare}})$	$B_4(\langle\bar{\psi}\psi\rangle_{\text{sub}})$
5.300	2.92 (11)	3.18 (25)	2.44 (51)	4.5 (13)
5.355	3.26 (14)	3.17 (19)	2.74 (26)	5.1 (10)
5.370	3.02 (9)	3.02 (16)	3.42 (45)	6.4 (13)
5.380	2.81 (7)	2.82 (12)	2.99 (30)	9.6 (20)
5.390	2.97 (9)	2.82 (16)	3.62 (70)	5.2 (9)
5.400	2.93 (9)	2.88 (15)	3.09 (44)	4.6 (5)
5.410	3.06 (10)	2.41 (11)	3.35 (31)	7.6 (25)
5.420	2.90 (8)	2.71 (11)	2.94 (44)	3.1 (3)
5.430	2.97 (7)	3.12 (15)	2.64 (62)	6.2 (9)
5.440	3.10 (10)	2.86 (13)	2.32 (46)	7.6 (11)
5.450	2.91 (11)	3.39 (24)	2.57 (70)	15.6 (4)
5.470	2.96 (10)	2.69 (16)	2.81 (124)	8.3 (22)
5.500	2.97 (8)	2.89 (15)	5.24 (119)	53.6 (184)

Table D.13: Results for the Binder cumulants of the bare Polyakov loop, the APE-smeared Polyakov loop, the bare chiral condensate and the subtracted condensate for scan **C1**.

D.6 Gaussian fits

This section collects the results from Gaussian fits of the form

$$f(T) = A\,\exp\left[-\frac{(T-T_C)^2}{2\,\sigma^2}\right] \tag{D.6}$$

to the data for the susceptibilities from scan **C1** in the critical region. Note, that the quoted uncertainties for the fit parameter T_C do not represent the estimate for the uncertainty of T_C as quoted in table 9.5. The uncertainty is estimated conservatively from the range of points that have been included in the Gaussian fits. The results for the fits are listed in the table below. In the case where the temperature range included only three points there is no true fit and consequently no value for χ^2/dof and no error bars are listed.

quantity	T [MeV]	T_C	σ	A	χ^2/dof
χ_L	$[194, 224]$	221 (18)	66 (44)	0.0581 (14)	1.2
τ_L	$[206, 217]$	211.3 (7)	6.6 (19)	1.36 (17)	2.9
$\chi_{L_{\text{SM}}}$	$[209, 217]$	212.523	3.4688	5.9847	—
$\tau_{L_{\text{SM}}}$	$[206, 217]$	210.7 (4)	4.4 (6)	99 (11)	0.2
$\chi_{\langle\bar{\psi}\psi\rangle_{\text{bare}}}$	$[206, 217]$	211.1 (7)	6.1 (14)	$5.7(6)\,10^{-5}$	2.6
$\tau_{\langle\bar{\psi}\psi\rangle_{\text{bare}}}$	$[209, 217]$	212,882	2.0271	19.129	—
$\chi_{\langle\bar{\psi}\psi\rangle_{\text{sub}}}$	$[206, 217]$	211.352	3.4505	0.00032	—
$\tau_{\langle\bar{\psi}\psi\rangle_{\text{sub}}}$	$[206, 220]$	213.4 (6)	5.6 (9)	35 (6)	0.3

D.7 Data for screening masses

β	$M_P/(2\pi\,T)$	$M_S/(2\pi\,T)$	$M_V/(2\pi\,T)$	$M_A/(2\pi\,T)$
5.300	0.129 (21)	0.87 (19)	1.067 (77)	1.355 (78)
5.355	0.454 (32)	—	0.970 (44)	—
5.370	0.455 (13)	0.57 (3)	0.919 (25)	1.006 (24)
5.380	0.526 (17)	0.80 (11)	0.972 (14)	0.997 (20)
5.390	0.513 (23)	0.58 (14)	0.936 (18)	1.061 (22)
5.400	0.477 (20)	0.78 (35)	0.882 (25)	0.938 (27)
5.410	0.492 (24)	0.90 (10)	1.048 (23)	1.046 (34)
5.420	0.583 (19)	0.69 (3)	0.966 (16)	1.007 (21)
5.430	0.608 (17)	0.70 (5)	0.988 (16)	0.967 (18)
5.440	0.583 (25)	0.71 (6)	0.933 (19)	0.962 (19)
5.450	0.563 (28)	0.64 (5)	0.955 (26)	0.976 (27)
5.470	0.525 (32)	0.73 (7)	0.992 (19)	1.094 (18)
5.500	0.700 (20)	0.76 (3)	0.963 (12)	0.954 (13)

Table D.14: Results for the screening masses in P, S, V and A channels in units of $2\pi\,T$ for scan **C1**.

β	$(M_S - M_P)$ $/(2\pi\,T)$	$(M_A - M_V)$ $/(2\pi\,T)$	M_P/M_S	M_V/M_A	$\chi_P - \chi_S$	$(\chi_A - \chi_V)$ 10^3
5.300	-0.64 (16)	-0.134 (72)	0.52 (8)	0.866 (57)	0.162 (19)	1.76 (22)
5.355	—	-0.086 (215)	—	0.618 (300)	0.141 (43)	2.10 (15)
5.370	-0.27 (5)	-0.039 (16)	0.79 (3)	0.943 (23)	0.050 (5)	2.26 (7)
5.380	-0.31 (12)	-0.024 (17)	0.66 (10)	0.981 (13)	0.031 (5)	2.11 (5)
5.390	-0.24 (18)	-0.048 (19)	0.80 (21)	0.964 (17)	0.043 (7)	2.12 (5)
5.400	—	0.020 (43)	—	0.976 (11)	0.067 (18)	2.25 (14)
5.410	-0.40 (8)	-0.025 (17)	0.57 (11)	0.977 (12)	0.062 (11)	2.01 (7)
5.420	-0.17 (4)	-0.010 (9)	0.84 (3)	0.990 (7)	0,022 (4)	2.03 (5)
5.430	-0.24 (7)	0.005 (7)	0.83 (5)	1.000 (7)	0.021 (4)	1.99 (5)
5.440	-0.28 (8)	-0.003 (7)	0.78 (4)	1.003 (5)	0.022 (3)	2.02 (4)
5.450	-0.10 (5)	-0.003 (5)	0.93 (5)	1.005 (3)	0.013 (4)	1.92 (7)
5.470	-0.15 (5)	-0.030 (12)	0.85 (4)	1.003 (3)	0.011 (2)	1.85 (5)
5.500	-0.03 (2)	0.003 (2)	0.97 (2)	1.002 (2)	0.005 (1)	1.87 (3)

Table D.15: Results for the difference of screening masses in units of $2\pi\,T$, the ratios of screening masses and the difference of the hadronic susceptibilities in (P, S) and (V, A) channels for scan **C1**.

References

[1] D.J. Gross and F. Wilczek, *Ultraviolet Behavior of Non-abelian Gauge Theories*, Phys. Rev. Lett. **30**, 1343 (1973)

[2] H.D. Politzer, *Reliable Perturbative Results for Strong interactions?*, Phys. Rev. Lett. **30**, 1346 (1973)

[3] N. Cabibbo and G. Parisi, *Exponential Hadronic Spectrum and Quark Liberation*, Phys. Lett. B **59**, 67 (1975)

[4] J. C. Collins and M. J. Perry, *Superdense Matter: Neutrons Or Asymptotically Free Quarks?*, Phys. Rev. Lett. **34**, 1353 (1975)

[5] E. V. Shuryak, *Quark-Gluon Plasma and Hadronic Production of Leptons, Photons and Psions*, Phys. Lett. B **78**, 150 (1978)

[6] R. Hagedorn, *Statistical thermodynamics of strong interactions at high-energies*, Nuovo Cim. Suppl. **3**, 147 (1965)

[7] `www.bnl.gov/rhic`

[8] `lhc.web.cern.ch/lhc`

[9] `http://www.gsi.de/portrait/fair.html`

[10] K. G. Wilson, *The Renormalization Group and Strong Interactions*, Phys. Rev. D **3**, 1818 (1971)

[11] K. G. Wilson, *Renormalization group and critical phenomena. 1. Renormalization group and the Kadanoff scaling picture*, Phys. Rev. B **4**, 3174 (1971)

[12] K. G. Wilson, *Renormalization group and critical phenomena. 2. Phase space cell analysis of critical behavior*, Phys. Rev. B **4**, 3184 (1971)

[13] F. J. Dyson, *The S matrix in quantum electrodynamics*, Phys. Rev. **75**, 1736 (1949)

[14] J. S. Schwinger, *On the Green's functions of quantized fields. 1.*, Proc. Nat. Acad. Sci. **37**, 452 (1951)

[15] J. S. Schwinger, *On the Green's functions of quantized fields. 2.*, Proc. Nat. Acad. Sci. **37**, 455 (1951)

[16] M. A. Shifman, A. I. Vainshtein and V. I. Zakharov, *QCD and Resonance Physics. Sum Rules*, Nucl. Phys. B **147**, 385 (1979)

[17] M. A. Shifman, A. I. Vainshtein and V. I. Zakharov, *QCD and Resonance Physics: Applications*, Nucl. Phys. B **147**, 448 (1979)

[18] J. Gasser and H. Leutwyler, *Chiral Perturbation Theory to One Loop*, Annals Phys. **158**, 142 (1984)

[19] J. M. Pawlowski, *Aspects of the functional renormalisation group*, Annals Phys. **322**, 2831 (2007) [hep-th/0512261]

[20] C. D. Roberts, *Strong QCD and Dyson-Schwinger Equations*, arXiv:1203.5341

[21] P. Colangelo and A. Khodjamirian, *QCD sum rules, a modern perspective*, In Shifman, M. (ed.): *At the frontier of particle physics*, vol. 3, 1495-1576 [hep-ph/0010175]

[22] S. Scherer, *Introduction to chiral perturbation theory*, Adv. Nucl. Phys. **27**, 277 (2003)

[23] K.G. Wilson, *Confinement of Quarks*, Phys. Rev. **D10**, 2445 (1974)

[24] K. Fukushima and T. Hatsuda, *The phase diagram of dense QCD*, Rept. Prog. Phys. **74**, 014001 (2011) [arXiv:1005.4814]

[25] M. Creutz, L. Jacobs and C. Rebbi, *Monte Carlo Study of Abelian Lattice Gauge Theories*, Phys. Rev. D **20**, 1915 (1979)

[26] M. Creutz, *Monte Carlo Study of Quantized SU(2) Gauge Theory*, Phys. Rev. **D21**, 2308 (1980)

[27] Z. Fodor and C. Hoelbling, *Light Hadron Masses from Lattice QCD*, Rev. Mod. Phys. **84**, 449 (2012) [arXiv:1203.4789]

[28] S. Durr *et al.*, *Ab-Initio Determination of Light Hadron Masses*, Science **322**, 1224 (2008) [arXiv:0906.3599]

[29] G. Colangelo *et al.*, *Review of lattice results concerning low energy particle physics*, Eur. Phys. J. **C71**, 1695 (2011) [arXiv:1011.4408]

[30] C. Alexandrou, *Hadron Structure and Form Factors*, PoS LATTICE **2010**, 001 (2010) [arXiv:1011.3660]

[31] H. Wittig, *Low-energy particle physics and chiral extrapolations*, PoS LATTICE **2011**, 025 (2011) [arXiv:1201.4774]

[32] K. Kanaya, *Finite Temperature QCD on the Lattice – Status 2010*, PoS LATTICE **2010**, 012 (2010) [arXiv:1012.4247]

[33] L. Levkova, *QCD at nonzero temperature and density*, PoS LATTICE **2011**, 011 (2011) [arXiv:1201.1516]

[34] R.D. Pisarski and F. Wilczek, *Remarks on the Chiral Phase Transition in Chromodynamics*, Phys. Rev. **D29**, 338 (1984)

[35] B. Sheikholeslami, R. Wohlert, *Improved Continuum Limit Lattice Action for QCD with Wilson Fermions*, Nucl. Phys. **B259**, 572 (1985)

[36] L. Susskind, *Lattice fermions*, Phys. Rev. **D16**, 3031 (1977)

[37] D.B. Kaplan, *A Method for Simulating Chiral Fermions on the Lattice*, Phys. Lett. **B288**, 342 (1992) [hep-lat/9206013]

[38] V. Fuhrman, Y. Shamir, *Axial symmetries in lattice QCD with Kaplan fermions*, Nucl. Phys. **B439**, 54 (1995) [hep-lat/9405004]

[39] V. Furman and Y. Shamir, *Axial symmetries in lattice QCD with Kaplan fermions*, Nucl. Phys. B **439**, 54 (1995) [hep-lat/9405004]

[40] H. Neuberger, *Exactly massless quarks on the lattice*, Phys. Lett. **B417**, 141 (1998) [hep-lat/9707022]

[41] H. Neuberger, *More about exactly massless quarks on the lattice*, Phys. Lett. **B427**, 353 (1998) [hep-lat/9801031]

[42] J. Gasser and H. Leutwyler, *Low-Energy Expansion of Meson Form-Factors*, Nucl. Phys. B **250**, 517 (1985)

[43] J. Bijnens, G. Colangelo and P. Talavera, *The Vector and scalar form-factors of the pion to two loops*, JHEP **9805**, 014 (1998) [hep-ph/9805389]

[44] J. Bijnens and P. Talavera, *Pion and kaon electromagnetic form-factors*, JHEP **0203**, 046 (2002) [hep-ph/0203049]

[45] S. R. Amendolia *et al.* [NA7 Collaboration], *A Measurement of the Space - Like Pion Electromagnetic Form-Factor*, Nucl. Phys. B **277**, 168 (1986)

[46] W. R. Frazer and J. R. Fulco, *Effect of a pion pion scattering resonance on nucleon structure*, Phys. Rev. Lett. **2**, 365 (1959)

[47] W. R. Frazer and J. R. Fulco, *Effect of a Pion-Pion Scattering Resonance on Nucleon Structure. II*, Phys. Rev. **117**, 1609 (1960)

[48] P.F. Bedaque, *Aharonov-Bohm effect and nucleon nucleon phase shifts on the lattice*, Phys. Lett. **B593**, 82 (2004) [nucl-th/0402051]

[49] G. M. de Divitiis, R. Petronzio and N. Tantalo, *On the discretization of physical momenta in lattice QCD*, Phys. Lett. B **595**, 408 (2004) [hep-lat/0405002]

[50] C.T. Sachrajda, G. Villadoro, *Twisted boundary conditions in lattice simulations*, Phys. Lett. **B609**, 73 (2005) [hep-lat/0411033]

[51] P. A. Boyle, *et al*, *Hadronic form factors in Lattice QCD at small and vanishing momentum transfer*, JHEP **0705**, 016 (2007) [hep-lat/0703005]

[52] P. A. Boyle, *et al*, *The Pion's electromagnetic form-factor at small momentum transfer in full lattice QCD*, JHEP **0807**, 112 (2008) [arXiv:0804.3971]

[53] F. Burger, *et al*, *The thermal QCD transition with two flavours of twisted mass fermions*, arXiv:1102.4530

[54] C. E. Detar and J. B. Kogut, *The Hadronic Spectrum of the Quark Plasma*, Phys. Rev. Lett. **59**, 399 (1987)

[55] C. E. Detar and J. B. Kogut, *Measuring the Hadronic Spectrum of the Quark Plasma*, Phys. Rev. D **36**, 2828 (1987)

[56] A.M. Ferrenberg, R.H. Swendsen, *New Monte Carlo Technique for Studying Phase Transitions*, Phys. Rev. Lett. **61**, 2635 (1988)

[57] A. M. Ferrenberg and R. H. Swendsen, *Optimized Monte Carlo analysis*, Phys. Rev. Lett. **63**, 1195 (1989)

[58] M. Gell-Mann, *A schematic Model of Baryons and Mesons*, Phys. Lett. **8**, 214 (1964)

[59] G. Zweig, *An $SU(3)$ model for strong interaction symmetry and its breaking*, CERN-TH-401, CERN-TH-412 (1964), published in *Developments in the Quark theory of Hadrons*, Vol. 1, editors D. Lichtenberg and S. Rosen, Hadronic Press (1980)

[60] C. Yang and R. Mills, *Conservation of isotopic spin and isotopic gauge invariance*, Phys. Rev. **69**, 191 (1954)

[61] A. Salam, *Gauge Unification of Fundamental Forces*, Rev. Mod. Phys. **52**, 525 (1980); Nobel lecture of 1979

[62] S. Weinberg, *Conceptual Foundations of the Unified Theory of Weak and Electromagnetic Interactions*, Rev. Mod. Phys. **52**, 515 (1980); Nobel lecture of 1979

[63] M.Y. Han and Y. Nambu, *Three-triplet model with double $SU(3)$ symmetry*, Phys. Rev. **B139**, 1006 (1965)

[64] O.W. Greenberg, *Spin and Unitary Spin Independence in a Paraquark Model of Baryons and Mesons*, Phys. Rev. lett. **13**, 598 (1964)

[65] M. Gell-Mann, *Quarks: Developments in the Quark Theory of Hadrons*, Acta Phys. Austriaca **9**, 733 (1972)

[66] H. Fritzsch, M. Gell-Mann and H. Leutwyler, *Advantages of the colour octet gluon picture*, Phys. Lett. **47B**, 365 (1973)

[67] `http://lhc.web.cern.ch/lhc/`

[68] G. Aad *et al.* [ATLAS Collaboration], *Observation of a new particle in the search for the Standard Model Higgs boson with the ATLAS detector at the LHC*, arXiv:1207.7214

[69] G. Aad *et al.* [ATLAS Collaboration], *Combined search for the Standard Model Higgs boson in pp collisions at* $\sqrt{s} = 7$ *TeV with the ATLAS detector*, Phys. Rev. D **86**, 032003 (2012) [arXiv:1207.0319]

[70] S. Chatrchyan *et al.* [CMS Collaboration], *Combined results of searches for the standard model Higgs boson in pp collisions at sqrt(s) = 7 TeV*, Phys. Lett. B **710**, 26 (2012) [arXiv:1202.1488]

[71] M.E. Peskin and D.V. Schroeder, *An Introduction to Quantum Field Theory*, Westview Press (1995)

[72] S. Weinberg, *The quantum theory of fields, Volume I-III*, Cambridge University Press (1995-2000), Cambridge, UK

[73] R.P. Feynman, *Spacetime approach to nonrelativistic quantum mechanics*, Revs. Mod. Phys. **20**, 367 (1948)

[74] L. D. Faddeev and V. N. Popov, *Feynman Diagrams for the Yang-Mills Field*, Phys. Lett. B **25**, 29 (1967)

[75] I. Montvay, G. Münster, *Quantum fields on a lattice*, Cambridge University Press (1994), Cambridge, UK

[76] W.M. Yao, *et al*, *Review of particle physics*, Journal of Physics **G37**, 075021 (2010); Particle data group: `http://pdg.lbl.gov`

[77] P. Fritzsch, *et al*, *"The strange quark mass and Lambda parameter of two flavor QCD*, arXiv:1205.5380

[78] J. Goldstone, A. Salam and S. Weinberg, *Brokem Symmetries*, Phys. Rev. **127**, 965 (1962)

[79] S. Scherer, *Chiral Perturbation Theory: Introduction and Recent Results in the One-Nucleon Sector*, Prog. Part. Nucl. Phys. **64**, 1 (2010) [arXiv:0908.3425]

[80] C. Gale and J.I. Kapusta, *Finite-temperature field theory: Principles and applications*, Cambridge University Press (2006), Cambridge, UK

[81] C. Gattringer and C. B. Lang, *Quantum chromodynamics on the lattice*, Lect. Notes Phys. **788**, 1 (2010)

[82] M. Lüscher, *Advanced lattice QCD*, Les Houches 1997, Probing the standard model of particle interactions, Pt. 2, (1997) [hep-lat/9802029]

[83] H. Wittig, *QCD on the lattice*, In Landolt-Boernstein I 21A: *Elementary particles*, 5

[84] O. Philipsen, *Lattice QCD at finite temperature and density*, arXiv:0708.1293

[85] C. DeTar, U.M. Heller, *QCD thermodynamics from the lattice*, arXiv:0905.2949

[86] K. Symanzik, *Continuum Limit and Improved Action in Lattice Theories. 1. Principles and ϕ^4 Theory*, Nucl. Phys. **B226**, 187 (1983)

[87] K. Symanzik, *Continuum Limit and Improved Action in Lattice Theories. 2. O(N) Nonlinear Sigma Model in Perturbation Theory*, Nucl. Phys. **B226**, 205 (1983)

[88] S. Capitani, *Lattice perturbation theory*, Phys. Rept. **382**, 113 (2003) [hep-lat/0211036]

[89] M. Lüscher *et al*, *Nonperturbative O(a) improvement of lattice QCD*, Nucl. Phys. **B491**, 323 (1997) [hep-lat/9609035]

[90] M. Lüscher, *et al*, *Chiral symmetry and O(a) improvement in lattice QCD*, Nucl. Phys. **B478**, 365 (1996) [hep-lat/9605038]

[91] M. Lüscher, *et al*, *Nonperturbative O(a) improvement of lattice QCD*, Nucl. Phys. **B491**, 323 (1997) [hep-lat/9609035]

[92] K. Jansen, R. Sommer, *The Nonperturbative O(a) improved action for dynamical Wilson fermions*, Nucl. Phys. Proc. Suppl. **63**, 853 (1998) [hep-lat/9709022]

[93] M. Lüscher and P. Weisz, *O(a) improvement of the axial current in lattice QCD to one loop order of perturbation theory*, Nucl. Phys. **B479**, 429 (1996) [hep-lat/9606016]

[94] P. Weisz, *Continuum Limit Improved Lattice Action for Pure Yang-Mills Theory. 1.*, Nucl. Phys. **B212**, 1 (1983)

[95] P. Weisz, R. Wohlert, *Continuum Limit Improved Lattice Action for Pure Yang-Mills Theory. 2.*, Nucl. Phys. **B236**, 397 (1984)

[96] Y. Iwasaki, *Renormalization Group Analysis of Lattice Theories and Improved Lattice Action: Two-Dimensional Nonlinear O(N) Sigma Model.*, Nucl. Phys. **B258**, 141 (1985)

[97] S. Sint and P. Weisz, *Further results on O(a) improved lattice QCD to one loop order of perturbation theory*, Nucl. Phys. **B502**, 251 (1997) [hep-lat/9704001]

[98] P. Weisz, *Renormalization and lattice artifacts*, arXiv:1004.3462

[99] R. Sommer, *Non-perturbative QCD: Renormalization, O(a)-improvement and matching to Heavy Quark Effective Theory*, hep-lat/0611020

[100] R. Sommer, *A New way to set the energy scale in lattice gauge theories and its applications to the static force and alpha-s in SU(2) Yang-Mills theory*, Nucl. Phys. B **411**, 839 (1994) [hep-lat/9310022]

[101] M. Luscher, *Properties and uses of the Wilson flow in lattice QCD*, JHEP **1008**, 071 (2010) [arXiv:1006.4518]

[102] S. Borsanyi, *et al.*, *High-precision scale setting in lattice QCD*, arXiv:1203.4469

[103] S. Capitani, *et al.*, *Scale setting via the Ω baryon mass*, PoS LATTICE **2011**, 145 (2011) [arXiv:1110.6365]

[104] C.G. Callan Jr., *Broken scale invariance in scalar field theory*, Phys. Rev. **D2**, 1541 (1970)

[105] K. Symanzik, *Small distance behavior in field theory and power counting*, Commun. Math. Phys. **18**,227 (1970)

[106] K. Symanzik, *Small distance behavior analysis and Wilson expansion*, Commun. Math. Phys. **23**, 49 (1971)

[107] J. C. Ward, *An Identity in Quantum Electrodynamics*, Phys. Rev. **78**, 182 (1950)

[108] Y. Takahashi, *On the generalized Ward identity*, Nuovo Cim. **6**, 371 (1957)

[109] M. Luscher, *et al*, *Nonperturbative determination of the axial current normalization constant in O(a) improved lattice QCD*, Nucl. Phys. B **491**, 344 (1997) [hep-lat/9611015]

[110] P. Fritzsch, J. Heitger, N. Tantalo, *Non-perturbative improvement of quark mass renormalization in two-flavour lattice QCD*, JHEP **1008** , 074 (2010) [arXiv:1004.3978]

[111] K. Jansen *et al*, *Nonperturbative renormalization of lattice QCD at all scales*, Phys. Lett. **B372**, 275 (1996) [hep-lat/9512009]

[112] L. Giusti, *et al.*, *The QCD chiral condensate from the lattice*, Nucl. Phys. B **538**, 249 (1999) [hep-lat/9807014]

[113] S. Capitani *et al.* [ALPHA Collaboration], *Nonperturbative quark mass renormalization in quenched lattice QCD*, Nucl. Phys. B **544**, 669 (1999) [hep-lat/9810063]

[114] M. Della Morte *et al*, *Non-perturbative quark mass renormalization in two-flavor QCD*, Nucl. Phys. **B729**, 117 (2005) [hep-lat/0507035]

[115] R. Frezzotti, *et al*, *A local formulation of lattice QCD without unphysical fermion zero modes*, Nucl. Phys. Proc. Suppl. **83**, 941 (2000) [hep-lat/9909003]

[116] R. Frezzotti, *et al.* [Alpha Collaboration], *Lattice QCD with a chirally twisted mass term*, JHEP **0108**, 058 (2001) [hep-lat/0101001]

[117] R. Frezzotti and G. C. Rossi, *Chirally improving Wilson fermions. 1. O(a) improvement*, JHEP **0408**, 007 (2004) [hep-lat/0306014]

[118] P. Dimopoulos *et al*, *O(a^2) cutoff effects in lattice Wilson fermion simulations*, Phys. Rev. **D81**, 034509 (2010) [arXiv:0908.0451]

[119] A. Shindler, *Twisted mass lattice QCD*, arXiv:0707.4093

[120] S.R. Sharpe, *Rooted staggered fermions: Good, bad or ugly?*, PoS LATTICE **2006**, 022 (2006) [hep-lat/0610094]

[121] S. Dürr, *Theoretical issues with staggered fermion simulations*, PoS LATTICE **2005**, 021 (2006) [hep-lat/0509026]

[122] A. S. Kronfeld, *Lattice gauge theory with staggered fermions: How, where, and why (not)*, PoS LATTICE **2007**, 016 (2007) [arXiv:0711.0699]

[123] M. Creutz, *Why rooting fails*, PoS LATTICE **2007**, 007 (2007) [arXiv:0708.1295]

[124] G. C. Rossi, M. Testa, *A 0-dimensional counter-example to rooting?*, Phys. Lett. **B688** , 248 (2010) [arXiv:1005.3672]

[125] A. Bazavov, *et al.*, *Nonperturbative QCD simulations with 2+1 flavors of improved staggered quarks*, Rev. Mod. Phys. **82**, 1349 (2010) [arXiv:0903.3598]

[126] A. Bazavov *et al* [HotQCD Collaboration], *Taste symmetry and QCD thermodynamics with improved staggered fermions*, PoS LATTICE **2010**, 169 (2010) [arXiv:1012.1257]

[127] A. Bazavov, *et al.*, *The chiral and deconfinement aspects of the QCD transition*, Phys. Rev. D **85**, 054503 (2012) [arXiv:1111.1710]

[128] H.B. Nielsen, M. Ninomyia, *Absence of Neutrinos on a Lattice*, Nucl. Phys. **B185**, 20 (1981)

[129] H. B. Nielsen and M. Ninomiya, *Absence of Neutrinos on a Lattice. 2. Intuitive Topological Proof*, Nucl. Phys. B **193**, 173 (1981)

[130] P.H. Ginsparg, K.G. Wilson, *A Remnant of Chiral Symmetry on the Lattice.*, Phys. Rev. **D25**, 2649 (1982)

[131] M. Lüscher, *Exact chiral symmetry on the lattice and the Ginsparg-Wilson relation*, Phys. Lett. **B428**, 342 (1998) [hep-lat/9802011]

[132] L. H. Karsten, *Lattice Fermions In Euclidean Space-time*, Phys. Lett. B **104**, 315 (1981)

[133] F. Wilczek, *On Lattice Fermions*, Phys. Rev. Lett. **59**, 2397 (1987)

[134] M. Creutz, *Four-dimensional graphene and chiral fermions*, JHEP **0804**, 017 (2008) [arXiv:0712.1201]

[135] A. Borici, *Creutz fermions on an orthogonal lattice*, Phys. Rev. D **78**, 074504 (2008) [arXiv:0712.4401]

[136] S. Capitani, J. Weber and H. Wittig, *Minimally doubled fermions at one loop*, Phys. Lett. B **681**, 105 (2009) [arXiv:0907.2825]

[137] S. Capitani, *et al*, *Renormalization of minimally doubled fermions*, JHEP **1009**, 027 (2010) [arXiv:1006.2009]

[138] M. Lüscher, *Computational Strategies in Lattice QCD*, Les Houches 2009, Modern perspectives in lattice QCD (2009) [arXiv:1002.4232]

[139] P. de Forcrand, *Simulating QCD at finite density*, PoS LATTICE **2009**, 010 (2009) [arXiv:1005.0539]

[140] R. Frezzotti and K. Jansen, *A Polynomial hybrid Monte Carlo algorithm*, Phys. Lett. B **402**, 328 (1997) [hep-lat/9702016]

[141] R. Frezzotti and K. Jansen, *The PHMC algorithm for simulations of dynamical fermions: 1. Description and properties*, Nucl. Phys. B **555**, 395 (1999) [hep-lat/9808011]

[142] R. Frezzotti and K. Jansen, *The PHMC algorithm for simulations of dynamical fermions. 2. Performance analysis*, Nucl. Phys. B **555**, 432 (1999) [hep-lat/9808038]

[143] T. Takaishi and P. de Forcrand, *Odd flavor hybrid Monte Carlo algorithm for lattice QCD*, Int. J. Mod. Phys. C **13**, 343 (2002) [hep-lat/0108012]

[144] S. Aoki *et al.* [JLQCD Collaboration], *Polynomial hybrid Monte Carlo algorithm for lattice QCD with odd number of flavors*, Phys. Rev. D **65**, 094507 (2002) [hep-lat/0112051]

[145] A. D. Kennedy, I. Horvath and S. Sint, *A New exact method for dynamical fermion computations with nonlocal actions*, Nucl. Phys. Proc. Suppl. **73**, 834 (1999) [hep-lat/9809092]

[146] M. A. Clark and A. D. Kennedy, *Accelerating dynamical fermion computations using the rational hybrid Monte Carlo (RHMC) algorithm with multiple pseudofermion fields*, Phys. Rev. Lett. **98**, 051601 (2007) [hep-lat/0608015]

[147] N. Metropolis, *et al*, *Equation of state calculations by fast computing machines*, J. Chem. Phys. **21**, 1087 (1953)

[148] A. D. Kennedy and B. J. Pendleton, *Improved Heat Bath Method for Monte Carlo Calculations in Lattice Gauge Theories*, Phys. Lett. B **156**, 393 (1985)

[149] N. Cabibbo and E. Marinari, *A New Method for Updating SU(N) Matrices in Computer Simulations of Gauge Theories*, Phys. Lett. B **119**, 387 (1982)

[150] B. Bunk, *Monte Carlo methods and results for the electro-weak phase transition*, Nucl. Phys. Proc. Suppl. **42**, 566 (1995)

[151] S. Duane, *et al*, *Hybrid Monte Carlo,* Phys. Lett. B **195**, 216 (1987)

[152] M. Luscher, *Schwarz-preconditioned HMC algorithm for two-flavour lattice QCD*, Comput. Phys. Commun. **165**, 199 (2005) [hep-lat/0409106]

[153] J. C. Sexton and D. H. Weingarten, *Hamiltonian evolution for the hybrid Monte Carlo algorithm*, Nucl. Phys. B **380**, 665 (1992)

[154] T. Takaishi and P. de Forcrand, *Testing and tuning new symplectic integrators for hybrid Monte Carlo algorithm in lattice QCD*, Phys. Rev. E **73**, 036706 (2006) [hep-lat/0505020]

[155] I. Omelyan, I. Mryglod, R. Folk, *On the construction of high order force gradient algorithms for integration of motion in classical and quantum systems*, Phys. Rev. E **66**, 026701 (2002)

[156] Y. Saad, *Iterative Methods for Sparse Linear Systems*, 2nd edition, SIAM (2003), Philadelphia, US

[157] T.A. DeGrand, *A Conditioning Technique For Matrix Inversion For Wilson Fermions*, Comput. Phys. Commun. **52**, 161 (1988)

[158] T.A. DeGrand, P. Rossi, *Conditioning Techniques For Dynamical Fermions*, Comput. Phys. Commun. **60**, 211 (1990)

[159] M. Luscher, *Solution of the Dirac equation in lattice QCD using a domain decomposition method*, Comput. Phys. Commun. **156**, 209 (2004) [hep-lat/0310048]

[160] H.A. Schwarz, *Gesammelte Mathematische Abhandlungen*, Vol. 2, Springer Verlag (1890), Berlin, Germany

[161] A. Quarkoni, A. Valli, *Domain decomposition methods for partial differential equations*, Oxford University Press (1999), Oxford, GB

[162] W. M. Wilcox, *Deflation methods in fermion inverters*, PoS LATTICE **2007**, 025 (2007) [arXiv:0710.1813]

[163] T. Banks and A. Casher, *Chiral Symmetry Breaking in Confining Theories*, Nucl. Phys. B **169**, 103 (1980)

[164] L. Giusti, *et al*, *Numerical techniques for lattice QCD in the epsilon regime*, Comput. Phys. Commun. **153**, 31 (2003) [hep-lat/0212012]

[165] J. Frank, C. Vuik, *On the construction of deflation-based preconditioners*, SIAM J. Sci. Comput. **23**, 442 (2001)

[166] R. Nabben, C. Vuik, *A Comparison of Deflation and the Balancing Preconditioner*, SIAM J. Sci. Comput. **27**, 1742 (2006)

[167] M. Luscher, *Local coherence and deflation of the low quark modes in lattice QCD*, JHEP **0707**, 081 (2007) [arXiv:0706.2298]

[168] S. Aoki *et al.* [JLQCD Collaboration], *Light hadron spectroscopy with two flavors of O(a) improved dynamical quarks*, Phys. Rev. D **68**, 054502 (2003) [hep-lat/0212039]

[169] M. Hasenbusch, *Speeding up the HMC algorithm: Some new results*, PoS LATTICE **2005**, 116 (2006) [hep-lat/0509080]

[170] T. Lippert, *et al.*, *SESAM and T-chi-L results for Wilson action: A Status report*, Nucl. Phys. Proc. Suppl. **60A**, 311 (1998) [hep-lat/9707004]

[171] N. Eicker *et al.* [TXL Collaboration], *Light and strange hadron spectroscopy with dynamical Wilson fermions*, Phys. Rev. D **59**, 014509 (1999) [hep-lat/9806027]

[172] J.C. Sexton, D.H. Weingarten, *Hamiltonian evolution for the hybrid Monte Carlo algorithm*, Nucl. Phys. **B380**, 665 (1992)

[173] M. J. Peardon *et al.* [TrinLat Collaboration], *Multiple molecular dynamics time scales in hybrid Monte Carlo fermion simulations*, Nucl. Phys. Proc. Suppl. **119**, 985 (2003) [hep-lat/0209037]

[174] M. Hasenbusch, *Speeding up the hybrid Monte Carlo algorithm for dynamical fermions*, Phys. Lett. B **519**, 177 (2001) [hep-lat/0107019]

[175] M. Hasenbusch and K. Jansen, *Speeding up lattice QCD simulations with clover improved Wilson fermions*, Nucl. Phys. B **659**, 299 (2003) [hep-lat/0211042]

[176] M. Luscher, *Lattice QCD and the Schwarz alternating procedure*, JHEP **0305**, 052 (2003) [hep-lat/0304007]

[177] C. Urbach, K. Jansen, A. Shindler and U. Wenger, *HMC algorithm with multiple time scale integration and mass preconditioning*, Comput. Phys. Commun. **174**, 87 (2006) [hep-lat/0506011]

[178] M. Marinkovic and S. Schaefer, *Comparison of the mass-preconditioned HMC and the DD-HMC algorithm for two-flavour QCD*, PoS LATTICE **2010**, 031 (2010) [arXiv:1011.0911]

[179] M. Luscher, *Deflation acceleration of lattice QCD simulations*, JHEP **0712**, 011 (2007) [arXiv:0710.5417]

[180] M. Luscher, *Volume Dependence of the Energy Spectrum in Massive Quantum Field Theories. 1. Stable Particle States*, Commun. Math. Phys. **104**, 177 (1986)

[181] L. Del Debbio, L. Giusti, M. Luscher, R. Petronzio and N. Tantalo, *Stability of lattice QCD simulations and the thermodynamic limit*, JHEP **0602**, 011 (2006) [hep-lat/0512021]

[182] L. Del Debbio, H. Panagopoulos and E. Vicari, *θ dependence of SU(N) gauge theories*, JHEP **0208**, 044 (2002), [hep-th/0204125]

[183] S. Schaefer, R. Sommer and F. Virotta, *Investigating the critical slowing down of QCD simulations*, PoS LATTICE **2009**, 032 (2009) [arXiv:0910.1465]

[184] S. Schaefer, R. Sommer and F. Virotta, *Critical slowing down and error analysis in lattice QCD simulations*, arXiv:1009.5228

[185] M. Luscher and S. Schaefer, *Lattice QCD without topology barriers*, JHEP **1107**, 036 (2011) [arXiv:1105.4749]

[186] M. Luscher and S. Schaefer, *Lattice QCD with open boundary conditions and twisted-mass reweighting*, arXiv:1206.2809

[187] B. Knippschild, *Baryons in the Chiral Regime*, PhD-Thesis, Johannes Gutenberg-Universität Mainz (2012)

[188] G. M. de Divitiis, *et al.*, *Isospin breaking effects due to the up-down mass difference in Lattice QCD*, arXiv:1110.6294

[189] S. Aoki *et al.* [PACS-CS Collaboration], *Physical Point Simulation in 2+1 Flavor Lattice QCD*, Phys. Rev. D **81**, 074503 (2010) [arXiv:0911.2561 [hep-lat]]

[190] S. Durr, *et al.*, *Lattice QCD at the physical point: light quark masses*, Phys. Lett. B **701**, 265 (2011) [arXiv:1011.2403]

[191] S. Durr, *et al.*, *Lattice QCD at the physical point: Simulation and analysis details*, JHEP **1108**, 148 (2011) [arXiv:1011.2711]

[192] S. Gusken, *A Study of smearing techniques for hadron correlation functions*, Nucl. Phys. Proc. Suppl. **17**, 361 (1990)

[193] A. K. De, A. Harindranath and J. Maiti, *Investigation of Lattice QCD with Wilson fermions with Gaussian Smearing*, arXiv:0712.4354

[194] C. Michael and I. Teasdale, *Extracting Glueball Masses From Lattice Qcd*, Nucl. Phys. B **215**, 433 (1983)

[195] N. A. Campbell, *et al*, *Mesons With Excited Glue From Su(3) Lattice Gauge Theory*, Phys. Lett. B **142**, 291 (1984)

[196] B. Blossier, *et al*, *On the generalized eigenvalue method for energies and matrix elements in lattice field theory*, JHEP **0904**, 094 (2009) [arXiv:0902.1265]

[197] L. Maiani, *et al*, *Scalar Densities And Baryon Mass Differences In Lattice Qcd With Wilson Fermions*, Nucl. Phys. B **293**, 420 (1987)

[198] S. Gusken, *et al*, *Nonsinglet Axial Vector Couplings Of The Baryon Octet In Lattice Qcd*, Phys. Lett. B **227**, 266 (1989)

[199] J. Bulava, M. Donnellan and R. Sommer, *On the computation of hadron-to-hadron transition matrix elements in lattice QCD*, JHEP **1201**, 140 (2012) [arXiv:1108.3774]

[200] S. Capitani, *et al*, *The nucleon axial charge from lattice QCD with controlled errors*, arXiv:1205.0180

[201] S. Bernardson, P. McCarty and C. Thron, *Monte Carlo methods for estimating linear combinations of inverse matrix entries in lattice QCD*, Comput. Phys. Commun. **78**, 256 (1993)

[202] S. -J. Dong and K. -F. Liu, *Stochastic estimation with Z(2) noise*, Phys. Lett. B **328**, 130 (1994) [hep-lat/9308015]

[203] M. Foster, C. Michael [UKQCD collaboration], *Quark mass dependence of hadron masses from lattice QCD*, Phys. Rev. **D59**, 074503 (1998) [hep-lat/9810021]

[204] C. McNeile, C. Michael [UKQCD collaboration], *Decay width of light quark hybrid meson from the lattice*, Phys. Rev. **D73**, 074506 (2006) [hep-lat/0603007]

[205] J. Viehoff *et al* [TXL collaboration], *Improving stochastic estimator techniques for disconnected diagrams*, Nucl. Phys. Proc. Suppl. **63**, 269 (1998) [hep-lat/9710050]

[206] P. A. Boyle, A. Juttner, C. Kelly and R. D. Kenway, *Use of stochastic sources for the lattice determination of light quark physics*, JHEP **0808**, 086 (2008) [arXiv:0804.1501]

[207] S. Capitani, *et al*, *Mesonic and baryonic correlation functions at fine lattice spacings*, PoS LATTICE **2009**, 095 (2009) [arXiv:0910.5578]

[208] E. Endress, A. Juttner and H. Wittig, *On the efficiency of stochastic volume sources for the determination of light meson masses*, arXiv:1111.5988

[209] G. Martinelli and C. T. Sachrajda, *A Lattice Study Of Nucleon Structure*, Nucl. Phys. B **316**, 355 (1989)

[210] J. M. Flynn *et al.* [UKQCD Collaboration], *A Numerical study of partially twisted boundary conditions*, Phys. Lett. B **632**, 313 (2006) [hep-lat/0506016]

[211] P. A. Boyle, *et al.*, *$K \to \pi$ form factors with reduced model dependence*, Eur. Phys. J. C **69**, 159 (2010) [arXiv:1004.0886]

[212] M. Della Morte, *et al*, *Towards a precise lattice determination of the leading hadronic contribution to $(g-2)_\mu$*, JHEP **1203**, 055 (2012) [arXiv:1112.2894]

[213] B. B. Brandt, *et al.*, *Wilson fermions at fine lattice spacings: scale setting, pion form factors and $(g-2)_\mu$*, PoS LATTICE **2010**, 164 (2010) [arXiv:1010.2390]

[214] B. B. Brandt, *et al.*, *Form factors in lattice QCD*, Eur. Phys. J. ST **198**, 79 (2011) [arXiv:1106.1554]

[215] B. B. Brandt, A. Juttner and H. Wittig, *Calculation of the pion electromagnetic form factor from lattice QCD*, arXiv:1109.0196

[216] B. B. Brandt, *et al*, *Hadronic contribution to the lepton anomalous magnetic moment and pion form factor in lattice QCD*, Prog. Part. Nucl. Phys. **67**, 223 (2012)

[217] P. .Hagler, *Hadron structure from lattice quantum chromodynamics*, Phys. Rept. **490**, 49 (2010) [arXiv:0912.5483]

[218] S. Capitani, *et al*, *Systematic errors in extracting nucleon properties from lattice QCD*, PoS LATTICE **2010**, 147 (2010) [arXiv:1011.1358]

[219] G. M. Huber *et al.* [Jefferson Lab Collaboration], *Charged pion form-factor between Q**2 = 0.60-GeV**2 and 2.45-GeV**2. II. Determination of, and results for, the pion form-factor*, Phys. Rev. C **78**, 045203 (2008) [arXiv:0809.3052]

[220] J. van der Heide, *et al*, *The Pion form-factor in improved lattice QCD*, Phys. Lett. B **566**, 131 (2003) [hep-lat/0303006]

[221] A. M. Abdel-Rehim and R. Lewis, *Pion form-factor with twisted mass QCD*, Nucl. Phys. Proc. Suppl. **140**, 299 (2005) [hep-lat/0408033]

[222] F. D. R. Bonnet, *et al.* [Lattice Hadron Physics Collaboration], *Lattice computations of the pion form-factor*, Phys. Rev. D **72**, 054506 (2005) [hep-lat/0411028]

[223] S. Capitani, C. Gattringer and C. B. Lang, *Pion form-factor with chirally improved fermions*, PoS LATTICE **2005**, 126 (2006) [hep-lat/0509030]

[224] S. Capitani, *et al.* [Bern-Graz-Regensburg (BGR) Collaboration], *A Lattice calculation of the pion form-factor with Ginsparg-Wilson-type fermions*, Phys. Rev. D **73**, 034505 (2006) [hep-lat/0511040]

[225] D. Brommel, *et al.* [QCDSF/UKQCD Collaboration], *The Pion form-factor from lattice QCD with two dynamical flavours*, Eur. Phys. J. C **51**, 335 (2007) [hep-lat/0608021]

[226] P. -h. J. Hsu and G. T. Fleming, *The Pion Form Factor at Large Momentum Transfer*, PoS LATTICE **2007**, 145 (2007) [arXiv:0710.4538]

[227] S. Aoki, *et al.* [JLQCD and TWQCD Collaborations], *Pion form factors from two-flavor lattice QCD with exact chiral symmetry*, Phys. Rev. D **80**, 034508 (2009) [arXiv:0905.2465]

[228] R. Frezzotti, *et al.* [ETM Collaboration], *Electromagnetic form factor of the pion from twisted-mass lattice QCD at N(f) = 2*, Phys. Rev. D **79**, 074506 (2009) [arXiv:0812.4042]

[229] O. H. Nguyen, *et al*, *Electromagnetic form factor of pion from $N_f = 2 + 1$ dynamical flavor QCD*, JHEP **1104**, 122 (2011) [arXiv:1102.3652]

[230] H. B. Meyer, *Lattice QCD and the Timelike Pion Form Factor*, Phys. Rev. Lett. **107**, 072002 (2011) [arXiv:1105.1892]

[231] S. J. Brodsky and G. R. Farrar, *Scaling Laws at Large Transverse Momentum*, Phys. Rev. Lett. **31**, 1153 (1973)

[232] S. J. Brodsky and G. R. Farrar, *Scaling Laws for Large Momentum Transfer Processes*, Phys. Rev. D **11**, 1309 (1975)

[233] G. R. Farrar and D. R. Jackson, *The Pion Form-Factor*, Phys. Rev. Lett. **43**, 246 (1979)

[234] A. V. Radyushkin, *Deep Elastic Processes of Composite Particles in Field Theory and Asymptotic Freedom*, hep-ph/0410276

[235] A. V. Efremov and A. V. Radyushkin, *Asymptotical Behavior of Pion Electromagnetic Form-Factor in QCD*, Theor. Math. Phys. **42**, 97 (1980)

[236] A. V. Efremov and A. V. Radyushkin, *Factorization and Asymptotical Behavior of Pion Form-Factor in QCD*, Phys. Lett. B **94**, 245 (1980)

[237] V. Braguta, W. Lucha and D. Melikhov, *Pion form-factor at spacelike momentum transfers from local-duality QCD sum rule*, Phys. Lett. B **661**, 354 (2008) [arXiv:0710.5461]

[238] H. J. Kwee and R. F. Lebed, *Pion Form Factor in Improved Holographic QCD Backgrounds*, Phys. Rev. D **77**, 115007 (2008) [arXiv:0712.1811]

[239] H. J. Kwee and R. F. Lebed, *The Pion Form Factor in AdS/QCD*, arXiv:0807.4565

[240] W. Lucha and D. Melikhov, *Pion form factor from local-duality QCD sum rule*, PoS CONFINEMENT **8**, 072 (2008) [arXiv:0812.0323]

[241] C. A. Dominguez, *et al*, *Electromagnetic and Scalar Pion form factor in the Kroll-Lee-Zumino model*, Nucl. Phys. Proc. Suppl. **186**, 141 (2009) [arXiv:0904.4215]

[242] A. P. Bakulev, A. V. Pimikov and N. G. Stefanis, *Pion Form Factor in QCD Sum Rules with Nonlocal Condensates and in the Local-Duality Approach*, Mod. Phys. Lett. A **24**, 2848 (2009) [arXiv:0910.3077]

[243] A. F. Krutov, V. E. Troitsky and N. A. Tsirova, *Nonperturbative relativistic approach to pion form factor versus JLab experiments*, Phys. Rev. C **80**, 055210 (2009) [arXiv:0910.3604]

[244] M. Della Morte, R. Hoffmann and R. Sommer, *Non-perturbative improvement of the axial current for dynamical Wilson fermions*, JHEP **0503**, 029 (2005) [hep-lat/0503003]

[245] M. Della Morte, *et al*, *Non-perturbative renormalization of the axial current with dynamical Wilson fermions*, JHEP **0507**, 007 (2005) [hep-lat/0505026]

[246] M. Della Morte, R. Sommer and S. Takeda, *On On cutoff effects in lattice QCD from short to long distances*, Phys. Lett. **B672**, 407 (2009) [arXiv:0807.1120]

[247] B. Leder, *et al.* [ALPHA Collaboration], *Scale r_0 and the static potential from the CLS lattices*, PoS LATTICE **2010**, 233 (2010) [arXiv:1012.1141]

[248] Personal communications with Georg von Hippel.

[249] H. Horch, *Extraction of semileptonic form factors of the kaon from lattice QCD*, Diploma Thesis, Johannes Gutenberg-Universität Mainz (2012)

[250] C. Michael, *Fitting correlated data*, Phys. Rev. D **49**, 2616 (1994) [hep-lat/9310026]

[251] L. Del Debbio, *et al*, *QCD with light Wilson quarks on fine lattices (I): First experiences and physics results*, JHEP **0702**, 056 (2007) [hep-lat/0610059]

[252] T. Bhattacharya, R. Gupta, W. -J. Lee and S. R. Sharpe, *Order a improved renormalization constants*, Phys. Rev. D **63**, 074505 (2001) [hep-lat/0009038]

[253] U. Burgi, *Charged pion polarizabilities to two loops*, Phys. Lett. B **377**, 147 (1996) [hep-ph/9602421]

[254] U. Burgi, *Charged pion pair production and pion polarizabilities to two loops*, Nucl. Phys. B **479**, 392 (1996) [hep-ph/9602429]

[255] J. Bijnens, *et al*, *Pion pion scattering at low-energy*, Nucl. Phys. B **508**, 263 (1997) [Erratum-ibid. B **517**, 639 (1998)] [hep-ph/9707291]

[256] G. Colangelo and S. Durr, *The Pion mass in finite volume*, Eur. Phys. J. C **33**, 543 (2004) [hep-lat/0311023]

[257] G. Colangelo, S. Durr and C. Haefeli, *Finite volume effects for meson masses and decay constants*, Nucl. Phys. B **721**, 136 (2005) [hep-lat/0503014]

[258] F. -J. Jiang and B. C. Tiburzi, *Flavor twisted boundary conditions, pion momentum, and the pion electromagnetic form-factor*, Phys. Lett. B **645**, 314 (2007) [hep-lat/0610103]

[259] F. -J. Jiang and B. C. Tiburzi, *Flavor Twisted Boundary Conditions in the Breit Frame*, Phys. Rev. D **78**, 037501 (2008) [arXiv:0806.4371]

[260] G. Colangelo, J. Gasser and H. Leutwyler, *pi pi scattering*, Nucl. Phys. B **603**, 125 (2001) [hep-ph/0103088]

[261] F. Schwabl, *Statistische Mechanik*, Springer Verlag (2000-2004), Berlin, Germany

[262] J.M. Drouffe and C. Itzykson, *Statistical field theory: Vol 1 and 2*, Cambridge University Press (1989-1997), New York, US

[263] A. Pelissetto and E. Vicari, *Critical phenomena and renormalization group theory*, Phys. Rept. **368**, 549 (2002) [cond-mat/0012164]

[264] M. E. Fisher and M. N. Barber, *Scaling Theory for Finite-Size Effects in the Critical Region*, Phys. Rev. Lett. **28**, 1516 (1972)

[265] E. Brezin, *An Investigation Of Finite Size Scaling*, J. Phys. (France) **43**, 15 (1982)

[266] K. Binder, *Finite size scaling analysis of Ising model block distribution functions*, Z. Phys. B **43**, 119 (1981)

[267] P. Braun-Munzinger and J. Stachel, *The quest for the quark-gluon plasma*, Nature **448**, 302 (2007)

[268] P. Braun-Munzinger and J. Wambach, *Colloquium: Phase diagram of strongly interacting matter*, Rev. Mod. Phys. **81**, 1031 (2009)

[269] P. Braun-Munzinger, *et al*, *Thermal and hadrochemical equilibration in nucleus-nucleus collisions at the SPS*, Phys. Lett. B **365**, 1 (1996) [nucl-th/9508020]

[270] P. Braun-Munzinger and J. Stachel, *Probing the phase boundary between hadronic matter and the quark - gluon plasma in relativistic heavy ion collisions*, Nucl. Phys. A **606**, 320 (1996) [nucl-th/9606017]

[271] P. Braun-Munzinger, K. Redlich and J. Stachel, *Particle production in heavy ion collisions*, In *Hwa, R.C. (ed.) et al.: Quark gluon plasma*, 491 (2003) [nucl-th/0304013]

[272] F. Becattini, *et al*, *Chemical equilibrium in nucleus nucleus collisions at relativistic energies*, Phys. Rev. C **69**, 024905 (2004) [hep-ph/0310049]

[273] A. Andronic, P. Braun-Munzinger and J. Stachel, *Hadron production in central nucleus-nucleus collisions at chemical freeze-out*, Nucl. Phys. A **772**, 167 (2006) [nucl-th/0511071]

[274] F. Becattini, J. Manninen and M. Gazdzicki, *Energy and system size dependence of chemical freeze-out in relativistic nuclear collisions*, Phys. Rev. C **73**, 044905 (2006) [hep-ph/0511092]

[275] P. Braun-Munzinger, J. Stachel and C. Wetterich, *Chemical freezeout and the QCD phase transition temperature*, Phys. Lett. B **596**, 61 (2004) [nucl-th/0311005]

[276] P. de Forcrand, *Simulating QCD at finite density*, PoS LATTICE **2009**, 010 (2009) [arXiv:1005.0539]

[277] O. Philipsen, *Lattice QCD at non-zero temperature and baryon density*, arXiv:1009.4089

[278] G. Endrodi, *et al*, *The QCD phase diagram at nonzero quark density*, JHEP **1104**, 001 (2011) [arXiv:1102.1356]

[279] J. Adams, *et al.* [STAR Collaboration], *Azimuthal anisotropy in Au+Au collisions at s(NN)**(1/2) = 200-GeV*, Phys. Rev. C **72**, 014904 (2005) [nucl-ex/0409033]

[280] KAamodt, *et al.* [ALICE Collaboration], *Elliptic flow of charged particles in Pb-Pb collisions at 2.76 TeV*, Phys. Rev. Lett. **105**, 252302 (2010) [arXiv:1011.3914]

[281] P. Huovinen, *et al*, *Radial and elliptic flow at RHIC: Further predictions*, Phys. Lett. B **503**, 58 (2001) [hep-ph/0101136]

[282] D. Teaney, J. Lauret and E. V. Shuryak, *Hydro+cascade, flow, the equation of state, predictions and data*, Nucl. Phys. A **698**, 479 (2002) [nucl-th/0104041]

[283] H. B. Meyer, *Transport Properties of the Quark-Gluon Plasma: A Lattice QCD Perspective*, Eur. Phys. J. A **47**, 86 (2011) [arXiv:1104.3708]

[284] O. Philipsen, *The QCD equation of state from the lattice*, arXiv:1207.5999

[285] C. R. Allton, *et al*, *The QCD thermal phase transition in the presence of a small chemical potential*, Phys. Rev. D **66**, 074507 (2002) [hep-lat/0204010]

[286] C. R. Allton, *et al*, *Thermodynamics of two flavor QCD to sixth order in quark chemical potential*, Phys. Rev. D **71**, 054508 (2005) [hep-lat/0501030]

[287] I. M. Barbour, *et al*, *The Critical points of strongly coupled lattice QCD at nonzero chemical potential*, Phys. Rev. D **56**, 7063 (1997) [hep-lat/9705038]

[288] Z. Fodor and S. D. Katz, *A New method to study lattice QCD at finite temperature and chemical potential*, Phys. Lett. B **534**, 87 (2002) [hep-lat/0104001]

[289] P. de Forcrand, S. Kim and T. Takaishi, *QCD simulations at small chemical potential*, Nucl. Phys. Proc. Suppl. **119**, 541 (2003) [hep-lat/0209126]

[290] G. Parisi, *On Complex Probabilities*, Phys. Lett. B **131**, 393 (1983)

[291] G. Aarts and I. -O. Stamatescu, *Stochastic quantization at finite chemical potential*, JHEP **0809**, 018 (2008) [arXiv:0807.1597]

[292] J. M. Pawlowski, *The QCD phase diagram: Results and challenges*, AIP Conf. Proc. **1343**, 75 (2011) [arXiv:1012.5075]

[293] C. S. Fischer, J. Luecker and J. A. Mueller, *Chiral and deconfinement phase transitions of two-flavour QCD at finite temperature and chemical potential*, Phys. Lett. B **702**, 438 (2011) [arXiv:1104.1564]

[294] S. Borsanyi, *et al*, *The QCD equation of state and the effects of the charm*, PoS LATTICE **2011**, 201 (2011) [arXiv:1204.0995]

[295] L. G. Yaffe and B. Svetitsky, *First Order Phase Transition in the SU(3) Gauge Theory at Finite Temperature*, Phys. Rev. D **26**, 963 (1982)

[296] F. Karsch, E. Laermann and C. Schmidt, *The Chiral critical point in three-flavor QCD*, Phys. Lett. B **520**, 41 (2001) [hep-lat/0107020]

[297] P. de Forcrand and O. Philipsen, *The QCD phase diagram for three degenerate flavors and small baryon density*, Nucl. Phys. B **673**, 170 (2003) [hep-lat/0307020]

[298] S. Kim, *et al*, *The 3-state Potts model as a heavy quark finite density laboratory*, PoS LATTICE **2005**, 166 (2006) [hep-lat/0510069]

[299] P. de Forcrand and O. Philipsen, *The Chiral critical line of N(f) = 2+1 QCD at zero and non-zero baryon density*, JHEP **0701**, 077 (2007) [hep-lat/0607017]

[300] P. de Forcrand, S. Kim and O. Philipsen, *A QCD chiral critical point at small chemical potential: Is it there or not?*, PoS LATTICE **2007**, 178 (2007) [arXiv:0711.0262]

[301] G. Endrodi, *et al*, *The Nature of the finite temperature QCD transition as a function of the quark masses*, PoS LATTICE **2007**, 182 (2007) [arXiv:0710.0998]

[302] Y. Aoki, *et al*, *The Order of the quantum chromodynamics transition predicted by the standard model of particle physics*, Nature **443**, 675 (2006) [hep-lat/0611014]

[303] S. Borsanyi, *et al.* [Wuppertal-Budapest Collaboration], *Is there still any T_c mystery in lattice QCD? Results with physical masses in the continuum limit III*, JHEP **1009**, 073 (2010) [arXiv:1005.3508]

[304] A. Butti, A. Pelissetto and E. Vicari, *On the nature of the finite temperature transition in QCD*, JHEP **0308**, 029 (2003) [hep-ph/0307036]

[305] K. Rajagopal and F. Wilczek, *Static and dynamic critical phenomena at a second order QCD phase transition*, Nucl. Phys. B **399**, 395 (1993) [hep-ph/9210253]

[306] F. Karsch, *Scaling of pseudocritical couplings in two flavor QCD,* Phys. Rev. D **49**, 3791 (1994) [hep-lat/9309022]

[307] F. Karsch and E. Laermann, *Susceptibilities, the specific heat and a cumulant in two flavor QCD*, Phys. Rev. D **50**, 6954 (1994) [hep-lat/9406008]

[308] A. Berera, *Second order scaling in the two flavor QCD chiral transition*, Phys. Rev. D **50**, 6949 (1994) [hep-ph/9409218]

[309] S. Aoki *et al.* [JLQCD Collaboration], *Scaling study of the two flavor chiral phase transition with the Kogut-Susskind quark action in lattice QCD*, Phys. Rev. D **57**, 3910 (1998) [hep-lat/9710048]

[310] E. Laermann, *Thermodynamics using Wilson and staggered quarks*, Nucl. Phys. Proc. Suppl. **63**, 114 (1998) [hep-lat/9802030]

[311] C. W. Bernard *et al.* [MILC Collaboration], *Scaling tests of the improved Kogut-Susskind quark action*, Phys. Rev. D **61**, 111502 (2000) [hep-lat/9912018]

[312] Y. Iwasaki, *et al*, *Scaling of chiral order parameter in two flavor QCD*, Phys. Rev. Lett. **78**, 179 (1997) [hep-lat/9609022]

[313] S. Aoki, *et al*, *Finite temperature chiral transitions in QCD with the Wilson quark action*, Nucl. Phys. Proc. Suppl. **63**, 397 (1998) [hep-lat/9710031]

[314] M. D'Elia, A. Di Giacomo and C. Pica, *Two flavor QCD and confinement*, Phys. Rev. D **72**, 114510 (2005) [hep-lat/0503030]

[315] G. Cossu, *et al*, *A Test of first order scaling in N(f) = 2 QCD*, PoS LATTICE **2007**, 219 (2007) [arXiv:0710.0174]

[316] C. Bonati, *et al*, *A Test of first order scaling in Nf =2 QCD: A Progress report*, PoS LATTICE **2008**, 204 (2008) [arXiv:0901.3231]

[317] T. Umeda, *et al.* [WHOT-QCD Collaboration], *Equation of state in 2+1 flavor QCD with improved Wilson quarks by the fixed scale approach*, Phys. Rev. D **85**, 094508 (2012) [arXiv:1202.4719]

[318] S. Borsanyi, *et al.*, *QCD thermodynamics with continuum extrapolated Wilson fermions I*, arXiv:1205.0440

[319] M. Creutz, *Chiral anomalies and rooted staggered fermions*, Phys. Lett. B **649**, 230 (2007) [hep-lat/0701018]

[320] V.G. Bornyakov, *et al.*, *Probing the finite temperature phase transition with $N_f =$ 2 non-perturbatively improved Wilson fermions*, Phys. Rev. **D82**, 014504 (2010) [arXiv:0910.2392]

[321] V. G. Bornyakov, *et al*, *Finite temperature phase transition with two flavors of improved Wilson fermions*, arXiv:1102.4461

[322] F. Burger, *et al.* [tmfT Collaboration], *Thermal transition temperature from twisted mass QCD*, PoS LATTICE **2010**, 220 (2010) [arXiv:1009.3758]

[323] O. Philipsen and L. Zeidlewicz, *Cut-off effects of Wilson fermions on the QCD equation of state to $O(g^2)$*, Phys. Rev. D **81**, 077501 (2010) [arXiv:0812.1177]

[324] A. Bazavov, *et al.* [HotQCD Collaboration], *The chiral transition and $U(1)_A$ symmetry restoration from lattice QCD using Domain Wall Fermions*, arXiv:1205.3535

[325] S. Borsanyi, *et al.*, *QCD thermodynamics with dynamical overlap fermions*, Phys. Lett. B **713**, 342 (2012) [arXiv:1204.4089]

[326] L. D. McLerran and B. Svetitsky, *Quark Liberation at High Temperature: A Monte Carlo Study of SU(2) Gauge Theory*, Phys. Rev. D **24**, 450 (1981)

[327] O. Kaczmarek, *et al*, *Heavy quark anti-quark free energy and the renormalized Polyakov loop*, Phys. Lett. B **543**, 41 (2002) [hep-lat/0207002]

[328] H. Wittig, *Improved Calculational Methods For Monte Carlo Simulations Of The Su(2) Higgs Model*, Nucl. Phys. B **325**, 242 (1989)

[329] M. Teper, *An Improved Method for Lattice Glueball Calculations*, Phys. Lett. B **183**, 345 (1987)

[330] A. Hasenfratz and F. Knechtli, *Flavor symmetry and the static potential with hypercubic blocking*, Phys. Rev. D **64**, 034504 (2001) [hep-lat/0103029]

[331] M. Bochicchio, *et al*, *Chiral Symmetry on the Lattice with Wilson Fermions*, Nucl. Phys. B **262**, 331 (1985)

[332] A. Ali Khan, *et al.* [CP-PACS Collaboration], *Phase structure and critical temperature of two flavor QCD with renormalization group improved gauge action and clover improved Wilson quark action*, Phys. Rev. D **63**, 034502 (2001) [hep-lat/0008011]

[333] L. Giusti and M. Luscher, *Chiral symmetry breaking and the Banks-Casher relation in lattice QCD with Wilson quarks*, JHEP **0903**, 013 (2009) [arXiv:0812.3638]

[334] F. Karsch and H. W. Wyld, *Thermal Green's Functions And Transport Coefficients On The Lattice*, Phys. Rev. D **35**, 2518 (1987)

[335] G. Aarts and J. M. Martinez Resco, *Transport coefficients, spectral functions and the lattice*, JHEP **0204**, 053 (2002) [hep-ph/0203177]

[336] T. Matsui and H. Satz, *J/psi Suppression by Quark-Gluon Plasma Formation*, Phys. Lett. B **178**, 416 (1986)

[337] R. Rapp, J. Wambach and H. van Hees, *The Chiral Restoration Transition of QCD and Low Mass Dileptons*, arXiv:0901.3289

[338] H. -T. Ding, *et al*, *Thermal dilepton rate and electrical conductivity: An analysis of vector current correlation functions in quenched lattice QCD*, Phys. Rev. D **83**, 034504 (2011) [arXiv:1012.4963]

[339] G. Boyd, *et al*, *Two flavor QCD phase transition*, hep-lat/9607046

[340] C. W. Bernard, *et al.*, *Which chiral symmetry is restored in high temperature QCD?*, Phys. Rev. Lett. **78**, 598 (1997) [hep-lat/9611031]

[341] F. Karsch and E. Laermann, *Thermodynamics and in medium hadron properties from lattice QCD*, In Hwa, R.C. (ed.) et al.: *Quark gluon plasma*, 1 (2003) [hep-lat/0305025]

[342] M. Cheng, *et al.*, *Meson screening masses from lattice QCD with two light and the strange quark*, Eur. Phys. J. C **71**, 1564 (2011) [arXiv:1010.1216]

[343] T. Appelquist and R. D. Pisarski, *High-Temperature Yang-Mills Theories and Three-Dimensional Quantum Chromodynamics*, Phys. Rev. D **23**, 2305 (1981)

[344] V. L. Eletskii and B. L. Joffe, *On Temperature Dependence of Correlators of Hadronic Currents*, Sov. J. Nucl. Phys. **48**, 384 (1988)

[345] W. Florkowski and B. L. Friman, *Spatial dependence of the finite temperature meson correlation function*, Z. Phys. A **347**, 271 (1994)

[346] M. Laine and M. Vepsalainen, *Mesonic correlation lengths in high temperature QCD*, JHEP **0402**, 004 (2004) [hep-ph/0311268]

[347] W. M. Alberico, *et al*, *Meson Screening Masses in the Interacting QCD Plasma*, Nucl. Phys. A **792**, 152 (2007) [hep-ph/0703298]

[348] S. Wissel, *et al*, *Meson correlation functions at high temperaturesf*, PoS LATTICE **2005**, 164 (2006) [hep-lat/0510031]

[349] S. Mukherjee [RBC-Bielefeld Collaboration], *Screening masses of mesons in 2+1 flavour QCD*, PoS LATTICE **2007**, 210 (2007) [arXiv:0710.0963]

[350] S. Mukherjee, *Screening of light mesons and charmonia at high temperature*, Nucl. Phys. A **820**, 283C (2009) [arXiv:0810.2906]

[351] D. Banerjee, R. Gavai and S. Gupta, *The scalar does not decay at finite temperatures*, PoS LATTICE **2010**, 168 (2010) [arXiv:1011.0310]

[352] D. Banerjee, R. V. Gavai and S. Gupta, *Quasi-static probes of the QCD plasma*, Phys. Rev. D **83**, 074510 (2011) [arXiv:1102.4465]

[353] Private communication with Saumen Datta at the Lattice conference 2012 in Cairns, Australia.

[354] K. Kanaya and S. Kaya, *Critical exponents of a three dimensional O(4) spin model*, Phys. Rev. D **51**, 2404 (1995) [hep-lat/9409001]

[355] D. P. Landau and K. Binder, *Phase diagrams and critical behavior of Ising square lattices with nearest-, next-nearest-, and third-nearest-neighbor couplings*, Phys. Rev. B **31**, 5946 (1985)

[356] M. S. S. Challa, D. P. Landau and K. Binder, *Finite size effects at temperature driven first order transitions*, Phys. Rev. B **34**, 1841 (1986)

[357] M. Fukugita, M. Okawa and A. Ukawa, *Finite Size Scaling Study Of The Deconfining Phase Transition In Pure Su(3) Lattice Gauge Theory*, Nucl. Phys. B **337**, 181 (1990)

[358] J. Engels, *et al*, *Finite size scaling functions for 3-d O(4) and O(2) spin models and QCD*, Phys. Lett. B **514**, 299 (2001) [hep-lat/0105028]

[359] S. Ejiri, *et al.*, *On the magnetic equation of state in (2+1)-flavor QCD*, Phys. Rev. D **80**, 094505 (2009) [arXiv:0909.5122]

[360] S. Z. Huang, *et al*, *Using Histograms In The Study Of The Thermodynamics Of Qcd At Finite Temperature*, Nucl. Phys. Proc. Suppl. **17**, 281 (1990)

[361] S. -z. Huang, *et al*, *The density of states method and the velocity of sound in hot QCD*, Z. Phys. C **50**, 221 (1991)

[362] H. Saito, *et al.* [WHOT-QCD Collaboration], *Phase structure of finite temperature QCD in the heavy quark region*, Phys. Rev. D **84**, 054502 (2011) [Erratum-ibid. D **85**, 079902 (2012)] [arXiv:1106.0974]

[363] B. B. Brandt, *et al*, *Towards the $N_f = 2$ deconfinement transition temperature with $O(a)$ improved Wilson fermions*, PoS LATTICE **2010**, 172 (2010) [arXiv:1008.2143]

[364] Y. Nakagawa, *et al.* [WHOT-QCD Collaboration], *Histogram method in finite density QCD with phase quenched simulations*, PoS LATTICE **2011**, 208 (2011) [arXiv:1111.2116]

[365] S. Ejiri, *Remarks on the multiparameter reweighting method for the study of lattice QCD at nonzero temperature and density*, Phys. Rev. D **69**, 094506 (2004) [hep-lat/0401012]

[366] M. Luscher and F. Palombi, *Fluctuations and reweighting of the quark determinant on large lattices*, PoS LATTICE **2008**, 049 (2008) [arXiv:0810.0946]

[367] `http://www.ginac.de/CLN`

[368] `http://gmplib.org/`

[369] B. B. Brandt, *et al*, *Towards the $N_f = 2$ deconfinement transition temperature with $O(a)$ improved Wilson fermions: An update*, AIP Conf. Proc. **1343**, 516 (2011) [arXiv:1011.6172]

[370] S. Aoki, A. Ukawa and T. Umemura, *Finite temperature phase structure of lattice QCD with Wilson quark action*, Phys. Rev. Lett. **76**, 873 (1996) [hep-lat/9508008]

[371] S. Aoki, *Phase structure of lattice QCD with Wilson fermion at finite temperature*, Nucl. Phys. Proc. Suppl. **60A**, 206 (1998) [hep-lat/9707020]

[372] M. Guagnelli, *et al.* [ALPHA Collaboration], *Precision computation of a low-energy reference scale in quenched lattice QCD*, Nucl. Phys. B **535**, 389 (1998) [hep-lat/9806005]

[373] L. Zeidlewicz, *The Thermal Transition of Quantum Chromodynamics with Twisted Mass Fermions*, PhD-Thesis, Goethe-Universität Frankfurt (2011)

[374] B. Grossman, *et al*, *Glueball - like screening masses in pure SU(3) at finite temperatures*, Nucl. Phys. B **417**, 289 (1994) [hep-lat/9309007]

[375] S. Datta and S. Gupta, *Dimensional reduction and screening masses in pure gauge theories at finite temperature*, Nucl. Phys. B **534**, 392 (1998) [hep-lat/9806034]

[376] S. Datta and S. Gupta, *Screening masses in SU(2) pure gauge theory*, Phys. Lett. B **471**, 382 (2000) [hep-lat/9906023]

[377] D. T. Son and M. A. Stephanov, *Pion propagation near the QCD chiral phase transition*, Phys. Rev. Lett. **88**, 202302 (2002) [hep-ph/0111100]

[378] D. T. Son and M. A. Stephanov, *Real time pion propagation in finite temperature QCD*, Phys. Rev. D **66**, 076011 (2002) [hep-ph/0204226]

[379] M. Cheng, *et al.*, *Study of the finite temperature transition in 3-flavor QCD using the R and RHMC algorithms*, Phys. Rev. D **75**, 034506 (2007) [hep-lat/0612001]

[380] F. Karsch, C. Schmidt and S. Stickan, *Common features of deconfining and chiral critical points in QCD and the three state Potts model in an external field*, Comput. Phys. Commun. **147**, 451 (2002) [hep-lat/0111059]

[381] B. B. Brandt, A. Francis, H. B. Meyer and H. Wittig, in preparation

[382] H. B. Meyer, *A Calculation of the shear viscosity in SU(3) gluodynamics*, Phys. Rev. D **76**, 101701 (2007) [arXiv:0704.1801]

[383] H. B. Meyer, *A Calculation of the bulk viscosity in SU(3) gluodynamics*, Phys. Rev. Lett. **100**, 162001 (2008) [arXiv:0710.3717]

[384] V. Gülpers, Talk presented at the *30th International Symposium on Lattice Field Theory*, Cairns, Australia (2012)

[385] Personal communications with Andreas Jüttner.

[386] D. Djukanovic, *et al*, *Universality of the rho-meson coupling in effective field theory*, Phys. Rev. Lett. **93**, 122002 (2004) [hep-ph/0407239]

[387] D. Djukanovic, *et al*, *Quantum electrodynamics for vector mesons*, Phys. Rev. Lett. **95**, 012001 (2005) [hep-ph/0505180]

[388] U. Wolff [ALPHA Collaboration], *Monte Carlo errors with less errors*, Comput. Phys. Commun. **156**, 143 (2004) [Erratum-ibid. **176**, 383 (2007)] [hep-lat/0306017]

[389] B. Efron, *The jackknife, the bootstrap and other resampling plans*, SIAM, 117 S. 17th st., Philadelphia, PA 19103 (1982)

[390] W. H. Press *et al*, *Numerical Recipes: The Art of Scientific Computing*, Cambridge University Press, Cambridge, UK, Third Edition (2007), `ISBN-10:0521880688`

[391] G.E.P. Box and M.E. Müller, *A Note on the Generation of Random Normal Deviates*, Ann. Math. Statist. **29** Number 2, 610 (1958)

[392] S. Aoki and Y. Kuramashi, *Determination of the improvement coefficient c(SW) up to one loop order with the conventional perturbation theory*, Phys. Rev. D **68**, 094019 (2003) [hep-lat/0306015]

[393] S. Aoki, *et al*, *Perturbative renormalization factors in domain wall QCD with improved gauge actions*, Phys. Rev. D **67**, 094502 (2003) [hep-lat/0206013]

[394] A. Athenodorou, H. Panagopoulos and A. Tsapalis, *The Lattice Free Energy of QCD with Clover Fermions, up to Three-Loops*, Phys. Lett. B **659**, 252 (2008) [arXiv:0710.3856]

[395] H. Panagopoulos and Y. Proestos, *The Critical hopping parameter in O(a) improved lattice QCD*, Phys. Rev. D **65**, 014511 (2002) [hep-lat/0108021]

[396] A. Bode, H. Panagopoulos and Y. Proestos, *O(a) improved QCD: The Three loop beta function, and the critical hopping parameter*, Nucl. Phys. Proc. Suppl. **106**, 832 (2002) [hep-lat/0110225]

[397] S. Adler, *Overrelaxation method for the Monte Carlo evaluation of the partition function for multiquadratic actions*, Phys. Rev. **D23** (1981)

[398] S. Adler, *Overrelaxation algorithms for lattice field theories*, Phys. Rev. **D37** (1988)

[399] M. Creutz, *Overrelaxation and Monte Carlo simulation*, Phys. Rev. **D36** (1987)

[400] B. Alles, M. Campostrini, A. Feo and H. Panagopoulos, *The Three loop lattice free energy*, Phys. Lett. B **324**, 433 (1994) [hep-lat/9306001]

[401] Personal communications with Owe Philipsen.

[402] Personal communication with Marina Marinkovic, Stefan Schäfer and Rainer Sommer.

[403] Personal communication with Rainer Sommer, Michael Donellan and Francesco Virotta.